UNIVERSITEIT VAN PRETORIA
UNIVERSITY OF PRETORIA
YUNIBESITHI YA PRETORIA

IMPROVING OFF-ROAD VEHICLE LATERAL STABILITY WITH INTEGRATED CHASSIS CONTROL

by

Simon Johan Scholtz (15016766)

A research study submitted in partial fulfilment of the degree
Master of Engineering
(Mechanical Engineering)

Faculty of Engineering, Built Environment
and Information Technology (EBIT)
University of Pretoria, South Africa
Submitted in October 2022

SUMMARY

Title:	Improving off-road vehicle lateral stability with integrated chassis control
Author:	Simon Johan Scholtz (15016766)
Supervisor:	Dr. Herman Adendorff Hamersma
Department:	Department of Mechanical and Aeronautical Engineering
Keywords:	off-road vehicle stability control; off-road vehicle integrated chassis control (ICC); off-road vehicle active rear steering; off-road vehicle differential braking; sliding mode stability control

Advanced driver assistance systems (ADAS) such as the anti-lock braking system (ABS), active suspension and active steering are shown to improve vehicle safety by reducing accident occurrence and severity for a wide range of driving conditions. Several studies indicate that an even greater level of safety may be attained by the integrated control of individual systems, although not much research specific to off-road driving conditions have been done.

The aim of this study is to investigate whether there is an improvement achievable in the lateral stability of an off-road vehicle by integrated control of chassis control systems and how the performance of such systems compares for smooth and rough roads.

The following research questions are posed:

a. What are objective indicators of lateral stability?
b. What are the causes of lateral instability for on-road and off-road conditions?
c. Which chassis control systems can be integrated to improve lateral stability for on-road and off-road conditions?
d. How does integrated chassis control system performance compare to stand-alone systems for lateral stability on on-road and off-road conditions?
e. How does the performance of chassis control systems for lateral stability differ for on-road versus off-road conditions; is there a universal configuration?

For (a) it was determined that the understeer gradient, phase plane location and kinematic model reference error are indicators of vehicle lateral stability. (b) It was found that factors which reduce a vehicle's lateral force generating capability cause lateral instability. These are factors such as lateral load transfer which occurs on all terrains and tyre normal force fluctuations which occurs on rough terrain. (c) Consequently, systems which retain a vehicle's lateral force generating capability improve lateral stability. This study improves lateral stability by directly controlling vehicle sideslip and yaw rate with rear differential braking (RDB) and active rear steering (ARS).

Two stability control reference models were investigated, namely the kinematic model reference error, which determines a reference yaw rate and sideslip angle from vehicle

geometry, and a sideslip model (phase plane location error) which limits sideslip angle and rate development within a bounded region. It was determined that the kinematic model reference error is a superior reference model for both smooth and rough roads and both ARS and RDB control strategies. Stability controllers with this model improved on the baseline vehicle (without stability control) lateral stability on both terrains.

(d) It was found that integrated chassis control systems improve on stand-alone system performance and can be tuned to obtain a desired blended response. The study found that RDB tends to improve on the baseline vehicle path following ability for a double lane change (DLC) manoeuvre, but has a larger loss of speed compared to ARS. ARS, on the other hand, also improves on the baseline vehicle path following ability, but to a lesser degree, and exhibits lower loss of speed compared to RDB. Rear wheel slip angle was shown to be an effective, tuneable integration rule to combine the two stand-alone systems of ARS and RDB. Proper tuning of the integration rule resulted in an integrated control system that has the good path following ability of RDB but low loss of speed associated with ARS. This was observed for both smooth and rough roads. Which of either RDB or ARS has the lowest peak yaw rate, sideslip angle or roll angle is terrain dependant, however the integrated system improved on the worst performing system for those metrics after tuning.

For (e) it was observed that each stand-alone system (RDB or ARS) requires a tuned gain that depends on the road classification and the reference model used. If the gains are properly tuned, their strengths on smooth roads are also realised on rough roads. If there is a big difference in the optimal gains of a system on two terrains and the system is placed on a terrain for which it has too high a gain, the system becomes unstable. A universal configuration would make provision for the lowest gain of all terrains, providing robustness. If it were possible to know the terrain conditions such as road profile classification and surface friction coefficient before a loss of control event, the vehicle can switch to the optimal gain and system performance is not suboptimal as with a universal configuration.

Future work should focus on:

1. Experimental validation of results.
2. Creating a gain schedule for a larger range of operating conditions.
3. Developing or including existing means of accurately estimating the ISO8608:2016 road classification while driving.
4. Including active or semi-active suspension control in the integrated chassis controller.

AKNOWLEDGEMENTS

This thesis has been done at the Vehicle Dynamics Group (VDG) of the University of Pretoria to which I gratefully acknowledge their professional contribution and financial support. I extend my gratitude towards Prof. Schalk Els, leader of VDG and Dr. Herman Hamersma, my supervisor at the group for his mentorship. I would like to thank Andries Peenze, a friend and VDG colleague with whom I could often discuss ideas and get valuable feedback. I am appreciative of my VDG colleagues who have become friends through our ritual coffee-time conversations and who have contributed in one way or another to this study.

Finally, I would like to thank my friends and family for continued support throughout my studies. I am fortunate to have been working at my father's mechanic workshop from a young age which inspired me to pursue an education in vehicle engineering.

Soli Deo Gloria

TABLE OF CONTENTS

LIST OF TABLES AND FIGURES

Figure	Description	Page

Chapter 1 INTRODUCTION

Chapter 2 LITERATURE REVIEW

Chapter 3 VEHICLE DYNAMICS AND MODELING

APPENDIX A-D

LIST OF SYMBOLS

Symbol	Unit	Description
$\boldsymbol{A}$	$[rad \cdot s^{-2}]$	ABS upper wheel acceleration threshold
$\boldsymbol{a}$	$[-][rad \cdot s^{-2}]$	Stable wheel deceleration zone or wheel angular acceleration
$\boldsymbol{a_i}$		MF lateral force parameters ($i = 0 \dots 13$)
$\boldsymbol{a_{max}}$	$[rad \cdot s^{-2}]$	ABS upper wheel acceleration threshold
$\boldsymbol{a_{min}}$	$[rad \cdot s^{-2}]$	ABS lower wheel acceleration threshold
$\boldsymbol{a_y}$	$[m \cdot s^{-2}][g]$	Centripetal acceleration or lateral acceleration
$\boldsymbol{\hat{a}_y}$	$[m \cdot s^{-2}][g]$	Estimated centripetal acceleration
$\boldsymbol{B}$		Magic formula stiffness factor
$\boldsymbol{BCD}$		Magic formula linear cornering stiffness coefficient
$\boldsymbol{b}$	$[m]$[-]	Distance from front axle to CG or unstable wheel deceleration zone
$\boldsymbol{b_i}$		MF longitudinal force parameters ($i = 0 \dots 10$)
$\boldsymbol{C}$		Magic formula shape factor
$\boldsymbol{C_\alpha}$	$[N/rad]$	Cornering stiffness
$\boldsymbol{C_{\alpha f}}$	$[N/rad]$	Front axle tyre cornering stiffness
$\boldsymbol{C_{\alpha r}}$	$[N/rad]$	Rear axle tyre cornering stiffness
$\boldsymbol{c_1}$		SI sideslip angle parameter
$\boldsymbol{c_2}$		SI sideslip rate parameter
$\boldsymbol{c}$	$[m]$	Distance from rear axle to CG
$\mathbf{c_t}$	$[N \cdot m^{-1}s^{-1}]$	Vertical tyre damping
$\boldsymbol{D}$		Magic formula peak value
$\boldsymbol{E}$		Magic formula curvature factor
$\boldsymbol{e}$		Error
$\boldsymbol{e_i}$		Error applicable to each wheel ($i = 1 \dots 4$)
$\boldsymbol{F_{FL}}$	$[N]$	Front left suspension force
$\boldsymbol{F_{FR}}$	$[N]$	Front right suspension force
$\boldsymbol{F_R}$	$[N]$	Tyre friction limit
$\boldsymbol{F_{RL}}$	$[N]$	Rear left suspension force
$\boldsymbol{F_{RR}}$	$[N]$	Rear right suspension force
$\boldsymbol{F_{max}}$	$[N]$	Maximum force generated
$\boldsymbol{F_{steering}}$	$[N]$	Force imposed on linear actuator
$\boldsymbol{F_x}$	$[N]$	Tyre longitudinal force

$\boldsymbol{F_{x3}}$	$[N]$	Rear left longitudinal force
$\boldsymbol{F_{x4}}$	$[N]$	Rear right longitudinal force
$\boldsymbol{F_{x\,combined}}$	$[N]$	Combined loading tyre longitudinal force (Magic formula)
$\boldsymbol{F_{xi(SC)}}$	$[N]$	Reference rear longitudinal force ($i = 3{,}4$)
$\boldsymbol{F_{y}}$	$[N]$	Tyre lateral force
$\boldsymbol{F_{y\,combined}}$	$[N]$	Combined loading tyre lateral force (Magic formula)
$\boldsymbol{F_{yf}}$	$[N]$	Front axle lateral force
$\boldsymbol{F_{yr}}$	$[N]$	Rear axle lateral force
$\boldsymbol{F_{yr(SC)}}$	$[N]$	Stability control reference additional rear lateral force
$\boldsymbol{F_{yr(SC\,disabled)}}$	$[N]$	Rear lateral force of the reference (SC disabled) vehicle
$\boldsymbol{F_{z}}$	$[N]$	Tyre normal force
$\boldsymbol{f_{s}}$	$[Hz]$	Sampling frequency
$\boldsymbol{G_{x}}$	$[g]$	Longitudinal acceleration
$\boldsymbol{G_{y}}$	$[g]$	Lateral acceleration
$\boldsymbol{g}$	$[m \cdot s^{-2}]$	Gravity acceleration (constant: $g = 9.81\ m \cdot s^{-2}$)
$\boldsymbol{I_{a}}$	$[A]$	Armature current
$\boldsymbol{I_{xx}}$	$[kgm^2]$	Mass moment of inertia about the longitudinal axis
$\boldsymbol{I_{yy}}$	$[kgm^2]$	Mass moment of inertia about the lateral axis
$\boldsymbol{I_{zz}}$	$[kgm^2]$	Mass moment of inertia about the vertical axis
$\boldsymbol{i_{v}}$		Varying steer ratio factor
$\boldsymbol{K_1}$	$[m]$	Power screw force to torque gain
$\boldsymbol{K_2}$	$[Nm \cdot \sqrt{W}^{-1}]$	Motor torque constant
$\boldsymbol{K_3}$		Motor rotational to linear velocity gain
$\boldsymbol{K_4}$	$[V \cdot (rad^{-1})^{-1}]$	Motor back-EMF constant
$\boldsymbol{K_d}$		PID error derivative gain
$\boldsymbol{K_i}$		PID error integral gain
$\boldsymbol{K_p}$		PID error proportional gain
$\boldsymbol{K_{us}}$	$[°/g]$	Understeer gradient
$\mathbf{K}_{v_y}$		Sideslip angle estimator gain
$\boldsymbol{k}$		SMC discontinuous term design variable
$\boldsymbol{k_1}$		STA tuning parameter
$\boldsymbol{k_2}$		STA tuning parameter
$\boldsymbol{k_{SMC}}$		Sliding mode controller gain
$\boldsymbol{k_{SMC(ARS)}}$		ARS sliding mode controller gain
$\boldsymbol{k_{SMC(RDB)}}$		RDB sliding mode controller gain
$\boldsymbol{k_t}$	$[N \cdot m^{-1}]$	Vertical tyre stiffness
$\boldsymbol{L}$	$[m]$	Wheelbase

$\boldsymbol{l_f}$	$[m]$	Distance from front axle to CG
$\boldsymbol{l_r}$	$[m]$	Distance from rear axle to CG
$\boldsymbol{M_{ARS}}$	$[Nm]$	ARS reference yaw moment
$\boldsymbol{M_B}$	$[Nm]$	Braking torque
$\boldsymbol{M_R}$	$[Nm]$	Road surface frictional torque
$\boldsymbol{M_{Rmax}}$	$[Nm]$	Road surface frictional torque limit
$\boldsymbol{M_{RDB}}$	$[Nm]$	RDB reference yaw moment
$\boldsymbol{M_y}$	$[Nm]$	Tyre rolling resistance moment
$\boldsymbol{M_z}$	$[Nm]$	Yaw moment or tyre self-aligning moment
$\boldsymbol{m}$	$[kg]$	Vehicle mass
$\boldsymbol{m_f}$	$[kg]$	Vehicle mass apportioned to the front axle
$\boldsymbol{m_{grad}}$		Connecting line gradient (Phase plane)
$\boldsymbol{m_r}$	$[kg]$	Vehicle mass apportioned to the rear axle
$\boldsymbol{m_s}$	$[kg]$	Sprung mass
$\boldsymbol{m_u}$	$[kg]$	Unsprung mass
$\boldsymbol{n}$		SMC relative degree or the number of sampling points
$\boldsymbol{P_B}$	$[MPa]$	Brake line pressure
$\boldsymbol{P_{B_i(SC)}}$	$[MPa]$	Stability control reference brake line pressure $(i = 1 \dots 4)$
$\boldsymbol{P_{B(ref)}}$	$[MPa]$	Reference brake line pressure
$\boldsymbol{q}$		Cost function
$\boldsymbol{R}$	$[m]$	Radius of turn
$\boldsymbol{r}$	$[rad/s]$ $[m][m]$	Yaw rate or moment arm or loaded tyre radius
$\boldsymbol{r_e}$	$[m]$	Free-rolling tyre effective radius
$\boldsymbol{r_{e0}}$	$[m]$	Reference free-rolling tyre effective radius
$\boldsymbol{r_f}$	$[m]$	Unloaded tyre radius
$\boldsymbol{S_f}$	$[m]$	Distance between front suspension struts
$\boldsymbol{S_h}$		Magic formula horizonal shift
$\boldsymbol{S_r}$	$[m]$	Distance between rear suspension struts
$\boldsymbol{S_v}$		Magic formula vertical shift
$\boldsymbol{s}$	$[-][m]$	Sliding variable or unit vector along wheel spin axis
$\boldsymbol{T}$	$[s]$	Time delay between braking torque and road-surface frictional torque
$\boldsymbol{t}$	$[s]$	Time
$\boldsymbol{t_{hold}}$	$[s]$	ABS phase time limit
$\boldsymbol{t_{up}}$	$[s]$	ABS maximum pressure build time
$\boldsymbol{t_v}$	$[m]$	Vehicle width
$\boldsymbol{t_w}$	$[m]$	Track width
$\boldsymbol{teeth_{LA}}$		Number of teeth on the linear actuator sprocket
$\boldsymbol{teeth_m}$		Number of teeth on the motor sprocket

$\hat{\boldsymbol{u}}$		Best estimate of equivalent control
$\boldsymbol{u}$		Controller input
$\boldsymbol{u_k}$		Estimator input vector
$\boldsymbol{V}$	$[m \cdot s^{-1}]$	Velocity of CG or Wheel centre
$\boldsymbol{V_a}$	$[V]$	Armature voltage
$\boldsymbol{V_{in}}$	$[V]$	Motor input voltage
$\boldsymbol{v_x}$	$[m \cdot s^{-1}]$	Longitudinal velocity
$\dot{\hat{\boldsymbol{v}}}_{\boldsymbol{y}}$	$[m \cdot s^{-2}]$	Estimated lateral acceleration
$\boldsymbol{v_y}$	$[m \cdot s^{-1}]$	Lateral velocity
$\boldsymbol{w_f}$	$[kg]$	Vehicle weight apportioned to the front axle
$\boldsymbol{w_r}$	$[kg]$	Vehicle weight apportioned to the rear axle
$\boldsymbol{w}$		STA error integral component
$\boldsymbol{X}$		Independent variable in magic formula with horizontal shift
$\boldsymbol{X_{CG}}$	$[m]$	CG longitudinal displacement
$\tilde{\boldsymbol{x}}$		Difference between desired and actual system states
$\hat{\boldsymbol{x}}_{\boldsymbol{k}}$		Estimated system state vector
$\boldsymbol{x}$		System states or independent variable in magic formula without horizontal shift
$\boldsymbol{x_{FL}}$	$[m]$	Front left suspension displacement
$\boldsymbol{x_{FR}}$	$[m]$	Front right suspension displacement
$\boldsymbol{x_{LA}}$	$[m]$	Linear actuator displacement
$\boldsymbol{x_{RL}}$	$[m]$	Rear left suspension displacement
$\boldsymbol{x_{RR}}$	$[m]$	Rear right suspension displacement
$\boldsymbol{x_{des}}$		Desired system states
$\boldsymbol{x_t}$		System states at timestep t
$\boldsymbol{x_{(t+\Delta t)}}$		System states at next timestep after t
$\boldsymbol{Y}$	$[N]$	Magic formula output force with vertical shift
$\boldsymbol{Y_{CG}}$	$[m]$	CG lateral position
$\boldsymbol{YRR_{1s}}$		Yaw rate ratio at 1 s after COS (Sine with dwell test)
$\boldsymbol{YRR_{1.75s}}$		Yaw rate ratio at 1.75 s after COS (Sine with dwell test)
$\boldsymbol{y}$	$[N]$	Magic formula output force without vertical shift
$\boldsymbol{z}$	$[m]$	Vehicle CG vertical displacement
$\hat{\boldsymbol{z}}_{\boldsymbol{i}}$	$[m]$	Estimated unsprung mass displacement ($i = 1 \dots 4$)
$\boldsymbol{z_i}$	$[m]$	Unsprung mass displacement ($i = 1 \dots 4$)
$\boldsymbol{z_{0i}}$	$[m]$	Tyre contact patch vertical displacement ($i = 1 \dots 4$)
$\boldsymbol{z_5}$	$[m]$	Sprung mass displacement
$\boldsymbol{z_k}$		Estimator observation vector
$\boldsymbol{\alpha}$	$[rad]$ $[rad \cdot s^{-2}]$	Tyre slip angle or wheel acceleration
$\boldsymbol{\alpha_f}$	$[rad]$	Slip angle at the front wheels

$\boldsymbol{\alpha_r}$	$[rad]$	Slip angle at the rear wheels
$\boldsymbol{\alpha_{r(reference)}}$	$[rad]$	Reference slip angle at the rear wheels
$\boldsymbol{\beta}$	$[rad]$	Vehicle sideslip angle
$\boldsymbol{\beta_{boundary}}$	$[rad]$	Sideslip angle boundary (phase plane)
$\boldsymbol{\beta_{des}}$	$[rad]$	Desired sideslip angle
$\boldsymbol{\beta_{estimated}}$	$[rad]$	Estimated sideslip angle
$\boldsymbol{\beta_{lim}}$	$[rad]$	Sideslip angle at which tyre non linearity starts
$\boldsymbol{\beta_{max}}$	$[rad]$	The maximum sideslip angle on a phase plane for zero sideslip rate
$\boldsymbol{\beta_{measured}}$	$[rad]$	Measured sideslip angle
$\boldsymbol{\beta_{ref}}$	$[rad]$	Vehicle reference sideslip angle
$\boldsymbol{\dot{\beta}_{max}}$	$[rad]$	The maximum sideslip rate on a phase plane for zero sideslip angle
$\boldsymbol{\dot{\beta}_{ref}}$	$[rad]$	Vehicle reference sideslip rate
$\boldsymbol{\gamma}$	$[rad]$	Tyre camber angle
$\boldsymbol{\delta}$	$[rad][-]$	Steering angle or rate of disturbance
$\boldsymbol{\delta_f}$	$[rad]$	Steering angle at the front wheels
$\boldsymbol{\delta_G}$	$[rad]$	Pinion angle
$\boldsymbol{\delta_M}$	$[rad]$	Motor supplied additional steering angle
$\boldsymbol{\delta_r}$	$[rad]$	Steering angle at the rear wheels
$\boldsymbol{\delta_{r(SC)}}$	$[rad]$	Stability control reference rear steering angle
$\boldsymbol{\delta_s}$	$[rad]$	Steering angle
$\boldsymbol{\zeta}$		Sideslip angle error weighting
$\boldsymbol{\zeta_{ARS}}$		Sideslip angle error weighting for the ARS control strategy
$\boldsymbol{\zeta_{RDB}}$		Sideslip angle error weighting for the RDB control strategy
$\boldsymbol{\eta}$		Positive design scalar for the η-reachability condition
$\boldsymbol{\theta}$	$[rad]$	Tyre angular displacement along lateral axis or vehicle pitch
$\boldsymbol{\theta_x}$	$[rad]$	Sprung mass roll angle
$\boldsymbol{\theta_y}$	$[rad]$	Sprung mass pitch angle
$\boldsymbol{\kappa}$		Tyre longitudinal slip ratio
$\boldsymbol{\kappa_i}$		Tyre longitudinal slip ratio ($i = 1 \dots 4$)
$\boldsymbol{\lambda}$		Tyre longitudinal slip ratio or error weighting (SMC)
$\boldsymbol{\lambda_{max}}$	$[rad \cdot s^{-1}]$	ABS upper wheel longitudinal slip threshold for braking
$\boldsymbol{\mu}$		Coefficient of friction
$\boldsymbol{\mu_{HF}}$		Coefficient of friction for high-friction road
$\boldsymbol{\mu_{HFmax}}$		Peak coefficient of friction for high-friction road
$\boldsymbol{\rho}$	$[m]$	Tyre deflection

$\boldsymbol{\sigma^*}$		Ratio of current- to peak combined slip
$\boldsymbol{\sigma_x^*}$		Ratio of current- to peak longitudinal slip ratio
$\boldsymbol{\sigma_y^*}$		Ratio of current- to peak lateral slip angle
$\boldsymbol{\sigma_{xmtot}}$		Peak longitudinal slip ratio
$\boldsymbol{\sigma_{ymtot}}$		Peak lateral slip angle
$\boldsymbol{\tau}$	$[s]$	Time constant
$\boldsymbol{\tau_B}$	$[Nm]$	Braking torque
$\boldsymbol{\tau_{B_i}}$	$[Nm]$	Applied brake torque ($i = 1 \dots 4$)
$\boldsymbol{\tau_{load}}$	$[Nm]$	Steering torque
$\boldsymbol{\tau_m}$	$[Nm]$	Motor torque
$\boldsymbol{\tau_{net}}$	$[Nm]$	Motor net torque
$\boldsymbol{\phi}$	$[rad]$	Vehicle CG roll angle
$\boldsymbol{\phi_{max}}$	$[rad]$	Max vehicle CG roll angle (sine with dwell test)
$\boldsymbol{\psi}$	$[rad]$	Vehicle yaw angle
$\boldsymbol{\dot{\psi}_{des}}$	$[rad \cdot s^{-1}]$	Desired yaw rate
$\boldsymbol{\dot{\psi}_{lim}}$	$[rad \cdot s^{-1}]$	Yaw rate limit before sliding
$\boldsymbol{\dot{\psi}_{peak}}$	$[rad \cdot s^{-1}]$	Sine with dwell peak yaw rate
$\boldsymbol{\dot{\psi}_{ref}}$	$[rad \cdot s^{-1}]$	Reference yaw rate
$\boldsymbol{\omega}$	$[rad \cdot s^{-1}]$	Tyre angular velocity
$\boldsymbol{\omega_0}$	$[rad \cdot s^{-1}]$	Reference free-rolling tyre angular velocity
$\boldsymbol{\omega_i}$	$[rad \cdot s^{-1}]$	Wheel angular velocity ($i = 1 \dots 4$)
$\boldsymbol{\omega_{i(ref)}}$	$[rad \cdot s^{-1}]$	Wheel reference angular velocity ($i = 1 \dots 4$)
$\boldsymbol{\omega_R}$	$[rad \cdot s^{-1}]$	Motor rotor angular velocity

LIST OF ABBREVIATIONS

Abbreviation	Description
3D	Three-dimensional
$4S_4$	Four-state semi-active suspension
4WAS	Four-wheel active steering
4WIS	Four-wheel independent steering
4WS	Four-wheel steering or active rear steering
ABS	Anti-lock braking system
ACEA	European automobile manufacturers association
ADAS	Advanced driver assistance systems
AFIS	Active front independent steering
AFS	Active front steering
ARS	Active rear steering
AS	Active steering
ASC	Advanced stability control
ASR	Active steering ratio
BOS	Beginning of steer
CAN	Controller area network
CG	Centre of gravity
COS	Completion of steer
DIC	Digital image correlation
DLC	Double lane change
DOF	Degree(s) of freedom
DSD	Displacement spectral density
DSF	Damping scaling factor
DYC	Direct yaw control
ECU	Electronic control unit
ESC	Electronic stability control
ESP	Electronic stability program
FFT	Fast Fourier transform
FL	Front left tyre
FR	Front right tyre
FOD	First order delay
FTire	Flexible ring tyre model
FWIS	Front-wheel independent steering

ICC	Integrated chassis control
KMRE	Kinematic model reference error
LOC	Loss of control
MF	Magic formula
NCAP	New car assessment program
NHTSA	National highway traffic safety administration
PID	Proportional-integral-derivative (controller)
PPLE	Phase plane location error
RDB	Rear differential braking
RL	Rear left tyre
RR	Rear right tyre
RMSE	Root mean square error
RRMS	Running root mean square
SC	Stability control(er)
SI	Stability index
SMC	Sliding mode control(er)
STA	Super twisting algorithm
TC	Traction control
VDC	Vehicle dynamics control
VDG	Vehicle dynamics group (University of Pretoria)
VSA	Vehicle stability assist
WFT	Wheel force transducer
YRR	Yaw rate ratio

CHAPTER ONE
INTRODUCTION

Abstract – This chapter provides an overview of the need, historical development and what is now at the forefront of automotive safety systems, specifically advanced driver assistance systems (ADAS). The lack of research specific to off-road vehicles, in off-road conditions, is highlighted and a problem statement is formulated with clear objectives to be addressed in subsequent chapters.

1.1 Background

Driving a vehicle is a dynamic event that requires a human driver as the controller to use steering, throttle and brake inputs to steer a vehicle to an intended destination, avoiding obstacles and reacting to environmental influences along the way. Under certain conditions, the driver may no longer be able to anticipate appropriate inputs to reach a desired state and the vehicle is deemed uncontrollable. This state of controllability or uncontrollability of the driver-vehicle pair is referred to as closed-loop stability and its performance is highly subjective as it depends (among other things) on driver skill. Conversely, the vehicle itself may be deemed unstable if it cannot return to an initial state after a disturbance. This is referred to as open-loop instability and an example thereof is when the vehicle reaches its critical limits so that further input or disturbance causes it to spin out. This criterion is a function of vehicle build and is independent of the driver (Gillespie, 1992). Both closed- and open-loop instability bring about loss of control (LOC) which may result in collision and injury or death. LOC is a major contributor to road traffic accidents that, combined with other causes, lead to 1.35 million road accident deaths globally. A tragic statistic is that road traffic accidents were declared the leading cause of death for children and young adults aged 5 – 29 in 2018 (World Health Organization, 2018). Due to these alarming rates, road accident fatalities is one of the major societal problems facing the world today.

Considering the contribution of LOC to road fatalities, statistics obtained from the US National Highway Traffic Safety Administration (NHTSA) on police reported vehicle crashes for 2017 show that 60.8% of fatal crashes are due to single vehicle crashes (National Highway Traffic Safety Administration, 2017). Single vehicle crashes are strongly linked to vehicle LOC which are caused by several factors such as excessive speed, slippery roads, sharp curves, and obstacles in the road. Statistics from the German Insurance Association indicate that the most common type of road accident resulting in fatalities for 2012 were due to LOC, attributing 1 316 out of the 3 600 fatalities on German roads for that year (German Insurance Association, 2014). In the report, accident causes were categorized as being due to LOC if a driver lost control of the vehicle from driving at an inappropriate speed for the course, cross-section, or road condition. These statistics highlight the need for research on safety systems that prevent LOC to promote safe use of vehicles with fewer fatalities.

An established solution to LOC is the electronic stability control (ESC) developed by Bosch that was first implemented on a commercial vehicle in 1995 (European Patent Office, 2016). This safety system has also seen increasing year-on-year adoption since its market introduction (National Highway Traffic Safety Administration, 2011). ESC uses differential braking, also referred to as direct yaw control (DYC), to brake individual wheels to generate a restoring yaw moment that counters the LOC motion. Since its inception, several studies have confirmed the positive impact of ESC on reducing road accidents and fatalities (European Commission, 2018) (Papelis, et al., 2010). Due to the proven benefit of ESC, a number of countries have made it a mandatory safety system on new passenger vehicles (Global NCAP, 2014), with Canada being the first, starting late 2011 (Transport Canada, 2017). Yet, older vehicles preceding mandatory ESC legislation remain on the road, and not all countries mandate ESC. This and other factors such as the need for reliable tyre-road contact in order for ESC to work are reasons why incidence of fatalities due to LOC are still prevalent.

ESC is one of many systems that collectively are referred to as advanced driver assistance systems (ADAS), all of which improve vehicle safety either directly or indirectly. Examples of such systems are: early warning features such as blind spot monitoring, crash avoidance systems such as lane keep assist, crash severity mitigation systems such as the anti-lock braking system (ABS) and an alternative to brake-based stability control namely active steering (AS) (European Commission, 2018). Together, these systems are considered the next generation safety systems that supplement the passive safety or protective devices where the former enhances the vehicle's ability to avoid a collision and the latter protects occupants from injury (Hu, et al., 2015). In this study, further mention of ADAS refers to those systems that directly affect the vehicle's dynamics by actuators such as the brakes, steering and suspension system that form the chassis control systems.

To understand how ADAS systems influence accident events, the European Automobile Manufacturers Association (ACEA) describes the phases of accident development as shown in Figure 1-1. The idea is that an accident starts with a "normal driving" phase in which the accident is not yet foreseeable. This phase ends with an accident-triggering critical situation that precedes every accident (for example loss of traction on a low friction road). The situation is followed by a "danger" phase which might be an upcoming obstacle in the road or the risk of running off-track. These three phases occur frequently in everyday driving and do not always result in an accident. They are also the phases in which the benefit of ADAS systems are realized to circumvent a dangerous event or to mitigate the effects of collision once the point of no return is passed. If the point of no return of an accident is passed, collision becomes unavoidable and first impact occurs. This is followed by the "during collision" phase and ends when all road users involved come to a standstill in the final situation of the accident. The greatest injuries of those involved occur in the "during collision" phase, which ADAS systems attempt to reduce by intervening in early stages of the accident development phases (German Insurance Association, 2014).

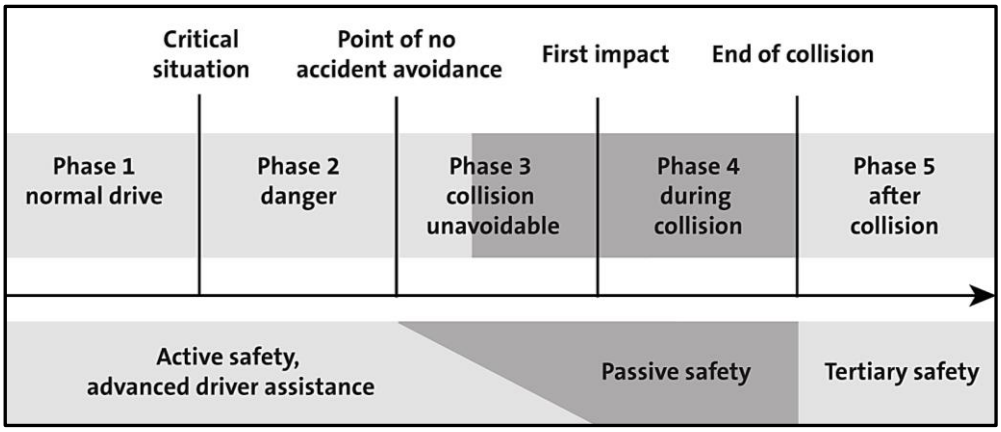

Figure 1-1: The ACEA model for accident phases (German Insurance Association, 2014)

While studies indicate that stand-alone chassis control systems are effective at accident prevention (European Commission, 2018) the forefront of ADAS and chassis control research is now on the integration of individual sub-systems called integrated chassis control (ICC), with promising results. The benefit of ICC is mainly better utilization of tyre-road friction and a greater range of stable vehicle motion compared to stand-alone systems, which improves overall vehicle safety.

With increased complexity of safety systems, there is also a growing concern for potential conflict of sub-systems. The vehicle sprung mass has six degrees of freedom with strong couplings among them which makes it difficult to control individual motion states without affecting others. This interference may compromise the effectiveness of individual systems (Zhu, et al., 2014). Interference occurs when, for example, the brake and steering systems attempt to control the same yaw degree of freedom (DOF) of the vehicle. The role of ICC is to both improve on the effective tyre-road friction range and to minimize the overlap of systems.

While a plethora of on-road ICC for improved vehicle lateral stability exist in literature, off-road specific ADAS and ICC systems research is sparse. ICC systems are largely developed for on-road vehicles driving in on-road conditions while off-road vehicles, posing unique risks due to factors such as a higher centre of gravity (CG) and rough road excitations, have not received the same research effort (Hamersma, et al., 2014) (Kyriakidis, et al., 2015). This study aims to address the gap between on-road and off-road ICC for vehicle lateral stability by exploring the use of selected integrated systems on rough terrain.

For this study, the integration of active rear steering (ARS) and rear differential braking (RDB) is considered. Differential braking is an existing control strategy for ESC equipped commercial vehicles but impose longitudinal force on the vehicle which reduces vehicle speed. ARS imposes lateral force on the vehicle and has a lower utilization of tyre-road friction to generate the same yaw moment as for braking (Ackermann, et al., 1999). Their distinct advantages make ARS and RDB a popular on-road vehicle integration format with proven benefits (Savitski, et al., 2015).

1.2 Problem statement and research objective

The aim of this study is to investigate whether there is an improvement achievable in the lateral stability of an off-road vehicle by integrated control of chassis control systems.

The specific objectives of this study are to determine:

a. What are objective indicators of lateral stability?
b. What are the causes of lateral instability for on-road and off-road conditions?
c. Which chassis control systems can be coordinated to improve lateral stability for on-road and off-road conditions?
d. How does coordinated chassis control system performance compare to stand-alone systems for lateral stability on on-road and off-road conditions?
e. How does the performance of chassis control systems for lateral stability differ for on-road versus off-road conditions, is there a universal configuration?

1.3 Overview of study

The structure of this study is shown in Figure 1-2.

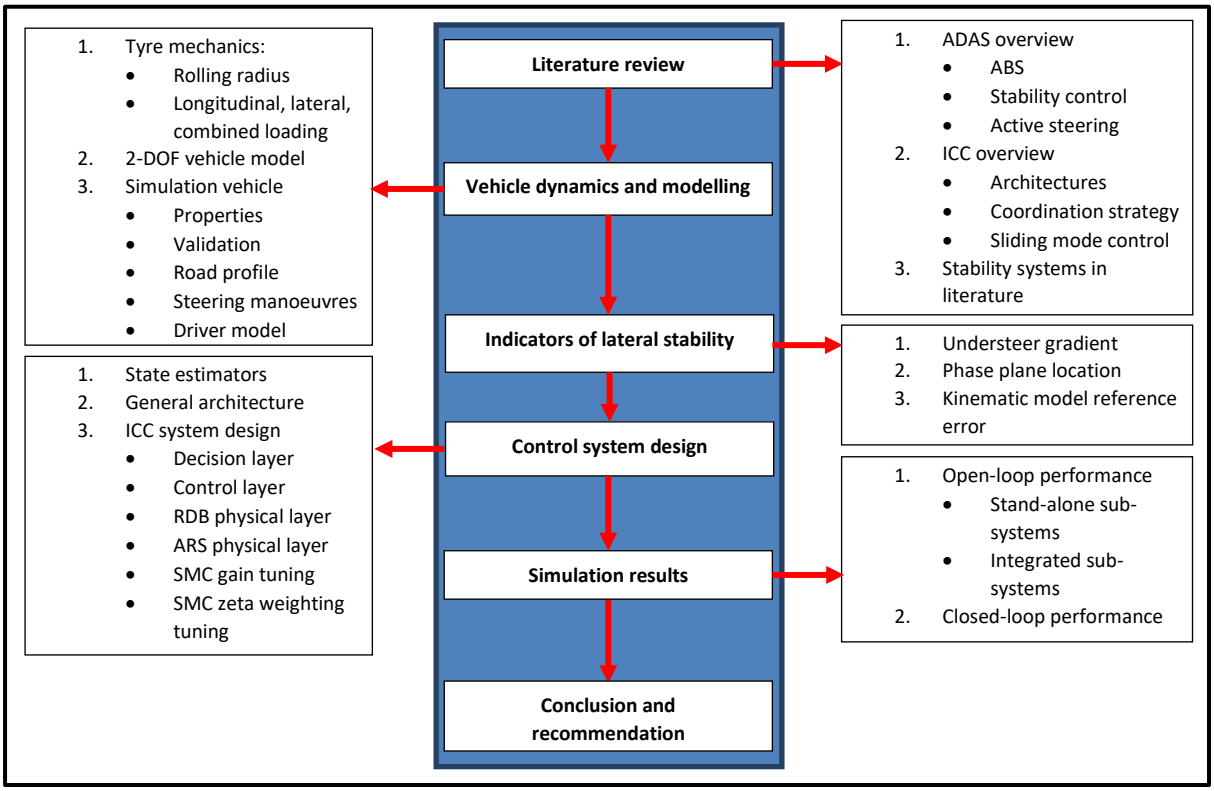

Figure 1-2: The study structure overview

A literature study is performed, starting with an overview of existing stand-alone ADAS such as ABS, stability control and active steering. Various integrated systems are then considered along with the different architectures and coordination strategies. Sliding mode control (SMC) and the relevant theory for control design is discussed followed by an overview of published integrated stability systems.

The following chapter deals with topics on vehicle dynamics modelling such as tyre mechanics and tyre models. The simulation vehicle and its properties are laid out along with the intended road profile, steering manoeuvre and driver model used for simulation testing.

The chapter thereafter considers indicators of lateral stability, some of which are used as a reference for stability control systems. Then, an integrated controller is designed that makes

provision for the individual activation of three integrated system configurations so that the different configurations can be compared. Since the controller has a multi-layer architecture, each of the layers, namely the decision layer, control layer and physical layers, are described in detail. The final section of the chapter deals with selection of the optimal SMC gain and SMC sliding variable zeta weighting per configuration which is a function of stability control reference model, ARS or RDB control strategy and the road classification.

The controller simulation results follow with a series of tests that are used to evaluate the performance of the different systems. Initially, open-loop lane change tests are performed followed by closed-loop double lane change (DLC) tests. The study ends with a final conclusion and recommended future work.

CHAPTER TWO
LITERATURE REVIEW

Abstract – Based on the available actuators and the fact that it is a popular configuration, the control strategies for integration in this study are rear differential braking (RDB) and active rear steering (ARS). This chapter aims to provide an overview of these chassis control systems along with their detailed working and contribution to lateral stability. The theory of integration is considered along with a chosen control method which lays the groundwork for a look at published integrated systems.

2.1 Advanced driver assistance systems (ADAS)

2.1.1 *Anti-lock braking system (ABS)*

It is possible for wheel lockup to occur during emergency braking in hazardous driving conditions, deteriorating braking performance and compromising steerability which places the vehicle at danger of collision or leaving the road. Under these conditions, the role of the ABS is to detect if one or more wheels are about to lockup under braking and, if so, ensure that brake pressure remains constant or is reduced to return the wheel to a non-sliding state. ABS generally improves vehicle steerability during braking by preventing wheel lockup and has the advantage of possibly decreasing stopping distance on both dry and slippery surfaces. On loose gravel or snow-covered roads, ABS may increase braking distance, although still improving vehicle control (Khachane & Shrivastav, 2016). This is because a locked wheel may allow build-up of material in front of the sliding wheel on such surfaces (Burton, et al., 2004), aiding deceleration. With it not being its primary purpose, ABS does not improve stopping distance on all road conditions as proven on rough terrain through experimental testing by Hamersma (2017). The results showed that ABS and conventional braking on a rigid rough road substantially increase stopping distance and time compared to the same metrics on a smooth road. This is illustrated in Figure 2-1, that compares a flat, level road with Belgian paving (discussed in Section 3.3.6). Hamersma (2017) attributed the worsened braking performance on rough terrain to the tyre force generation properties and concluded that suspension configuration has a significant influence on tyre normal force variation typical of a rough road. A discussion of a commercial ABS algorithm can be found in Appendix A.

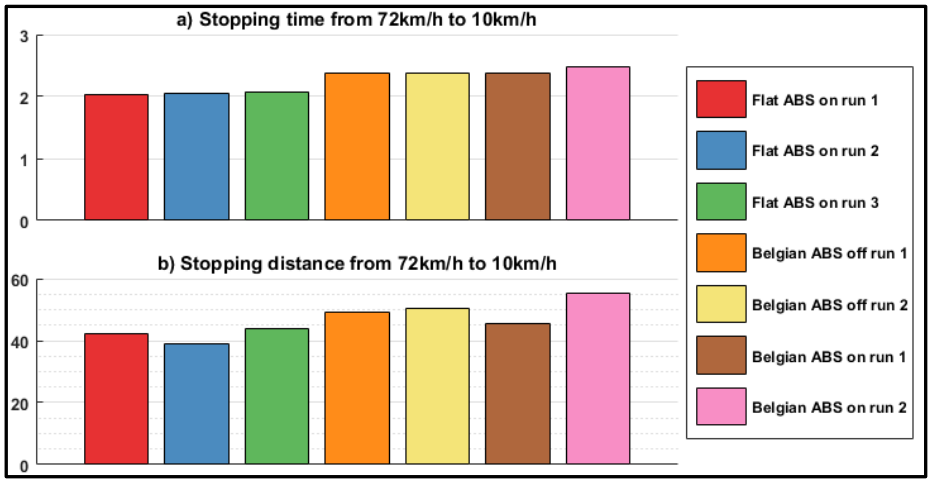

Figure 2-1: A comparison of stopping times and distances with ABS on/off on different terrains (Hamersma, 2017)

2.1.2 *Vehicle stability control*

Vehicle stability control is a closed-loop control system designed for improved vehicle handling by considering the vehicle lateral dynamics. The system establishes control by intervention with the braking system and/or drivetrain to ensure the vehicle obeys steering corrections while preventing vehicle break-away. Since Bosch introduced the first commercial stability control solution in 1995 (European Patent Office, 2016), many manufacturers have created their own variation with different names such as vehicle stability assist (VSA), electronic stability control (ESC), electronic stability program (ESP), direct yaw moment control (DYC), advanced stability control (ASC), and vehicle dynamics control (VDC). These programs all perform a similar feature which is to enhance vehicle stability and tracking performance so long as the vehicle is within its physical limits.

Papelis, et al. (2010) investigated the effectiveness of stability control by having participants perform an emergency obstacle avoidance manoeuvre at a cross section in a simulation environment. The study found a 5% rate of LOC for vehicles with ESP and 30% LOC for vehicles without ESP. The findings match several other epidemiological studies on real-world crashes, pointing to the effectiveness of ESP in accident prevention.

Stability control relies on the vehicle's ABS hydraulic modulator as a way of "steering" the vehicle with the brake generated yaw moment (Reif, 2014). This is where stability control is integrated with ABS; utilizing its ability to brake individual wheels such as to brake the right rear wheel to counter understeer in a right turn. The control system normally takes the steering wheel angle, accelerator position, brake pressure and the angular speed of the wheels as input and contrasts this with the vehicle lateral acceleration, yaw rate and individual wheel speed sensors to determine if a driver is at risk of losing control over the vehicle (Reif, 2014). If the algorithm detects an impending LOC, such as in severe over- or under-steer situations, the system reduces the throttle and regulates brake pressure on select wheels to generate a restoring moment and minimize deviation from the intended motion. Throttle reduction is done via traction control (TC), which normally regulates engine throttle to prevent wheel spin during acceleration, similar to how ABS regulates brake pressure during deceleration.

2.1.3 *ESP controllers*

The requirements of the ESP as listed by Reif (2014) are as follows:

1. To enhance vehicle stability in all operating conditions such as emergency stops, coasting, acceleration, load shift and standard braking.
2. Increased vehicle stability at the friction limit such as during sharp cornering in an emergency situation.
3. To further improve traction potential in a variety of different situations, providing shorter braking distance and higher levels of steering response.

Achieving the listed requirements is realized by the controller hierarchy illustrated in Figure 2-2 that shows the in- and output signal paths of each controller. ESP embraces capabilities extending beyond those of ABS and TC and acts as the higher-level controller. The controller is responsible for measuring or estimating parameters, determining a reference yaw response and specifying setpoints to the ABS and TC controllers (Reif, 2014).

Figure 2-3 and Figure 2-4 illustrate how ESP enhances vehicle stability for a rapid steering and counter steering manoeuvre with Figure 2-3 showing the steering-wheel angle, lateral acceleration, yaw velocity and sideslip angle curves and Figure 2-4 the vehicle trajectory. The figures compare the response of a vehicle with and without ESP.

In the illustration, both vehicles start out with the same initial conditions. Phase 1 starts with an abrupt steering input, causing the same response for both vehicles which is increased lateral acceleration, yaw velocity and slip angle. At the beginning of phase 2, both vehicles have similar lateral acceleration but yaw velocity and slip-angle of the vehicle without ESP start to indicate imminent LOC. The rear wheels of the vehicle without ESP have been slow to respond to the lateral forces generated at the front due to steering input, causing an inward yaw. The vehicle with ESP braked the left front wheel to counter the threat of instability, reducing the tendency to yaw and limiting the sideslip angle. Phase 3 marks the second steering input: counter steer. The vehicle without ESP does not respond to the new steering input and becomes uncontrollable. The vehicle with ESP has responded to the new steering input, reversing the yaw velocity. In phase 4, the vehicle without ESP starts to skid while the vehicle with ESP applies the brakes at the front right wheel in order to restore vehicle stability once more. Section 4 deals with different stability indicators found in literature as it is not exactly known how the different closed-source commercial products determine stability.

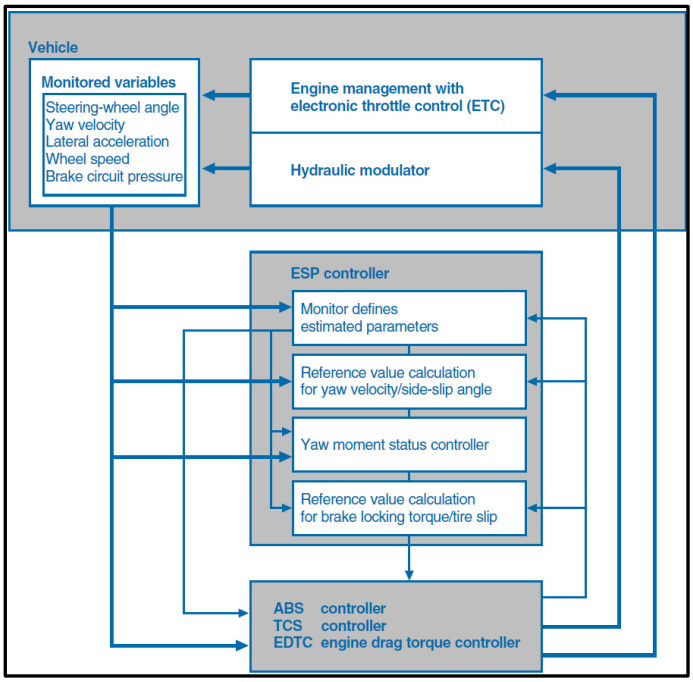

Figure 2-2: Simplified control hierarchy of ESP, ABS and TC (Reif, 2014)

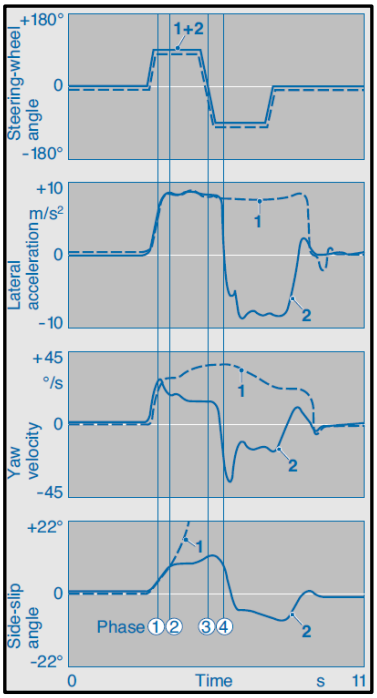

Figure 2-3: A comparison of different parameters of a vehicle equipped with ESP (2) vs. without ESP (1) (Reif, 2014)

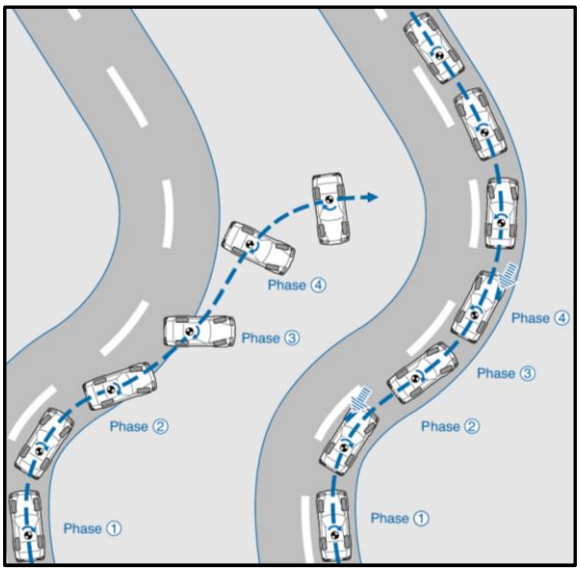

Figure 2-4: A comparison of vehicle trajectory for a vehicle equipped with ESP (right) vs. without ESP (left) (Reif, 2014)

2.1.4 *Active steering*

Active steering is a tyre steering method for controlling vehicle yaw or sideslip angle, based on either improving driver comfort or as a stability control strategy. Active steering systems include active front steering (AFS), active rear steering or four-wheel steering (ARS/4WS), and four-wheel active steering (4WAS).

An AFS system, illustrated in Figure 2-5, creates a desirable driving experience by realising a superposition between an ideal and driver steering angle with a variable steer ratio. The driver controls the vehicle heading with the steering wheel angle (δ_s) that is supplemented with an additional angle (δ_M) supplied by an electric motor. The combination of both angles result in a pinion angle (δ_G) at the steering rack and ultimately - a road wheel angle (δ_f) as formulated in Equation 2-1 (Reinelt, et al., 2004). The varying ratio (i_v) is low at low speed, amplifying steering input and high at high speed, attenuating steering input. In this way the steering effort remains largely constant over a wide speed range.

$$\delta_f(t) = \frac{1}{v_i} \cdot \delta_s(t) \tag{2-1}$$

Capabilities of all active steering systems (AFS, AR/4WS, 4WAS) extend to support stability control by working as an alternative or in combination with brake-based stability control where active steering has a lower utilization of tyre-road friction (Ackermann, et al., 1999). This is shown in Figure 2-6 that demonstrates how brake generated yaw moments provide a maximum torque of $F_{max} \cdot \frac{t}{2}$, and wheel steering a maximum torque of $2 \cdot F_{max} \cdot t$, meaning that yaw moment generated with steering requires only a quarter of the tyre friction force to generate the same yaw moment as for braking.

Active steering can also be used to compensate for asymmetric braking torque, for example when braking on μ-split surfaces, with one side of the vehicle on a low friction surface and the other on a high friction surface. Assuming equal braking on both sides, a yaw torque will be generated that the brake system itself cannot oppose but can be countered by steering (Ackermann, et al., 1999). Use of active steering for yaw control has the safety advantage that normal vehicle dynamics are retained, leaving the brake system in charge of longitudinal control and yaw control reserved for the steering system.

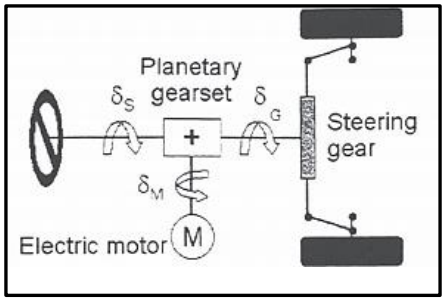

Figure 2-5: AFS schematic view (Reinelt, et al., 2004)

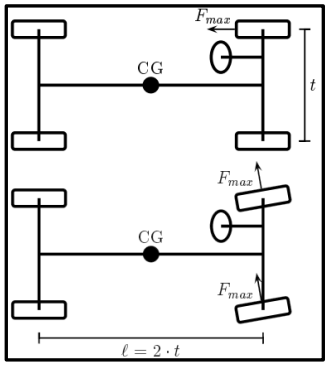

Figure 2-6: Yaw generated by braking (top) and by steering (bottom) (Reinelt, et al., 2004)

Of the three active steering systems, only 4WAS can control both the yaw rate and body side-slip simultaneously (Li & Fu, 2016). Such control has the advantage that it separates the two basic driving tasks of path following and disturbance attenuation. With 4WAS the driver focusses on the former while the controller manages the latter, making for a less demanding driving experience. Figure 2-7 from a study by Yim (2020) compares the stability performance of AFS, front-wheel independent steering (FWIS), 4WS and four-wheel independent steering

(4WIS) for a DLC manoeuvre at a vehicle speed of 80 km/h. Of all the systems, the ones with more actuators performed better as measured by the yaw rate error and side slip angle. FWIS and 4WIS outperforms AFS and 4WS respectively. When comparing AFS to 4WAS, the results indicate that 4WAS is far superior to AFS, outperforming the system on yaw rate error, sideslip angle and trajectory. These plots also hint to a control strategy that many stability control studies employ (Zheng, et al., 2006) (Fu, et al., 2015) which is to take the desired sideslip angle as zero throughout the manoeuvre, although this may reduce the responsiveness of the vehicle.

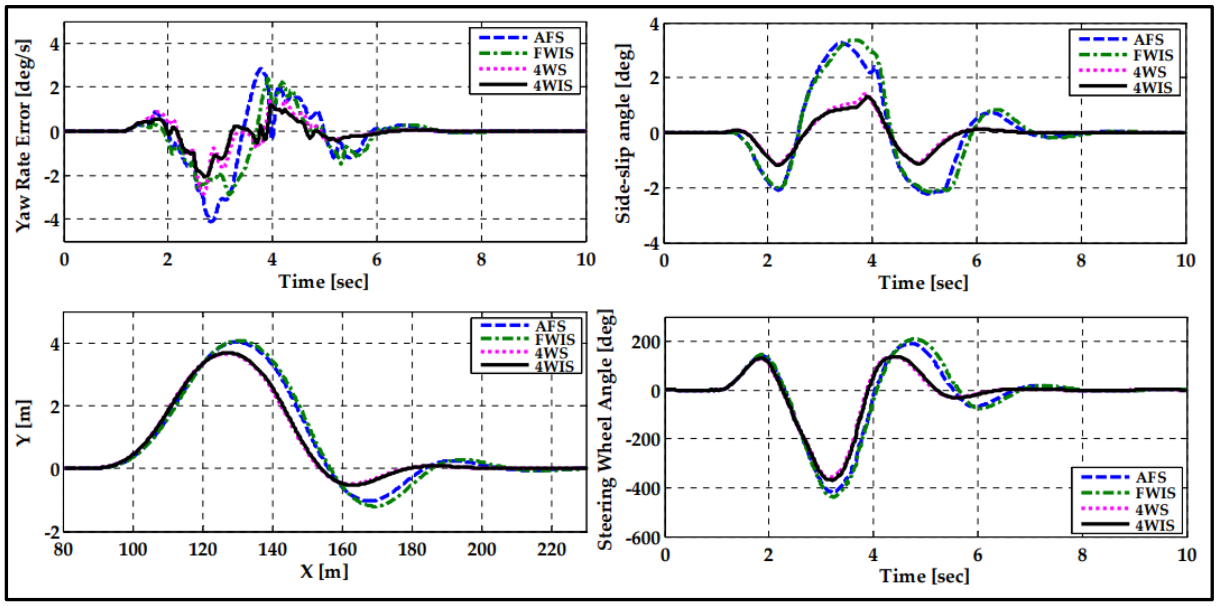

Figure 2-7: A double lane change manoeuvre with AFS, four-wheel independent steering (FWIS), 4WS, four-wheel independent steering (4WIS) at 80 km/h (Yim, 2020)

2.2 Integrated chassis control (ICC)

2.2.1 *Potential benefit of integrated chassis control (ICC)*

Integrated chassis control (ICC) may provide increased utilization of tyre-road friction and a greater range of stable vehicle motion which greatly improves vehicle safety and comfort (Savitski, et al., 2015). The default configuration of current sub-systems is largely to operate in parallel, as different manufacturers and suppliers each develop their own individual systems that are later installed on the same vehicle (Gordon, et al., 2003). The physical constraint of having stand-alone sub-systems is then that each system has its own limited effective range, as illustrated by the hatched $G - G$ diagram regions in Figure 2-8. The first example on the left is of active front and rear steering, indicating an effective range far from the friction limit, this is different from active roll control (middle) with an effective range near the tyre lateral friction limit. The diagram on the far right shows active differential with an effective range near the friction limit, with exclusion of pure lateral or longitudinal friction saturation. By careful coordination of different systems, the areas of benefit may be blended seamlessly, yielding an overall handling (or comfort) advantage throughout a wide range of longitudinal or lateral accelerations.

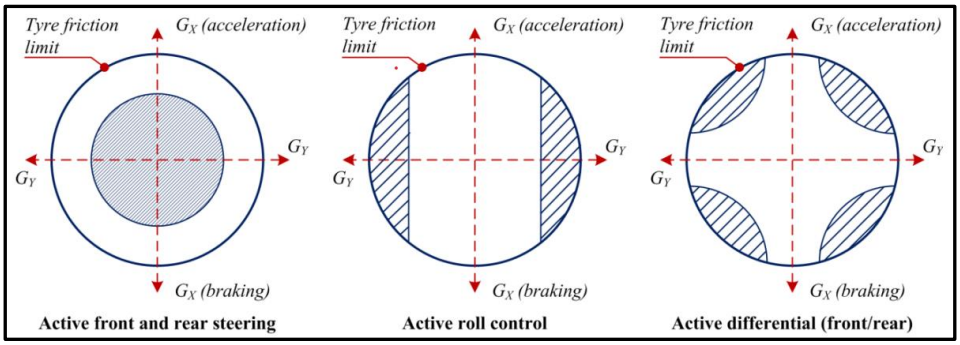

Figure 2-8: The effective range of AFS/ARS, Active roll, Active differential (hatched regions) (Savitski, et al., 2015)

2.2.2 *Control architectures*

Figure 2-9 shows the hierarchy of vehicle control functionality where higher levels of functionality employ more of an integrated approach i.e., use more actuators to perform a task. An example of a high-level layer system would be lane detection and tracking that employs lower-level systems to perform its task. The bottom layer represents the minimum hardware required for the vehicle to operate and are components such as the brakes, transmission and suspension.

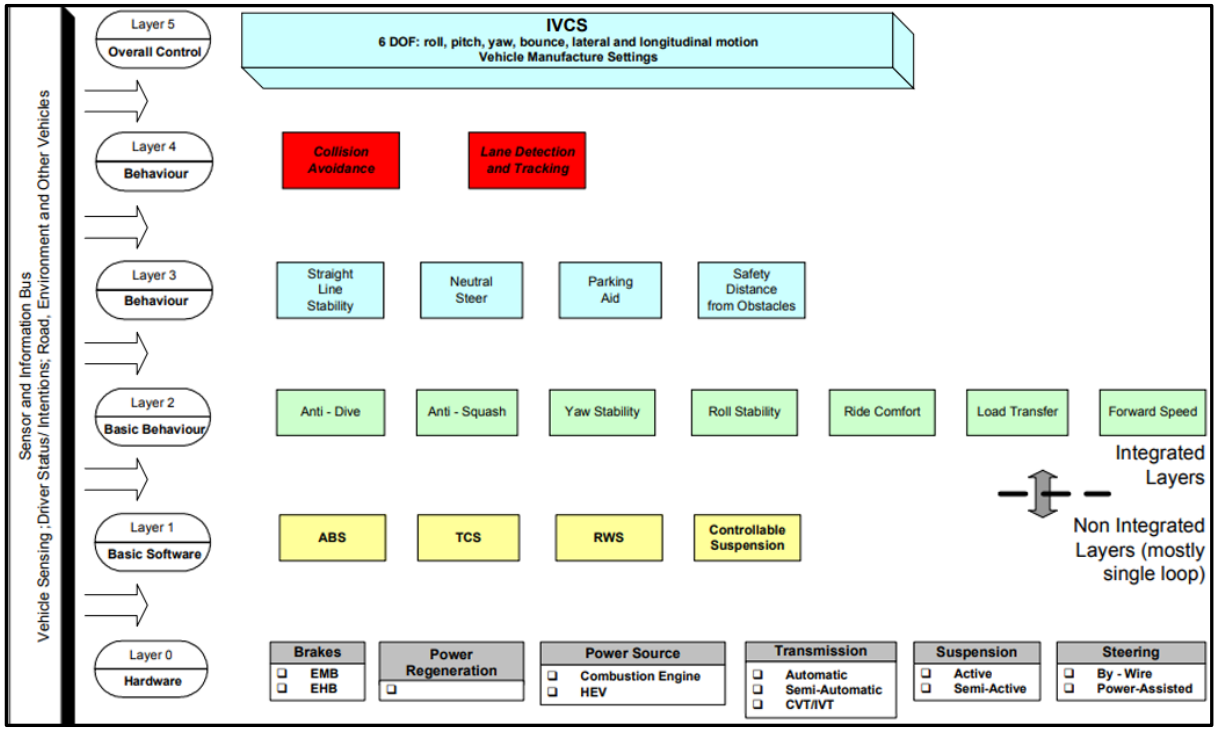

Figure 2-9: The structure of multi-layered vehicle control (Gordon, et al., 2003)

There are different architectures to connect parent or same-layer sub-systems, one of which is the centralized approach, shown in Figure 2-10. Here, the intention is to have one supervisory controller designed to make all control decisions and has the advantage that all control inputs can be computed with the controller having full authority of sub-systems. This approach allows for stability and performance predictions at the design stage, limiting possible interference (Gordon, et al., 2003). An example of this architecture would be for a

manoeuvre requiring yaw stability control were the central controller would decide to apply either steering-based control or brake-based control depending on the slip ratio of all four tyres and then implement the control sequence itself. The disadvantages of a centralized approach are that failure of the central controller would lead to total chassis controls failure and that the curse of dimensionality would mean an increasing number of sub-systems create a tremendous design difficulty.

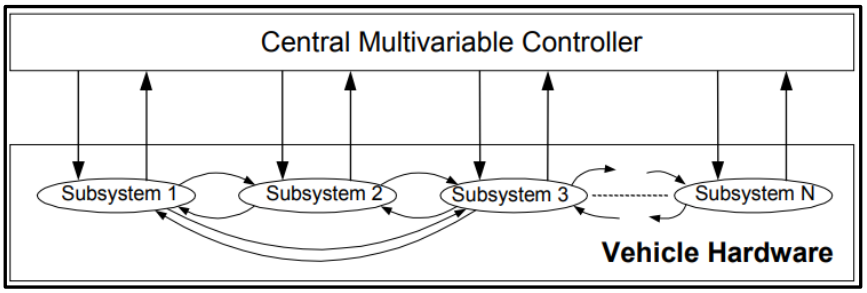

Figure 2-10: The centralised control structure (Gordon, et al., 2003)

The supervisory approach, shown in Figure 2-11 adds a level of supervision to sub-systems where the role of the supervisor is to supply setpoints to the intermediate control layer that consists of the 'traditional' sub-system controllers. The benefits of such a configuration are that the intermediate controllers can still operate should the supervisor fail and it provides a modular approach to the design of sub-systems (Gordon, et al., 2003). An example of this architecture would be for the supervisor to set the TC target slip ratio, which the TC would then maintain by its own operation.

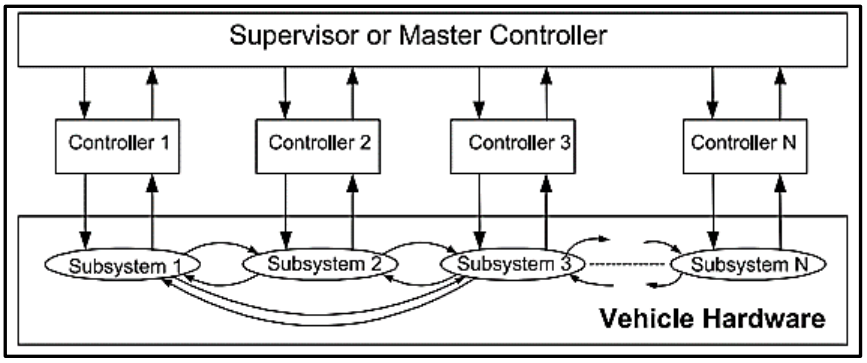

Figure 2-11: The supervisory control structure (Gordon, et al., 2003)

2.2.3 *Control coordination*

There are four basic sub-system coordination types, shown in Figure 2-12 (Gordon, et al., 2003). Coordinator type a outputs the highest ranked or prioritized non-zero command. This is an example of conflict resolution of competing sub-systems where only a single behaviour dominates and may take control of an actuator. A coordinator of type c outputs the largest modulus signal wherein the 'loudest voice' sub-system will take control of the actuator. A downside to coordinators type a and c is that the switching of control authority may be discontinuous which will create undesirable transients in the vehicle dynamic response. A possible remedy would be to either employ a low-pass filter or a ramped response between controls or to perform an averaging or superposition of controls via a neural network such as is done with coordinator b. Coordinator type d is fuzzy rule based and establishes an output

that is non-linear but not as discontinuous as those of types a and b. The type d controller works well with sub-systems that are already rule-based.

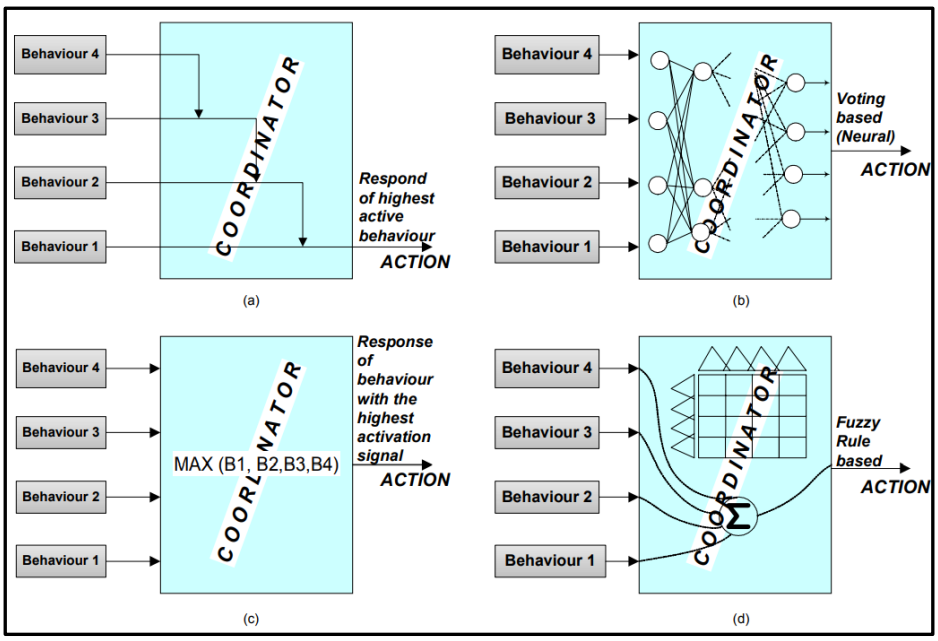

Figure 2-12: Four simple control methods for ICC (Gordon, et al., 2003)

2.2.4 *Sliding mode control (SMC)*

Sliding mode control (SMC) is a simple, robust technique for dealing with non-linear control of an nth-order model by replacing the control problem with a 1st-order alternative. This alternative is referred to as the sliding surface and ideal sliding motion occurs when the system moves along its cross-section, however this requires actuators with infinite bandwidth. In practice this state is not perfectly maintained. SMC provides remarkable robustness against model uncertainties and perturbations and is a popular control technique for vehicle stability systems as used by authors such as Rajamani (2006), Strauss (2016) and Mokhiamar & Abe (2006).

Utkin (1992) outlines a two-step procedure for SMC design:

1. Sliding surface design.
2. Selection of a discontinuous control law that ensures the sliding motion.

For step one, sliding surface design entails the thoughtful selection of a sliding surface (or sliding variable) that tailors the system behaviour according to a desired dynamic. Often this surface depends on an error together with its derivatives, with a typical form as shown in Equation 2-2 (Slotine & Li, 1991), where n represents the relative degree between the system input and output.

$$s = \left(\frac{d}{dt} + \lambda\right)^{n-1} \tilde{x} \tag{2-2}$$

Where, $\tilde{x} = x - x_{des} = \left[\tilde{x} \quad \dot{\tilde{x}} \quad \tilde{x}^{n-1}\right]^T$.

Step two requires the selection of a control law that satisfies the η-reachability condition (Equation 2-3) to arrive at the discontinuous input (Equation 2-4) so chosen as to account for modelling imprecision and disturbances (Slotine & Li, 1991). Due to actuator delays in practice, the discontinuous input causes chattering as shown in Figure 2-13. This theoretically infinite frequency control activity is undesirable and may excite unmodeled dynamics. A smoothing function may be used to balance control bandwidth and tracking performance although that invariably compromises on both metrics.

$$s\dot{s} < -\eta|s| \tag{2-3}$$

$$u = \hat{u} - k \times sgn(s) \tag{2-4}$$

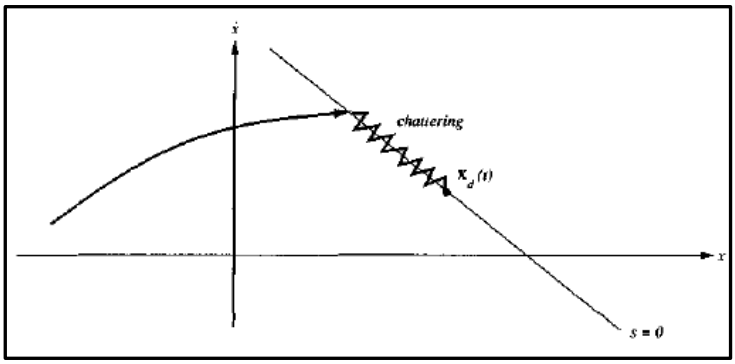

Figure 2-13: Chattering of the input signal of an unsmoothed first order SMC (Slotine & Li, 1991)

A more elegant solution to the chattering problem is the second order SMC which provides a continuous control signal while maintaining controller robustness to uncertainties and perturbations. The key difference is that for a second order SMC both $s, \dot{s}$ = 0 as opposed to just $s = 0$ with discontinuous $\dot{s}$ which is seen with a first order SMC. Having both $s, \dot{s}$ = 0 ensures a continuous control signal. A variation of the second order SMC is the super-twisting algorithm (STA) as pioneered by Levant (1993) that only depends on two tuning parameters. Further work by Levant (1998) reduced the two possible tuning parameters to only one by constructing a suitable relationship between those two parameters that result in an inherently stable controller. This is formulated in Equation 2-5 to Equation 2-8 where δ is the rate of disturbance. The controller guarantees exact finite time convergence if $k_{SMC} \geq |\delta|$ (Seeber & Horn, 2017), meaning that the absolute rate of matched disturbance must not exceed the gain value (k_{SMC}).

$$u = -k_1\sqrt{|s|}\, sgn(s) + w \tag{2-5}$$

$$\dot{w} = -k_2 sgn(s) + \delta \tag{2-6}$$

$$k_1 = 1.5\sqrt{k_{SMC}} \tag{2-7}$$

$$k_2 = 1.1k_{SMC} \tag{2-8}$$

2.3 Stability systems in literature

A study by Canale & Fagiano (2010) compares the performance of stand-alone RDB and ARS systems for stability control. The authors used the Euro NCAP sine with dwell manoeuvre (Euro NCAP, 2011) as the performance indicator which measures the vehicle damping of yaw rate after a fast-transient steer input. This was combined with a criterion of spin-out which Forkenbrock & Boyd (2008) defines as a vehicle heading angle greater than 90° at 4 s after completion of the steer manoeuvre. The authors note that RDB increases the front steer angle threshold to achieve vehicle spin-out compared to an uncontrolled (baseline) vehicle and that ARS increases the threshold on average more than differential braking. The authors note that differential braking retains vehicle responsiveness better than ARS but that differential braking worsens lateral stability at extreme oversteer scenarios when wheel-lock occurs. This is due to the rear tyres saturating during braking which drastically reduce the tyres' ability to maintain lateral forces.

Several studies have integrated active rear steering and differential braking according to the stability index (SI) such as Bardawil, et al. (2014) and Xie, et al. (2018). The latter authors note that active rear steering provides some advantages over differential braking in that drivers do not prefer frequent differential braking intervention and that braking leads to a decrease in vehicle longitudinal velocity. Differential braking should consequently be reserved for greater LOC scenarios and care should be taken not to have wheel-lock occur as in that instance the stability performance would be worse than for ARS. The proposed solution of both cited authors is to have the rear steering operate whenever the vehicle is within the stable phase plane region and combine ARS and RDB once outside the stable region.

Other methods of integration include the optimum control strategy (Mokhiamar & Abe, 2006) which in this case distributes longitudinal and lateral tyre forces according to an optimum cost function. The function is a sum of the percentage friction used for all four tyres which includes a weighting coefficient per tyre. Joa & Sohn (2018) employ differential braking once the rear tyres have reached the non-linear lateral response region. Of the two methods, the first relies on accurately estimating tyre force which is technically challenging, especially on off-road conditions, and the second relies on knowing the rear axle slip angle which can be estimated by use of the vehicle yaw rate, CG location and vehicle velocity or directly measured (Botes, et al., 2020).

The studies mentioned in this section consider only on-road performance while similar studies for off-road conditions are scarce and those that are accessible focus on vertical or longitudinal vehicle motion. This highlights the need for off-road performance studies, especially for handling and lateral stability.

2.4 Chapter conclusion

This section considered ADAS such as ABS, ESP, ARS, their working and areas of application. Control theory was discussed, and the options for an integrated control system structure presented. It was determined that a supervisory control structure is a safe and practical control architecture for ICC due to its modular design. Two integration methods of ARS and RDB were identified in a literature review: rear axle slip angle based and SI based.

CHAPTER THREE
VEHICLE DYNAMICS AND MODELING

Abstract – This chapter considers aspects of tyre mechanics that are relevant to control system design. These aspects are the rolling radius from which slip ratio is derived and the longitudinal, lateral and combined loadings which are used to generate the target yaw moment. Different tyre models are considered for use on rough terrain and the simulation vehicle and its properties are discussed. The road classifications, steering manoeuvres and driver model for use in the simulation environment test setup are outlined.

3.1 Tyre mechanics

All primary control and disturbance forces, except for aerodynamic loads, are generated by the tyre-road interface (contact patch). Through the contact patch the vehicle generates the critical forces required for accelerating, decelerating, and cornering. A tyre exhibits highly non-linear behaviour, dependant on many factors which may be too complex or impractical for inclusion in a control system, yet the accuracy of the tyre model ultimately determines the controller's performance. The following paragraphs regard the mechanics of tyres and considers suitable simplifications of the complex tyre variables for use with real-time control systems.

3.1.1 *Tyre rolling radius*

Many ADAS systems such as ABS, TC and ESP depend on properties derived from tyre radius called the dynamic or effective rolling radius (Hamersma, et al., 2014). Common uses are to estimate vehicle velocity or contact patch velocity and longitudinal slip. Effective radius can refer to either the kinetic or kinematic rolling radius where the kinetic radius relates the effective radius to moments and forces and the kinematic rolling radius by velocities and accelerations (Hamersma, et al., 2014). In this context, the effective tyre radius refers to the kinematic rolling radius. Besides effective rolling radius, other types of radii also exist, termed the unloaded and loaded or static rolling radii, respectively. All three types of radii are indicated in Figure 3-1. Of the three, the unloaded radius is the most straight forward and is simply the radius of a tyre without any load while the effective rolling radius can be derived from the vehicle velocity as formulated in Equation 3-1, provided the vehicle velocity is not derived from the wheel angular velocity. The equation assumes zero slip between the tyre and road interface.

$$r_e = \frac{V}{\omega} \tag{3-1}$$

The loaded radius is the height taken from the contact patch of a loaded tyre to the wheel centre which varies as different road forces are imposed on the tyre. Figure 3-2 shows the

variation in effective and loaded rolling radius with tread depth, velocity, and normal force, indicating that effective rolling radius is somewhat insensitive to velocity, but greatly influenced by normal force. A study by Gough (1963) found that a tyre rolled at constant velocity and axle height, over a cleat much smaller than the contact length exhibits three responses namely (1) variations in the vertical and (2) longitudinal force and (3) variations in the angular velocity of the wheel. It is the ratio of the angular velocity of the wheel to the travelled distance of the wheel axle that causes the change in effective rolling radius, which can be formulated as in Equation 3-2 and Equation 3-3 for the case of a short timestep.

$$r_e = \frac{V}{\omega}, \quad V = \frac{ds}{dt}, \quad \omega = \omega_0 - \frac{d\theta}{dt}, \quad r_{eo} = \frac{V}{\omega_0} \tag{3-2}$$

$$r_e \approx r_{eo}\,(1 + r_{eo}\frac{d\theta}{ds}) \tag{3-3}$$

Experimental work by Lippmann & Nanny (1967) found that the response of a passenger tyre rolling over a short, sharp unevenness exhibits an almost linear relationship between tyre force variation and step height. The findings determine that the response to any arbitrarily shaped unevenness can be obtained by taking the sum of responses to a series of step changes in the road surface height. This method is only applicable if the obstacle height is not too large (Pacejka, 2006). Figure 3-3 shows how much the effective rolling radius can fluctuate when crossing a relatively small obstacle.

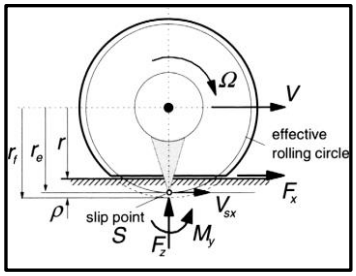

Figure 3-1: A free-rolling wheel showing unloaded radius (r_f), loaded radius (r) and effective radius (r_e) (Pacejka, 2006)

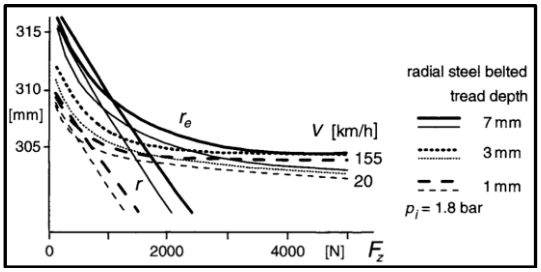

Figure 3-2: Radial tyre effective radius as a function of tread depth, vehicle velocity and normal force (Pacejka, 2006)

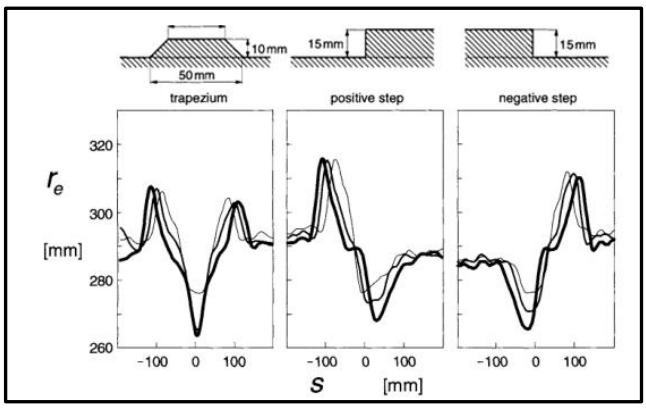

Figure 3-3: Variations in effective rolling radius of a 205/60R15 tyre rolling over a trapezium cleat, upward and downward step at low speed and for different axle heights (Pacejka, 2006)

Experimental work by Hamersma (2017) compared the contact patch velocity error due to assuming a constant effective radius and the contact patch velocity as measured by digital image correlation (DIC) techniques. Here the DIC obtained velocity is taken as the true velocity value. Testing was performed on Gerotek Belgian paving corresponding to an ISO8608:2016 Class D road roughness. The vehicle was braked from a velocity of 12 $m.s^{-1}$ to a complete stand-still. The results shown in Figure 3-4 indicate a velocity error magnitude around 0.7 $m.s^{-1}$ average, reaching a maximum of 2 $m.s^{-1}$ just as the vehicle velocity starts to decrease. This possibly indicates a large fluctuation due to load transfer while the contribution due to road inputs are comparably small. The takeaway is that inclusion of a variable effective radius purely due to road input as in Figure 3-3 is redundant as it is overshadowed by load transfer effects.

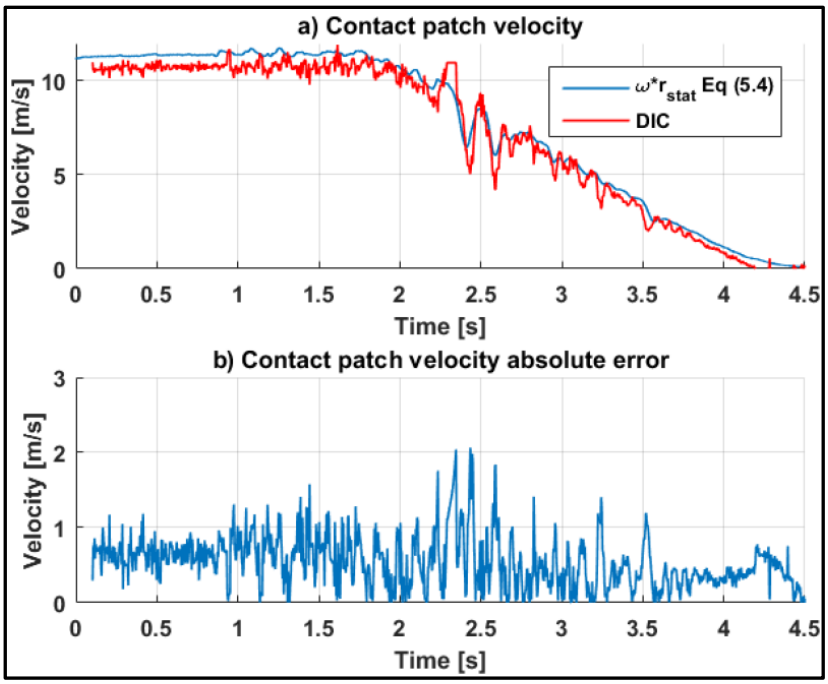

Figure 3-4: Contact patch velocity and error as determined by DIC and constant effective rolling radius (Hamersma, 2017)

3.1.2 *Tyre longitudinal force*

For a longitudinal force to be generated, a tyre requires a differential between tread and tyre velocity because the tyre material needs to deflect to sustain a friction force at the contact patch. During braking of a forward moving vehicle, a brake torque is applied about the wheel centre that opposes the rolling motion of the wheel, causing tyre material to deflect, moving the contact patch rearwards and giving rise to slip of the tyre relative to the road (Blundell & Harty, 2015).

A tread element entering the contact patch initially has zero deflection and zero slip so that it cannot generate a friction force, but it experiences an increasing deflection and slip as it moves towards the trailing edge, developing an increasingly larger friction force. Near the trailing edge of the contact patch, the normal load diminishes and the element begins to slip so that the friction force drops off, approaching zero as the element leaves the contact patch (Gillespie, 1992).

Figure 3-5 shows a plot of braking force against slip ratio and illustrates that braking force for each normal load setting is linear for a small slip ratio region around the origin with a peak value typically occurring at slip ratios between $\kappa = 0.15$ and $\kappa = 0.3$. After the peak, the brake force steadily decreases with increasing slip ratio up to wheel lock. The figure also shows that, generally, the peak value is larger for a larger normal load. The initial braking force gradient at zero slip is called the longitudinal slip stiffness and is a measure of the braking force; generally, a larger stiffness value corresponds to a larger peak brake force. Peak and slide coefficients are also used, which refer to the peak and sliding forces, respectively. Figure 3-6 shows a plot of braking force again, but now for different surfaces with a constant normal load. Key takeaways are that wet roads have reduced braking force and that with poor tread, braking force may diminish as the tyre can no longer displace water on the wet road and aquaplaning occurs.

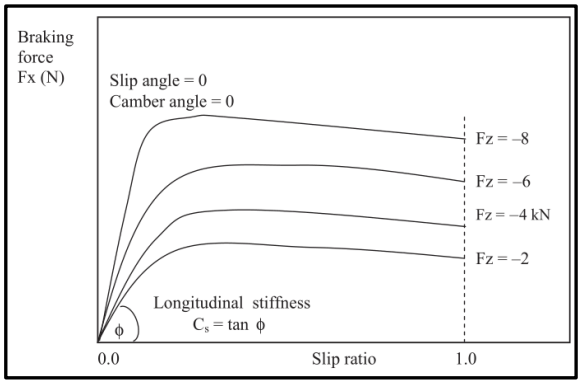

Figure 3-5: A plot of braking force vs slip ratio for different normal loads (Blundell & Harty, 2015)

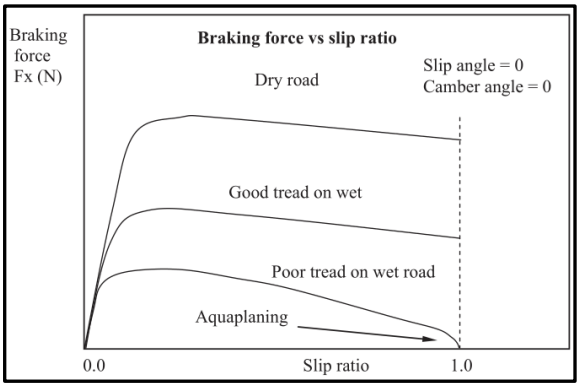

Figure 3-6: A plot of braking force vs slip ratio for different road surfaces (Blundell & Harty, 2015)

3.1.3 *Tyre lateral force*

Lateral deflection of a tyre tread gives rise to an elastic force acting perpendicular to the tire that can be used to control the direction of the vehicle, generate lateral acceleration in corners and resist external forces such as wind gusts and road cross-slope (Gillespie, 1992). For a tyre rolling with a slip angle at zero camber there is an asymmetric shear stress distribution in the contact patch, creating a lever arm known as the pneumatic trail that forms in the rear of the contact patch. This mechanism introduces a restoring moment that tends towards zero slip angle and provides a notable steering 'feel' for the driver of the vehicle (Blundell & Harty, 2015).

Figure 3-7 shows the shear stress distribution and pneumatic trail causing an aligning moment in the contact path of a wheel with a non-zero slip angle. Like longitudinal force generation, a tread element entering the contact patch initially has no deflection but steadily deforms in a lateral direction as it moves through the contact patch, generating an increasing lateral stress. There exists a limit lateral stress boundary that if the lateral stress in a portion of the contact patch exceeds this limit, it would slip. At a certain point in the contact patch, the tread element reaches the limit lateral stress boundary, after which sliding takes place until the tread element leaves the trailing edge of the contact patch and lateral stress returns to zero. As slip angle increases, the area under the lateral stress curve increases, generating a larger lateral force (Blundell & Harty, 2015).

Experimental measurements of lateral force vs. slip angle exhibit the characteristic curve shown in Figure 3-8 where the lateral force of a rolling wheel builds rapidly for the 5° to 10° slip angle attitude and thereafter diminishes as the slip area grows larger with increasing slip angle (Gillespie, 1992). The initial slope of the curve for the rolling tyre is known as cornering stiffness and greater values will generate larger lateral force. The linear region allows for a simple formulation of lateral force as in Equation 3-4.

$$F_y = C_\alpha \times \alpha \tag{3-4}$$

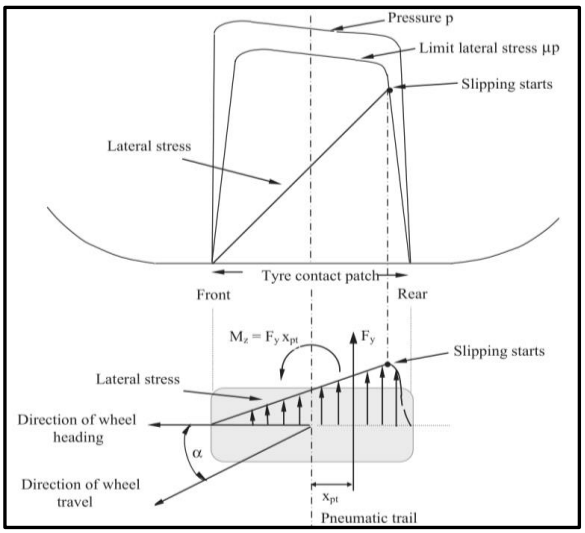

Figure 3-7: Tyre lateral stress and pneumatic trail (Blundell & Harty, 2015)

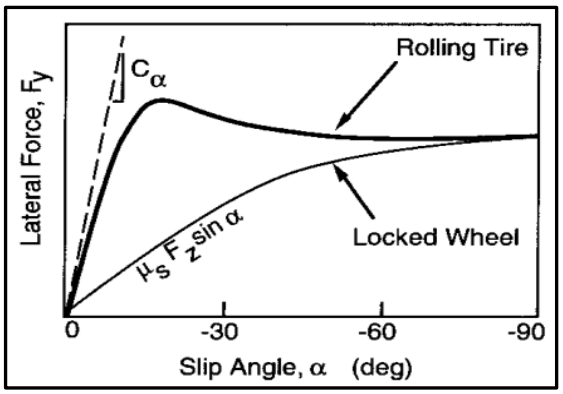

Figure 3-8: Tyre lateral force vs. slip angle for locked and rolling tyres (Gillespie, 1992)

3.1.4 *Combined braking, driving, and cornering*

Longitudinal and lateral forces often occur simultaneously during vehicle manoeuvres, which cause the tyre friction characteristics to deviate from those generated by pure traction, braking, or cornering. During this combined loading condition, the total friction force available remains the same as for the pure slip conditions regardless of direction of slip; therefore, the lateral and longitudinal forces are now components of the resultant force and would be less than that of the pure case. This forms the basis of the friction circle or friction ellipse for tyres with more capability in traction or cornering, recognizing that friction can be used for lateral or longitudinal force or a combination of the two but in no case can the vector total force exceed the friction limit (Gillespie, 1992). The friction limit forms a circle in the plane of the lateral and longitudinal forces and is shown in Figure 3-9 for a tyre with zero camber angle and can be formulated as in Equation 3-5.

$$F_R = \sqrt{F_x^{\,2} + F_y^{\,2}} \tag{3-5}$$

Figure 3-9 represents one quadrant of the circle for positive slip angle and an applied braking force but can be extended to include driving force and negative slip angle. As the friction circle curves approach the friction limit with increasing longitudinal force and growing contact patch slip, both lateral and longitudinal force will reduce, causing the curves to bend back. It can be noted that the curves for each slip angle are not symmetric in that moderate levels of

brake force increases the lateral force developed. This is due to braking force adding to the circumferential tension of the tyre material entering the contact patch, causing a stress stiffening effect that raises the lateral force slightly (Blundell & Harty, 2015). This effect is shown in Figure 3-10 that also shows that aligning moment tends to decrease with increasing braking force. The presence of braking force acts to stiffen the tyre structure, causing the aligning moment to decrease to a point it may go negative. A negative aligning moment then attempts to steer the wheel to a greater slip angle which may adversely affect stability in braking (Gillespie, 1992).

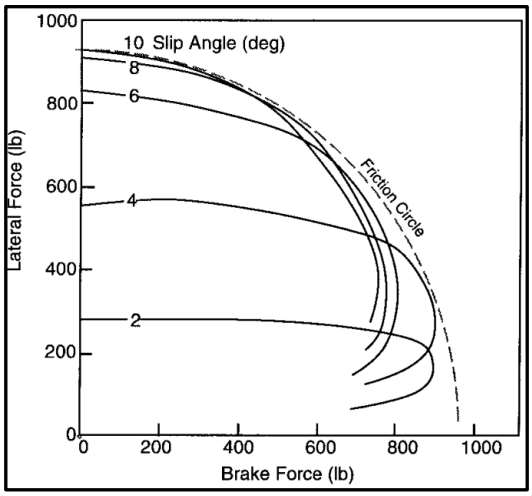

Figure 3-9: Friction circle of tyre lateral force plotted against longitudinal force (Gillespie, 1992)

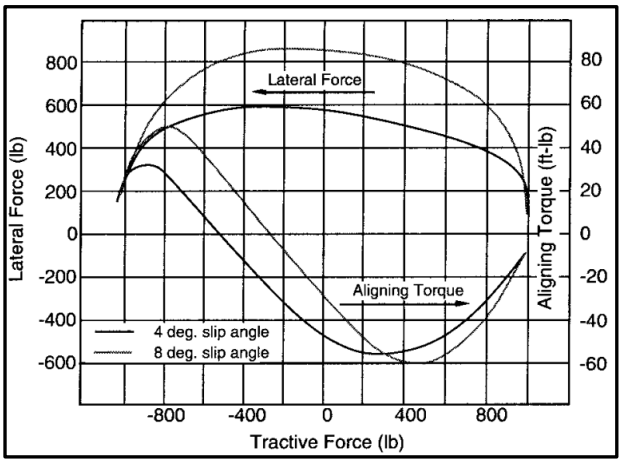

Figure 3-10: Lateral force and aligning torque plotted against tractive force (Gillespie, 1992)

3.1.5 *Tyre models overview*

Tyre models provide a mathematical model of complex tyre behaviour and different models are suitable depending on the driving manoeuvre and road condition, as shown in Table 3-1. The table indicates that PAC2002 with transient effects or the FTire model are best suited for simulating rough terrain driving.

Table 3-1: Comparison of different tyre models per manoeuvre (MSC Software, 2021)

Event/Maneuver	PAC89	PAC94	PAC2002	PAC2002*	Fiala	FTire
ABS braking distance	o/+	o/+	+	+	o	+
Braking/power-off in a turn	o	o	+	+	o	o/+
Cornering on uneven roads	o	o	o/+	+	o	+
Braking on uneven roads	o	o	o/+	+	o	+
Driving over uneven road	-	-	-	+	-	+
ABS braking control	o	o	o/+	+	o	+
Chassis control systems >8 Hz	-	-	o/+	+	-	+

* PAC2002 with belt dynamics

-	Not possible / Not realistic
o	Possible
o/+	Better
+	Best to use

In choosing tyre models for this study, two use cases are considered, namely a tyre model for the simulation environment and another for use by the control system. The use cases differ in that the simulation environment should accurately compute tyre-terrain interaction forces in order to simulate real vehicle response, and the control system tyre model should provide a usable real-time capable estimate of tyre forces to the control system. All states such as road surface displacements and detailed vehicle states are readily available in the simulation environment, which allows for a complex and accurate simulation environment tyre model. The control system has a limited number of states that are measured and does not allow for a complex tyre model. Consequently, the control system tyre model is expected to be simple and less accurate than the simulation environment tyre model.

This study uses the FTire model in the simulation environment to accurately compute tyre-terrain interaction forces as it is suitable for use on rough roads (Table 3-1). The Pacejka 89 tyre model is used by the control system since it can predict tyre forces based on few parameters that can be measured or estimated for a real-world application, although it does not have suitable accuracy for the purpose of simulating real vehicle response on rough roads.

3.2 Mathematical vehicle model

3.2.1 *Yaw-plane 2-DOF model*

A classic model for vehicle yaw-plane analysis is the single track (bicycle) model shown in Figure 3-11 that assumes zero camber and simplifies the normal two tyres per axle location to one tyre per axle location. The model assumes the turning radius to be much larger than the wheelbase of the vehicle and that only the front wheel is steerable. The model is developed starting from a slow-moving vehicle as shown in Figure 3-12 where the radius of turn is thought to be determined by only the average front wheel steering angle and the wheel base. This is because no lateral acceleration is experienced and consequently the tyres have zero slip angle. As with the formulation of a radian in Equation 3-6, the average front steering angle is similarly obtained with Equation 3-7.

$$angle = \frac{\boldsymbol{arc}}{\boldsymbol{radius}} \tag{3-6}$$

$$\delta = \frac{\mathrm{L}}{R} \tag{3-7}$$

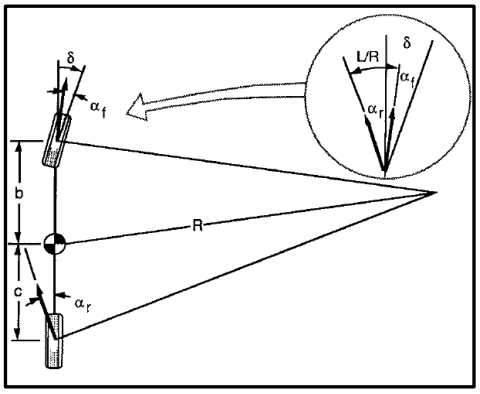

Figure 3-11: The bicycle model for high-speed cornering (Gillespie, 1992)

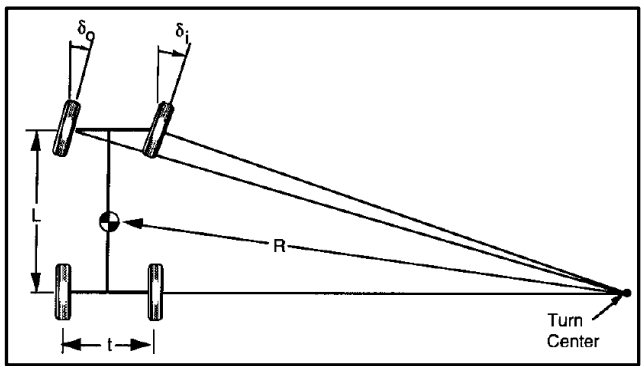

Figure 3-12: The bicycle model for low-speed cornering (Gillespie, 1992)

At high-speed, the vehicle experiences lateral acceleration countered by tyre lateral forces through running at a non-zero slip angle. This is indicated in Figure 3-11 from which the relation between front steering angle and radius of turn is formulated in Equation 3-8 (with angle units in degrees).

$$\delta = \frac{57.3L}{R} + \alpha_f - \alpha_r \tag{3-8}$$

Equation 3-9 to 3-11 formulates the single track (bicycle) model lateral and yaw dynamic equations. Considering Equation 3-9, the term $v_x\dot{\psi}$ represents the centripetal acceleration and originates from the kinematics formula shown in Equation 3-10. The term $v_x\dot{\beta}$ represents the lateral translation acceleration ($\dot{v_y}$) which is obtained by using the same radian-arc principle of Equation 3-6, assuming small sideslip angle. Equation 3-11 is merely the sum of moments about the CG z-axis.

$$m(v_x\dot{\beta} + v_x\dot{\psi}) = F_{yf} + F_{yr} \tag{3-9}$$

$$a_y = \omega \times v_x = \dot{\psi}v_x \tag{3-10}$$

$$I_{zz}\ddot{\psi} = F_{yf}b - F_{yr}c \tag{3-11}$$

Considering a case of the single track (bicycle) model operating under stead state conditions, Equation 3-9 becomes as in Equation 3-12 and Equation 3-11 becomes as in Equation 3-13. If Equation 3-13 is rearranged so that $F_{yf} = \frac{F_{yr}c}{b}$ can be substituted into Equation 3-12, we arrive at Equation 3-14 which proves that the lateral force developed at the rear axle equals the lateral acceleration times the portion of vehicle mass thereon. The same can be found when solving for the front axle lateral force.

$$\mathrm{F_y} = F_{yf} + F_{yr} = \frac{mv_x^2}{R} \tag{3-12}$$

$$\mathrm{M_z} = 0 = F_{yf}b - F_{yr}c \tag{3-13}$$

$$\mathrm{F_{yr}} = \frac{mb}{L}\left(\frac{v_x^2}{R}\right) \tag{3-14}$$

With the lateral forces known, the front and rear slip angles of Equation 3-8 are solved using the linear relationship of Equation 3-4 to arrive at Equation 3-15 (with angle units in degrees), where the front and rear masses are written as $m_f = \frac{w_f}{g}$ and $m_r = \frac{w_r}{g}$.

$$\delta = \frac{57.3L}{R} + \left(\frac{w_f}{C_{\alpha f}} - \frac{w_r}{C_{\alpha r}}\right)\frac{v_x^2}{Rg} \tag{3-15}$$

The second term can be formulated as in Equation 3-16 (with lateral acceleration unit in $g's$ and angle units in degrees). Parameter K_{US} represents the understeer gradient which has significant influence on vehicle cornering behaviour and is discussed in detail in Section 4.1.

$$\delta = \frac{57.3\mathrm{L}}{R} + K_{US} \times a_y \tag{3-16}$$

3.3 Simulation vehicle properties

Table 3-2 shows the properties of the testing platform which is a Land Rover 110 SUV illustrated in Figure 3-13.

Table 3-2: Properties of the Land Rover 110 used for simulation (Peenze, 2020)

Property	Symbol	Value	Unit
Total vehicle mass	m	2047	kg
Vehicle sprung mass	m_s	1582	kg
Mass moment of inertia around longitudinal axis	I_{xx}	839	kgm^2
Mass moment of inertia around lateral axis	I_{yy}	2471	kgm^2
Mass moment of inertia around vertical axis	I_{zz}	2057	kgm^2
Longitudinal distance from CG to front axle	l_f	1.55	m
Longitudinal distance from CG to rear axle	l_r	1.25	m
Track width (front and rear)	t_w	1.49	m
Distance between front suspension struts	s_f	1.01	m
Distance between rear suspensions struts	s_r	0.97	m
Effective rolling radius	r_e	0.386	m
Vehicle width	t_v	1.86	m

3.3.1 *MSC ADAMS model*

MSC ADAMS (MSC Software, 2021) is a multi-body dynamics simulation software in which a model can be built, excited and its response measured. Prior research by Els (2006) refined by Thoresson (2007), Uys (2007) and Cronjé (2008) established a 17-DOF non-linear ADAMS vehicle model of the Land Rover 110 shown in Figure 3-14 with associated body motion listed in Table 3-3. The vehicle has a CG imposed longitudinal force that tries to reach and maintain the reference velocity and no driving forces are generated by the tyre-road interfaces. The simulation sampling rate is set to $f_s = 2000\,Hz$ for all simulations, due to it being the minimum sampling rate required by FTire.

Figure 3-13: The Land Rover Defender 110 on the Belgian paving at Gerotek (Poovendran, 2018)

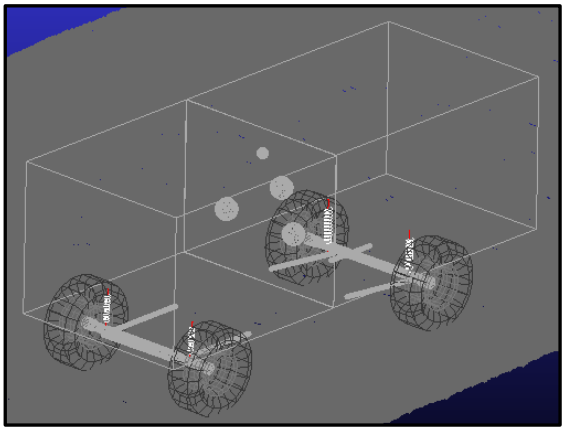

Figure 3-14: The Land Rover Defender 110 ADAMS model

Table 3-3: Land Rover 110 model bodies, DOF and associated motion (Thoresson, 2007)

Body	DOF	Associated motion
Vehicle body	7	Body torsion
(2 rigid bodies)		Longitudinal, lateral, vertical, roll, pitch, yaw
Front axle	2	Roll, vertical
Rear axle	2	Roll, vertical
Wheels	6	Rotation, front and rear steering

3.3.2 *Rear suspension*

Figure 3-15 indicates the schematic layout of the rear suspension components and joints along with their associated degrees of freedom (Els, 2006). It consists of two coil springs with translational dampers and rubber stops paired with an anti-roll bar. The suspension is connected to the vehicle body via two trailing arms and an A-arm where the trailing arm bush stiffnesses are also included in the model. Rear steering is achieved by a connecting rod between the two rear wheels that simultaneously adjusts the rear kingpin angle of both wheels.

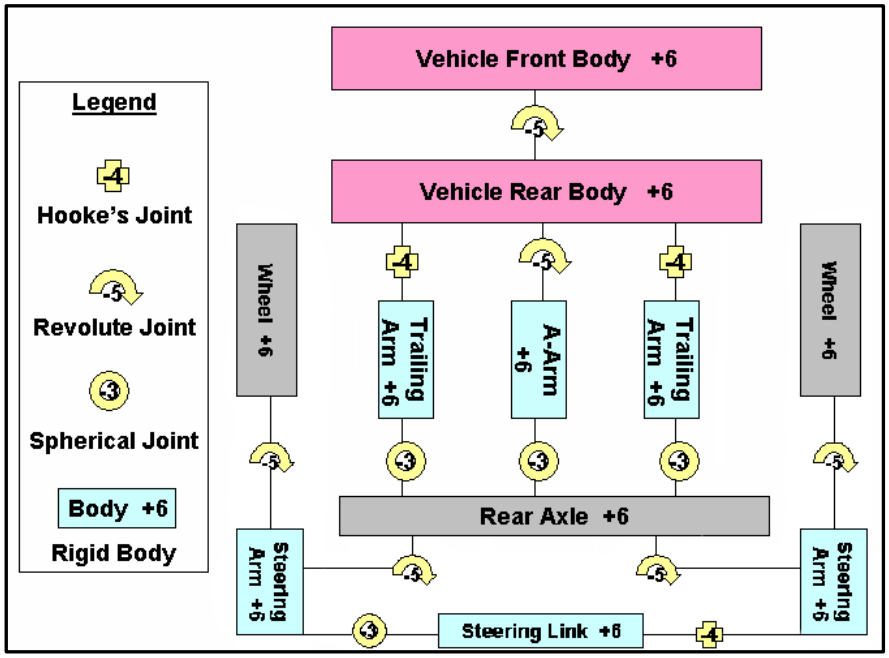

Figure 3-15: ADAMS model rear suspension schematic layout (Els, 2006)

3.3.3 *Front suspension*

Figure 3-16 indicates the front suspension schematic layout with the joint types and their associated degrees of freedom (Els, 2006). It consists of a rigid axle located laterally by a Panhard rod and longitudinally by two leading arms with rubber bushes. Front steering is achieved by a steering link connected to both front wheels that simultaneously adjust both wheels' kingpin angle. The vehicle body rests on the axle via two coil springs with translational dampers and rubber stops. The model makes provision for the ladder chassis torsional stiffness by treating the front and rear as two separate bodies connected by a revolute joint and a torsional spring.

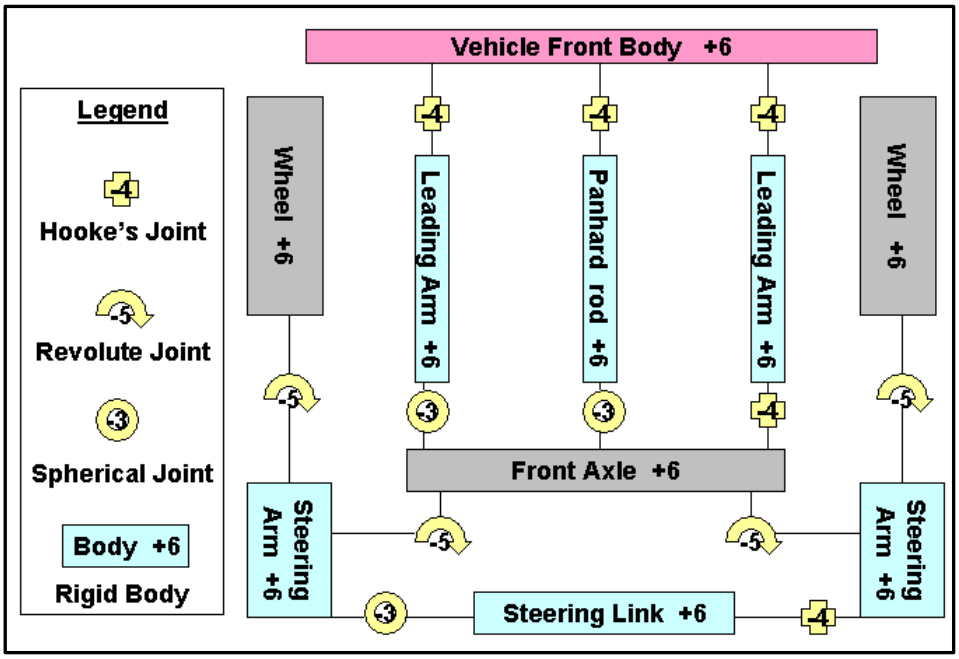

Figure 3-16: ADAMS model front suspension schematic layout (Els, 2006)

3.3.4 *Suspension properties*

The test vehicle is equipped with a semi-active suspension dubbed the $4S_4$ (Els, 2006) that has two discrete damping and two discrete spring rate settings. Figure 3-17 shows the modelled spring force curves for a given displacement of the $4S_4$ for the current version's two gas volume settings: $0.1\ L$ and $0.5\ L$. Figure 3-18 shows the damping force as a function of strut velocity for two damping scaling factors (DSF) namely 0.25 or 2. The DSF scales the damper to the original factory fitted damper. The simulation vehicle for this study employs the soft spring ($0.5\ L$) and low damping setting (DSF = 0.25).

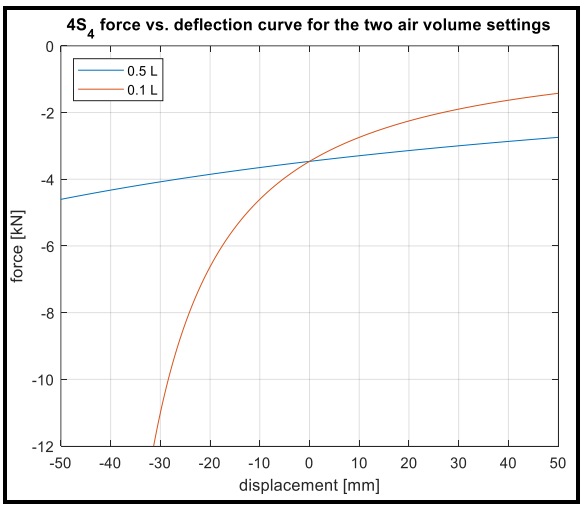

Figure 3-17: The spring characteristics of the $4S_4$ suspension

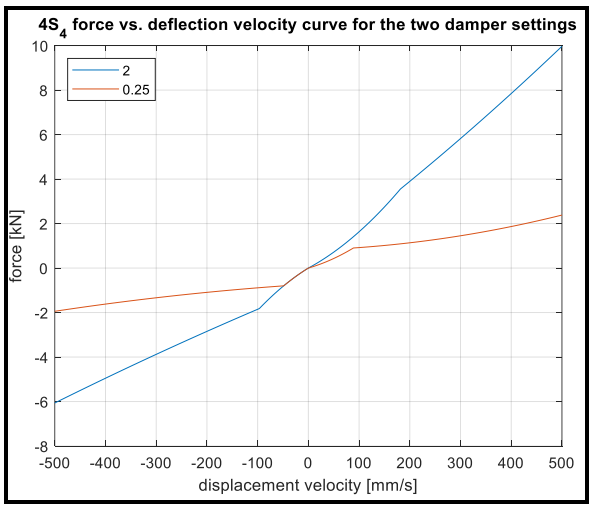

Figure 3-18: The damper characteristics of the $4S_4$ suspension

3.3.5 *Vehicle model validation*

The MSC Adams vehicle model has been proven through several validation runs to be an accurate representation of the actual vehicle. Figure 3-19 shows an excerpt from a report by Peenze (2020) comparing the actual and simulation vehicle lateral response for a DLC manoeuvre performed at 70 km/h on a smooth road. Table 3-4 lists the root mean squared error (RMSE) of lateral dynamics for various speeds along with a percentage of absolute error values that are below this mean. The lower the RMSE and the higher the percentage value, the better. The results show acceptable correlation of lateral dynamics, although factors such as unmodelled dynamics create small deviations.

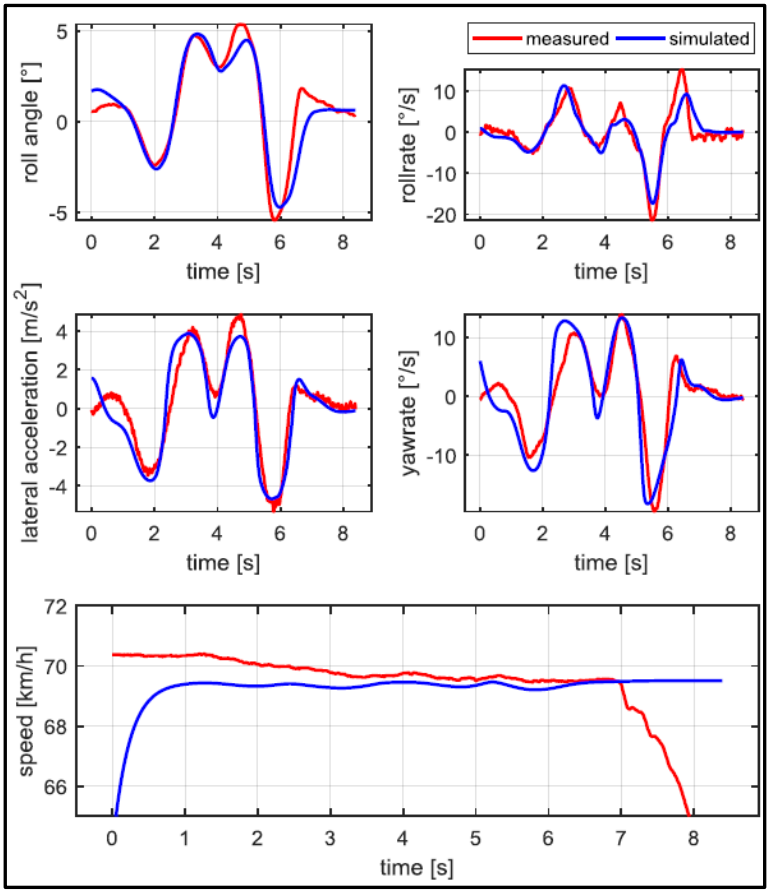

Figure 3-19: 70 km/h validation DLC (Peenze, 2020)

Table 3-4: Comparison of root mean squared error (RMSE) and percentage of absolute error values below RMSE (Peenze, 2020)

Vehicle speed [km/h]	Roll angle RMSE [deg]	Roll rate RMSE [deg/s]	Lateral acceleration RMSE [$m.s^{-2}$]	Yaw rate RMSE [deg/s]
60	0.81 [74%]	2.45 [80%]	0.82 [74%]	3.77 [77%]
70	0.92 [78%]	2.55 [75%]	0.87 [66%]	3.57 [75%]
80	1.49 [70%]	4.66 [72%]	1.40 [57%]	4.64 [65%]

Vertical vehicle dynamics are validated through comparison of the vertical acceleration at CG while driving over rough terrain. For the validation run, the rough terrain is the Gerotek

Belgian paving discussed in Section 3.3.6. The speed for the test run was limited to 47 km/h as it was done against the governor with the vehicle set to the second gear in high range and it becomes increasingly difficult to maintain control at higher speeds. Figure 3-20 shows a visual comparison of the simulated and measured vertical acceleration running RMS (RRMS) with a window of 0.25 s. Figure 3-21 shows a histogram of the vertical acceleration spread and Table 3-5 provides a comparison between the RRMS values over the whole manoeuvre. Considering the data presented, there is acceptable correlation between the simulation and actual vehicle vertical dynamics.

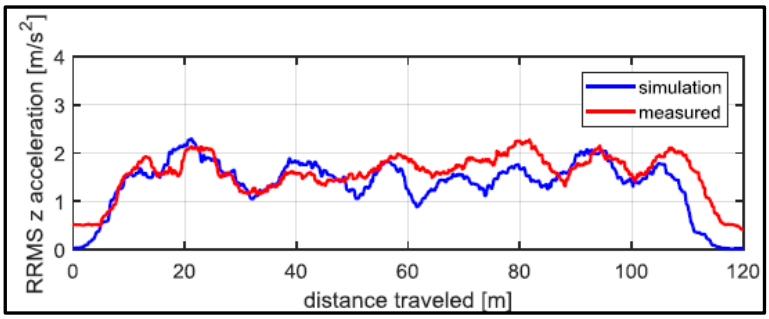

Figure 3-20: Vertical acceleration RRMS (Peenze, 2020)

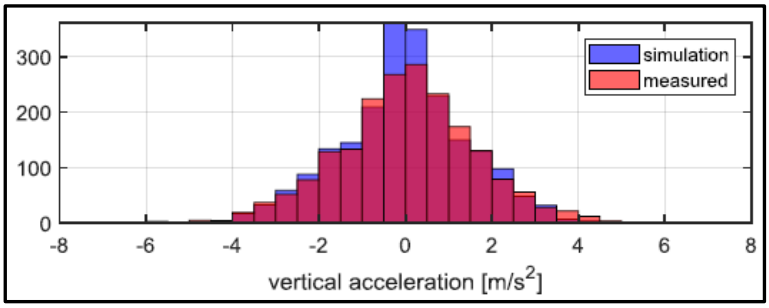

Figure 3-21: Vertical acceleration distribution (Peenze, 2020)

Table 3-5: A comparison of vertical RRMS (Peenze, 2020)

Vehicle	Mean $\ddot{Z}_{CG}$ $[m.s^{-2}]$	Standard deviation $\ddot{Z}_{CG}$ $[m.s^{-2}]$
Simulation	2.12	2.24
Actual	2.21	2.28

3.3.6 *Road profile*

The vehicle can drive on any user defined road in the MSC ADAMS environment. For this study, vehicle stability on a smooth road is compared with a rough road where the rough road is based on the Gerotek Belgian paving measured by Becker (2008) by use of a terrain profiler. Within the vehicle dynamics group (VDG) of the University of Pretoria, the Gerotek Belgian paving is often used as the reference for a rigid rough road. The measured and actual section of Belgian paving at the Gerotek test facility is however too narrow to accommodate the required stability evaluation manoeuvres. Instead, a substitute rough road is chosen based on the road classes as defined in ISO8608:2016 (International Organization for Standardization, 2016). Figure 3-22 shows the displacement spectral density (DSD) of the Belgian paving compared to different ISO8608:2016 (International Organization for

Standardization, 2016) class roads. The plot indicates that a Class D or extremely rough road is thought to be the nearest representative of the Gerotek Belgian paving and is a suitable substitute. Further mention to a rough road classification in this study refers to an ISO8608:2016 Class D road whereas a smooth road classification is a level road with a flat profile.

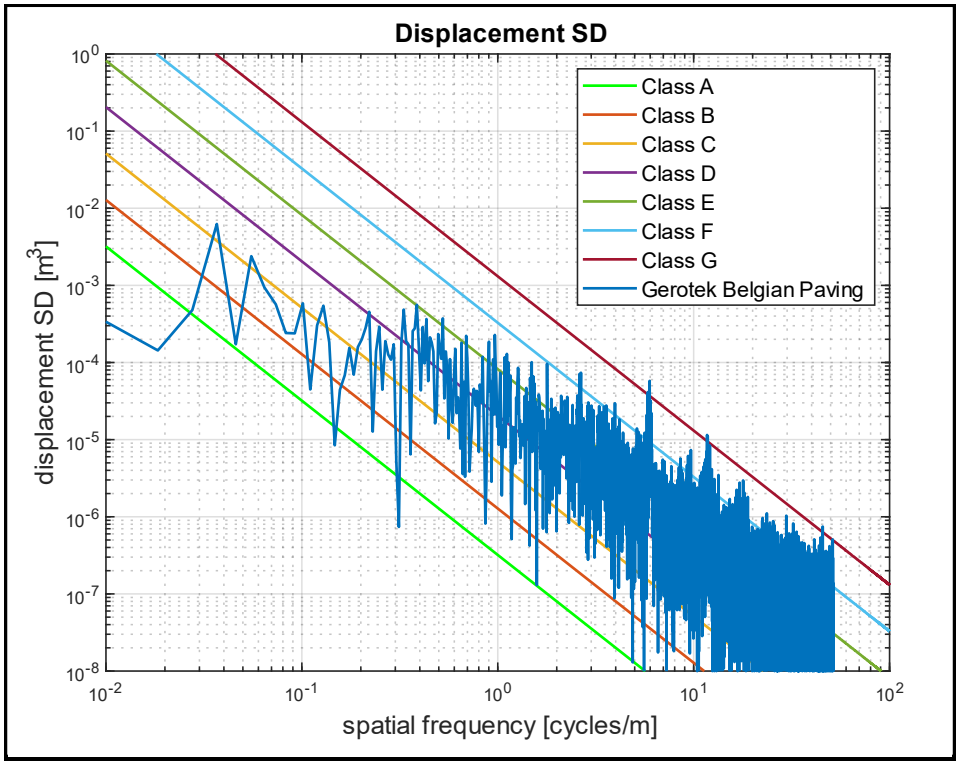

Figure 3-22: Gerotek belgian paving compared to different ISO8608:2016 class roads (Becker, 2008)

3.3.7 *Steering manoeuvres*

In order to assess lateral stability, lateral excitation is achieved by two steering manoeuvres; one being an ISO3888-1:2018 (International Organization for Standardization, 2018) double lane change (DLC) manoeuvre and the other the Euro NCAP sine with dwell test (Euro NCAP, 2011). The DLC manoeuvre simulates an emergency lane change during which the vehicle quickly swerves to the adjacent lane and back in order to avoid an “obstacle” in the road. The test serves as a measure of the closed-loop driver-vehicle pair’s ability to follow a set path during a highly transient manoeuvre. Figure 3-23 shows the DLC path with dimensions listed in Table 3-6. The track used for simulation will be a mirror image or normal right-hand drive road instead of left-hand, as is the road convention of South Africa.

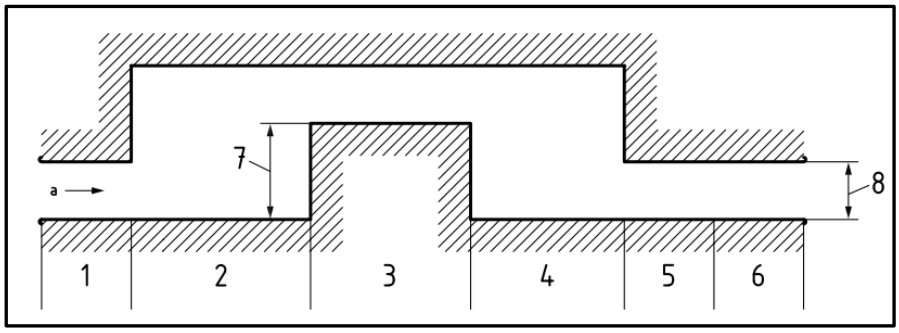

Figure 3-23: The ISO3888-1 DLC manoeuvre path (International Organization for Standardization, 2018)

Table 3-6: The ISO3888-1 DLC manoeuvre section dimensions (International Organization for Standardization, 2018)

Section	Length [m]	Lane offset [m]	Width [m]
1	15	–	$1.1 \times t_v + 0.25$
2	30	–	–
3	25	3.5	$1.2 \times t_v + 0.25$
4	25	–	–
5	15	–	$1.3 \times t_v + 0.25$
6	15	–	$1.3 \times t_v + 0.25$

The sine with dwell steer manoeuvre is a Euro NCAP (Euro NCAP, 2011) specified method for evaluating electronic stability control performance. It prescribes a steering input and mimics a lane change manoeuvre, with the difference being that it is a measure of the open-loop lateral stability of the vehicle. The test is conducted as follows:

1. The vehicle is driven at a speed of 80 $\pm$ 2 km/h and the steering wheel angle slowly increased at a rate of 13.5 °/s until a lateral acceleration of 0.5 g is generated. This is done for both counter- and clockwise steering. $\delta_{0.3g}$ is then the average steering wheel angle at 0.3 g and is taken to the nearest 0.1°. This study will perform testing at 60 km/h due to the vehicle not being able to drive on a rough road at 80 km/h.
2. The steering wheel angle is varied like a sine wave as shown in Figure 3-24, where the period of oscillation is 0.7 Hz. There is a 500 ms delay at the second peak. Two sets of runs are normally performed, one clockwise and the other counter-clockwise. This study will only consider the right-turn version, similar to the DLC.
3. The initial steering wheel angle amplitude is 1.5$\delta_{0.3g}$ and is increased by 0.5$\delta_{0.3g}$ for each run, up to 6.5$\delta_{0.3g}$ or 270°, whichever comes first. This study will use a steering wheel angle amplitude similar to when the vehicle performs a closed-loop DLC.
4. Beginning of steer (BOS) is noted as the first time the steering wheel angle reaches absolute 5° and completion of steer (COS) is noted as the time at which the steering wheel angle returns to zero after the sine with dwell test.
5. The peak yaw rate ($\dot{\psi}_{peak}$) is taken as the first local peak resulting from the sine with dwell steering reversal.
6. For each run, the yaw rate at 1 s (time t) after COS should be noted and the yaw rate ratio (YRR) calculated with Equation 3-17.

$$YRR = 100 \times (\frac{\dot{\psi}(at\ time\ t)}{\dot{\psi}_{peak}}) \quad (3\text{-}17)$$

The vehicle passes criteria 1 out of 3 if YRR does not exceed 35% of $\dot{\psi}_{peak}$ for all runs. Repeat the calculation of YRR but for 1.750 s after COS. The vehicle passes criteria 2 out of 3 if YRR does not exceed 20% of $\dot{\psi}_{peak}$ for all runs.

7. The vehicle passes criteria 3 out of 3 if for all runs, the lateral displacement at 1.07s from BOS is greater than 1.83 m, simulating a lane change.

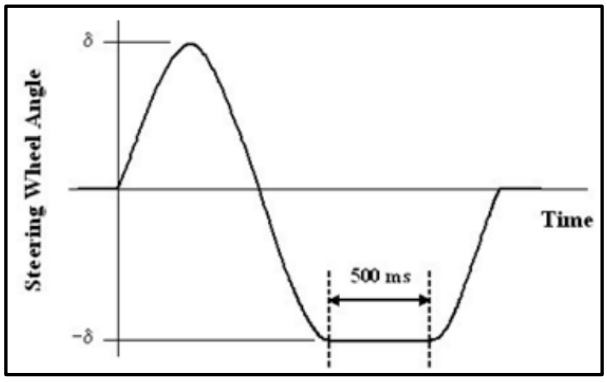

Figure 3-24: The Euro NCAP sine with dwell test steering input (Euro NCAP, 2011)

3.3.8 *Driver model*

The driver model was developed by Botha (2011) and verified for a smooth road, DLC manoeuvre up to near tyre saturation. The model determines a desired yaw acceleration for the next timestep based on the current timestep yaw rate, current heading and preview heading and applies a steer rate based on the steer rate, yaw acceleration models for a high-friction road as shown in Figure 3-25.

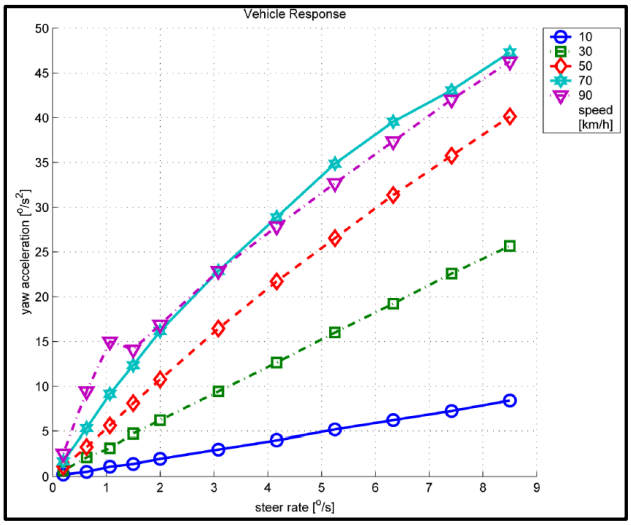

Figure 3-25: The driver model steer rate-yaw acceleration graph (Botha, 2011)

3.4 Chapter conclusion

This chapter presented an overview of tyre mechanics and tyre models, specifically for use on rough roads. The simulation vehicle properties were described along with the experimental

setup such as the road profile, steering manoeuvre and driver model. Figure 3-26 shows an overview of the test vehicle setup in the simulation environment and how the different topics relate.

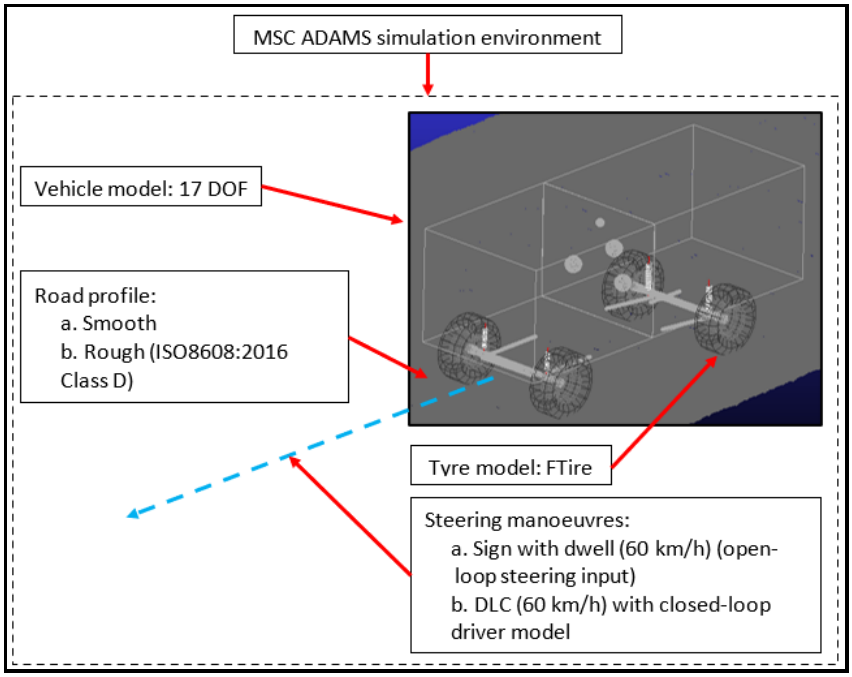

Figure 3-26: Overview of test vehicle setup

CHAPTER FOUR
INDICATORS OF LATERAL STABILITY

Abstract – This chapter focuses on different measures of lateral stability and their areas of application. The measures are: the understeer gradient, location on the phase plane and kinematic model reference error. The indicators are used to construct a stability control reference model that is based on what that particular indicator considers desirable (stable) vehicle behaviour.

4.1 Understeer gradient (K_{us})

The understeer gradient is a common measure of vehicle open-loop stability under steady-state or quasi-steady-state conditions and describes the relationship between steering angle and lateral acceleration whether that is a linear, super- or sub-linear relationship (Gillespie, 1992). During a constant radius turn, higher longitudinal velocity will require larger lateral forces to be developed by the tyres to follow the same path. This equates to increasing front and rear sideslip angles to generate larger lateral forces as discussed in Section 3.1.3. The understeer gradient determines how the difference between front and rear slip angles scale with lateral acceleration as formulated in Equation 4-1. The gradient of Equation 4-1 can be formulated as in Equation 4-2, where lateral acceleration in this context has the unit of $g's$.

$$\alpha_f - \alpha_r = K_{us} a_y \tag{4-1}$$

$$K_{us} = \frac{W_f}{C_{\alpha_f}} - \frac{W_r}{C_{\alpha_r}} \tag{4-2}$$

When there is no difference between the front and rear slip angles as a function of lateral acceleration ($\alpha_f = \alpha_r$) then $K_{us} = 0$ and no steer angle change is needed to follow a constant radius turn as lateral acceleration increases. This is referred to as neutral steer. The case of $K_{us} > 0$ implies that $\alpha_f > \alpha_r$ and a greater front slip angle compared to rear is needed to balance forces as lateral acceleration increases, meaning front steer angle would need to increase to follow a constant radius turn. If no change to the steering angle is made, the vehicle would follow an increasingly larger radius as lateral acceleration increases. This is referred to as understeer (Gillespie, 1992). When $K_{us} < 0$ it implies that $\alpha_f < \alpha_r$ and the front steering angle would need to decrease relative to the rear for increasing lateral acceleration or that for a fixed steering angle the rear would generate a larger slip angle compared to the front to balance lateral forces. If no change to the steering angle is made, the vehicle would follow a decreasing radius as lateral acceleration increases.

Figure 4-1 illustrates the above relationships for the different understeer gradient types in terms of the front steer angle needed to follow a constant radius at increasing speed. Of the

three understeer gradient types, oversteer is the most undesirable as it is counter-intuitive steering (to the average driver) that worsens for increasing velocity. Both neutral and slight understeer are desirable since it exhibits an intuitive relationship between increased lateral acceleration and steering for the understeer case and no change in steering angle for increased lateral acceleration for the neutral steer case. Severe understeer may also be undesirable considering that eventually the required increase in steering angle to increase lateral acceleration becomes so large that the vehicle appears unresponsive to the driver. The understeer gradient also relates yaw rate and front steering angle as shown in Figure 4-2. By selecting a suitable understeer gradient behaviour, a reference vehicle model can determine the appropriate yaw rate for a given steering angle and vehicle velocity that is passed on to the stability control. This method is employed in Section 4.3.

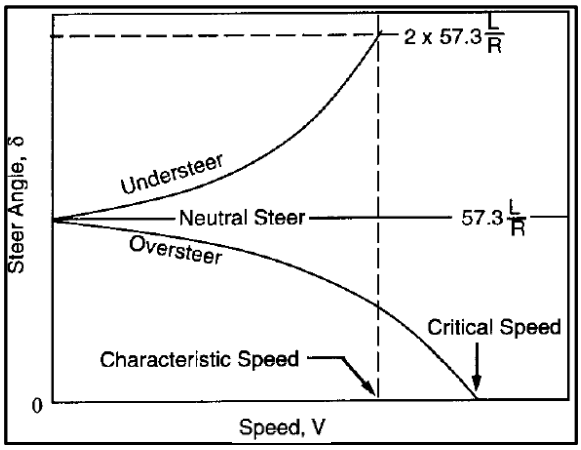

Figure 4-1: A plot of steering angle for increasing longitudinal velocity (increased lateral acceleration) to follow a constant radius path (Gillespie, 1992)

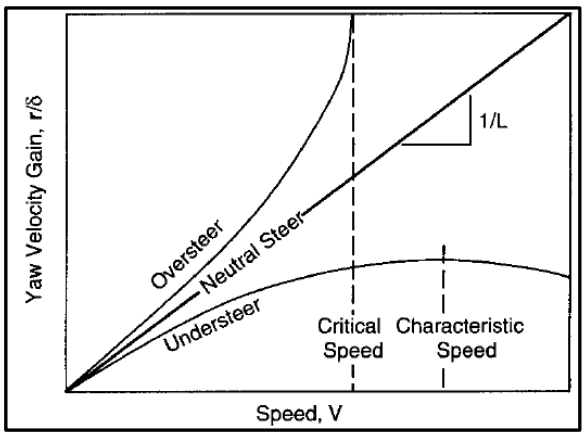

Figure 4-2: A plot of yaw velocity for increased longitudinal velocity (increased lateral acceleration) (Gillespie, 1992)

4.2 Phase plane location

Phase planes visualize the relationship between two state variables such as yaw rate against sideslip angle or sideslip rate against sideslip angle where the ideal relationship should be linear around the origin. This represents a predictable or safe vehicle response for the average driver. Of the two phase plane types mentioned, sideslip angle against sideslip rate is a better indication of vehicle stability (Xie, et al., 2018). Phase planes use instantaneous vehicle states such as front steering angle, rear steering angle, vehicle speed and surface friction to generate locus curves of vehicle states at that instant. That means that a change in one or all of those states would affect the phase plane curves. As an example, Figure 4-3 and Figure 4-4 are from an article by Chen, et al. (2016 (1)) and indicate a yaw rate vs. sideslip angle phase plane plot for two different vehicle velocity cases. The figures illustrate how the phase plane and its stable region about the origin decreases in size for increasing velocity.

Based on a sideslip angle against sideslip rate phase plane, Chen, et al. (2016 (2)) defines a stability region in the plane that is defined as formulated in Equation 4-3. The equation forms an ellipse with a fixed shape that is chosen to enclose the vehicle stable region. This criterion is referred to as the stability index (SI) where values withing the region are $SI \leq 1$ and those outside are $SI > 1$. Equation 4-4 formulates the stability index.

$$Stability\ Region:\ 1 \leq \frac{\beta^2}{c_1^2} + \frac{\dot{\beta}^2}{c_2^2} \tag{4-3}$$

$$Stability\ index\ (SI) = \frac{\beta^2}{c_1^2} + \frac{\dot{\beta}^2}{c_2^2} \tag{4-4}$$

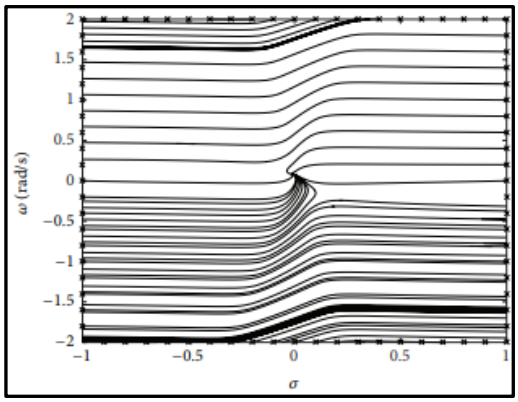

Figure 4-3: A yaw rate-sideslip phase plot with $\delta_f = 0.02\ rad$ and $V_x = 10\ m/s$ (Chen, et al., 2016 (1))

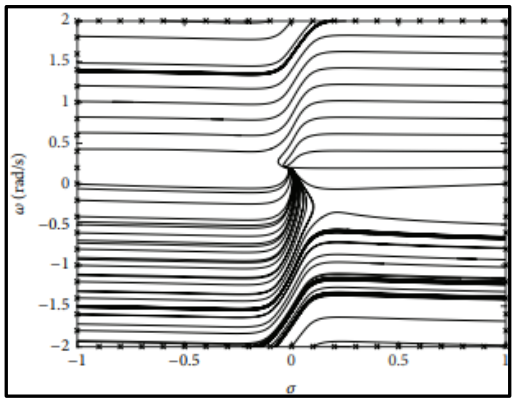

Figure 4-4: A yaw rate-sideslip phase plot with $\delta_f = 0.02\ rad$ and $V_x = 25\ m/s$ (Chen, et al., 2016 (1))

Using the concept of the stability region requires selection of suitable parameters c_1 and c_2. In order to determine their values, one can generate phase plane curves for a range of vehicle states and ensure that the SI ellipse encloses the stable region for all states (Xie, et al., 2018). A common approach to define the boundary of the stable region is to generate the phase plane curves for a zero front steer angle and to draw conclusions on the resulting curves, but this allows for high sideslip angles which may no longer be representative of the allowable limits at higher steering angles (Smakman, 2000). Control intervention should also happen before the vehicle becomes unstable, otherwise the stability controller cannot generate the forces needed to return the vehicle to the stable region. To address these issues, the stable region boundary is defined conservatively and it is important to note that in this study, a value of $SI > 1$ does not constitute an objective unstable vehicle, rather it indicates that the vehicle has left the determined conservative stable region and stability control should be activated.

Chen, et al. (2016 (2)) demonstrates a practical method for obtaining the values of c_1 and c_2 by performing a DLC steering manoeuvre with the vehicle and plotting the resulting sideslip against sideslip rate phase plane. Chen, et al. (2016 (2)) states that in the stable region, small sideslip angle values are associated with small sideslip rates. The sideslip angle which leads to large sideslip rates is the value of c_1 and the highest sideslip rate which originated from a sideslip angle below c_1 is c_2. Chen, et al. (2016 (2)) does not define what is considered a large sideslip rate.

To establish the c_1 and c_2 parameters for the simulation vehicle of this study, a DLC manoeuvre is performed with the vehicle at $40\ km/h$, $50\ km/h$ and $60\ km/h$ on both a smooth and an ISO8608:2016 class D (rough) road and the sideslip angle against sideslip rate phase plots for each run compared. This is done on a high friction surface ($\mu = 1.0$). Figure 4-5 to Figure 4-8 presents plots of measured vehicle states for the runs. The "CG pass boundary" lines shown in Figure 4-7 and Figure 4-8 of the DLC manoeuvre indicate the CG

lateral displacement limits that when crossed, would likely mean that the vehicle would knock over cones and fail a physical DLC test. Naturally, a faster driving vehicle on the same unchanged reference path experiences larger lateral forces and is more difficult to control. That means that the likelihood of failing the DLC test becomes higher with increasing entry speed. This is observed in Figure 4-5 which shows larger absolute yaw rate- and roll angle peaks with increasing entry speed, while the vehicle also increasingly struggles to follow the reference path and fails at 60 km/h. This is observed for both the smooth and rough road, although the vehicle on the smooth road generally has lower roll-angle peaks and follow the reference path better. With greater speed, the increasingly larger roll angles are accompanied by tyre normal force troughs that move closer to a zero value, as shown in Figure 4-6. This effect is more prominent on the rough road, where rapid tyre normal force fluctuations occur. The results indicate that although both the smooth and rough road $60\ km/h$ runs fail the DLC test, the rough road fares the worst. It is important to note for the following chapters that due to the soft suspension setting, the vehicle is able to reach a high roll angle of 10° without rolling over.

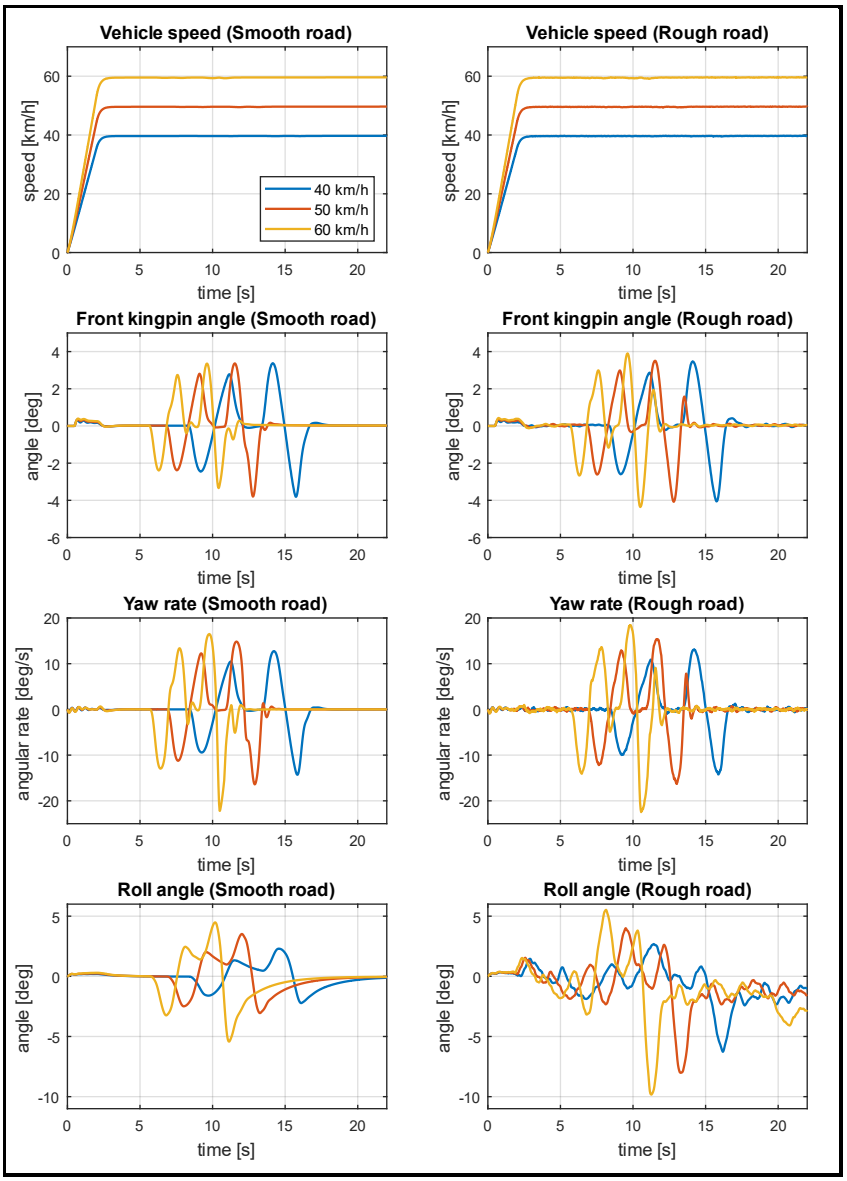

Figure 4-5: DLC manoeuvre on a rough road for different speeds

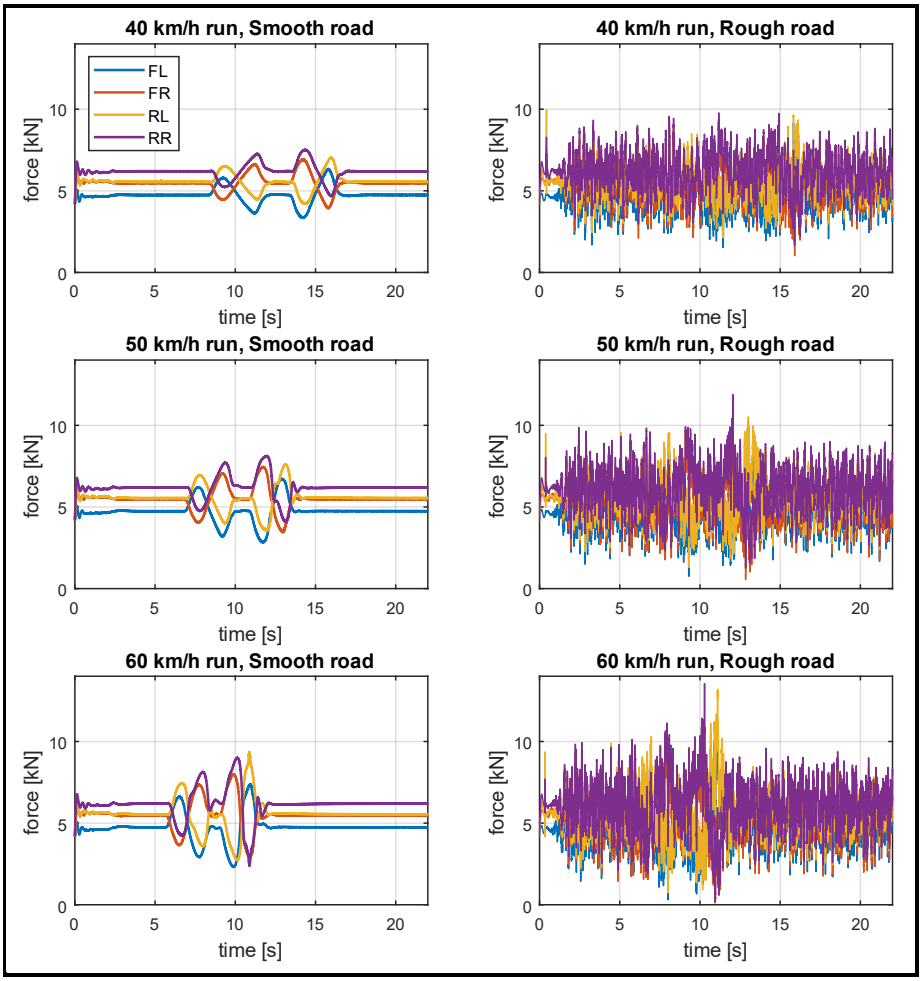

Figure 4-6: Tyre normal forces for a DLC manoeuvre

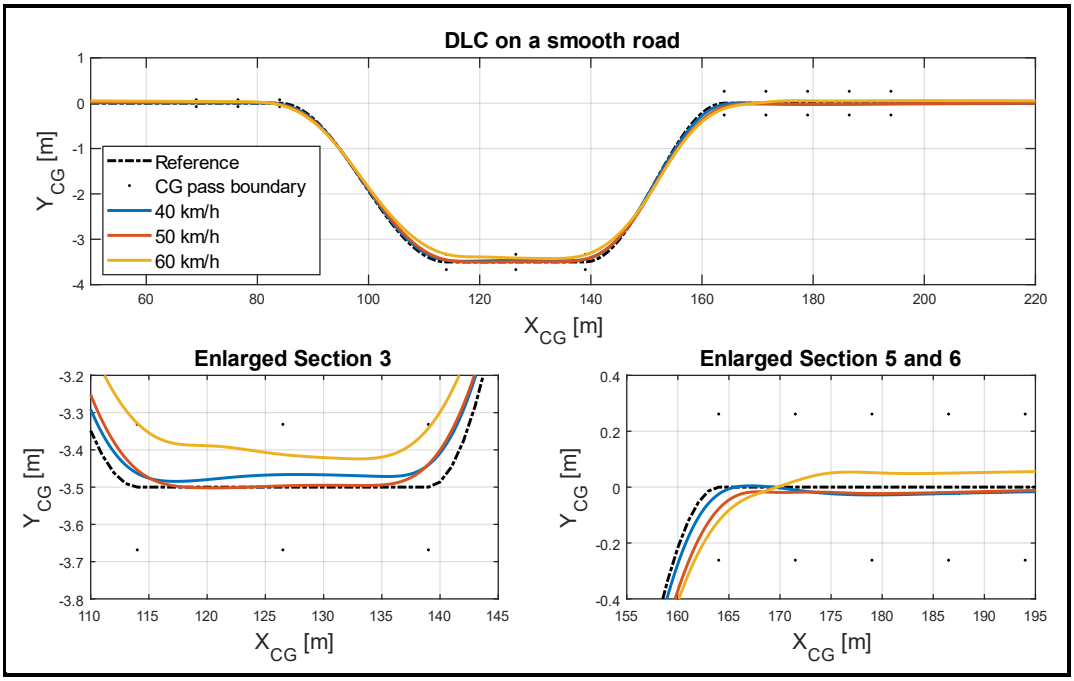

Figure 4-7: A DLC on a smooth road at different speeds

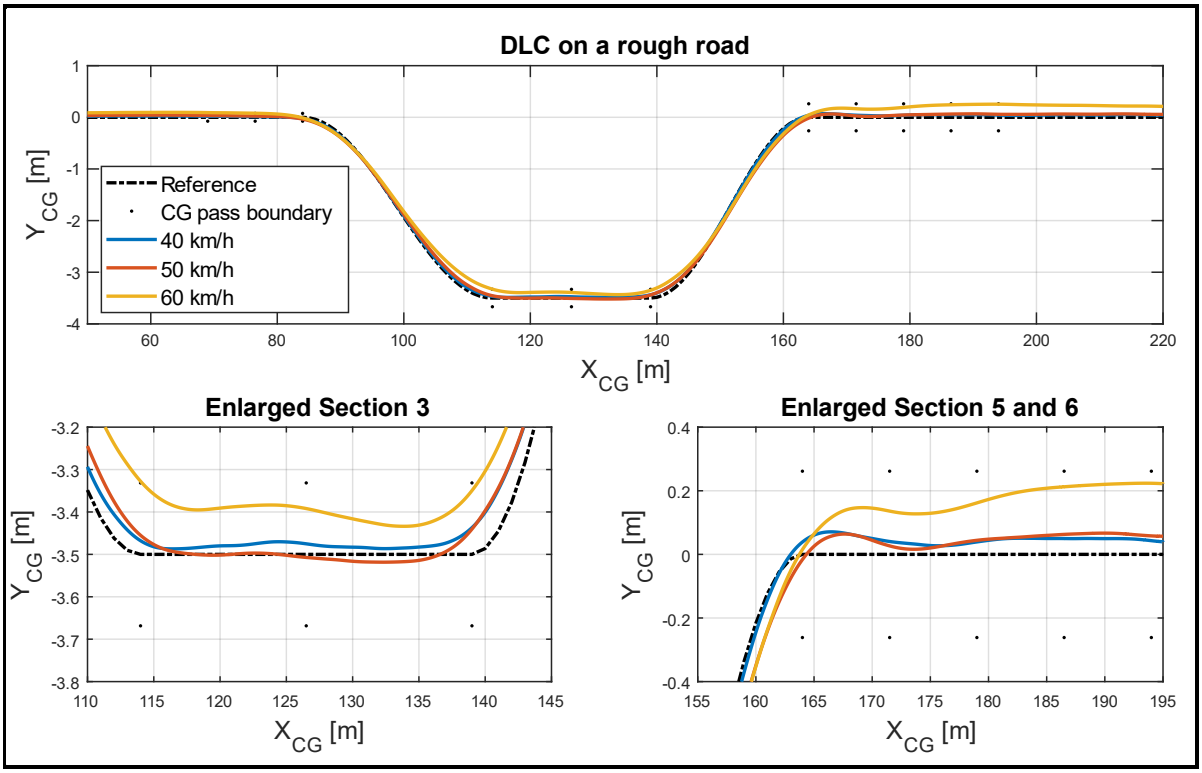

Figure 4-8: A DLC on a rough road at different speeds

Plots of sideslip angle against sideslip rate are constructed for the runs on both road classifications at the different speeds, as shown in Figure 4-9. Following the parameter c_1 and c_2 selection process, $c_1 = |\beta_{\max}| = 1$ is chosen since peak sideslip rates are associated with sideslip angles which are larger than one. The sideslip rate parameter, $c_2 = |\dot{\beta}_{max}| = 2$ is chosen since the largest sideslip rate associated with sideslip angles below c_1 is generally two. The two parameters describe the conservative stable region boundary as illustrated by the ellipse in the figure.

According to sideslip angle against sideslip rate plots of Figure 4-9, the vehicle is most unstable for DLC Section 4 and 5 (green and yellow), regardless of the choice of road. Intuitively, Section 4 and 5 is expected to be the most unstable sections as the vehicle yaw rate and roll angle are at their peak values. Due to this congruence, it may be reasonable to conclude that the phase plane method is able to indicate when the vehicle has left the conservative stable region and stability control intervention is required. Moreover, this is achieved with a fixed set of parameters (c_1, c_2) for both a smooth and a rough road.

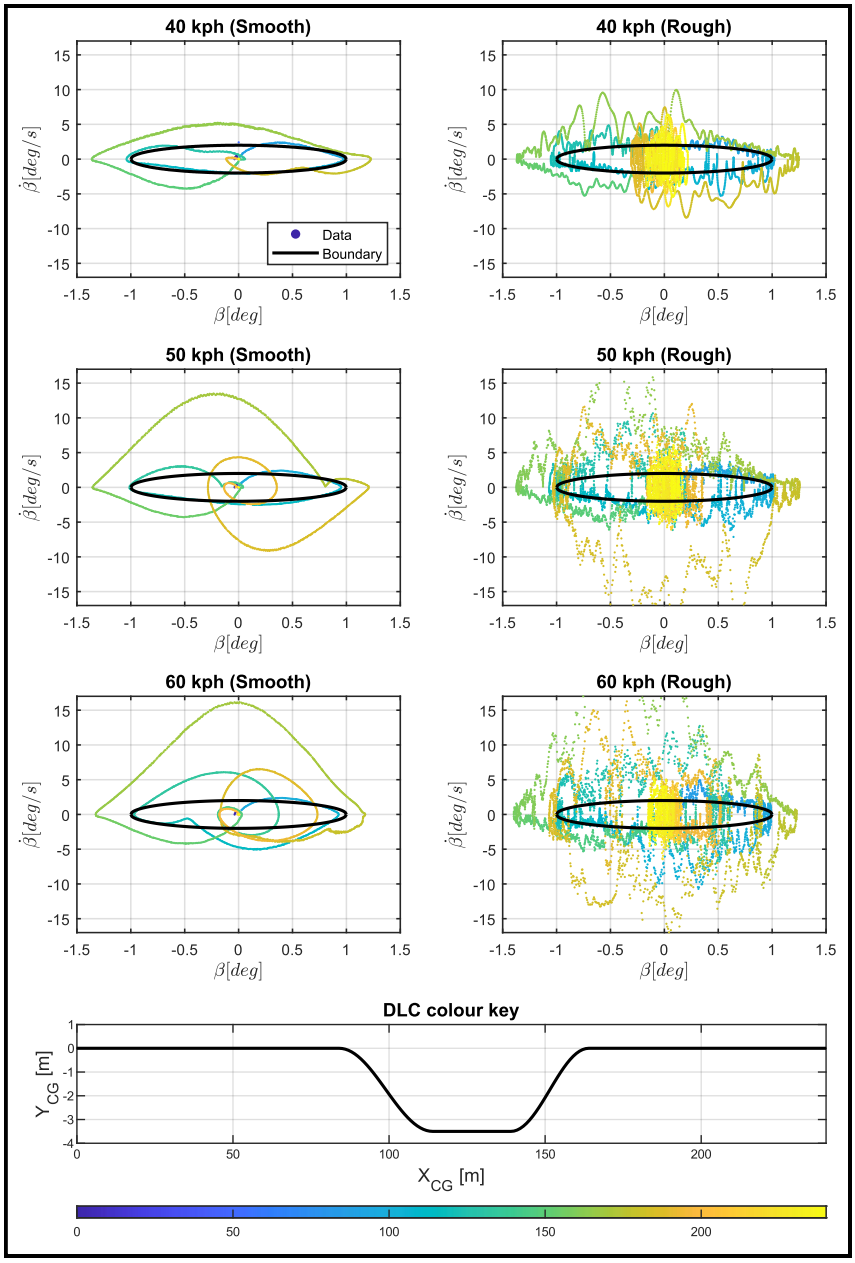

Figure 4-9: The sideslip angle, sideslip rate phase plane plots for a DLC manoeuvre performed with the baseline vehicle on different roads at different speeds for μ = 1.0

The empirically tuned SI boundary may be investigated on the phase plane which is generated for the test vehicle by solving differential Equation 4-5 and Equation 4-6 (adapted from Equation 3-9 and Equation 3-11 respectively). This is done for zero front steering angle at a speed of $60\ km/h$. The 89 MF tyre model of Section 5.1 is used to calculate tyre lateral force. The resulting phase portrait is shown in Figure 4-10 and indicates that the chosen SI boundary encapsulates a portion of the linear $\beta - \dot{\beta}$ region.

$$\dot{\beta} = \frac{F_{yf}+F_{yr}}{mv_x} - \dot{\psi} \tag{4-5}$$

$$\ddot{\psi} = \frac{l_f F_{yf} - l_r F_{yr}}{I_{zz}} \tag{4-6}$$

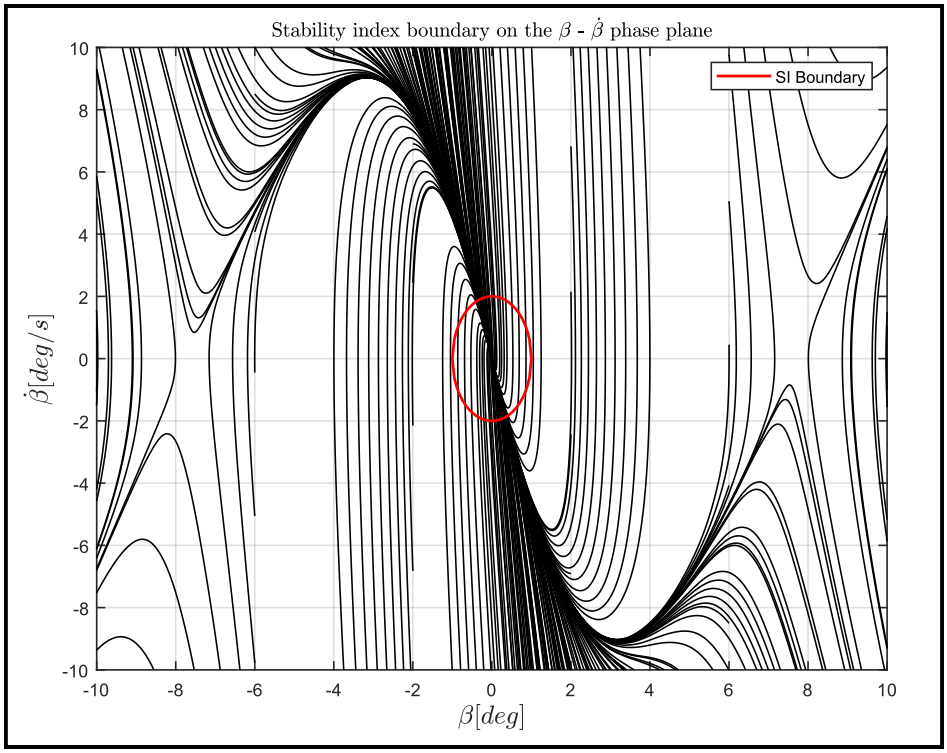

Figure 4-10: Test vehicle $\beta - \dot{\beta}$ phase plane curves showing the SI boundary for zero front steer angle at 60 km/h

It has been established that the stability region may indicate whether a vehicle is in a conservative stable state or if the stability control should be activated. The SI boundary may serve as a reference to the stability control system which tries to maintain the vehicle within the stability region. Such a controller is referred to as a sideslip controller and the control objective is to minimize Equation 4-7 (Rajamani, 2006).

$$e = \dot{\beta} - \dot{\beta}_{ref} + \zeta(\beta - \beta_{ref}) \tag{4-7}$$

$$\beta_{ref} = \begin{cases} \beta_{boundary} \times sgn(\beta) & |\beta| \geq \beta_{boundary} \\ \beta & |\beta| < \beta_{boundary} \end{cases} \tag{4-8}$$

$$\dot{\beta}_{ref} = \begin{cases} \dot{\beta}_{boundary} \times sgn(\dot{\beta}) & |\dot{\beta}| \geq \dot{\beta}_{boundary} \\ \dot{\beta} & |\dot{\beta}| < \dot{\beta}_{boundary} \end{cases} \tag{4-9}$$

Where $\beta_{boundary}$ and $\dot{\beta}_{boundary}$ are determined by straight line connecting the sampling point outside the stability region and noting the cross-over point with the boundary. This process is represented by Equation 4-10 and Equation 4-11 and illustrated in Figure 4-11.

$$\beta_{boundary} = \sqrt{\frac{1}{\frac{m_{grad}^2}{c_2^2} + \frac{1}{c_1^2}}} \tag{4-10}$$

$$\dot{\beta}_{boundary} = m_{grad} \times \beta_{boundary} \tag{4-11}$$

Where,

$$m_{grad} = \frac{\dot{\beta}}{\beta} \tag{4-12}$$

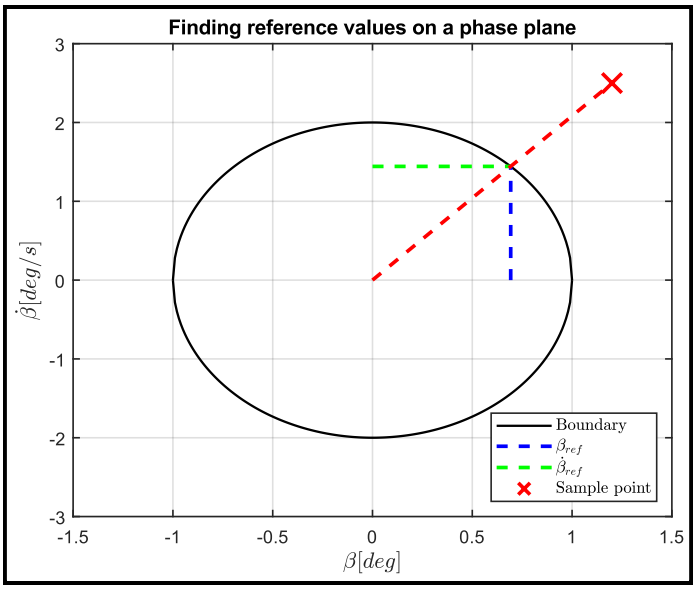

Figure 4-11: Visual representation of how the reference sideslip angle and rate are determined

4.3 Kinematic model reference error

By substituting the kinematic relationship $R = \frac{57.3 v_x}{\dot{\psi}}$ into Equation 3-15 from Section 3.2.1, a formulation for a reference yaw rate based on a front steering input is found. This is shown in Equation 4-13.

$$\dot{\psi}_{des} = \frac{1}{\frac{L}{v_x} + \frac{\left(\frac{w_f}{C_{\alpha f}} - \frac{w_r}{C_{\alpha r}}\right)}{57.3g} v_x} \delta_f = \frac{1}{\frac{L}{v_x} + \frac{K_{US}}{57.3g} v_x} \delta_f \tag{4-13}$$

This formulation is however undefined at $v_x = 0\ m.s^{-1}$ and so a conditional function as in Equation 4-14 is used.

$$\dot{\psi}_{des} = \begin{cases} 0°/s & v_x = 0\ m.s^{-1} \\ \dot{\psi}_{des} & v_x > 0\ m.s^{-1} \end{cases} \tag{4-14}$$

The total lateral acceleration of the CG can be limited by the available surface friction where the lateral acceleration is formulated in Equation 4-15.

$$a_{y\,(CG)} = v_x \dot{\psi} + \dot{v}_y \tag{4-15}$$

If it is assumed that the sideslip angle and rate is small, (Rajamani, 2006) suggests using Equation 4-16 where only 85% of the available surface friction is dedicated to yaw rate and the remaining 15% to the sideslip rate (or lateral translation acceleration) component.

$$\dot{\psi}_{\lim} = 0.85\frac{\mu g}{v_x} \tag{4-16}$$

The reference yaw rate becomes as formulated in Equation 4-17.

$$\dot{\psi}_{ref} = \begin{cases} \dot{\psi}_{des} & |\dot{\psi}_{des}| \leq \dot{\psi}_{\lim} \\ \dot{\psi}_{\lim} \times sgn(\dot{\psi}_{des}) & |\dot{\psi}_{des}| > \dot{\psi}_{\lim} \end{cases} \tag{4-17}$$

The reference sideslip angle is derived by studying the geometry of the single track (bicycle) model during a high-speed turn, as shown in Figure 4-12. These angles are based on the principle that the rear drifts outward to create a slip angle. Front and rear tyre slip angles are perpendicular to the turn centre connecting line. As the point of sideslip angle measurement moves from the rear to front axle, its value is described by Equation 4-18. Equation 3-15 from Section 3.2.1 can be rearranged to yield an expression for R as in Equation 4-19 that is then substituted into Equation 4-18 to calculate the steady-state sideslip angle at the vehicle CG.

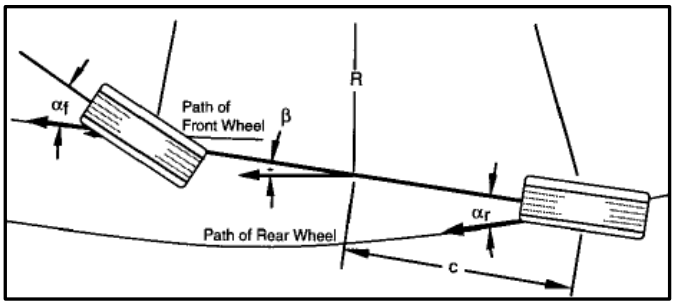

Figure 4-12: Bicycle model sideslip angle during high-speed cornering (Gillespie, 1992)

$$\beta_{des} = \frac{57.3c}{R} - \alpha_r = \frac{57.3c}{R} - \frac{w_f v_x^2}{C_f g R} \tag{4-18}$$

Where,

$$R = \left(57.3 \times L + \left(\frac{w_f}{C_f} - \frac{w_r}{C_r}\right)\right)\frac{1}{\delta_f} = (57.3 \times L + K_{US})\frac{1}{\delta_f} \tag{4-19}$$

The desired sideslip angle is limited by the slip angle of the rear axle tyres at which non-linearity starts. By studying Figure 5-2, that slip angle value is taken to be 3° so that the sideslip angle limit can be formulated as in Equation 4-20 with R as in Equation 4-19 (with angle units in degrees).

$$\beta_{\lim} = \frac{57.3c}{R} - (3 - \delta_r) \tag{4-20}$$

The reference sideslip angle becomes as in Equation 4-21.

$$\beta_{ref} = \begin{cases} \beta_{des} & |\beta_{des}| \leq \beta_{\lim} \\ \beta_{\lim} \times sgn(\beta_{des}) & |\beta_{des}| > \beta_{\lim} \end{cases} \tag{4-21}$$

The control objective is to minimize Equation 4-22 (Rajamani, 2006).

$$e = \dot{\psi} - \dot{\psi}_{ref} + \zeta(\beta - \beta_{ref}) \tag{4-22}$$

As long as the vehicle properties on which the stability control (SC) reference model is based are open-loop stable in terms of the understeer gradient, then the control system will always attempt to steer towards safe vehicle dynamics regardless of real CG location, tyre properties or mass. This means that effectively a yaw rate response is chosen which the vehicle will approximate. To determine an appropriate understeer gradient and thereby yaw rate response, the simulation vehicle understeer gradient is determined at stand-still by using Equation 4-2 which requires the front and rear axle weights and tyre cornering stiffnesses. The axle weights are calculated as in Equation 4-23 and Equation 4-24 and the tyre cornering stiffness obtained for each tyre normal force at standstill as listed in Table 4-1. The tyre normal force was measured in MSC ADAMS and the resulting cornering stiffness calculated with the 89 MF tyre model of Section 5.1. The understeer gradient is calculated with Equation 4-25.

Table 4-1: Wheel states and parameters at stand-still

Property	FL	FR	RL	RR
Normal force $[N]$	4159	4805	5235	5880
Cornering stiffness $[N/deg]$	952	1046	1099	1165

$$w_f = \frac{l_r}{lf + l_r} \times m \times g = \frac{1.25}{1.25 + 1.55} \times 2047 \times 9.81 = 8964.8\ N \tag{4-23}$$

$$w_r = \frac{l_f}{lf + l_r} \times m \times g = \frac{1.55}{1.25 + 1.55} \times 2047 \times 9.81 = 11116.3\ N \tag{4-24}$$

$$K_{us} = \frac{w_f}{C_{\alpha_f}} - \frac{w_r}{C_{\alpha_r}} = \frac{8964.8}{1998} - \frac{11116.3}{2264} = -0.4 \tag{4-25}$$

It is evident from Equation 4-25 that the simulation vehicle exhibits slight oversteer while a slight positive understeer gradient is desirable and should be used for the reference model. Table 4-2 explores how the understeer gradient changes for different tyre stiffness combinations while Table 4-3 explores the effect of moving the CG location forward (+) or backward (-) as percentage of the wheelbase.

Table 4-2: Understeer gradient for relative change in tyre cornering stiffness

		Understeer gradient (k_{Us})						
Front cornering stiffness (C_f)	+30%	-3,6	-2,7	-2	-1,5	-1	-0,6	-0,3
	+20%	-3,3	-2,4	-1,7	-1,2	-0,7	-0,4	0
	+10%	-2,9	-2,1	-1,4	-0,8	-0,4	0	0,3
	+0%	-2,5	-1,7	-1	-0,4	0	0,4	0,7
	-10%	-2	-1,2	-0,5	0,1	0,5	0,9	1,2
	-20%	-1,4	-0,5	0,2	0,7	1,1	1,5	1,8
	-30%	-0,6	0,3	1	1,5	1,9	2,3	2,6
		-30%	-20%	-10%	+0%	+10%	+20%	+30%
		Rear cornering stiffness (C_r)						

Table 4-3: Understeer gradient for relative change in CG location

Relative change	-10%	-5%	0%	+5%	+10%
$W_f\ [N]$	4948.5	6956.7	8964.8	10972.9	12981
$W_r\ [N]$	15132.5	13124.4	11116.3	9108.2	7100.1
K_{US}	-2,3	-1,4	-0,4	0,5	1,5

Based on these tables, a suitable choice of understeer gradient may be $K_{US} = 0.5$ as it assumes the CG location to be moved forward by 5% wheelbase, or that the rear tyres are 10% stiffer than they really are and the front tyres only 90% as stiff as they really are. This value represents a small but reasonable change in vehicle properties to ensure the model exhibits safe behaviour i.e., understeer. The reference vehicle model becomes as listed in Table 4-4. Figure 4-13 shows a comparison of the yaw rate gains obtained for the K_{US} values of $-2.3, -1.4, -0.4, 0, 0.5$ and 1.5 which correspond to the CG shifted by $-10\%, -5\%, 0\%, +5\%$ and $+10\%$. These values also represent the inner diagonal values of Table 4-3 which is along the highest gradient or most sensitive plane. The reference yaw rate curve will always approximate the same gain dynamics regardless of changing tyre or CG location properties which makes for a robust reference yaw rate model.

Table 4-4: Properties of the reference model

Property	Symbol	Value	Unit
Longitudinal distance from CG to front axle	l_f	1.41	m
Longitudinal distance from CG to rear axle	l_r	1.39	m

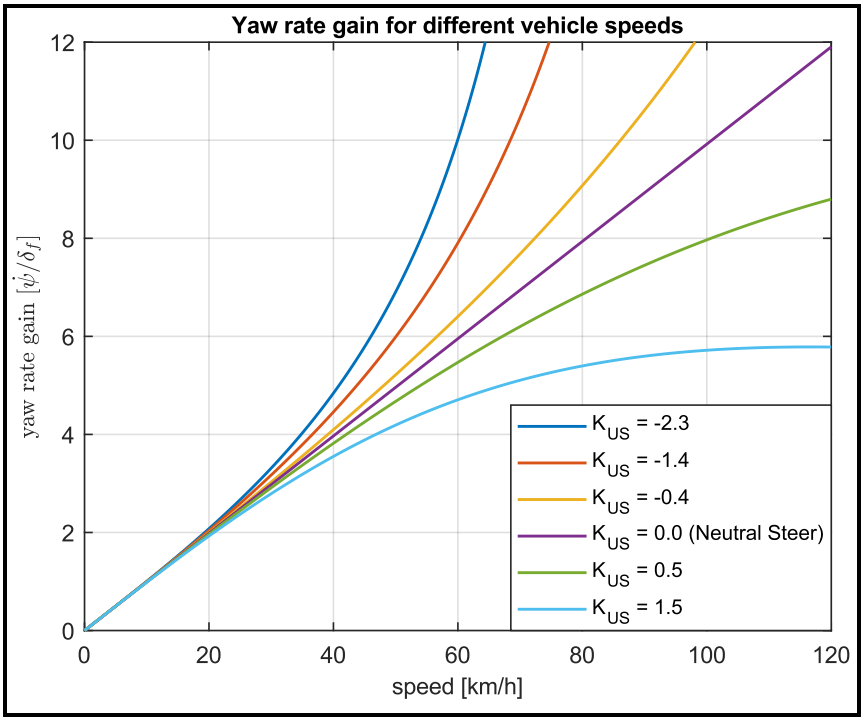

Figure 4-13: A plot of yaw rate gain as function of vehicle speed

4.4 Chapter conclusion

This chapter described indicators of lateral stability namely the understeer gradient, location on the phase plane and the kinematic model reference error. Since the indicators can define stable vehicle behaviour, they are used to construct SC reference models that is considered to describe desirable (stable) vehicle behaviour. Figure 4-14 shows a diagram of the connection between the lateral stability indicators and reference models.

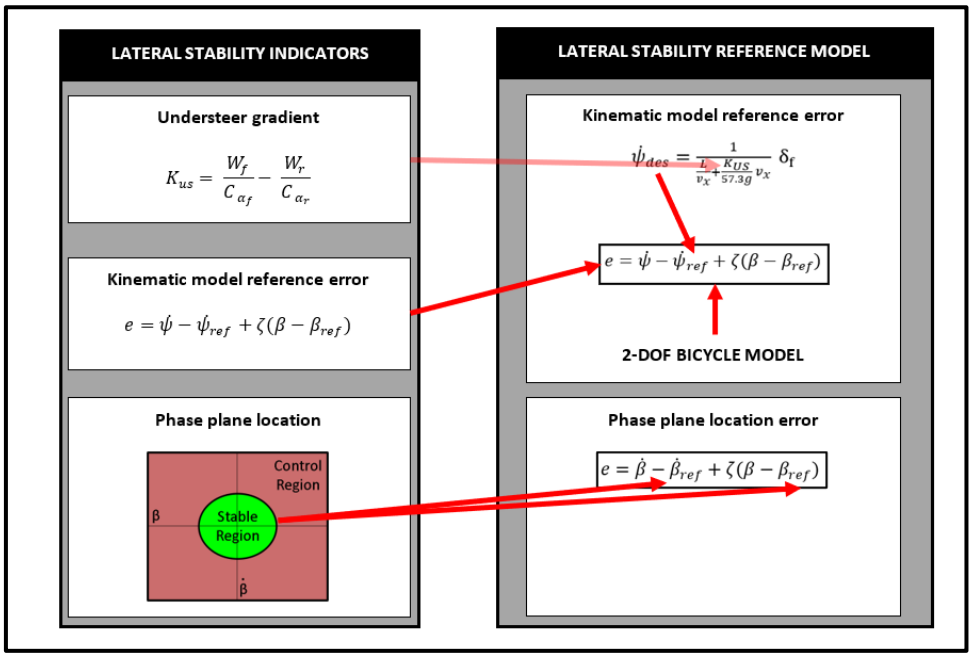

Figure 4-14: A block diagram showing the contribution of lateral stability indicators to a stability control reference model

CHAPTER FIVE
CONTROL SYSTEM DESIGN

Abstract – In a top-down approach, the state estimators and evaluators, and the three layers of the multi-layer control hierarchy are established. The three layers are the decision layer, from which the SC ARS and RDB corrective yaw moments are determined, the control layer from which ARS and RDB actuator setpoints are determined, and the physical layer, that contains the modelled ARS and RDB hardware. Following this, a bottom-up approach is taken to tune the various parameters of the three layers, starting with the PID gains of the RDB and ARS systems. The ability of the RDB and ARS systems to follow force setpoints are evaluated after PID tuning. Thereafter, the SMC gains and SMC sliding variable zeta weightings of the decision layer are tuned. Figure 5-1 presents an overview of Chapter 5 topics.

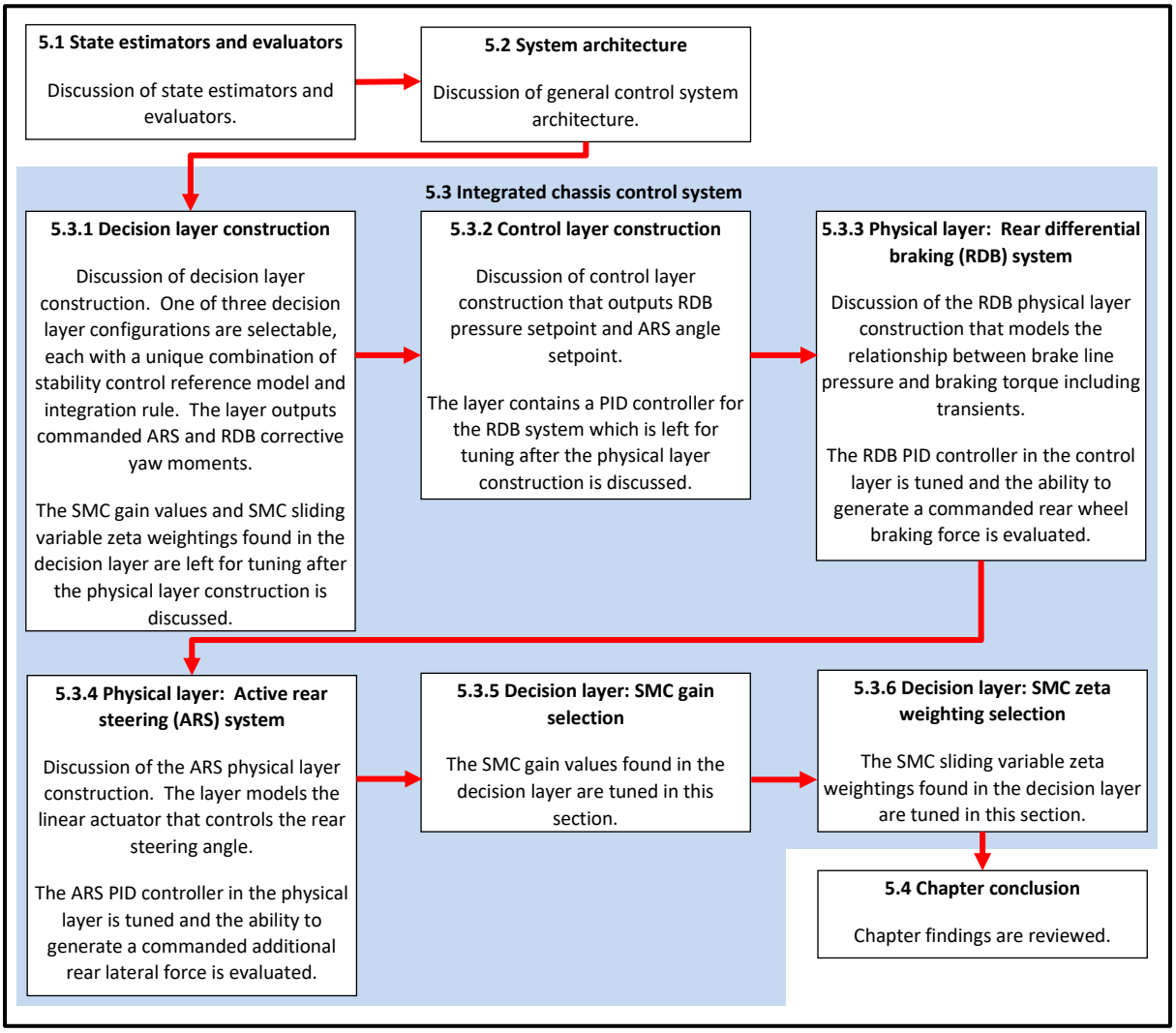

Figure 5-1: Overview of Chapter 5 topics

5.1 State estimators and evaluators

Even though all system states are readily available in the simulation environment, this does not reflect reality, which is that many states are not practically measurable. Those states are then either evaluated based on a mathematical relationship or estimated, which in both cases may introduce inaccuracies or delays that may impact controller performance. This study will only directly measure states that are practical to measure during real-world testing and estimate or evaluate the others, just like with physical testing. The state estimators do not consider sensor noise. The sideslip angle estimator, rear axle slip angle evaluator and tyre normal force estimators used in this study are discussed in Appendix B.

5.1.1 *Control system tyre model*

Based on the limited input parameters required, the 89 Pacejka-type tyre model (Bakker, et al., 1989), also known as the 89 magic-formula (MF), will be used by the control system to estimate tyre longitudinal and lateral forces. Table 5-1 and Table 5-2 lists the lateral and longitudinal coefficients respectively as fitted to data of the experimental vehicle's tyres (with the FTire model) in the simulation environment. Figure 5-2 shows the recreated lateral force curves and Figure 5-3 the longitudinal force curves for those coefficients.

Table 5-1: The lateral tyre force parameters for the 89 MF tyre model

Coefficient	Value
a_0	1.45
a_1	-24.48
a_2	1125
a_3	1313.4
a_4	9.6842
a_5	0
a_6	-0.021
a_7	0.77394
a_8	0.0001
a_9	0.0001
a_{10}	0.0001
a_{11}	0.0001
a_{12}	0.0001
a_{13}	0.0001

Table 5-2: The longitudinal tyre force parameters for the 89 MF tyre model

Coefficient	Value
b_0	0.8158
b_1	-9.9617
b_2	1499
b_3	99.98
b_4	249.991
b_5	0.23566
b_6	7.79×10^{-4}
b_7	-4.159×10^{-3}
b_8	1.0264
b_9	1.017×10^{-5}
b_{10}	2.6279×10^{-5}

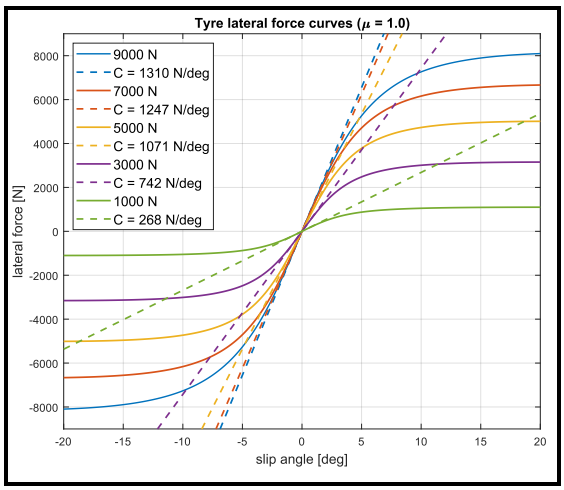

Figure 5-2: The 89 MF lateral force curves for different normal loads

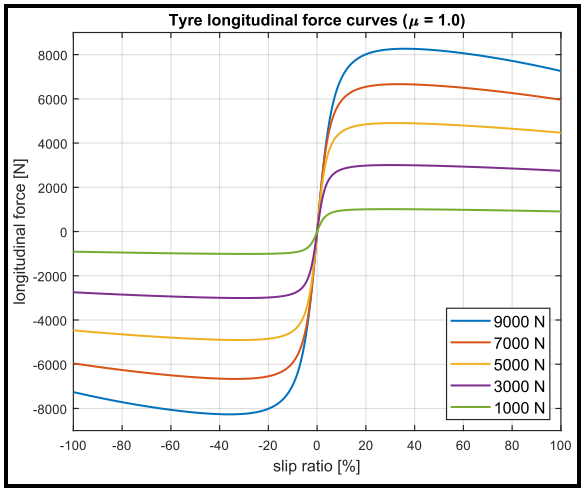

Figure 5-3: The 89 MF tyre model longitudinal force curves for different normal loads

The 89 MF tyre model may also be used to account for combined slip scenarios by considering how far from the peak braking or steering force a current slip angle and slip ratio combination is. This is represented by a ratio for braking and steering as Equation 5-1 and Equation 5-2 respectively that is combined to provide an overall ratio as in Equation 5-3.

$$\sigma_x^* = \frac{\kappa}{\sigma_{xmtot}} \tag{5-1}$$

$$\sigma_y^* = \frac{\alpha}{\sigma_{ymtot}} \tag{5-2}$$

$$\sigma^* = \sqrt{\sigma_x^{*2} + \sigma_y^{*2}} \tag{5-3}$$

The longitudinal and lateral forces are corrected to compensate for combined slip as in Equation 5-4 and Equation 5-5 respectively where $F_x(g(x))$ and $F_y(h(x))$ are the pure slip Pacejka 89 formulas. Figure 5-4 shows how lateral force is affected by increasing slip ratio and Figure 5-5 illustrates how longitudinal force is affected by increasing slip ratio for different slip angles.

$$F_{x\ combined} = \frac{\sigma_x^*}{\sigma^*} \times F_x(\sigma^* \times \sigma_{xmtot}) \tag{5-4}$$

$$F_{y\ combined} = \frac{\sigma_y^*}{\sigma^*} \times F_y(\sigma^* \times \sigma_{ymtot}) \tag{5-5}$$

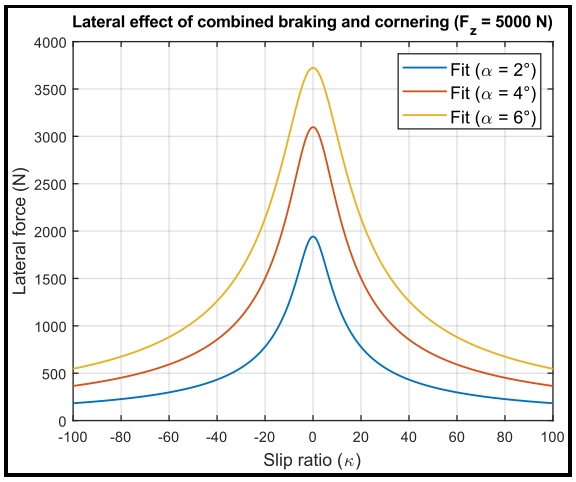

Figure 5-4: Effect of combined slip on lateral force generation

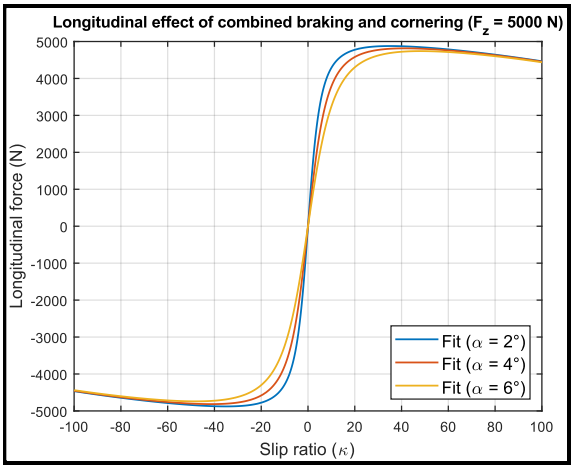

Figure 5-5: Effect of combined slip on longitudinal force generation

5.2 System architecture

A multi-layer supervisory approach as discussed in Section 2.2.2 is used for this study where in order to rule out confusion, the supervisor layer is termed the decision layer, the layer containing the RDB and ARS sub-system controllers termed the control layer and the hardware layer termed the physical layer. This is shown in Figure 5-6. The decision and control layer are collectively called the integrated controller. The physical layer forms part of the simulation vehicle and mimics real-world hardware response.

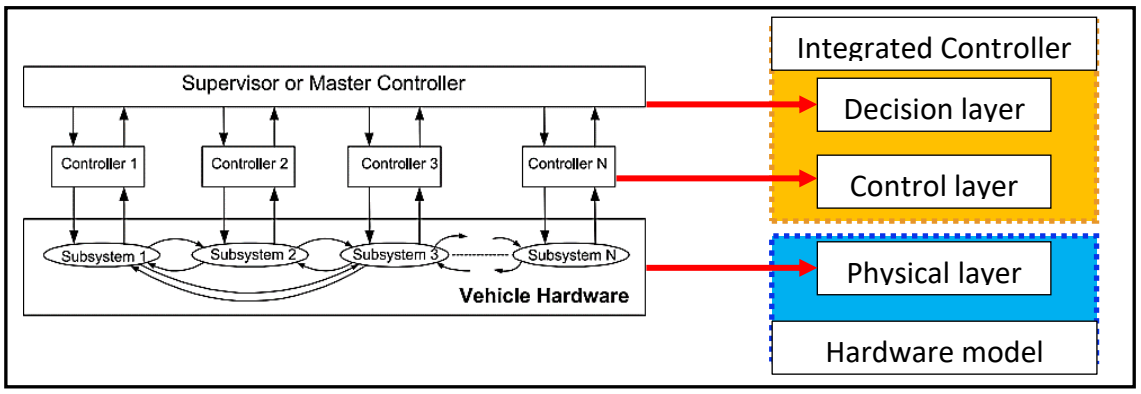

Figure 5-6: Layer terminology of the multi-layered supervisor for this study

The rationale behind the choice of the supervisory approach is that a modular system simplifies the design process as each controller is designed separately, with its own control system and objectives. When an integrated event appears, the decision layer passes down an objective or target to the control layer which may be programmed to prioritise the new objective or its own, depending on the control coordination for that system.

5.3 Integrated chassis control system

5.3.1 *Decision layer construction*

The decision layer contains the two sliding mode controllers (SMC), one for ARS and one for RDB, that determine the corrective yaw moment to be generated by the steering and braking systems respectively. The layer requires a reference model of desired vehicle lateral

dynamics, for use as an SMC sliding variable, along with an integration rule for integrating the ARS and RDB SCs.

Two SC reference models will be used for this study, namely the phase plane location error and the kinematic model reference error. Two integration rules will be used for this study: the stability index, which describes how vehicle lateral states evolve from the current state, and average rear wheel slip angle, which is an indicator of the tyre's lateral force generating capability.

By combining different reference models and integration rules, a combination of different decision layer configurations is possible. This study will investigate three different decision layer configurations as listed below.

Configuration no. 1:

Phase plane location based stability control, where the controller attempts to steer the vehicle back to within the conservative stable phase plane region whenever it is outside the region. This criterion employs Equation 4-7 as the SMC sliding variable. For the integration rule: ARS steering is enabled by default. When $\alpha_r \geq 3°$, RDB is activated and again deactivated if $\alpha_r < 3°$.

Configuration no. 2:

Kinematic model reference error based stability control, where a reference yaw rate and sideslip angle are determined from a single track (bicycle) model. This criterion employs Equation 4-22 as the SMC sliding variable. For the integration rule: ARS is enabled by default. When $\alpha_r \geq 3°$, RDB is activated and again deactivated if $\alpha_r < 3°$.

Configuration no. 3:

Combined phase plane location and kinematic model reference error based stability control, where the kinematic model reference error is used as the reference model and the SI used as the integration rule. The SMC sliding variable is as in Equation 4-22. For integration: ARS is enabled by default. When $SI \geq 1$, RDB is activated and again deactivated if $SI < 1$.

The different decision layer configurations are summarized in Table 5-3.

Table 5-3: The different decision layer configurations investigated in this study

Configuration	Stability control reference model	ARS-RDB Integration rule
1	Phase plane location error (PPLE)	a. ARS on by default b. When $\alpha_r \geq 3°$, RDB is activated c. When $\alpha_r < 3°$, RDB is deactivated
2	Kinematic model reference error (KMRE)	a. ARS on by default b. When $\alpha_r \geq 3°$, RDB is activated c. When $\alpha_r < 3°$, RDB is deactivated
3	Kinematic model reference error (KMRE)	a. ARS on by default b. When $SI \geq 1$, RDB is activated c. When $SI < 1$, RDB is deactivated

Figure 5-7 shows the decision layer block diagram which can switch between the different configurations, depending on the one investigated. Block one encloses the three configurations as listed above, and block 2 the moment to force conversion which is according to Equation 5-6 and Equation 5-7 for the ARS and RDB respectively. The layer outputs individual wheel braking- and additional rear lateral force.

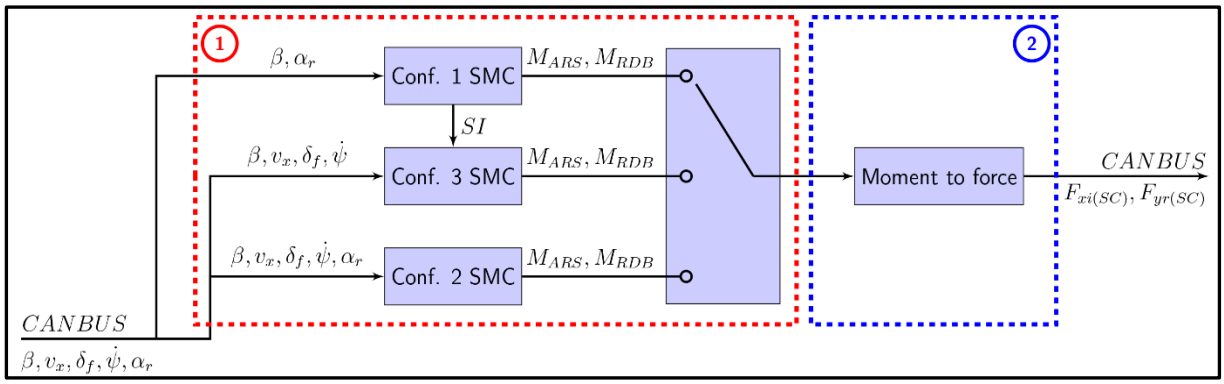

Figure 5-7: The decision layer block diagram

$$F_{yr(SC)} = \frac{M_{ARS}}{l_r} \tag{5-6}$$

$$F_{x3(SC)} = \begin{cases} \frac{M_{RDB}}{\frac{tw}{2}} & M_{RDB} > 0 \\ 0 & M_{RDB} \leq 0 \end{cases}$$

$$F_{x4(SC)} = \begin{cases} \frac{M_{RDB}}{\frac{tw}{2}} & M_{RDB} < 0 \\ 0 & M_{RDB} \geq 0 \end{cases} \tag{5-7}$$

5.3.2 *Control layer construction*

The control layer receives setpoints of braking force for each rear wheel and the additional lateral force of the rear wheels from the decision layer. The layer performs two functions for the RDB and two for the ARS systems as indicated in Figure 5-8 and Figure 5-9:

a. RDB:
1. Determining the required slip ratio (κ_i) and angular velocity $w_{i\,(ref)}$ for each wheel.
2. Determining the reference brake line pressure $(P_{Bi(SC)})$ based on the wheel speed error $\left(e = w_i - w_{i\,(ref)}\right)$ by use of a PID controller.

b. ARS:
1. Determining the current rear axle slip angle $(\alpha_{r(reference)})$, which acts as the centre point about which the additional lateral force is based.
2. Determining the rear steering angle change to generate the additional lateral force.

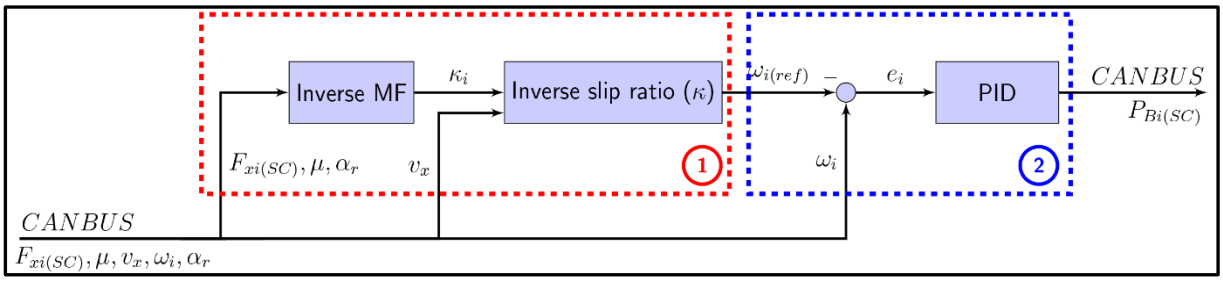

Figure 5-8: The rear differential braking (RDB) control layer block diagram

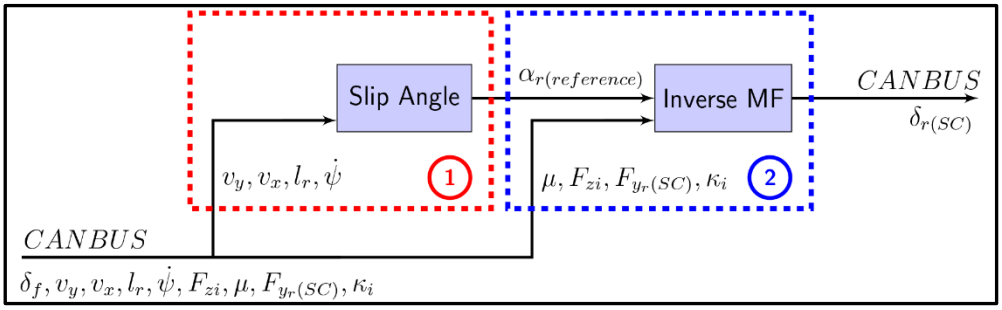

Figure 5-9: The active rear steering (ARS) control layer block diagram

With reference to Figure 5-8, the RDB sub-system blocks from left to right are the Inverse MF solver, which uses the secant method (Burden, et al., 2014) to determine which slip ratio will generate the required longitudinal force per tyre based on the 89 MF, the inverse slip ratio (Equation 5-8) and the PID controller (Equation 5-9). The PID gains are given in Section 5.3.3 where the complete brake system is tuned.

$$\omega_{i(ref)} = \frac{-\kappa v_x - v_x}{-r_e} \tag{5-8}$$

$$u(t) = K_p e(t) + K_i \int e(t)dt + K_d \frac{d}{dt} e(t) \tag{5-9}$$

With reference to Figure 5-9, the ARS sub-system blocks from left to right are the slip angle evaluator, which calculates the rear axle slip angle, and the inverse MF block which calculates the desired slip angle using Equation 5-10. The rear axle slip angle is steered to the desired slip angle by changing the rear steering angle. Figure 5-10 provides an illustration of the

concept on a 89 MF generated lateral force curve for varying slip angle, with a fixed normal force, slip ratio and camber.

$$\alpha_{r(reference)} = \tan^{-1}\left(\frac{v_y - l_r \times \dot{\psi}}{v_x}\right) \tag{5-10}$$

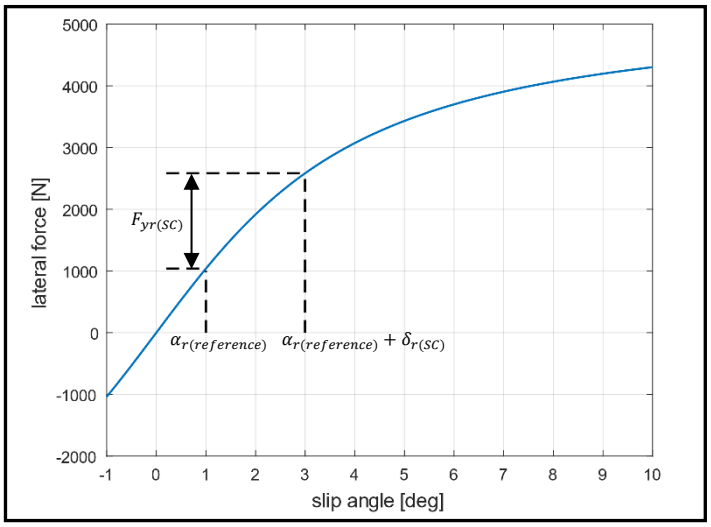

Figure 5-10: Illustration of the additive rear steering force concept on a 89 MF generated lateral force curve

Similar to the RDB sub-system, the inverse MF for the ARS is calculated with the secant method solving the 89 MF. This control system design works on the basis of forces and corrective yaw moments, as opposed to merely having two SMCs output a rear steering angle and brake pressure which are seemingly unrelated. This method relates actuator input to an imposed force or moment. There are also many works in ICC literature (Mokhiamar & Abe, 2006) that are based on having a good estimate of the tyre forces imposed. This study is an attempt at a practical approach to the forces method, the accuracy of which will be investigated in Section 5.3.3, Section 5.3.4 and Section 5.3.5.

5.3.3 *Physical layer: Rear differential braking (RDB) system*

Earlier work by Penny (2015) characterized the brake pressure to torque relationship of the Land Rover Defender 110 test vehicle by curve fitting measured data by use of a wheel force transducer (WFT) when braking. This is shown in Figure 5-11, which illustrates that a gain of 271 is sufficient to convert pressure at the brake calliper to disc applied braking torque. The fit only describes the relationship between brake line pressure and braking torque, irrespective of the actual tyre-road friction coefficient. This warrants the need for the slip ratio PID controller shown in Figure 5-8, as opposed to merely applying a brake pressure to reach a braking torque. Instead, the relationship shown in Figure 5-11 is used to simulate the brake torque response to brake line pressure.

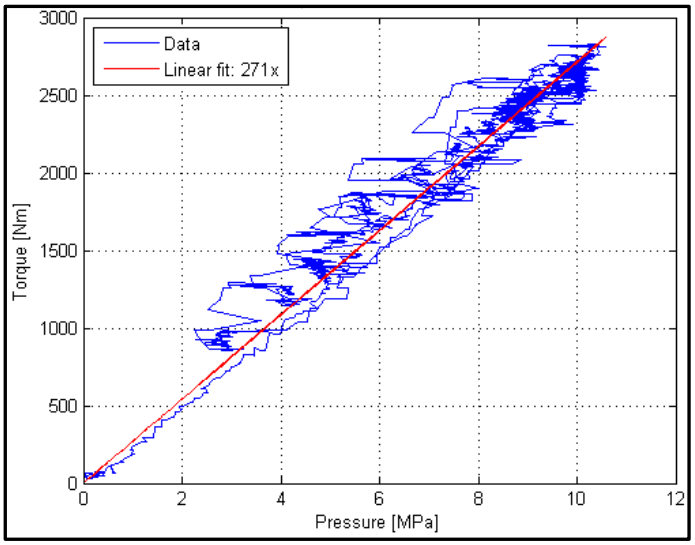

Figure 5-11: The Land Rover Defender 110 relationship between brake pressure and braking torque (Penny, 2015)

The Land Rover Defender 110 test vehicle is fitted with a 1997 WABCO ABS modulator and no dedicated ESP modulator. Differential braking is achieved by having a linear actuator apply the brake pedal inside the vehicle, which preloads the ABS modulator's accumulator before a braking manoeuvre. The ABS modulator is constantly set to the dump phase so that any increased brake pressure is stored in the accumulator to be used at the time of differential braking. The performance of this system does admittedly not match that of a dedicated ESP module since those modules can generate their own brake pressure while the ABS modulator relies on brake pedal actuation for pressure. Nonetheless, the system has been tried and tested for differential braking (Poovendran, 2018) but consideration has to be made for the longer pressure build-up or release delays once a brake-line is activated. Equation 5-11 to Equation 5-13 formulates the first order delay (FOD) of the brake-line pressure increase in time-step notation. Figure 5-12 shows the brake pressure response for a step reference brake pressure of 10 MPa, with an initial measured brake line pressure of 0 MPa.

$$P_{B_{(t+\Delta t)}} = P_{B_{(t)}} + \dot{P}_{B_{(t)}} \times \Delta t \tag{5-11}$$

$$\dot{P}_{B_{(t)}} = \frac{P_{B(ref)} - P_{B_{(t)}}}{\tau} \tag{5-12}$$

Where,

$$\tau = 0.2\ s \tag{5-13}$$

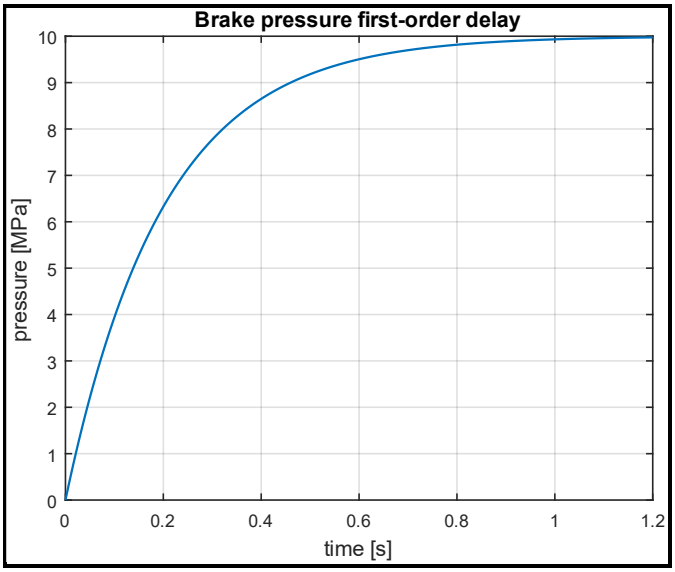

Figure 5-12: The brake pressure first-order delay plot for a reference pressure of 10 MPa applied at t=0

The physical brake emulating block diagram is shown in Figure 5-13. The control blocks from left to right are the ABS modulator, that converts the digital brake pressure value to an actual brake pressure. The ABS algorithm itself is not activated as it brings no advantage to the control system in addition to the PID controller that already regulates the brake pressure based on wheel angular velocity. This will be shown in the following paragraphs. The first order delay implements Equation 5-11 and the following saturation block ensures that the brake line pressure does not become negative or exceed the module's actual limit of $10\ MPa$. After the saturation block, the brake pressure is converted to a wheel torque that is applied to the vehicle in the simulation environment.

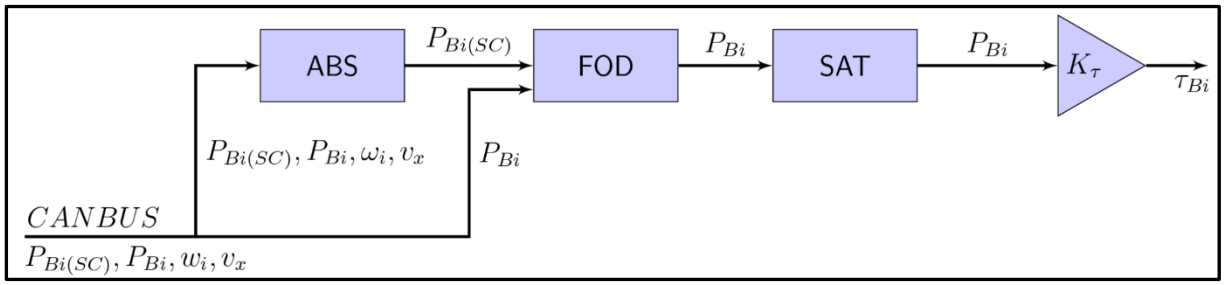

Figure 5-13: The physical brake emulating block diagram

With the RDB sub-system physical and control layer constructed, the PID response of the control layer RDB (Figure 5-8) is tuned. A manual tuning, or trial-and-error method, is employed where K_p with $K_I = K_d = 0$ is increased until the system is oscillating on the edge of stability. The gain is then reduced to yield a quarter of that amplitude after which K_I and K_D are steadily increased to yield a desired response. Using this method, the gain values of $K_p = 4: K_i = 0.2: K_d = 0.05$ are obtained.

Figure 5-14 shows vehicle states for a scenario where braking force is commanded while the tyre experiences a lateral load. Combined tyre loading is expected during operation of the stability control, which is what the scenario mimics. The scenario is performed at $60\ km/h$

on a smooth and a rough road. Combined loading is achieved by applying a step reference braking force of $F_{x4(SC)} = -5000\ N$, with the front steering angle at $\delta_f = 2°$ and the rear steering angle at $\delta_r = 0°$ according to the conditions in Equation 5-14 and Equation 5-15. A braking force of $-5000\ N$ is chosen since it is near the maximum friction force of the tyre, considering that the average tyre normal force at stand-still is $5000\ N$ (Table 4-1) and the surface friction is $\mu = 1$. The front steering angle of 2° is chosen since it is half the maximum steering angle measured when the vehicle performs a closed-loop DLC with the driver model (Figure 4-5), and stability control is expected to activate before the front steering angle extremes are reached. The advantage of using a step input scenario as opposed to a DLC or sine with dwell manoeuvre, is that the vehicle dynamics are slow-transient for a step input which makes it easier to isolate the effect of a commanded brake force, and parameters such as the rise time can be obtained. The braking force tracking performance of the system for a fast-transient, sine with dwell steer manoeuvre is evaluated in a later section (Section 5.3.5).

$$\delta_f = \begin{cases} 0 & t < 6 \\ 2° & t \geq 6 \end{cases} \tag{5-14}$$

$$F_{x4(SC)} = \begin{cases} 0 & t < 7 \\ -5000\ N & t \geq 7 \end{cases} \tag{5-15}$$

The figure shows two sets of results for the rough road, one with ABS enabled and another with ABS disabled. ABS did not activate for the smooth road as there was no wheel lock-up, but activated for the rough road. The plots indicate that having ABS enabled for differential braking does not notably improve the lateral force generating capability of the tyre compared to the PID controller. This might be because the PID control behaves similar to the ABS algorithm; it regulates the brake pressure around a target slip value. Considering that ABS is not beneficial for this scenario and may interfere with normal operation of the PID controller, the ABS algorithm does not feature in the stability control. This may not be the case in a simple control system that merely applies full brake pressure that is not regulated to a specific slip value.

The plots further indicate that the brake system, regardless of road classification and ABS activation status, reaches 63.2% of the reference braking force in 89 ms and the reference braking force in 187 ms. Overshoot is 44% of the reference value. These performance indicators are acceptable for the application as the brake force reaches the reference value and even exceeds it which is conservative, considering it is for stability control and dependant on estimated states. The performance of the chosen PID gains on both terrains are similar which implies that it is not necessary to use different gains on different terrains. For the conditions tested, the results show that the control system can generate a desired longitudinal force on demand.

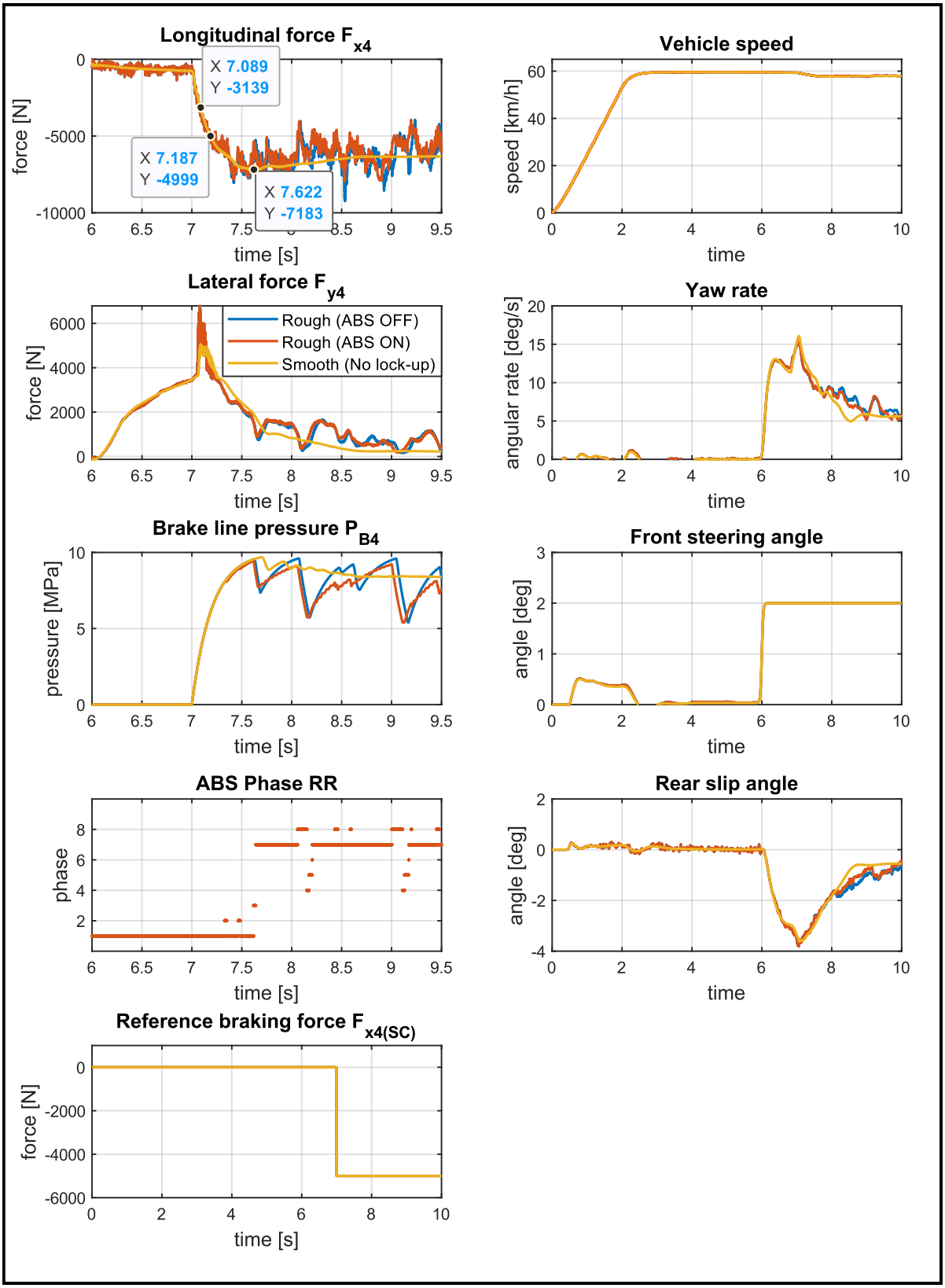

Figure 5-14: The RDB response to a step reference braking force value on the rear right (RR) wheel

5.3.4 *Physical layer: Active rear steering (ARS) system*

The ARS linear actuator model is shown in Figure 5-15 and the discussion of the component blocks found in Appendix C.

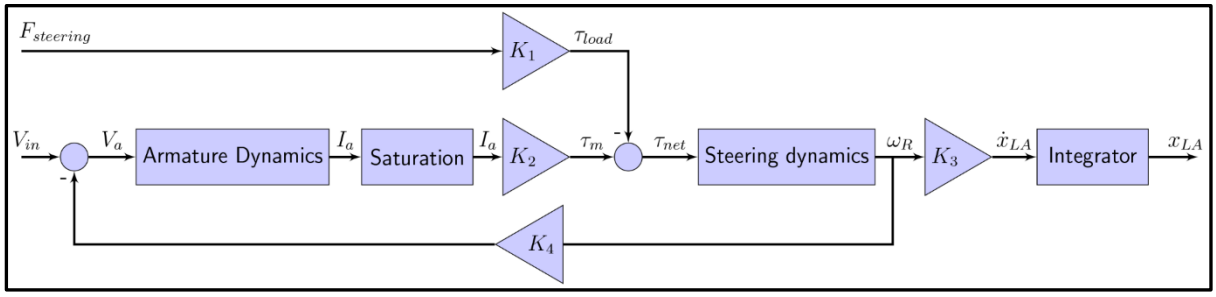

Figure 5-15: The linear actuator emulating block diagram

The actuator is mounted with a moment arm about the wheel centre of 209.89 mm. Since it requires feedback of the turn resisting force, the steering torque about the wheel centre is measured in real time during the simulation and fed back to the model where it converts the torque to an imposed force with Equation 5-16.

$$F_{steering} = \frac{\tau_{load}}{r} = \frac{\tau_{load}}{209.89 \times 10^{-3}} \tag{5-16}$$

The rear steering would only operate within a small angular range [-3°, 3°] and the small-angle assumption is made. Following this, the displacement-angle formula of Equation 5-17 can be used to calculate the required actuator displacement to reach a steering angle where the unit of δ_r is in degrees and x_{LA} is in meters.

$$x_{LA} = 3.672599 \times 10^{-3} \times \delta_r \tag{5-17}$$

Figure 5-16 shows the complete active rear steering hardware model, containing the linear actuator of Figure 5-15, where the motor input voltage (V_{in}) is limited to the range [$-12\ V$, $12\ V$] and the actuator displacement (x_{LA}) limited to [-11 mm, 11 mm]. The gain K_1 has a value of 3.672599×10^{-3} and the PID values: K_p 90, K_i 60, K_d 10 obtained using the same tuning method as for the brakes.

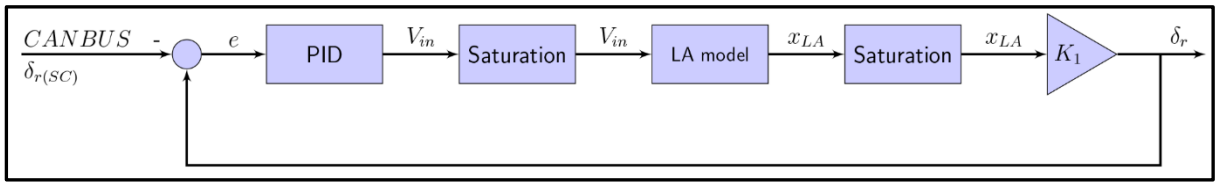

Figure 5-16: The active rear steering emulating block diagram

As with RDB, the ARS step response to an additional rear lateral force setpoint is characterized by running a scenario in the simulation environment. The scenario is performed at 60 km/h on both a smooth and rough road. With the vehicle at the desired speed, and a front steering angle of $\delta_f = 1°$, an additional lateral force of $F_{yr(SC)} = 1000\ N$ is set. ARS activates before

RDB for all decision layer configurations, therefore no longitudinal loading conditions are prescribed for this scenario and the scenario is different to the one performed for RDB. The purpose of introducing a front steering angle is to represent a scenario in which the vehicle already experiences a lateral force, to which the ARS must add the prescribed additional lateral force. The choice of $\delta_f = 1°$ and $F_{yr(SC)} = 1000\ N$ is made as it impacts the rear axle slip angle, where ARS can only effectively operate within a narrow range to generate an additional rear lateral force before rear axle slip angle exceeds $\alpha_r = 3°$ (and tyre lateral response becomes non-linear). The timing of the inputs are as in Equation 5-18 and Equation 5-19 with the results shown in Figure 5-17. The additional lateral force tracking performance of the system for a fast-transient, sine with dwell steer manoeuvre is evaluated in a later section (Section 5.3.5).

$$\delta_f = \begin{cases} 0 & t < 3 \\ 1° & t \geq 3 \end{cases} \tag{5-18}$$

$$F_{yr(SC)} = \begin{cases} 0 & t < 5 \\ 1000\ N & t \geq 5 \end{cases} \tag{5-19}$$

The results of Figure 5-17 show that the ARS system is able to generate the prescribed additional rear lateral force, with a time constant of 166 ms to reach a steering angle setpoint and a time constant of 544 ms to reach a lateral force setpoint. Even though the actuator can reach the steering angle setpoint quickly, the lateral force setpoint tracking performance is governed by slower vehicle dynamics. The figure also conveys that the response on a rough road is similar to the response on a smooth road.

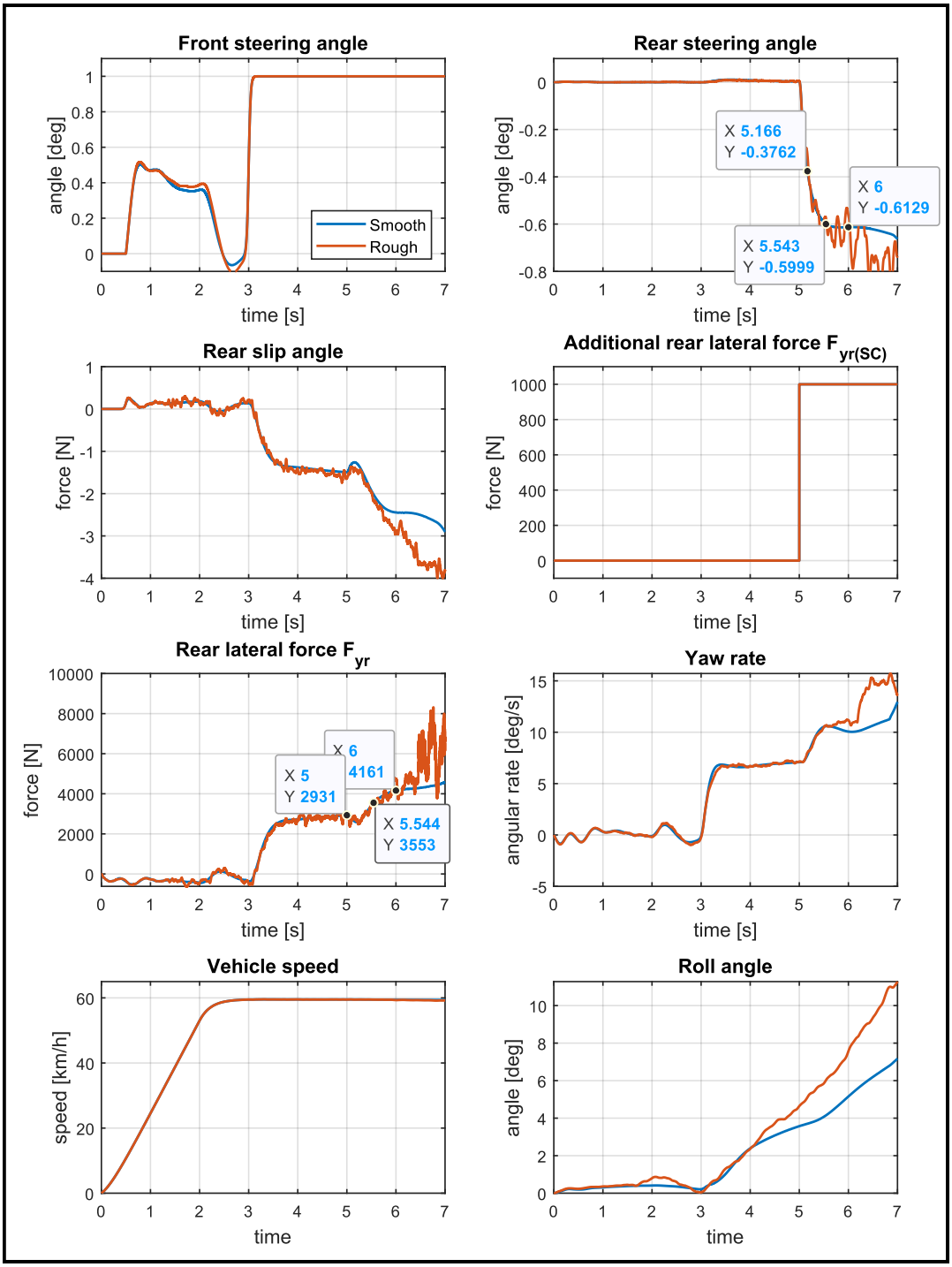

Figure 5-17: The rear axle lateral force step response to a demand of 1000 N on a high friction ($\mu = 1.0$) smooth and rough road

5.3.5 *Decision layer: SMC gain selection*

Since the integrated controller makes use of a supervisory control structure, both ARS and RDB should be able to operate as stand-alone SCs. This implies that both ARS and RDB should have its own SMC with its own SMC gain (k_{SMC}) and sliding variable zeta weighting (ζ) so that they may operate independently. It was decided to consider zeta weightings of $\zeta = 0, 0.5, 1$ and 2, which represent: no consideration for sideslip error, half weighting, same weighting and double weighting respectively of the sideslip error. Combining the variety of

ARS or RDB with different zeta weightings and two possible SC reference models operating on two possible road classifications result in 32 combinations of systems as listed in Table 5-4. The aim of this section is to tune the SMC gain for each of the 32 possible system combinations.

Table 5-4: Different system combinations based on control strategy, SC reference model, road classification and zeta weighting

System combination	Control strategy	Stability control reference model	Road classification	Group	Zeta weighting
1	ARS	Phase plane location error SMC sliding variable: $s = \dot{\beta} - \dot{\beta}_{ref} + \zeta(\beta - \beta_{ref})$	Smooth	A	0
2					0.5
3					1
4					2
5			Rough	B	0
6					0.5
7					1
8					2
9		Kinematic model reference error SMC sliding variable: $s = \dot{\psi} - \dot{\psi}_{ref} + \zeta(\beta - \beta_{ref})$	Smooth	C	0
10					0.5
11					1
12					2
13			Rough	D	0
14					0.5
15					1
16					2
17	RDB	Phase plane location error SMC sliding variable: $s = \dot{\beta} - \dot{\beta}_{ref} + \zeta(\beta - \beta_{ref})$	Smooth	E	0
18					0.5
19					1
20					2
21			Rough	F	0
22					0.5
23					1
24					2
25		Kinematic model reference error SMC sliding variable: $s = \dot{\psi} - \dot{\psi}_{ref} + \zeta(\beta - \beta_{ref})$	Smooth	G	0
26					0.5
27					1
28					2
29			Rough	H	0
30					0.5
31					1
32					2

With reference to Section 2.2.4, the SMC gain should be larger than the matched disturbance rate (Δ). The super-twisting algorithm can estimate the disturbance value once on the sliding surface when $\dot{w} = 0$ so that $\Delta = k_2 sgn(s)$ during control action (solve for Equation 2-6). Such measurement, however, requires maintained sliding motion throughout the manoeuvre, which relies on having unlimited actuator bandwidth. This does not reflect reality. Delays cause occasional break-away during emergency manoeuvres, meaning that

the matched disturbance cannot be measured for those points. The breakaway sections' matched disturbance is larger than those for which sliding motion is maintained, so one cannot infer the maximum matched disturbance from the sections that manage to maintain sliding. Instead, the control system relies on the inherent stability (Seeber & Horn, 2017) of the popular SMC parameter setting. Following this, the SMC gain per system is empirically set by cycling through a series of SMC gains and determining which gain value minimises the sum of the squared sliding variable over the duration of a manoeuvre. The objective is to minimize Equation 5-20, where n is the number of sampling points. This method identifies the SMC gain which causes the respective SMC to best approximate the appropriate reference model.

$$q = \sum_{i=1}^{n}(s^2) \tag{5-20}$$

The manoeuvre performed for the SMC gain tuning process is the sine with dwell front steering input, as it is an open-loop manoeuvre with high repeatability that allows direct comparison of different SMC gain values. The steering amplitude for this study is chosen to mimic the steering amplitude of the DLC manoeuvre as performed by the driver model. The data of the smooth and rough road $60\ km/h$ runs of Section 4.2 are re-used here to determine the driver model steering amplitude for that scenario. Figure 5-18 shows the steering input of the chosen sine with dwell amplitude compared to DLC manoeuvres performed with the driver model. It conveys that a 3.5° amplitude sine with dwell steering input is comparable to the driver model steer input for a DLC and will be used for this study.

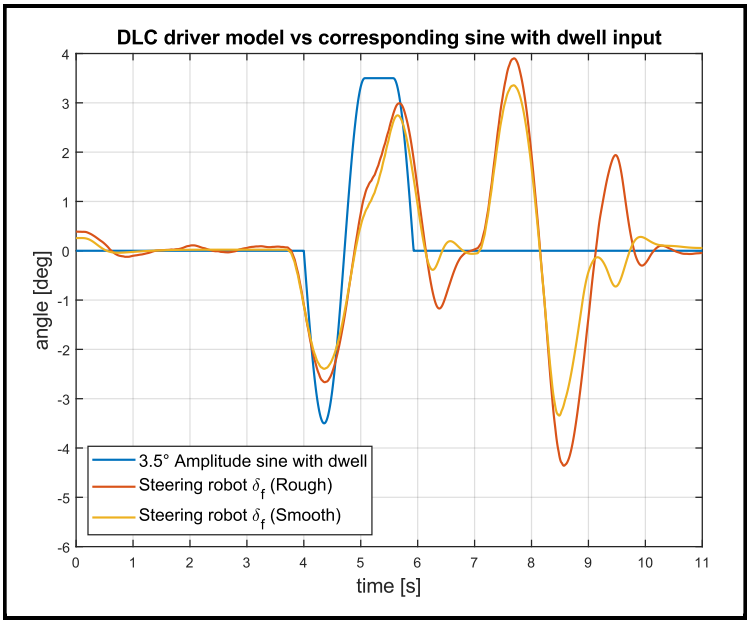

Figure 5-18: 3.5° sine with dwell steering amplitude compared to driver model performing a DLC at 60 km/h on a smooth and rough road

It is not practical to show system states for all the runs performed for the SMC gain tuning process, and so the system states of one ARS combination and one RDB combination is shown. For each control strategy, a look is taken at three runs: one SMC gain value smaller than optimal, the optimal SMC gain value, and one SMC gain value larger than optimal.

Starting with the ARS combination, system no. 15 of Table 5-4; Figure 5-19 shows measured states for different gains $k_{SMC} = [1000, 2000, 3000]$ (below optimal, optimal, and above optimal SMC gain). The system is a combination of ARS with the kinematic model reference error as the SC reference model on a rough road. The yaw rate and sideslip plots of the figure indicate the desired response as determined by the kinematic model. The system SMC gain variations shown do not have much influence on peak yaw rate but manage to dampen yaw rate once the steering manoeuvre is complete (when the front steering angle is zero). It is also seen from the plots that larger SMC gain values generate larger rear steering angles, but introduce oscillations in the yaw rate following the end of the steer manoeuvre. This is why larger SMC gains are not necessarily better, as they introduce oscillation.

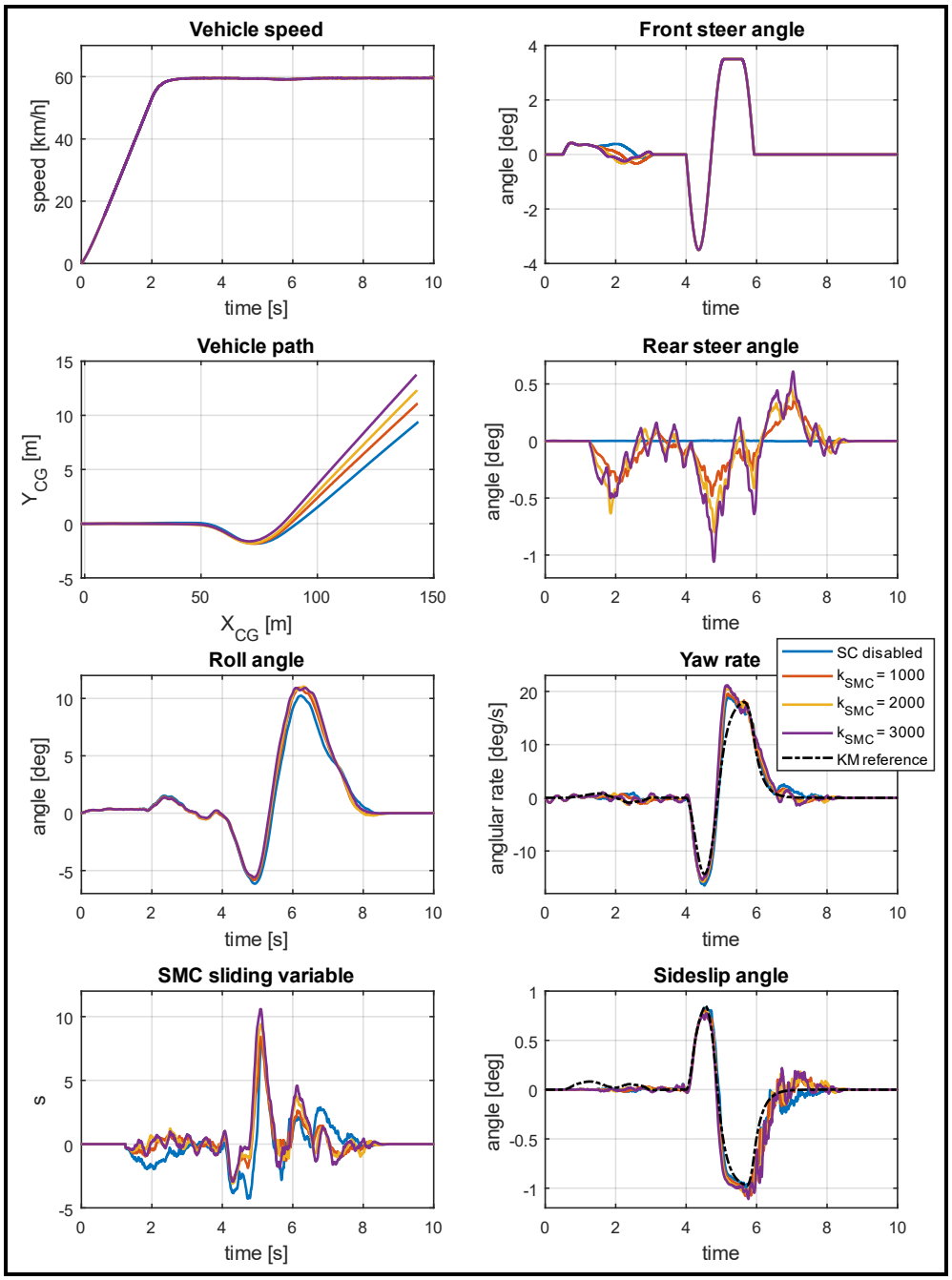

Figure 5-19: A comparison of SMC gain performance for Table 5-4 system no. 15 with an SMC gain smaller than, equal to and larger than the optimal value

Figure 5-20 shows the additional rear lateral force tracking ability of the same ARS combination, where $F_{yr(SC\ disabled)}$ is the rear lateral force measured for a vehicle when it performs the sine with dwell manoeuvre with SC disabled (baseline vehicle). This is the most practical way to measure additional rear lateral force, made possible due to the steering manoeuvre being open-loop with high repeatability. The additional lateral force setpoint signal has been delayed by 0.5 s for the plot, as there are transient vehicle dynamics which delay the vehicle force response. The systems' additional rear lateral force signals have an RMSE (Equation 5-21) of 406 N, 600 N and 657 N respectively with 79.6%, 79.8% and 77.2% of absolute error values below that RMSE respectively. The results show that the ARS stand-alone system is able to generate an additional rear lateral force on demand, albeit with force fluctuations.

$$RMSE = \sqrt{\frac{1}{n} \times \sum_{i=1}^{n} \left(\left(F_{yr} - F_{yr(SC\ disabled)} \right) - F_{yr(SC)} \right)} \tag{5-21}$$

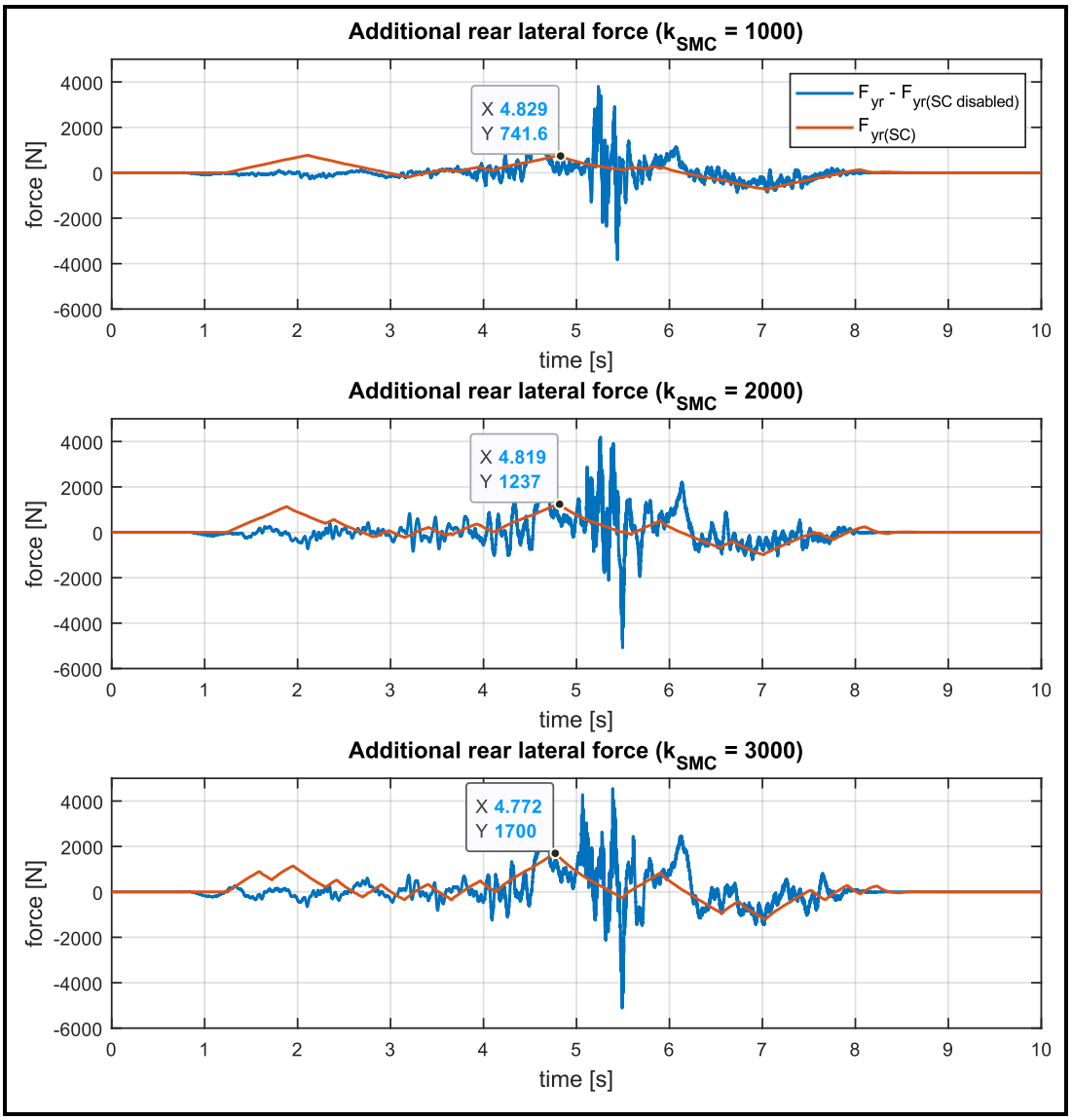

Figure 5-20: A comparison of additional rear lateral force tracking performance for Table 5-4 system no. 15 with SMC gain smaller than, equal to and larger than the optimal value

Considering an RDB combination: Figure 5-21 presents system states for runs performed with Table 5-4 system no. 23 for k_{SMC} = [500, 1000, 1500] (below optimal, optimal, above optimal SMC gain). The system uses RDB with the phase plane location error as the SC reference model on a rough road. The phase plane plot shows the SI boundary and indicates that the stability control enabled vehicle has a reduced presence outside the boundary, compared to the baseline vehicle. The stability control enabled vehicle also has lower peak values of roll angle, yaw rate and sideslip. Figure 5-22 compares brake force setpoints and measured values. Table 5-5 lists RMSE values, and percentage of absolute error values below that value where the error is the difference between setpoint and measured braking force. The results indicate that the RDB system can generate a specified braking force on demand, but the measured braking force has slower transients than the stability control setpoint.

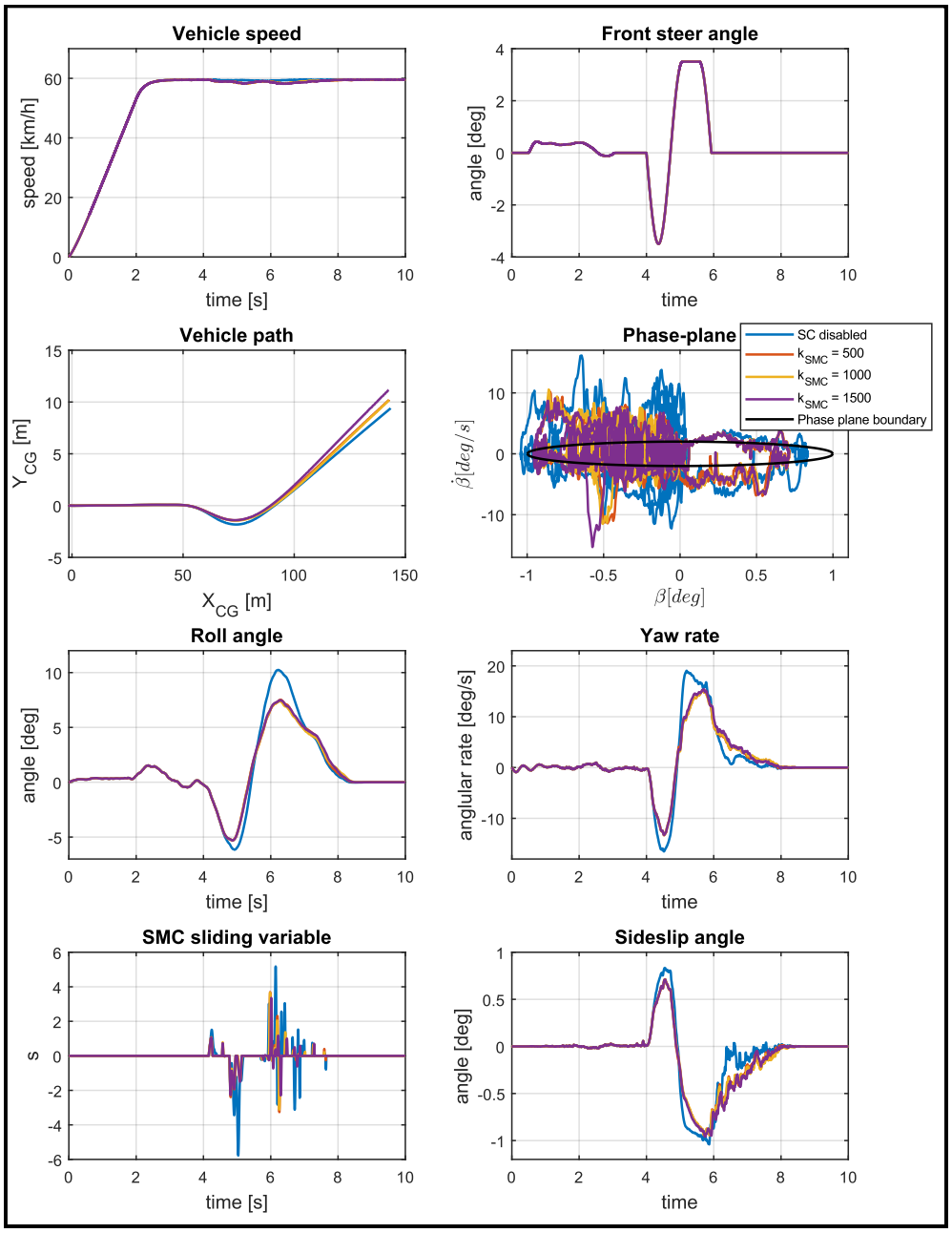

Figure 5-21: A comparison of SMC gain performance for Table 5-4 system no. 23 with a gain smaller than, equal to and larger than the optimal value

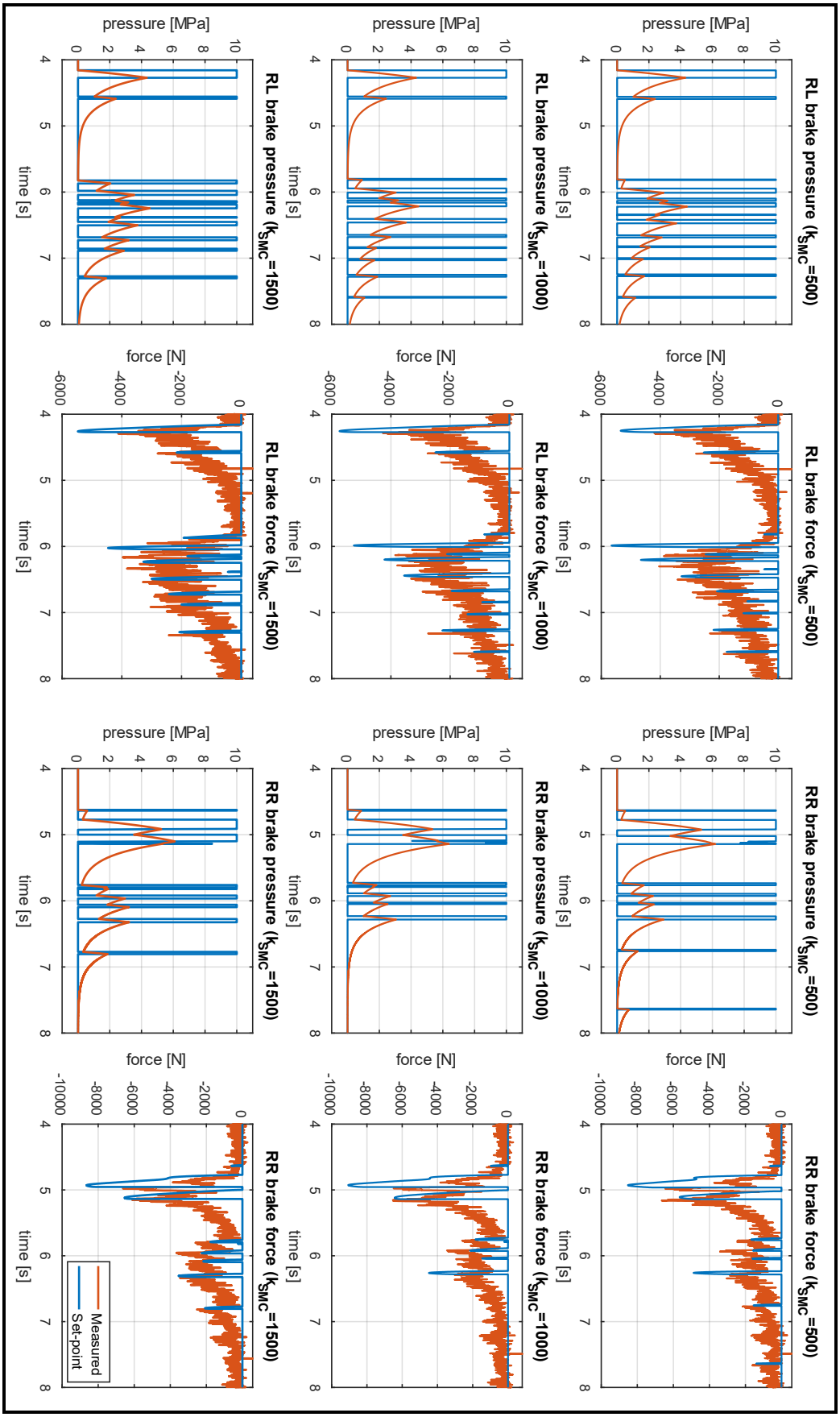

Figure 5-22: A comparison of braking force tracking performance for Table 5-4 system no. 15 with SMC gain smaller than, equal to and larger than the optimal value

Table 5-5: Comparison of RMSE and percentage of absolute error values below RMSE for braking during a sine with dwell steering manoeuvre

Table 5-6 system no. 23 k_{SMC} variation	RL $[N]$	RR $[N]$
500	929 [81%]	1143 [85%]
1000	924 [81%]	1158 [86%]
1500	922 [81%]	1137 [85%]

Arriving at the results for the SMC gain selection process; Figure 5-23 shows the cost function output per system combination of Table 5-4 for different gains. The resulting chosen SMC gain per system combination is the gain with the lowest cost function output, as listed in Table 5-6. Figure 5-23 shows how the cost function decreases initially with increasing SMC gain but then at some point increase as the SMC gain becomes too large. The figure also shows how the optimal SMC gain for RDB and ARS is different, generally being lower for RDB than for ARS. It is also evident that generally, the optimal SMC gain on rough roads is different than the optimal SMC gain for smooth roads. In conclusion, the SMC gain is influenced by control strategy, SC reference model and road classification.

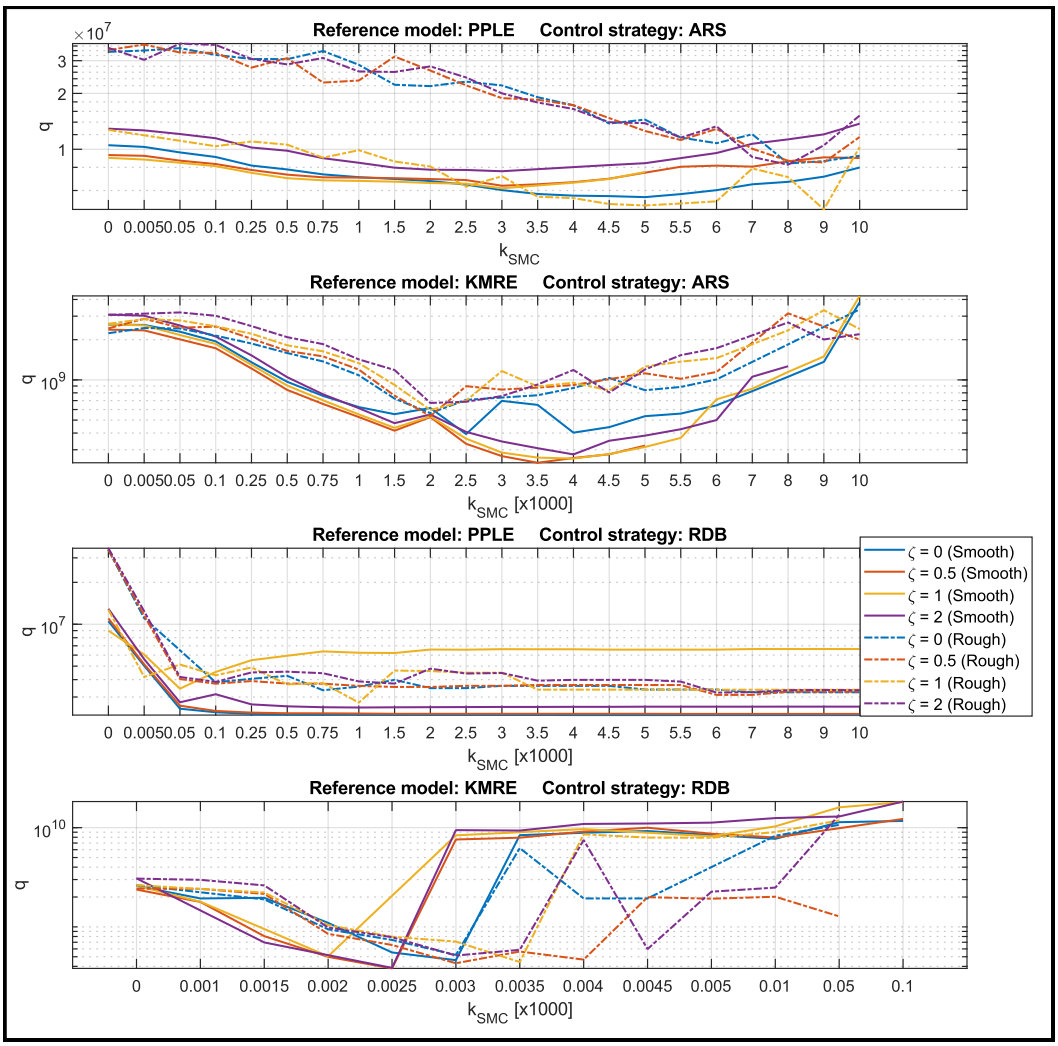

Figure 5-23: Sum of sliding variable squared for increasing SMC gain of the 32 system combinations listed in Table 5-4

Table 5-6: SMC gains for different systems based on minimum cost function (q) output

System combination	Control strategy	Stability control reference model	Road classification	Group	Zeta weighting	Gain
1	ARS	Phase plane location error SMC sliding variable: $s = \dot{\beta} - \dot{\beta}_{ref} + \zeta(\beta - \beta_{ref})$	Smooth	A	0	5000
2					0.5	3000
3					1	3000
4					2	3000
5			Rough	B	0	8000
6					0.5	9000
7					1	9000
8					2	8000
9		Kinematic model reference error SMC sliding variable: $s = \dot{\psi} - \dot{\psi}_{ref} + \zeta(\beta - \beta_{ref})$	Smooth	C	0	2500
10					0.5	3500
11					1	4000
12					2	4000
13			Rough	D	0	2000
14					0.5	2000
15					1	2000
16					2	2000
17	RDB	Phase plane location error SMC sliding variable: $s = \dot{\beta} - \dot{\beta}_{ref} + \zeta(\beta - \beta_{ref})$	Smooth	E	0	1500
18					0.5	1500
19					1	50
20					2	1000
21			Rough	F	0	7000
22					0.5	6000
23					1	1000
24					2	6000
25		Kinematic model reference error SMC sliding variable: $s = \dot{\psi} - \dot{\psi}_{ref} + \zeta(\beta - \beta_{ref})$	Smooth	G	0	3
26					0.5	2.5
27					1	2
28					2	2.5
29			Rough	H	0	3
30					0.5	3
31					1	3.5
32					2	3

5.3.6 *Decision layer: SMC zeta weighting selection*

System 1-32 of Table 5-6 was tuned according to which SMC gain best approximates the appropriate SC reference model, as measured by the sum of the squared sliding variable. The table lists groups of four system combinations with the same control strategy, SC reference model and road classification, but with different zeta weightings. The groups are labelled from A-H. It remains to choose one appropriate zeta weighting per group so that there is a unique system for the set of operating conditions, and that is done in this section. The chosen zeta weighting per group should represent the best performing system per group, from a stability control perspective.

There are many indicators for quantifying stability control performance. Ultimately, the goal of stability systems is to ensure that driver intention and actual vehicle states while driving are as consistent as possible with one another (Wang, et al., 2019). The Euro NCAP standard

(Euro NCAP, 2011) is developed specifically for stability control performance assessment and quantifies this goal by specifying three metrics that should be observed for a sine with well steer manoeuvre. A detailed discussion of the Euro NCAP standard is presented in Section 3.3.7.

The three metrics of the standard are summarized:

1. Yaw rate ratio (YRR_{1s}) taken at 1 s from completion of steer (COS) (Euro NCAP, 2011). At this point in time, the driver steering input is zero following a rapid steer input. The aim of this metric is to measure how well the yaw response is damped at a time shortly after (1 s) the steer input is set to zero.
2. Yaw rate ratio ($YRR_{1.75s}$) at 1.75 s from completion of steer (COS) (Euro NCAP, 2011). At this point in time, the driver steering input is zero following a rapid steer input. The aim of this measure is to provide a second measure of how well the yaw response is damped at a time shortly after (1.75 s) the steer input is set to zero.
3. Maximum lateral displacement (ΔY_{CG}) at $1.07\ s$ from beginning of steer (BOS) (Euro NCAP, 2011). The aim of this metric is to ensure that the open-loop steering input has excited a sufficient vehicle lateral response.

Although not listed as a stability control performance indicator by NCAP (2011), the vehicle roll angle is of interest for the SUV test vehicle with a high CG. The vehicle may have an increased risk of rollover during emergency manoeuvres which is a safety concern (Peenze, 2020). This metric is added to the list of metrics in addition to the three listed above:

4. Maximum roll angle during manoeuvre (ϕ_{max}).

The first two metrics are a measure of how well a stability control system can damp the vehicle yaw rate after a steering input. Higher damping is better. The third metric is a measure of vehicle responsiveness. Higher lateral displacement is better. For the roll angle, lower angles are better.

The performance comparison makes use of radar or spider plots with each axis representing a normalised value of the above four metrics so that the values represented by the largest polygon indicates well rounded performance. The data is arranged in a matrix with the columns representing a criterion ($j = 1 \dots 4$) and the rows, the results of each run ($i = 1 \dots 5$). The absolute values of the first two columns representing the YRR are taken since overshoot of the yaw rate is possible, however values closer to zero are sought and taken as the minimum. The values of each metric are normalized so that the best value is assigned a score of 100% and the remaining data a value relative thereto. The normalized value for values which are better when larger, is calculated with Equation 5-22 and values which are better when smaller is calculated with Equation 5-23 (Hamersma, 2017).

$$x_{i,j\,norm} = \frac{x_{ij}}{\max\,(x_j, \dots)} \times 100, i \in\ 1,2,3 \dots, m; j \in 1,2,3, \dots, n \qquad (5\text{-}22)$$

$$x_{i,j\,norm} = \frac{\min\,(x_j, \dots)}{x_{ij}} \times 100, i \in\ 1,2,3 \dots, m; j \in 1,2,3, \dots, n \qquad (5\text{-}23)$$

The radar plots shown in Figure 5-24 represent the performance of system Group A-H of Table 5-6 that is used to draw comparisons between system combinations. The systems were established in Section 5.3.5 and the data which was generated in that section is also re-used for this analysis. The testing performed was the sine with dwell manoeuvre at 60 km/h with a steering amplitude of $3.5°$. Choosing the best zeta weighting is done via the function formulated in Equation 5-24, that is evaluated for each polygon on the radar plot. The polygon with the highest function output represents the largest polygon and consequently, the best zeta weighing. Table 5-7 lists the chosen best zeta weighing per radar plot. The cost function output values are presented in Appendix D.

$$Area = \frac{1}{2} \times (YYR_{1s} \times (YYR_{1.75s} + \phi_{max}) + \Delta Y_{CG} \times (YYR_{1.75s} + \phi_{max})) \qquad (5\text{-}24)$$

The result is a unique system per Grouping A-H. This enables one to select the appropriate system combination based on the test conditions. For example, if the test setup requires RDB SC for operation on a rough road and one knows which SC reference model is desired, then there is a specific zeta weighting and SMC gain that should be used for the RDB control system.

Table 5-7: The best performing zeta weightings per Group A-H of Table 5-6

Control strategy	Stability control reference model	Road Classification	Group	Zeta weighting	System combination no.
ARS	Phase plane location error	Smooth	A	0	1
		Rough	B	2	8
	Kinematic model reference error	Smooth	C	1	11
		Rough	D	0	13
RDB	Phase plane location error	Smooth	E	2	20
		Rough	F	2	24
	Kinematic model reference error	Smooth	G	0	25
		Rough	H	0	29

It is evident that Group A-H, when comparing group to group, has different optimal zeta weightings, which implies that a single universal zeta weighting will not perform optimally for different test conditions. This is not to say that SC enabled vehicle performance is not better than baseline (a vehicle without stability control), merely not optimal. All the groups except for Group F have at least one stability control system that performs better than the baseline vehicle. Time histories of vehicle states for the best performing sub-system per group is presented in Section 6.1 where they are compared with integrated system performance.

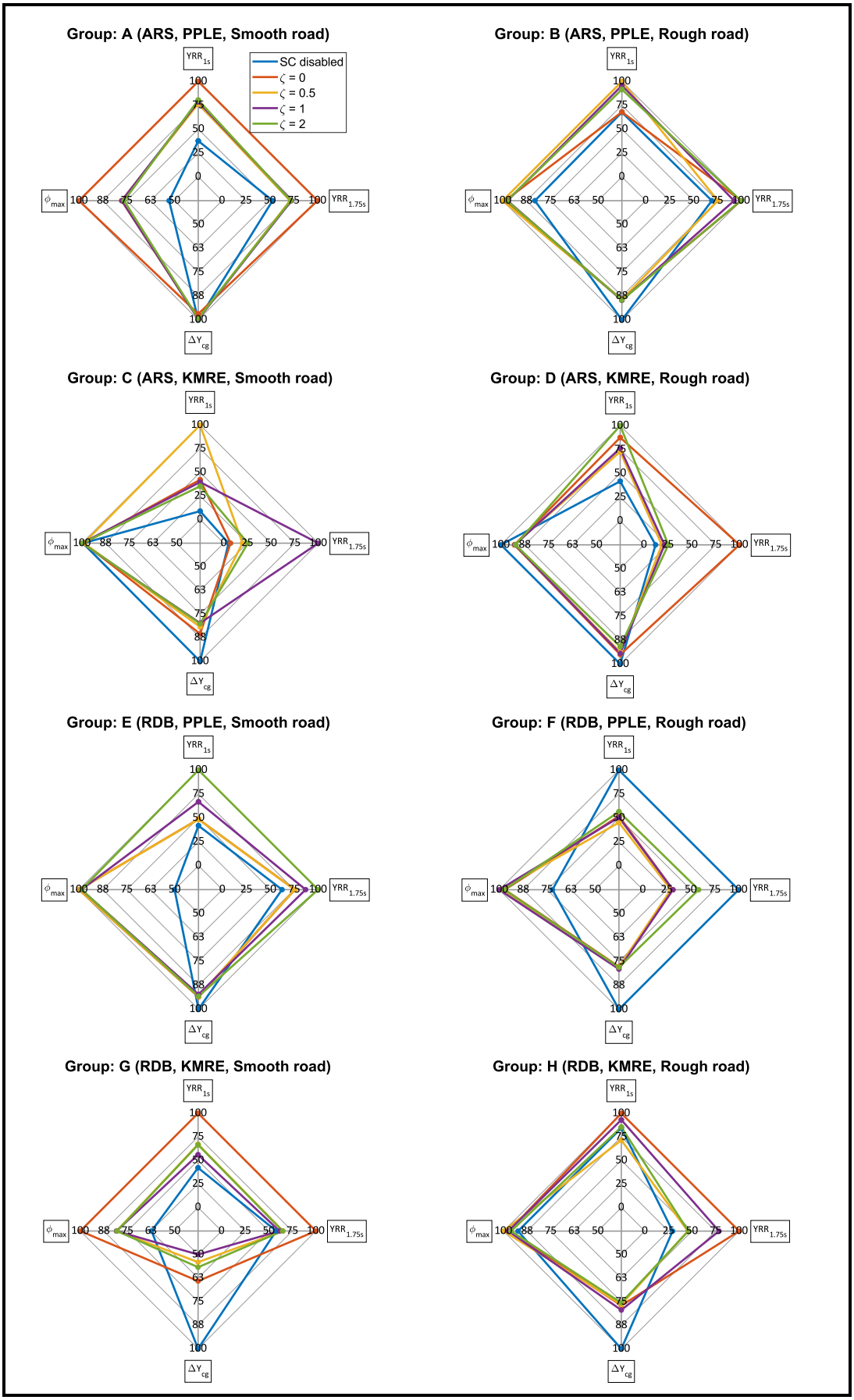

Figure 5-24: Radar plots for Group A-H of Table 5-6

5.4 Chapter conclusion

The different layers of the control system was designed in this chapter, consisting of the decision-, control- and physical layer. The decision layer compares actual vehicle response to a SC reference model and determines the yaw moment that must be imposed on the vehicle to minimize the difference in the two responses. Two SC reference models are considered, namely the kinematic model reference error and the phase plane location error. The decision layer assigns the required corrective moment to RDB, ARS or both, and coordinates the integration based on the integration rule that is set. Two integration rules are considered namely rear axle slip angle based or phase plane location based. By pairing different SC reference models and integration rules, three integrated control configurations of the decision layer are established.

As determined by the supervisory control structure, the control layer converts corrective yaw moment that is specified by the decision layer, to an actuator setpoint. In the case of RDB, it determines the required brake pressure per rear wheel, and in the case of ARS it determines the linear actuator displacement, which controls the rear steering angle. The physical layer models the vehicle hardware. Figure 5-25 is a control system diagram that shows how the different layers interact.

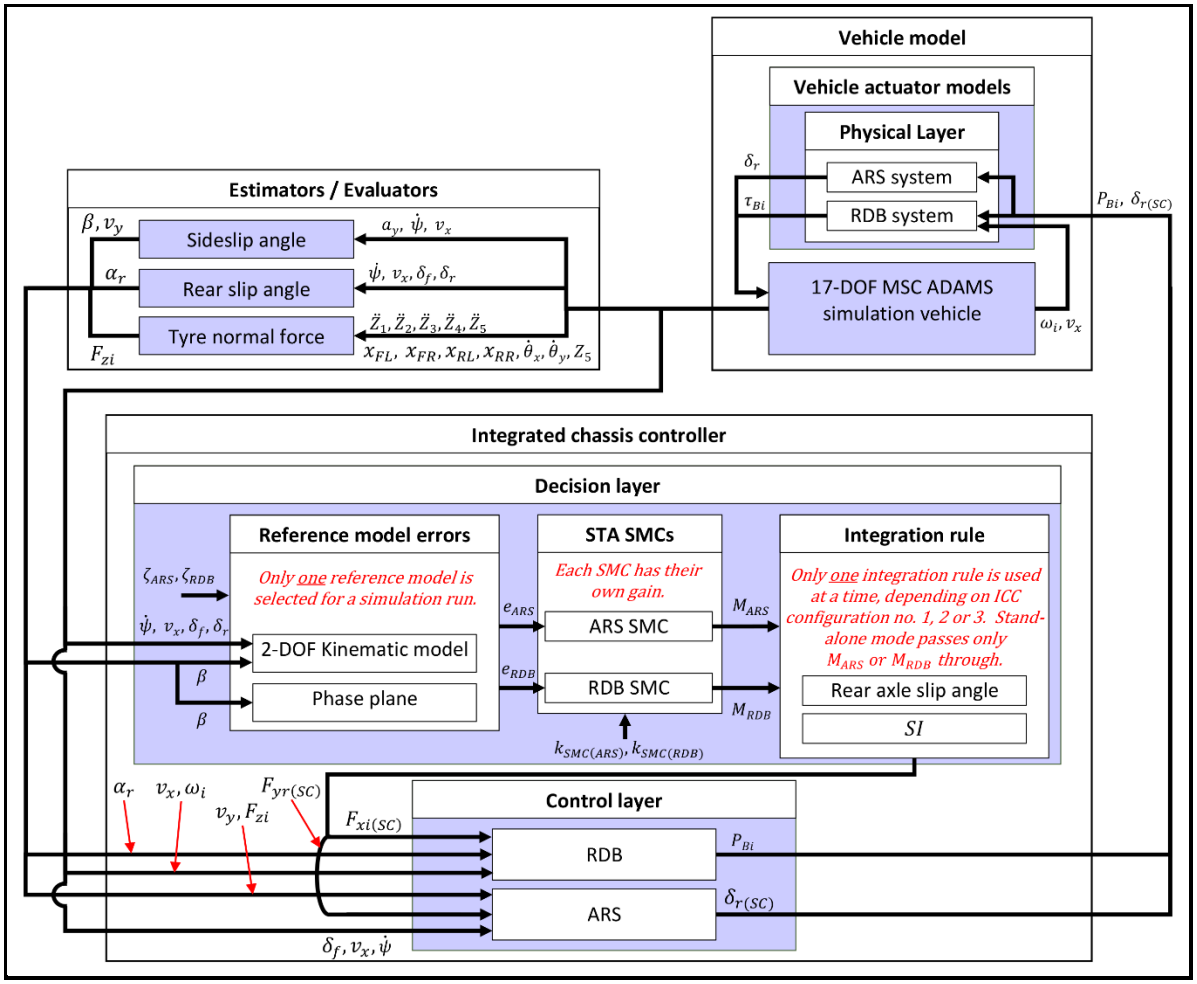

Figure 5-25: Control system block diagram

Since the ARS and RDB SCs are stand-alone sub-systems, they operate with their own control system and own control system variables. It was established that the RDB and ARS sub-systems can approximate a setpoint force on both smooth and rough roads without having separate PID tunings for each road (but separate PID tunings for each control strategy). On the contrary, it was found that the SMCs of the decision layer, which determine the required braking or steering corrective moments, have unique gain and zeta weighting values which differ depending on the control strategy, SC reference model, and road classification combination used. Table 5-8 lists the appropriate SC system combination to be used based on desired operating conditions.

Table 5-8: A summary of the Table 5-6 system combination numbers which comprise the stand-alone and integrated systems

System type	System name for this study	Stability control reference model	Default: Table 5-6 system no. on road classification		Switches to: Table 5-6 system no. on road classification		Integration parameter
			Smooth	Rough	Smooth	Rough	
Stand-alone sub-system SC	ARS, PPLE	Phase plane location error	1	8	-	-	-
	ARS, KMRE	Kinematic model reference error	11	13	-	-	-
	RDB, PPLE	Phase plane location error	20	24	-	-	-
	RDB, KMRE	Kinematic model reference error	25	29	-	-	-
Integrated sub-system SC	ICC Conf. 1	Phase plane location error	1	8	20	24	α_r
	ICC Conf. 2	Kinematic model reference error	11	13	25	29	α_r
	ICC Conf. 3	Kinematic model reference error	11	13	25	29	SI

CHAPTER SIX
SIMULATION RESULTS

Abstract – Integrated and stand-alone sub-system SC performance is compared with a SC disabled (baseline) vehicle. An open-loop performance comparison is done by conducting a sine with dwell steer manoeuvre and measuring system performance against four metrics. A closed-loop performance comparison is done by conducting a DLC manoeuvre and considering measures such as vehicle path, roll angle, yaw rate and sideslip angle. The chapter concludes with a discussion on system performance trends observed for the different manoeuvres.

6.1 Open-loop performance

This section compares stand-alone sub-system SC and integrated sub-system SC performance against a baseline, which is the response of a SC disabled vehicle when performing an open-loop steer manoeuvre. The stand-alone and integrated SCs were designed in the previous chapter. As with open-loop testing in the previous chapter, a $3.5°$ amplitude sine with dwell steer manoeuvre is performed (Euro NCAP, 2011) at $60\ km/h$ on a rough and a smooth road for each system. System performance is quantified with four metrics, namely two yaw rate ratio measurements, a lateral displacement measure and a maximum roll angle measure. These metrics were discussed in Section 5.3.6. The aim is to assess whether stand-alone SCs and integrated SCs show improvement for vehicle lateral stability compared to the baseline, to quantify the improvement, and to identify trends relating to SC control strategy, road classification and SC reference model combinations. This comparison is enabled by the repeatability of the sine with dwell steer manoeuvre.

6.1.1 *Stand-alone sub-system performance*

Figure 6-1 presents simulation vehicle input states for the sine with dwell manoeuvre performed on a smooth road with the four stand-alone sub-system SCs of Table 5-8 (on the previous page).

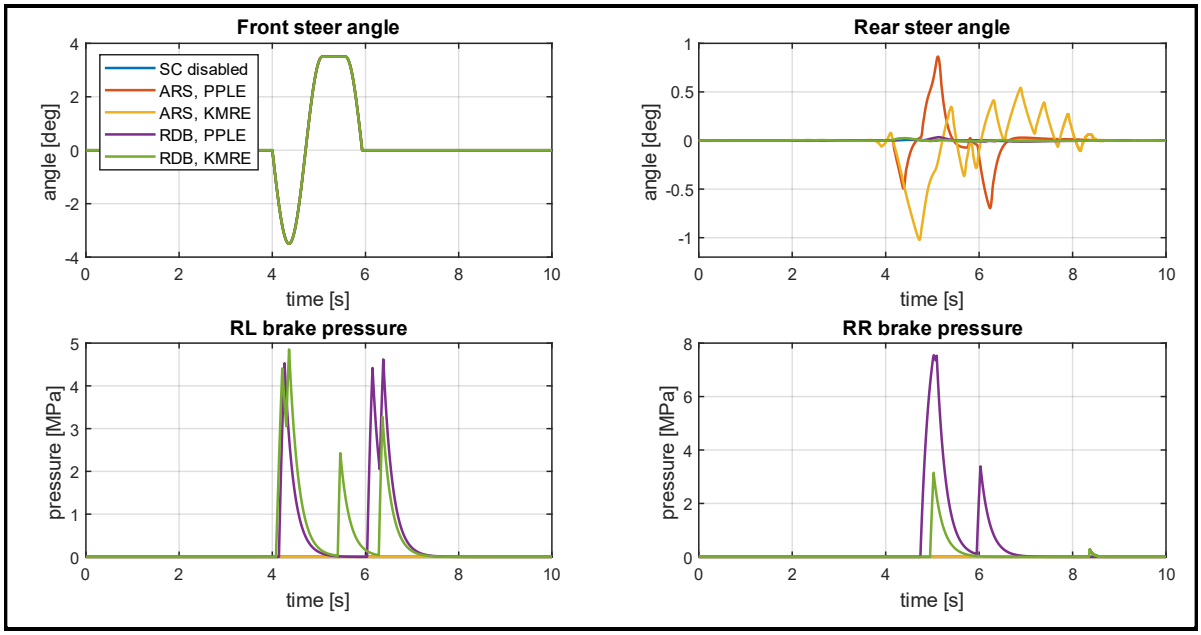

Figure 6-1: Input vehicle states for stand-alone sub-system stability control systems when performing a sine with dwell manoeuvre on a smooth road

With reference to the displacement shown in Figure 6-2, one should keep in mind that the sine with dwell test simulates a lane change with the benchmark of ΔY_{CG} taken at $1.07\ s$ from BOS. It is a responsiveness measure that determines the lateral displacement relative to the initial lane in order to avoid an "obstacle" in the road. From the displacement plot it is evident that the vehicles with the PPLE SC reference model are more responsive, based on this measure, than those with the KMRE model. All SC enabled vehicles are less responsive than baseline.

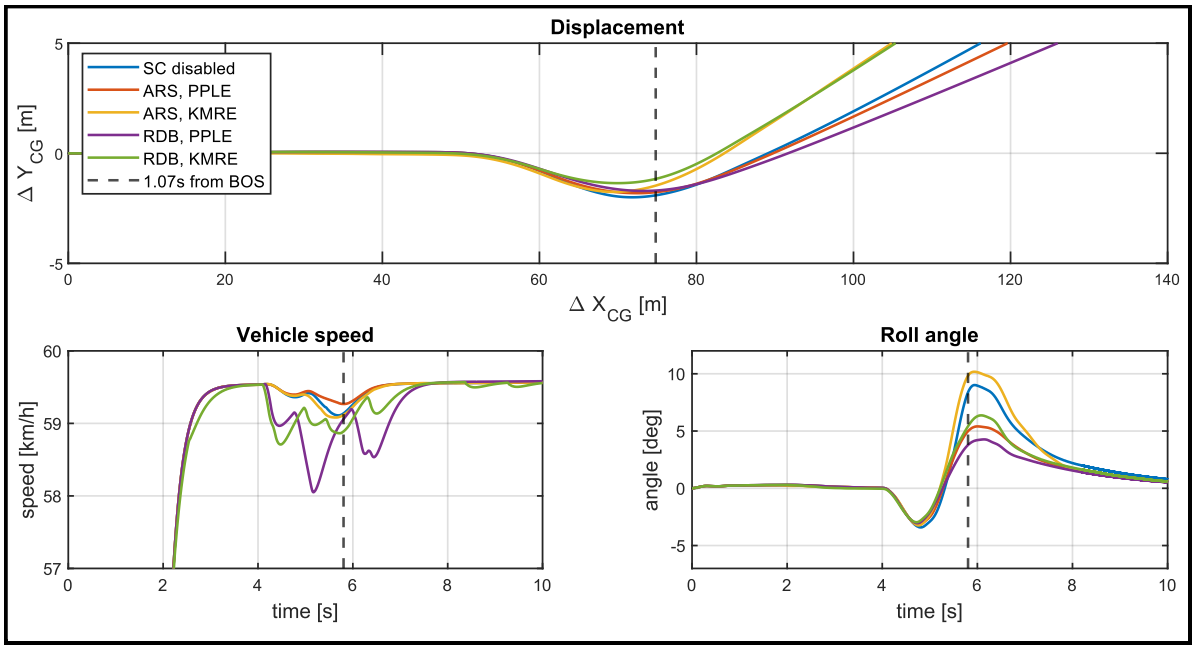

Figure 6-2: Displacement, velocity and roll angle comparison of sub-systems on a smooth road

The benefit of the PPLE SC reference model is highlighted by its roll angle performance. This is a consequence of it not allowing large peak yaw rates as shown in Figure 6-3, which keeps the roll angle small. The vehicle speed plot shown in Figure 6-2 confirms the motivation for delaying brake intervention with ICC since it has the greatest impact on vehicle velocity which makes its intervention obvious or uncomfortable to the driver. ARS SC on average has similar loss of velocity as the baseline SC disabled vehicle.

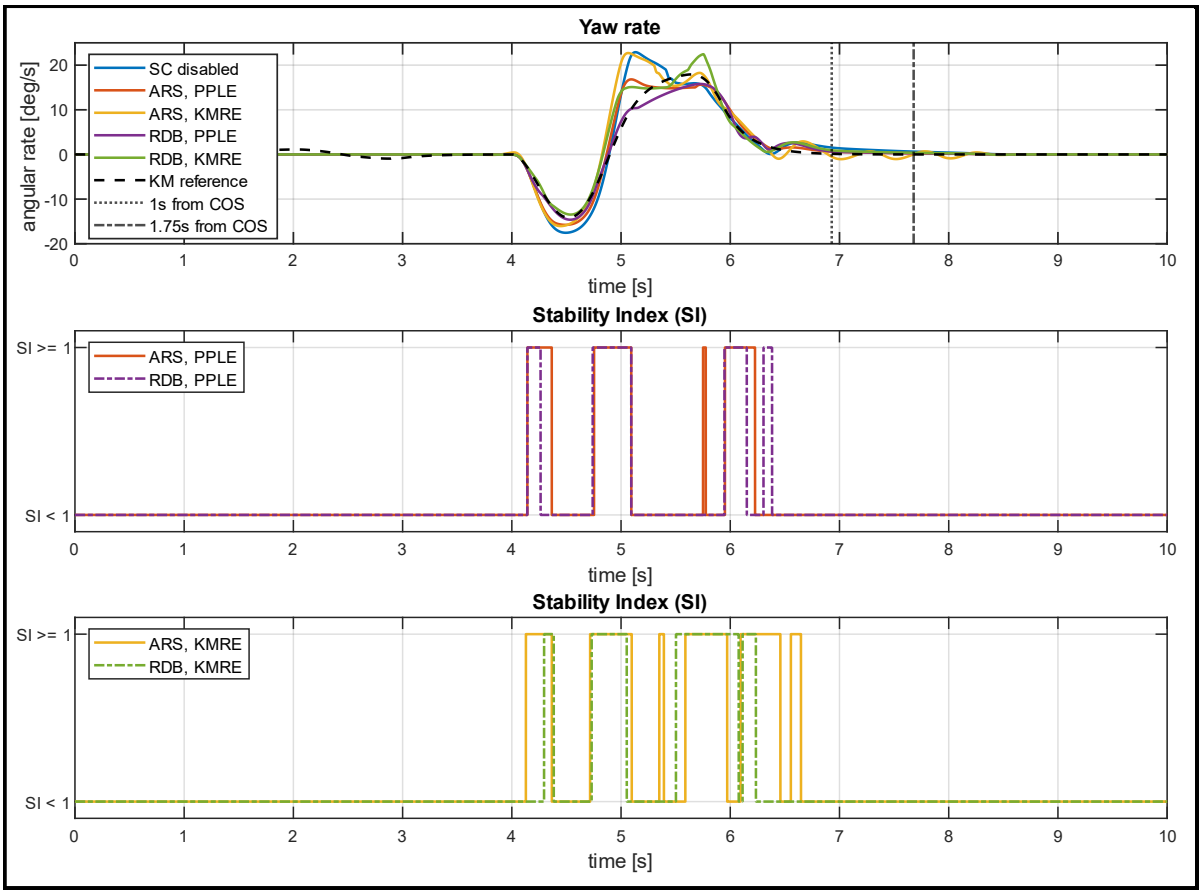

Figure 6-3: Yaw rate and SI comparison of stand-alone sub-systems on a smooth road

The sideslip angle plot of the two sub-system SCs using the KMRE shown in Figure 6-4 (top) is interesting since the RDB control strategy in this case does not take sideslip angle into account as per Table 5-7, which specifies a zeta weighting of zero. Yet, the only drawback in comparison to the ARS control strategy is a slight increase in peak absolute sideslip angle while otherwise still approximating the kinematic model reference better than the SC disabled vehicle and only slightly worse than ARS with a non-zero zeta weighting. For both ARS and RDB, the yaw rate and sideslip behave opposite when applying a yaw moment, i.e., when yaw rate/angle increases, sideslip angle decreases. This has the effect that steering the positive yaw rate back to zero after the manoeuvre would also steer the negative sideslip angle back to zero, without controlling for sideslip as per the sliding variable. This coupling explains why the PPLE SC reference model tends to lower peak yaw rates; by preventing further development of the sideslip angle and rate once outside the stability region, the yaw rate development is also limited. The coupling implies that both yaw rate and sideslip do not necessarily have to be explicitly controlled for. Controlling only for yaw rate has benefits such as that sideslip angle measurement is then not necessary. Estimation of the sideslip angle is

complex, expensive and has a high change of introducing system inaccuracies while yaw rate can be directly measured with a gyroscope and is thus comparatively cheap, simple and accurate.

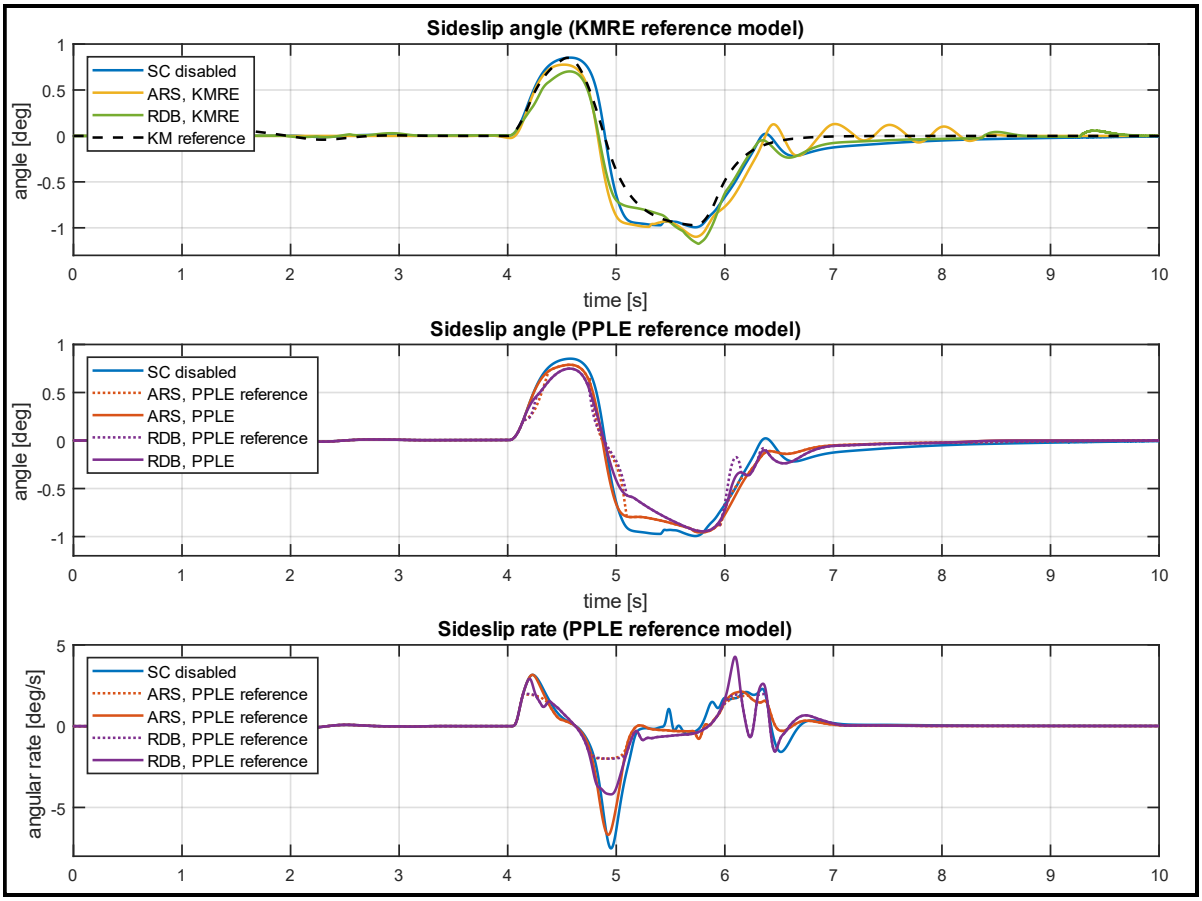

Figure 6-4: Sideslip angle and rate comparison of sub-systems on a smooth road

The plot of time periods where $SI \geq 1$ on Figure 6-3 reveal where actuator activation occurs for PPLE SC reference model systems. Those areas are: (1) just as the yaw rate starts to change at the beginning of the manoeuvre, (2) when the front steering angle passes through a zero angle at 4.9 s, where sideslip rate is large negative (3) shortly after the steering input has returned to zero at completion of the manoeuvre, where sideslip rate is large positive. This points to fundamental differences in control systems using the two SC reference models; the KMRE SC reference model will both try to reduce yaw rate that is higher than reference and try to increase yaw rate that is below reference, and it will do so continuously throughout the manoeuvre. The PPLE SC reference model will only try to decrease sideslip angle and/or rate if it is outside the stability region. The working of the KMRE SC reference model allows for development of large peak yaw rate and sideslip angle while better damping yaw rate and sideslip angle after the manoeuvre. The PPLE reference model on the other hand limits peak sideslip angle but offers little or no improved damping of sideslip angle once the maneavre is complete since the actuators are generally not activated during that time.

The following figures present data for the sine with dwell manoeuvre performed on a rough road with the different stand-alone sub-system SCs. Figure 6-5 presents simulation vehicle input states. The displacement plot of Figure 6-6 shows that there is a smaller difference in the lateral displacement metric between systems, compared to the larger difference

observed for a smooth road. The same is observed for the roll angle; the spread between the different system's peak roll angle is smaller in comparison to the larger spread seen for a smooth road. As for a smooth road, the PPLE SC reference model systems have the lowest peak roll angle. Concerning the changes in vehicle speed, compared to the smooth road, the RDB systems again cause the largest loss in speed but peak loss is lower than for a smooth road.

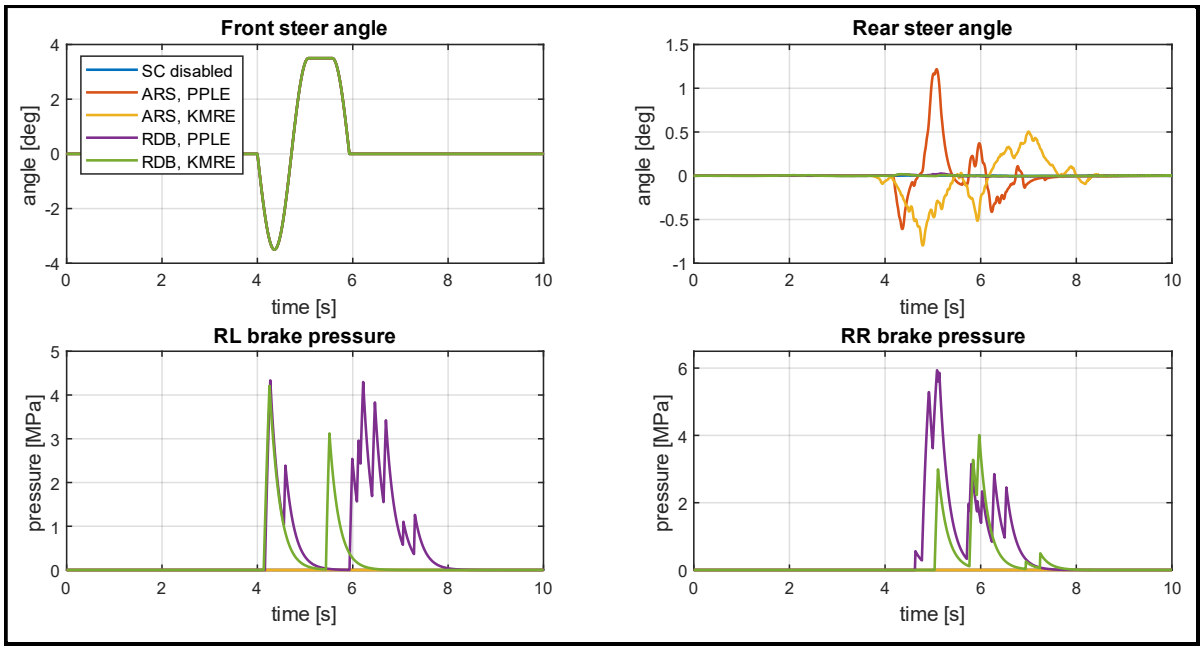

Figure 6-5: Input vehicle states for stand-alone stability control systems when performing a sine with dwell manoeuvre on a rough road

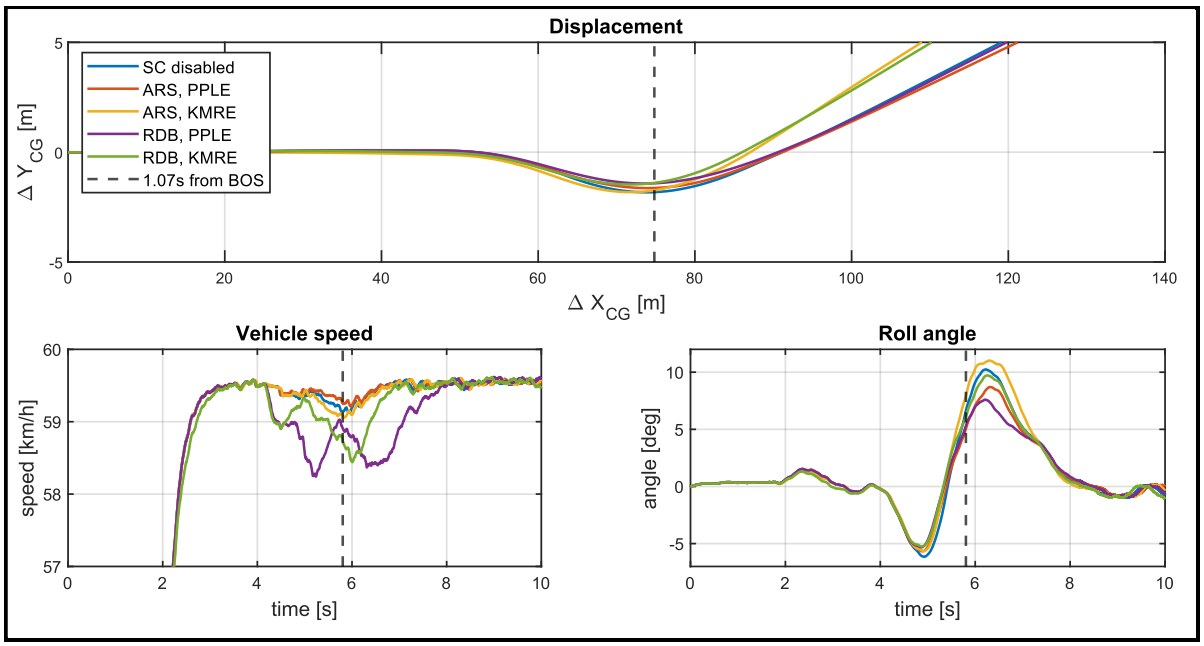

Figure 6-6: Displacement, velocity and roll angle comparison of sub-systems on a rough road

With reference to Figure 6-7, the effect of the rough road on the yaw rate is to have a larger spread between system performance at the points 1 s and 1.75 s from COS.

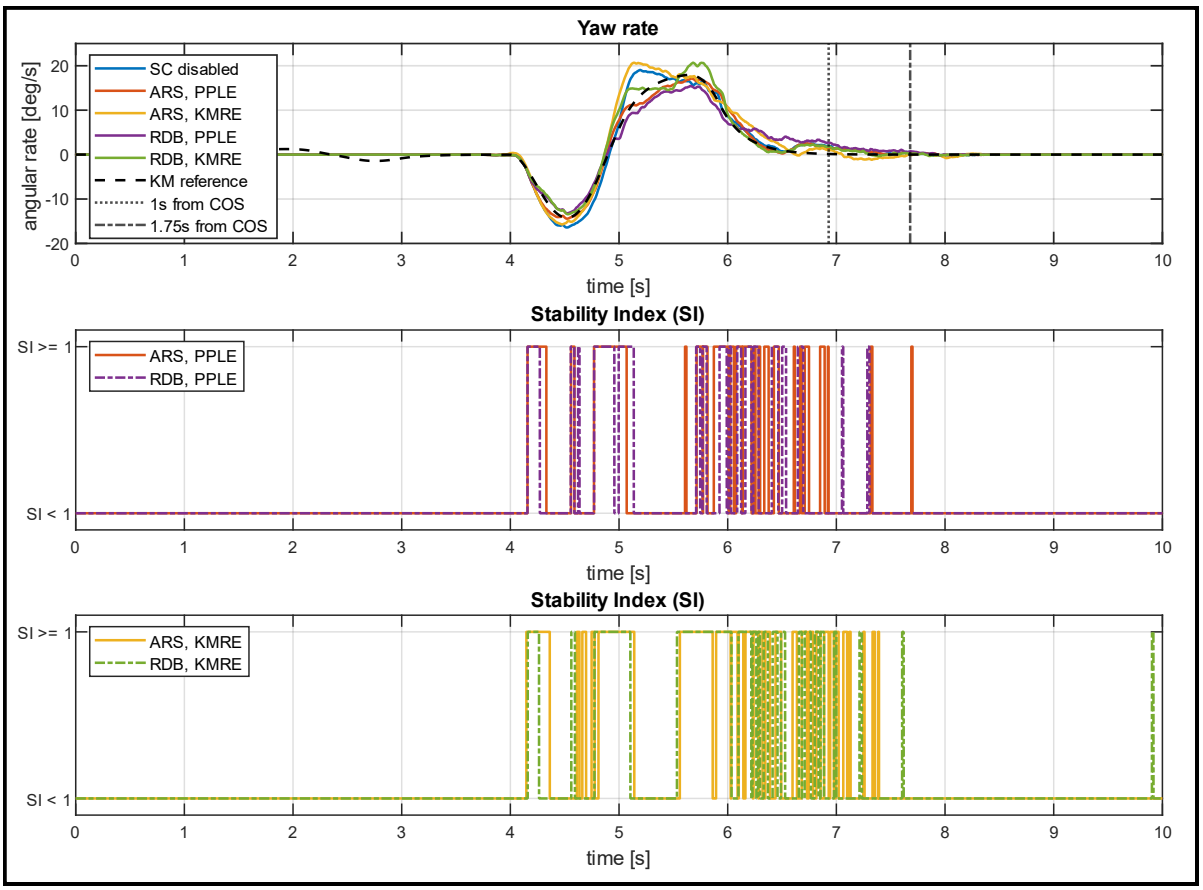

Figure 6-7: Yaw rate and SI comparison of sub-systems on a rough road

As shown in Figure 6-7 and Figure 6-8, the rough road causes rapid sideslip angle and rate fluctuations which bring about more periods of actuator activation for systems using the PPLE SC reference model compared to smooth road performance. Figure 6-8 conveys that the controlled vehicle has a lower sideslip amplitude than baseline for systems using the PPLE SC reference model while the sideslip angle is larger than baseline for the system using the KMRE reference model.

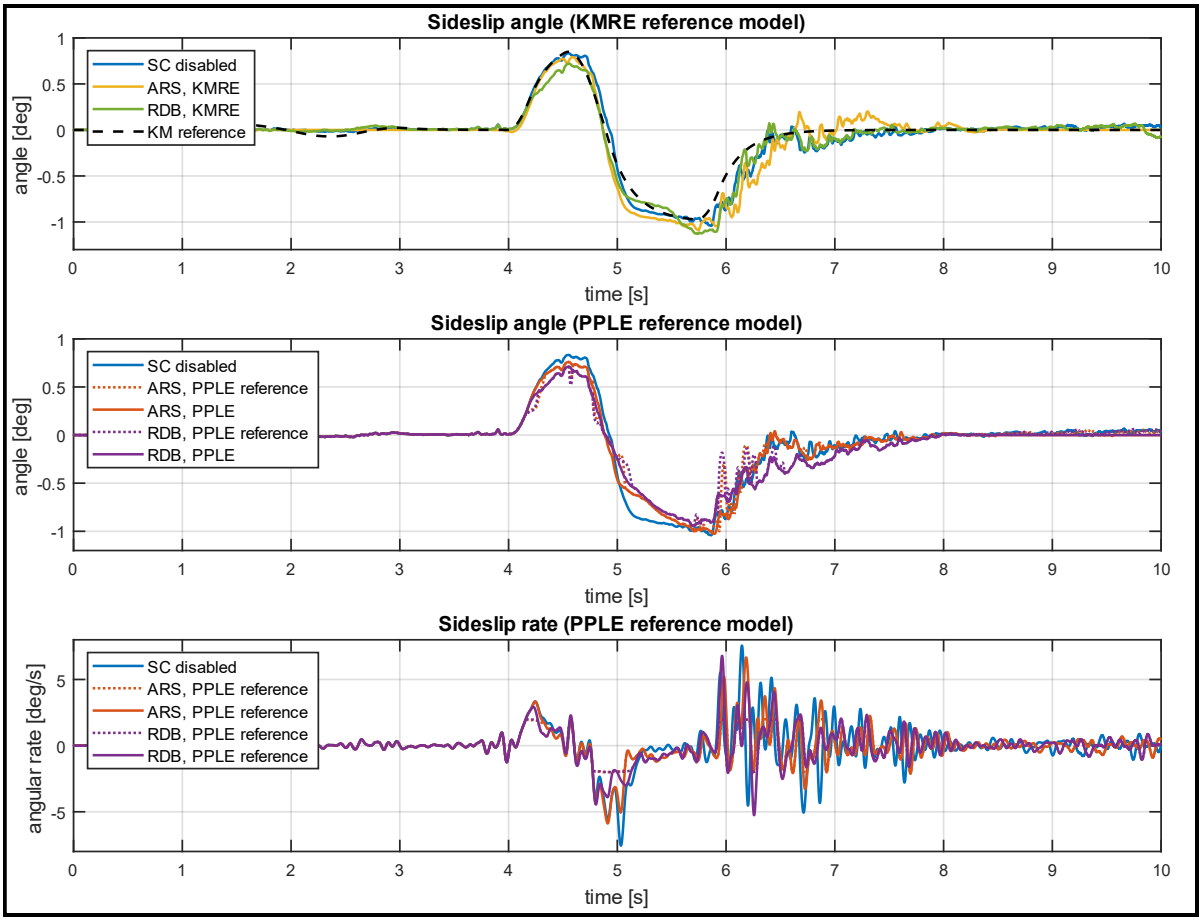

Figure 6-8: Sideslip angle and rate comparison on a rough road

Figure 6-9 shows a series of radar plots normalized for road classification, reference model and control strategy in an attempt to compare stand-alone sub-system SC performance in terms of a single variable. The following observations are made:

a. For the smooth road: In terms of the best SC reference model for yaw rate damping, the KMRE reference model is the best performer. In terms of the lateral displacement and roll angle metrics, the PPLE SC reference model is the best performer. The best control strategy using the KMRE SC reference model, based on yaw rate damping, is ARS while the best control strategy using the PPLE reference model, based on the same metric, is also ARS.

b. For the rough road: The KMRE SC reference model again provides superior yaw rate damping while the PPLE reference model provides the lowest roll angle. The lateral displacement for both SC reference models is similar. The best control strategy using the KMRE SC reference model, based on the yaw rate damping metric, is ARS while the best control strategy using the PPLE reference model, based on the same metric, is also ARS.

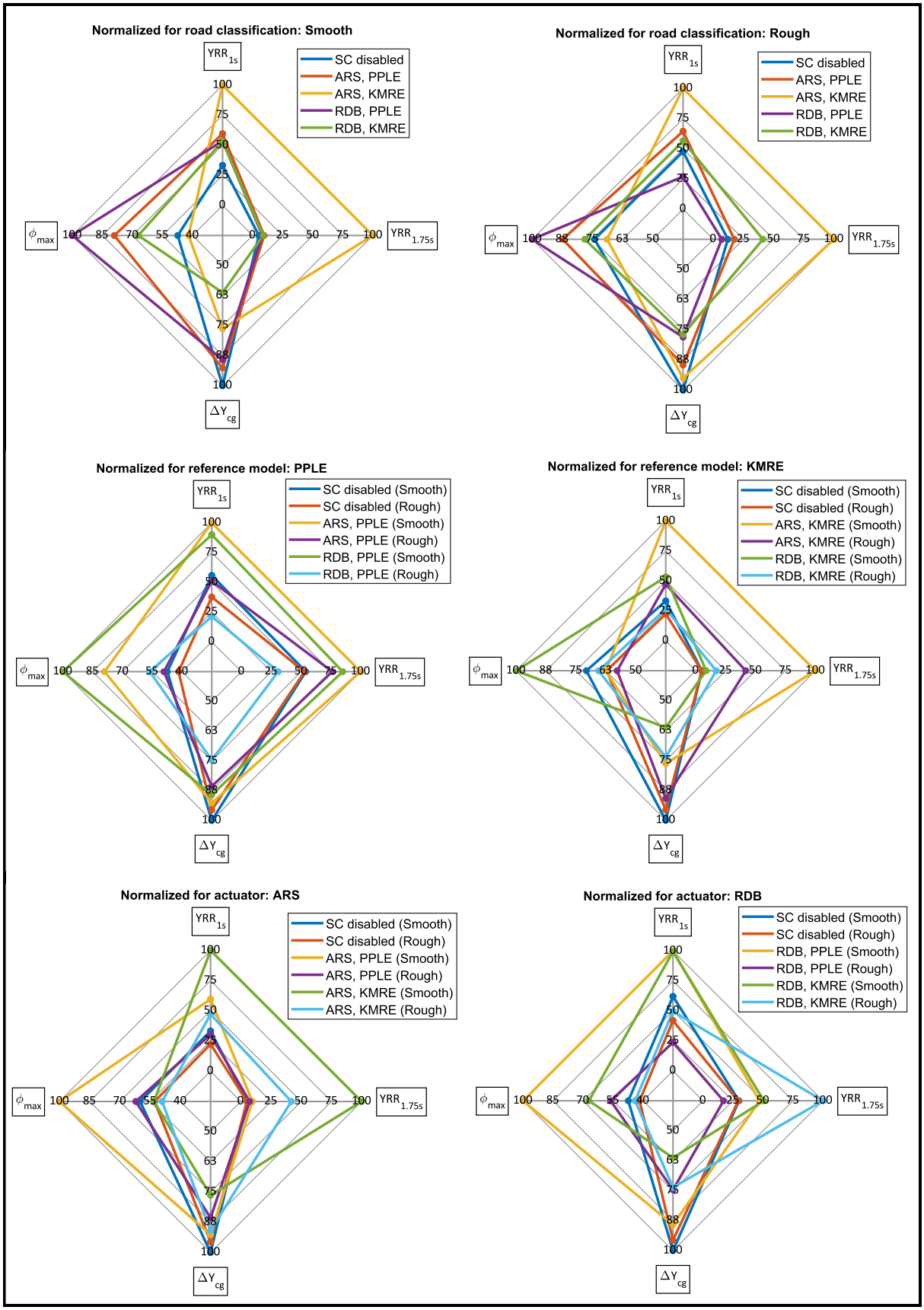

Figure 6-9: Radar plots of sub-system performance normalized for different variables

6.1.2 *Integrated sub-system performance*

Following the stand-alone sub-system SC comparison of Section 6.1.1, three integrated SC configurations are now investigated as discussed in Section 5.2, of which all initially use ARS while RDB is activated based on some integration rule. For the investigation, the steering manoeuvre is again the $3.5°$ sine with dwell steering input at $60\ km/h$ and performance is measured with the four metrics as was done in the previous section. Two questions can be posed for the integrated systems:

1. Does ARS and RDB integration help retain vehicle velocity better than stand-alone RDB systems?
2. What is the best ARS and RDB integration rule, between a_r and SI?

Figure 6-10 to Figure 6-13 show a series of plots of relevant data captured for a smooth road that are to be compared to the stand-alone sub-system SC systems of the previous section. Figure 6-10 shows the vehicle input states.

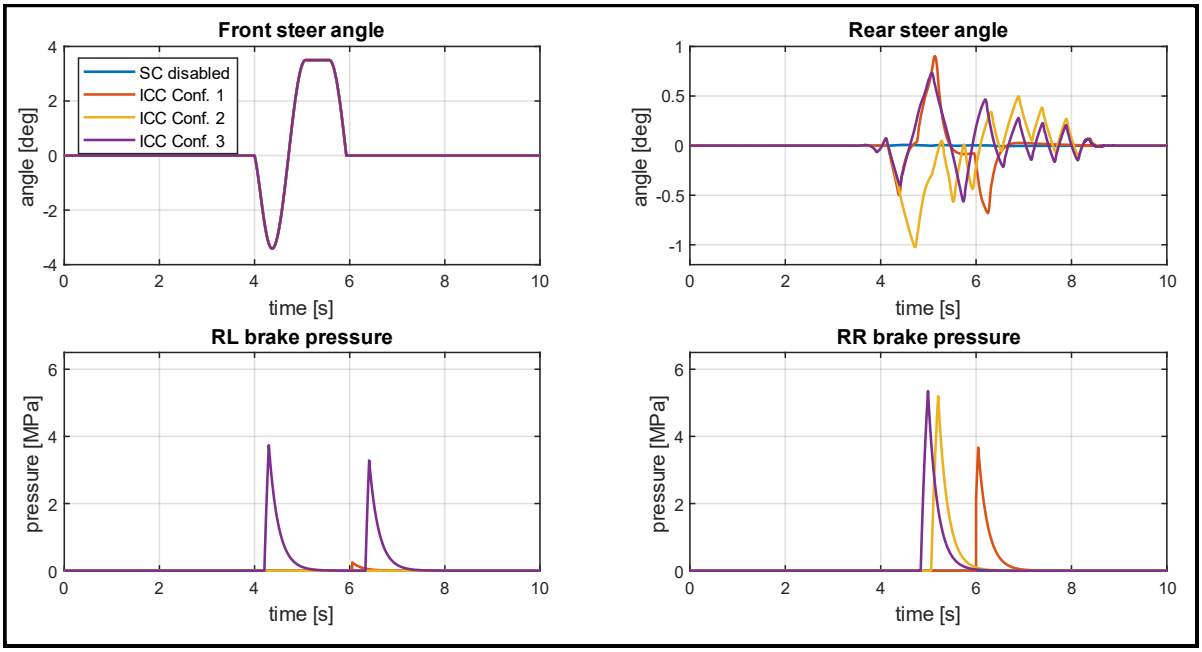

Figure 6-10: Vehicle input states for integrated stability control systems when performing a sine with dwell manoeuvre on a smooth road

The following observations are made regarding the displacement, vehicle speed and roll angle plots shown in Figure 6-11:

a. When comparing ICC Configuration 1 with the stand-alone control strategies, which also use the PPLE SC reference model, it is evident that the integrated system better retains vehicle speed than RDB but worse than ARS. Similarly, the peak roll angle is lower than for ARS but higher than for RDB. The integrated system has a further lateral displacement at $1.07\ s$ from BOS than either stand-alone SC systems which represents better responsiveness.

b. Comparing ICC Configuration 2 with stand-alone sub-system SCs, which also use the KMRE SC reference model, shows that the integrated SC system loses more vehicle

speed than either stand-alone system. The peak roll angle performance of the integrated system is lower than for ARS, higher than for RDB, but closer to stand-alone ARS performance. The integrated SC has a better responsiveness than either stand-alone SCs.

c. Comparing ICC Configuration 3 to stand-alone sub-system SCs, also using the KMRE SC reference model, shows that vehicle velocity is better retained than RDB but worse than ARS. The peak roll angle of the integrated system is much lower than for the ARS or RDB SCs. The integrated SC has a better responsiveness than either stand-alone sub-system SCs.

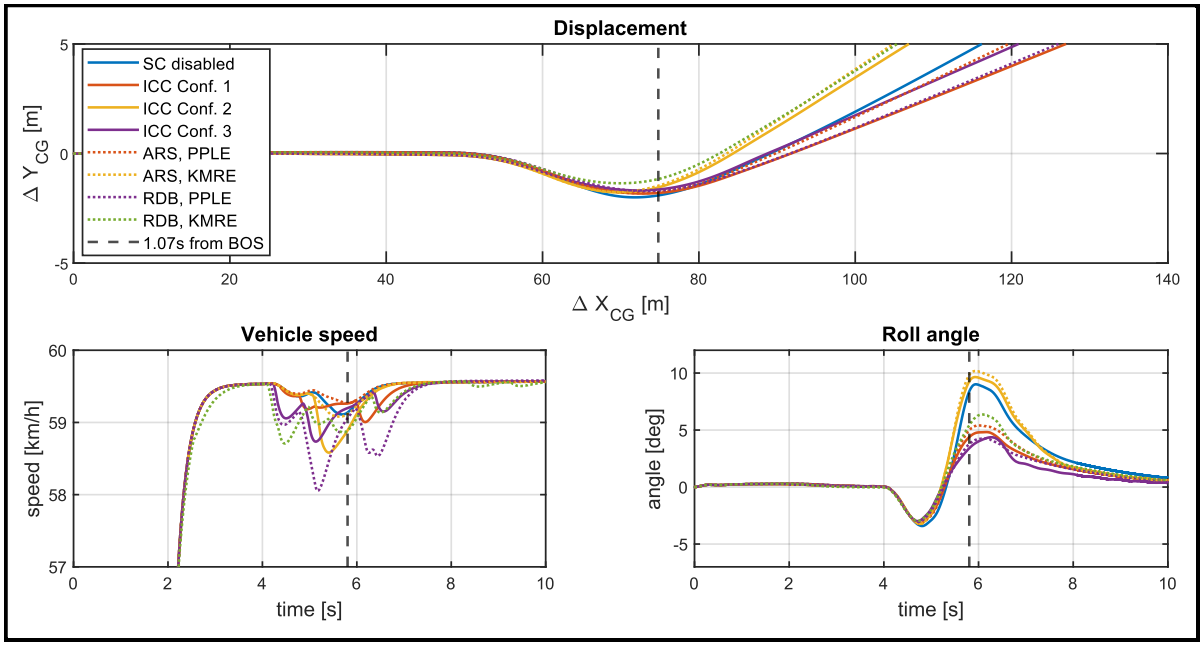

Figure 6-11: Displacement, vehicle speed and roll angle comparison of integrated stability controllers on a smooth road

The yaw rate response of the three integrated system configurations is shown in Figure 6-12. The plots indicate that ICC Configuration 1 has a peak yaw rate lower than stand-alone ARS but higher than RDB (all with the PPLE SC reference model). ICC Configuration 2 has a similar peak yaw rate to the stand-alone systems (all with the KMRE SC reference model). ICC Configuration 3 has a lower peak yaw rate than either stand-alone system (all with the KMRE reference model). It is interesting to note the activation areas for ICC Configuration 2 and 3 since they both use the same reference model but with different integration rules. It seems as though the RDB integration periods of the two systems rarely overlap even though SI and rear axle slip angle both indicate an aspect of vehicle stability. The rear axle slip angle rule appears more likely to activate at absolute yaw rate local peaks whereas the SI rule appears more likely to activate before or after such peaks.

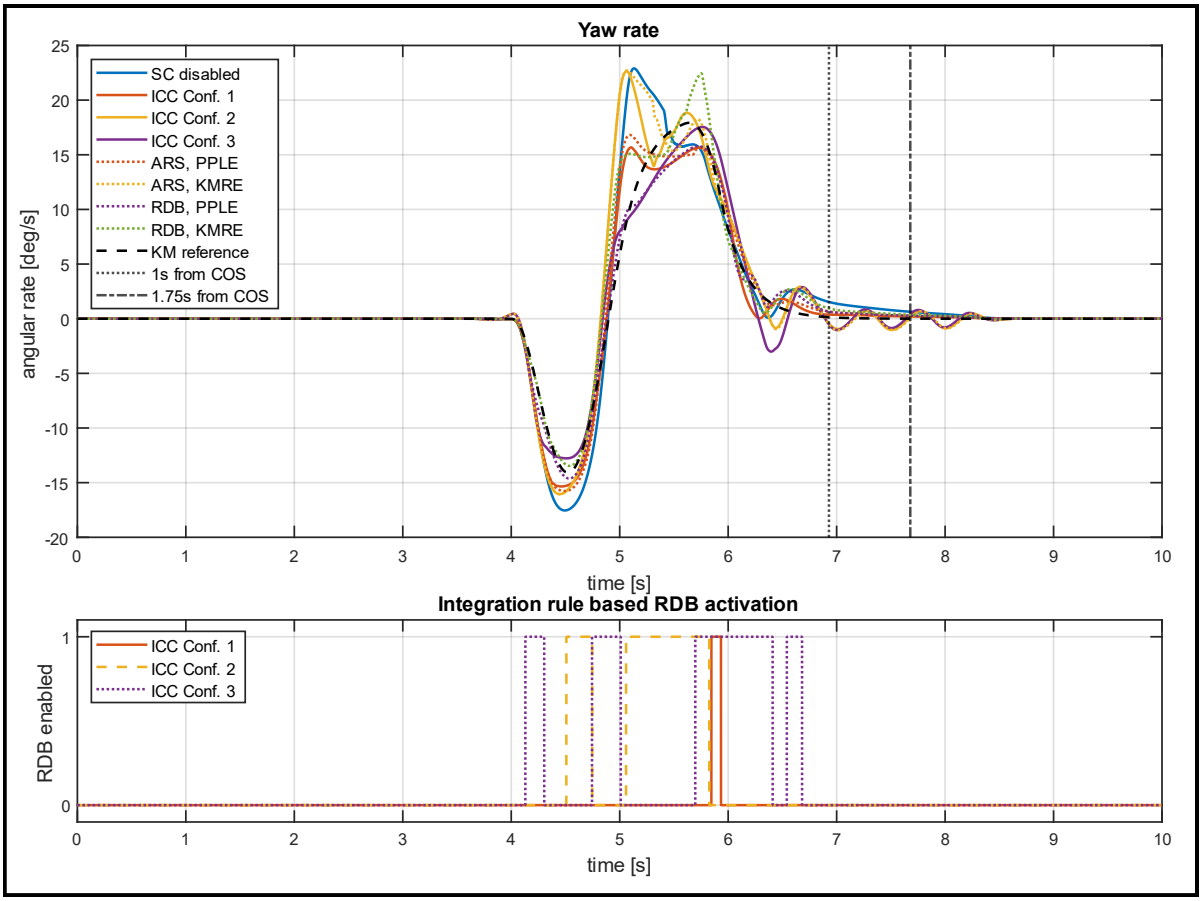

Figure 6-12: Yaw rate comparison of integrated stability controllers on a smooth road

In terms of the sideslip angle data presented in Figure 6-13:

a. ICC Configuration 1 has a similar peak absolute sideslip angle than ARS and RDB (all with the PPLE SC reference model).

b. ICC Configuration 2 has a similar peak absolute sideslip angle than ARS but a larger peak than RDB (all with the KMRE SC reference model).

c. ICC Configuration 3 has a lower peak absolute sideslip angle than either stand-alone system (all with the KMRE SC reference model).

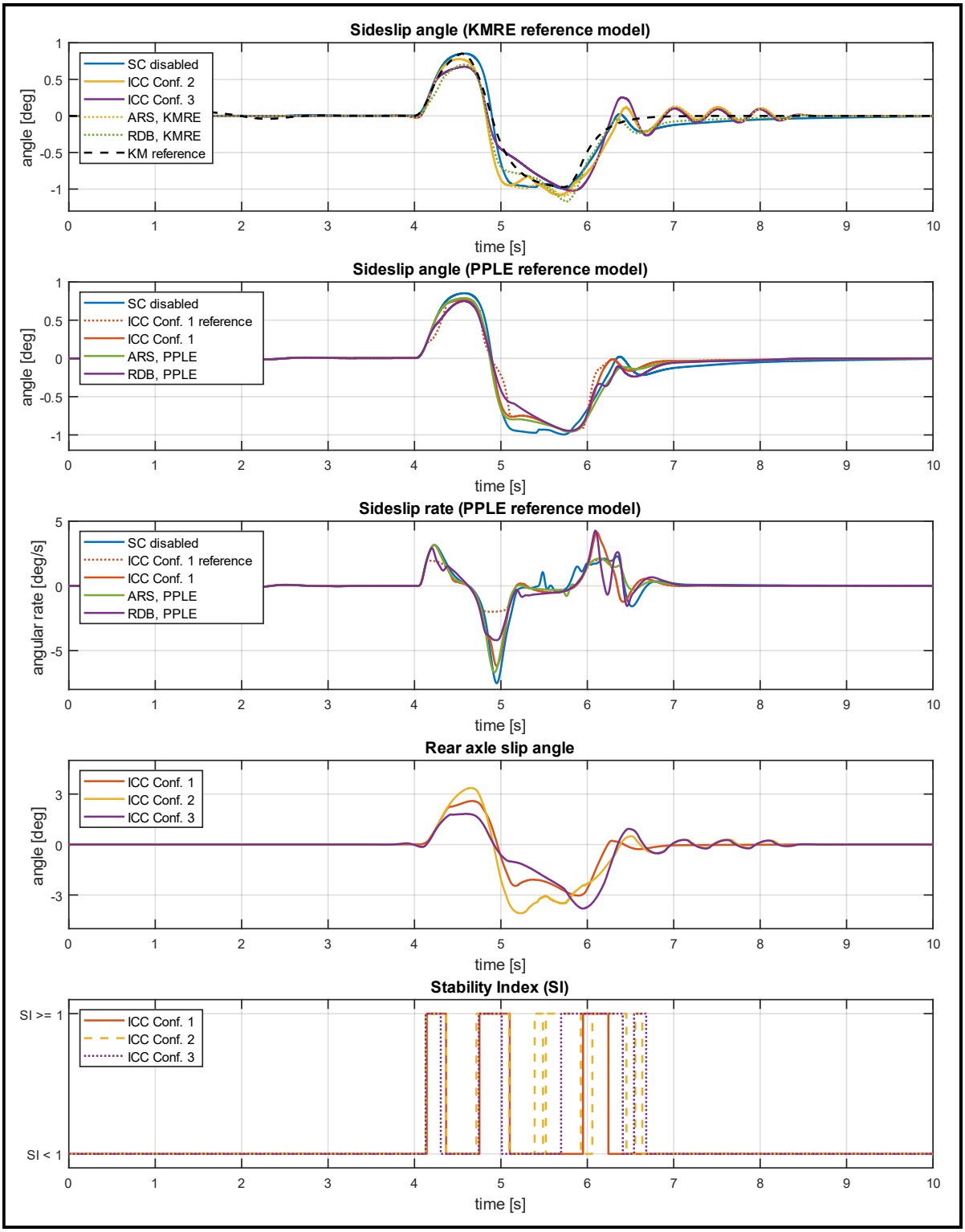

Figure 6-13: Sideslip angle and integration rule time histories on a smooth road

Figure 6-14 to Figure 6-17 show a series of plots of relevant data captured for integrated system performance on a rough road. Figure 6-14 shows the vehicle input states for the manoeuvre.

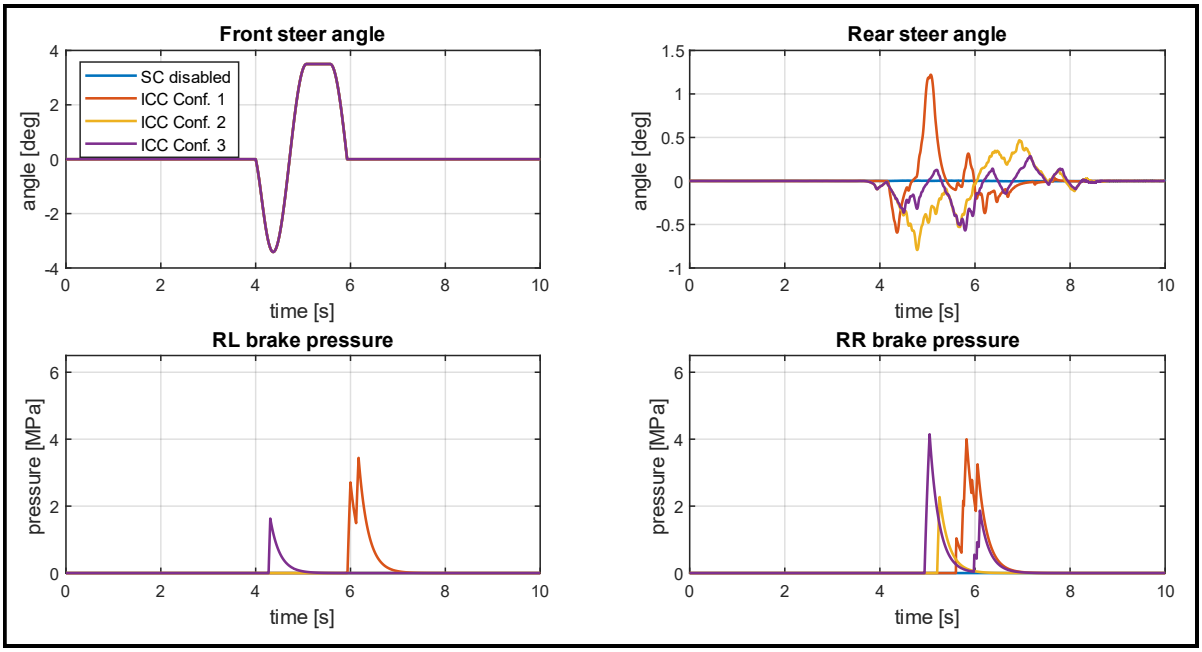

Figure 6-14: Vehicle input states for integrated stability control systems when performing a sine with dwell manoeuvre on a rough road

Considering the vehicle displacement, speed and roll angle plot of Figure 6-15, the following observations are made:

a. When comparing the responsiveness of ICC Configuration 1 to stand-alone ARS and RDB which also uses the PPLE SC reference model, the lateral displacement at 1.07 s from BOS for the integrated system is greater than for RDB but less than for ARS. The integrated system retains vehicle speed better than RDB but worse than ARS and the integrated system peak roll angle is greater than RDB but less than ARS.

b. When comparing ICC Configuration 2 with the same SC reference model (KMRE) stand-alone systems, the integrated system retains vehicle speed better than RDB but worse than ARS throughout the manoeuvre. The integrated system has a similar lateral displacement as the ARS system because RDB for the integrated system has not activated yet at that time. The peak roll angle of the integrated system is less than for ARS but greater than for RDB.

c. The responsiveness as measured by lateral displacement of the ICC Configuration 3 system is similar to ARS and greater than for RDB (all with the KMRE SC reference model). The integrated system retains vehicle speed better than RDB, but worse than ARS, and has a lower peak roll angle than both stand-alone systems.

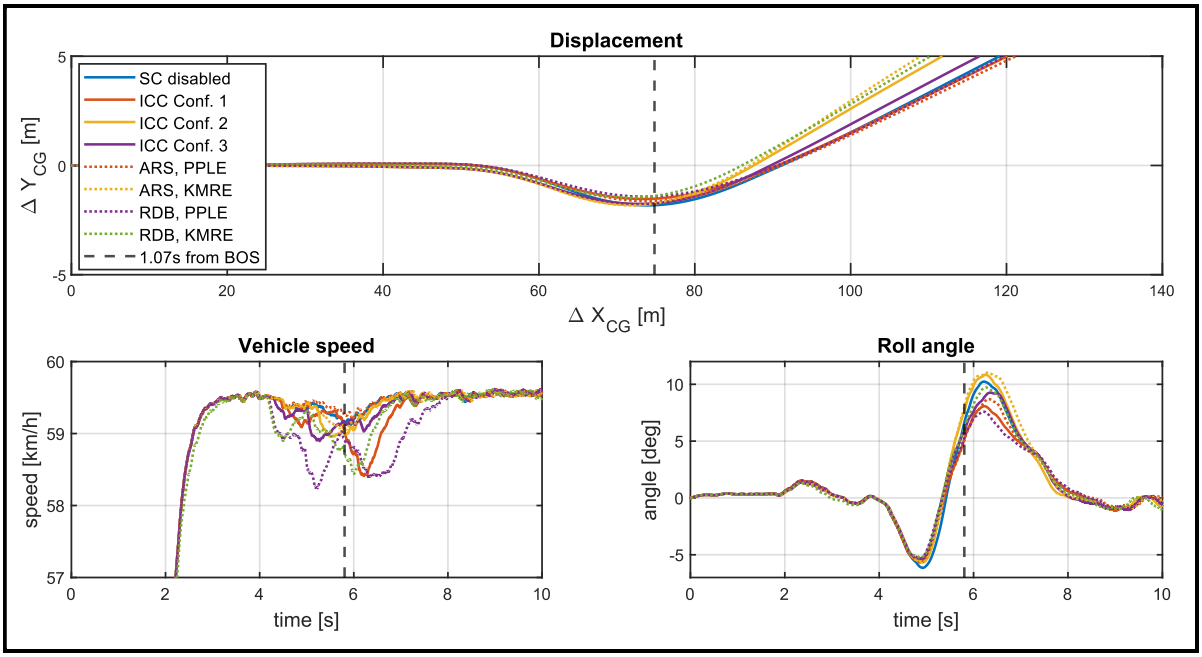

Figure 6-15: Displacement, velocity and roll angle comparison of integrated systems on a rough road

For the yaw rate plot of Figure 6-16 it is observed that ICC Configuration 1 has a lower peak yaw rate than ARS but higher than RDB (all with the PPLE SC reference model). ICC Configuration 2 has a similar peak yaw rate as ARS and RDB (all with the KMRE SC reference model). ICC Configuration 3 has a lower peak yaw rate than either ARS and RDB (all with the KMRE SC reference model). The RDB activation times for the ICC Configuration 3 system are more frequent but much shorter in comparison to the activation times of the other integrated systems. The high frequency activations are caused by rapid changes in sideslip angle and rate due to the influence of the road profile. This phenomenon may limit the suitability of the SI as integration rule on rough roads.

In terms of the sideslip angle data presented in Figure 6-17:

a. ICC Configuration 1 has a similar peak absolute sideslip angle to RDB, which is lower than for ARS (all with the PPLE SC reference model).

b. ICC Configuration 2 has a similar peak absolute sideslip angle to ARS and RDB (all with the KMRE SC reference model)

c. ICC Configuration 3 has a similar peak absolute sideslip angle to ARS and RDB (all with the KMRE SC reference model)

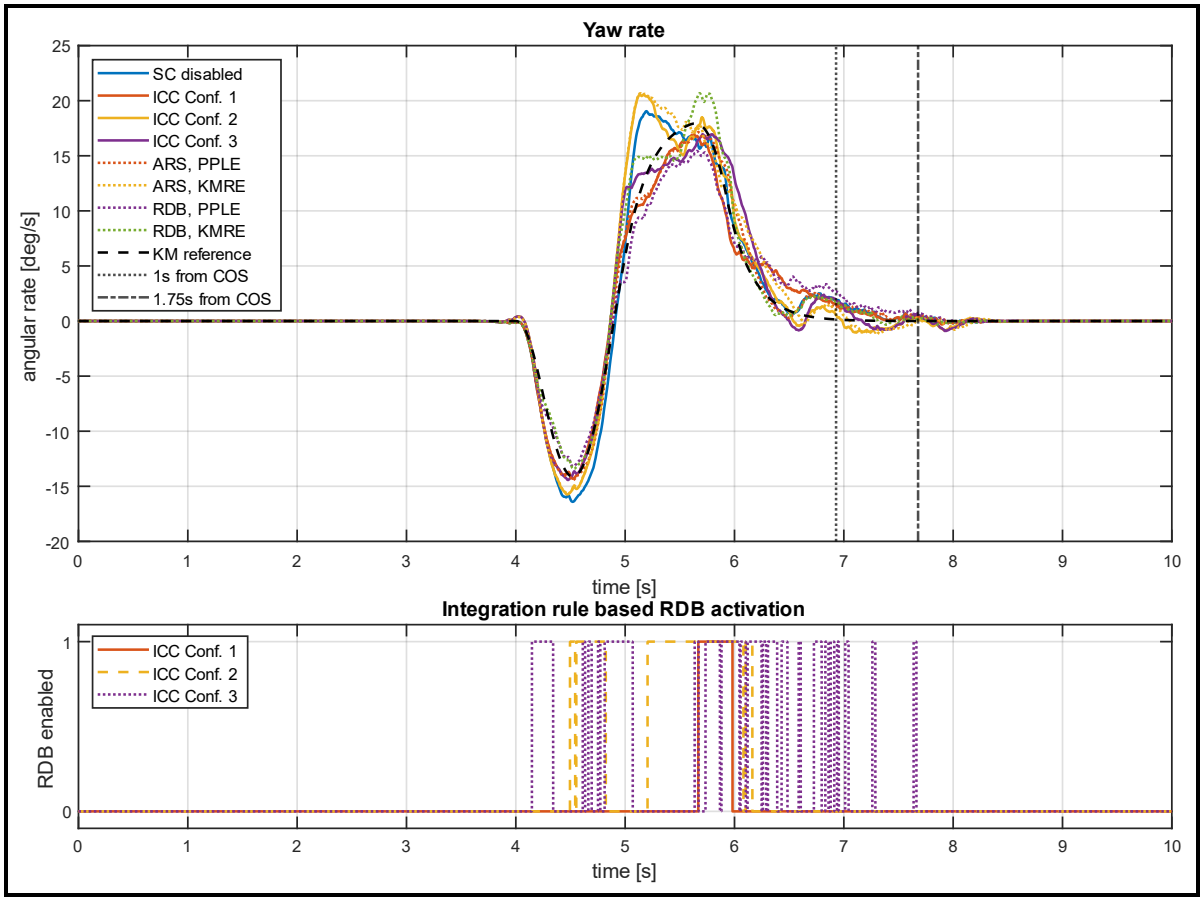

Figure 6-16: Yaw rate comparison of integrated systems on a rough road

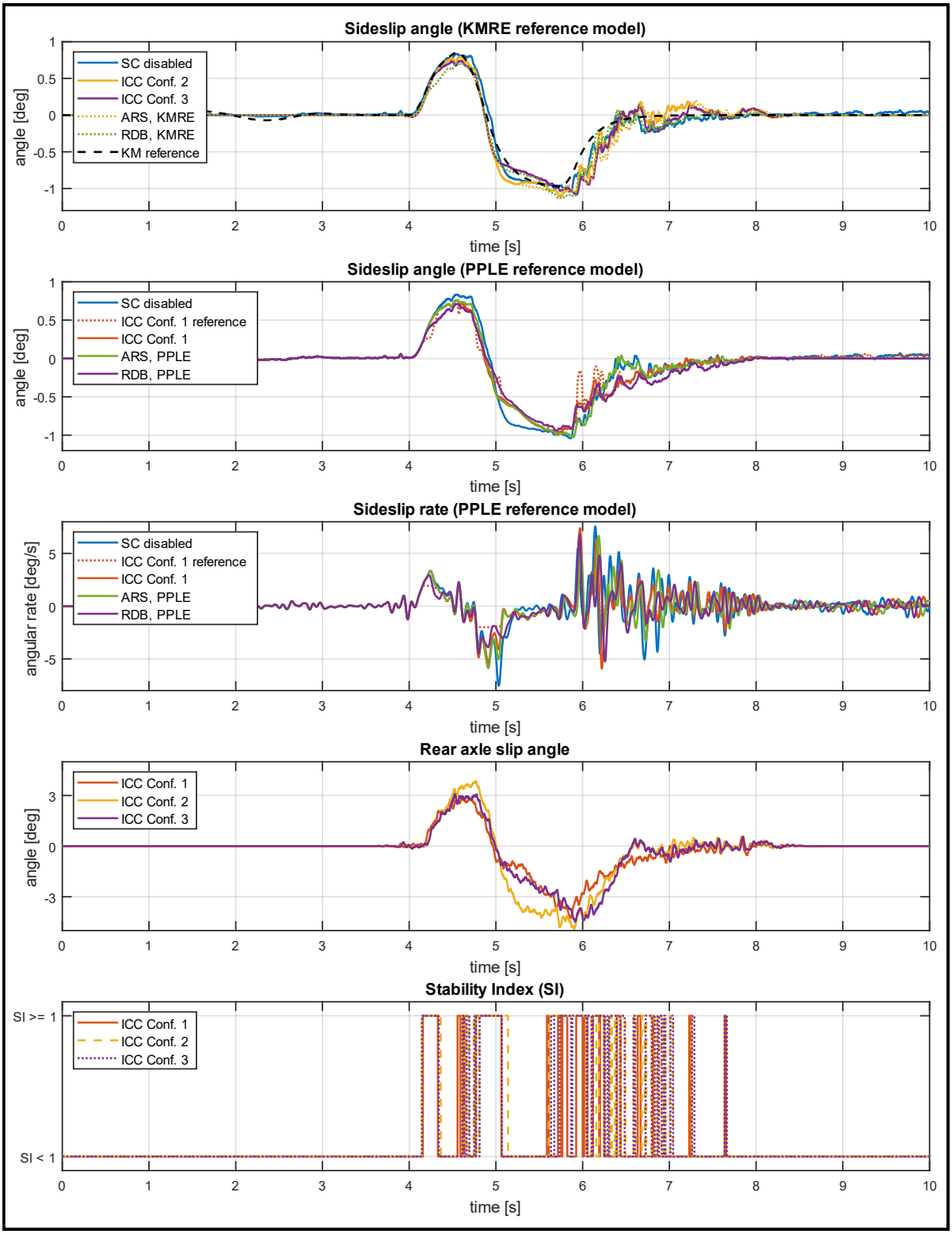

Figure 6-17: Sideslip angle and integration rule time histories on a rough road

The radar plots of Figure 6-18 compare the integrated systems in terms of the four metrics discussed in Section 5.3.6. The plots provide a quick comparison of the stand-alone SCs performance compared to the integrated systems. The plots indicate that integrated SC may improve on certain aspects of a stand-alone sub-system SC and consequently may result in a more favourable SC altogether. An example of this is with the maximum roll angle metric,

where ARS as a stand-alone SC, with the KMRE SC reference model, exhibits worse performance than RDB but the integrated SC consistently shows a better measure. The section is concluded by answering the two questions posed at its start:

1. The data shows that integrated systems are likely to better retain vehicle velocity but it is not observed for all cases.

2. It is found that SI and α_r based triggers would trigger at different times of the manoeuvre. A disadvantage of the SI trigger is that it shows high frequency trigger action on a rough road. Both SI and α_r integration rules provide an efficient means of combining ARS and RDB to obtain a blended response.

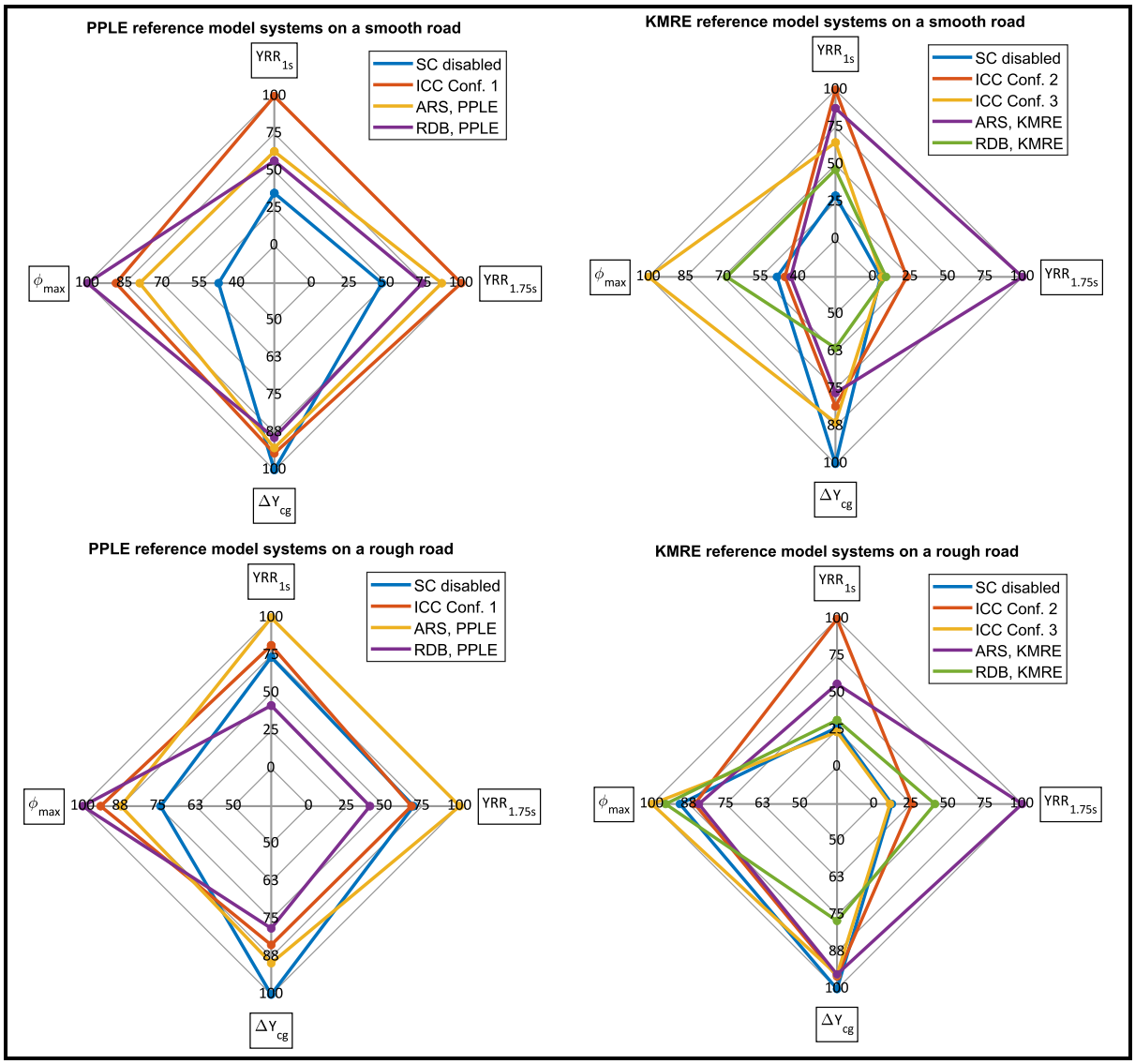

Figure 6-18: Radar plots for different integrated SC configurations

6.2 Closed-loop performance

Both the stand-alone and integrated systems are subjected to closed-loop testing where the vehicle is driven through a DLC manoeuvre with the driver model at a speed of $60\ km/h$. As discussed in Section 3.3.7, the DLC manoeuvre is a severe lane change manoeuvre that

evaluates a vehicle's road holding ability. The following tests are performed on both a smooth and rough road. The criterion of a superior system for this scenario is one that does not cause the vehicle CG to cross the dots at the DLC Sections 3, 5 and 6. The dots represent the CG point location which would likely result in the vehicle knocking over cones and do not represent the actual cone positions. One should note that failing the DLC test does not necessarily mean that a control system is objectively ineffective, as it is a subjective evaluation of vehicle dynamics (International Organization for Standardization, 2018).

Figure 6-19 shows the trajectories of stand-alone SC systems, along with the SC disabled (baseline) vehicle. Figure 6-20 shows vehicle states during the manoeuvre. The trajectories of Figure 6-19 show that only the ARS and RDB systems with the KMRE SC reference model were able to perform the manoeuvre without crossing the CG boundaries and between those, the vehicle with RDB better managed to follow the desired path. The trajectory plot also shows that the ARS and RDB systems with the PPLE SC reference model tend to be less responsive than baseline and in the case of RDB have poor damping of the yaw rate in DLC Section 5. The phase plane boundary, which is thought to maintain vehicle responsiveness by allowing development of sideslip angle up to a limit, causes high actuator setpoints to be imposed once the vehicle is outside the boundary and SC is activated. This shows that sideslip-based control systems are likely not a good option for stability control on a high friction smooth road if closed-loop responsiveness is the major concern.

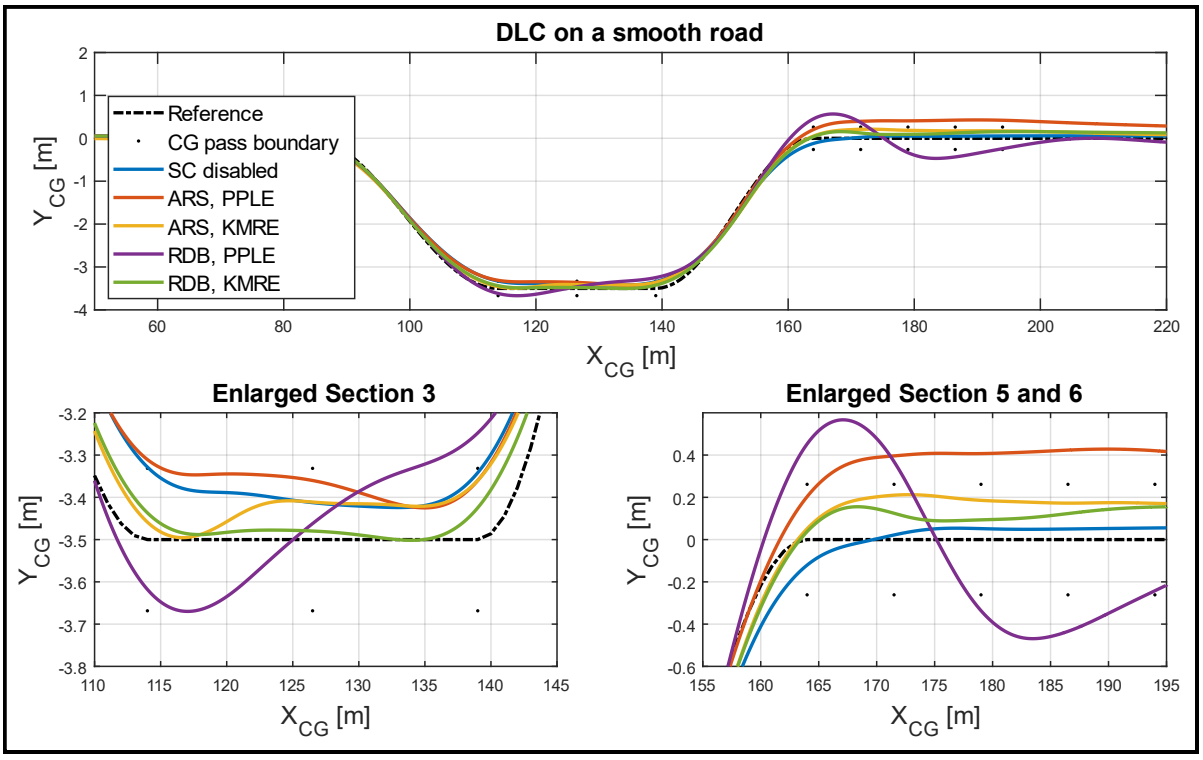

Figure 6-19: The DLC path on a smooth road for the stand-alone SC systems

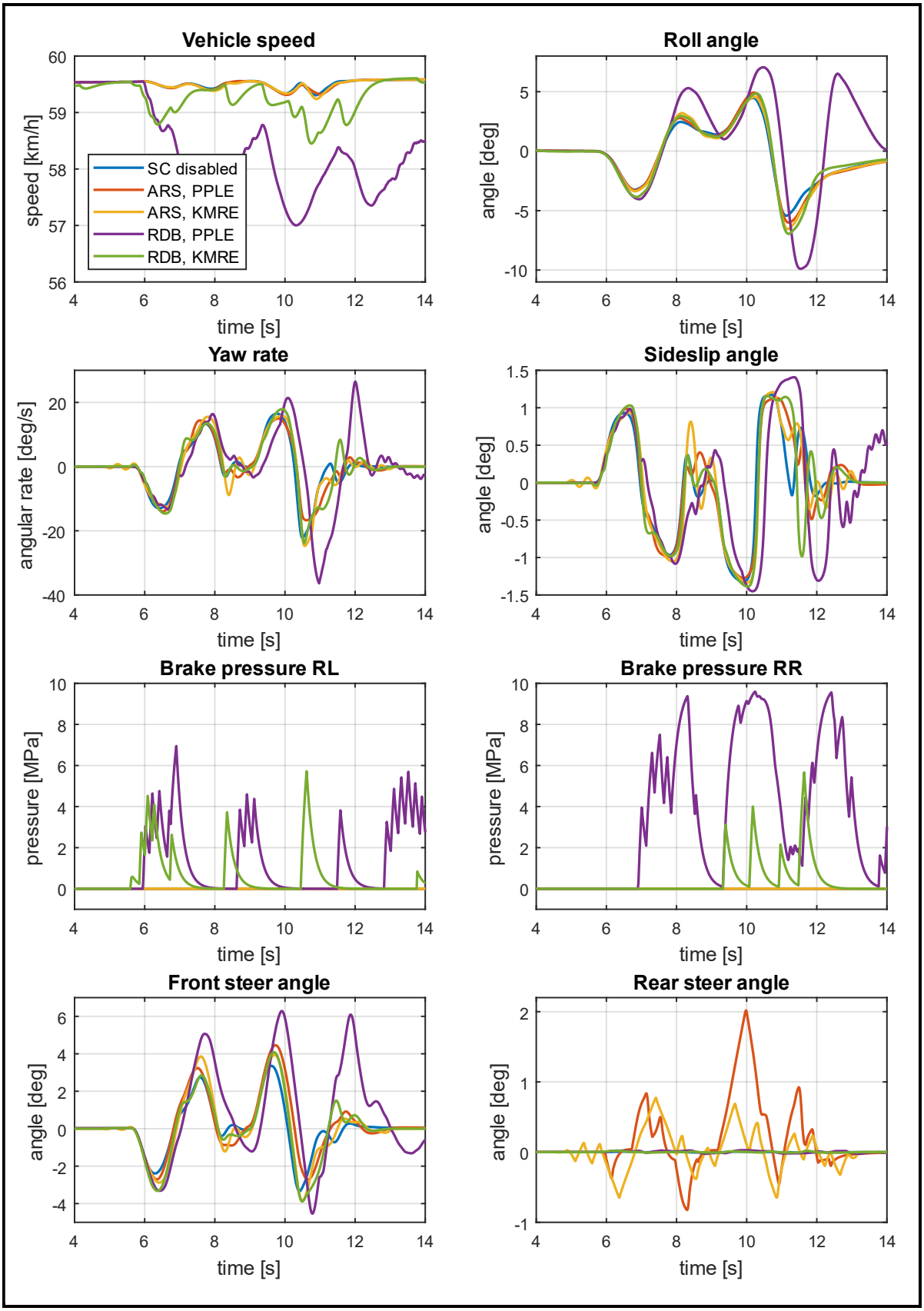

Figure 6-20: Vehicle states for the DLC on a smooth road with stand-alone SC systems

Figure 6-21 shows the vehicle trajectories when performing the DLC on a smooth road with integrated SC systems. Figure 6-22 presents vehicle states during the manoeuvre. The trajectories of Figure 6-21 show that ICC Configurations 2 and 3 initially follow a similar path, but the difference in integration rule causes the two to behave differently from Section 5 onwards. ICC Configuration 1 is the worst performer, already crossing the boundary in Section 3. ICC Configuration 2 seems the most promising of the integrated systems since it has the lowest path overshoot of all systems in Section 5. In line with the findings of the open-loop testing, where it was said that the integration rule provides a means of blending ARS and RDB response, it may be possible to tune the integration rule of ICC Configuration 2 to further improve its path following ability by integrating RDB at a lower threshold.

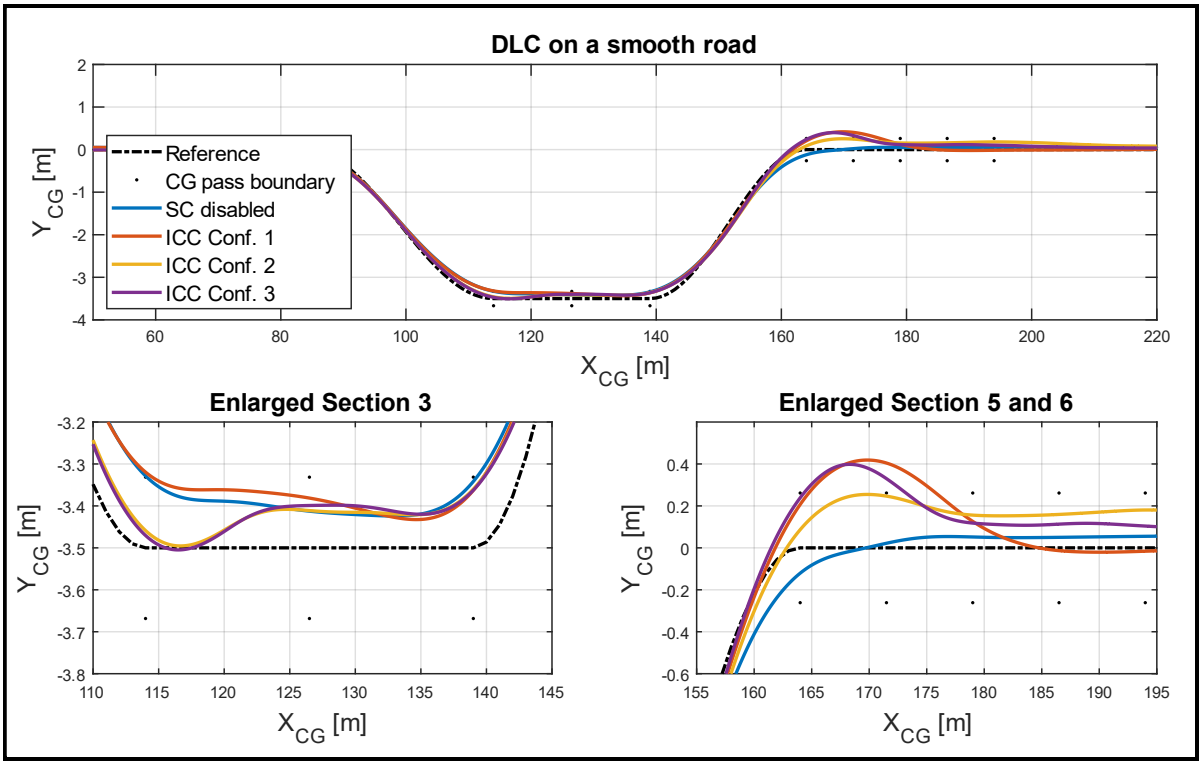

Figure 6-21: The DLC path on a smooth road for integrated SC systems

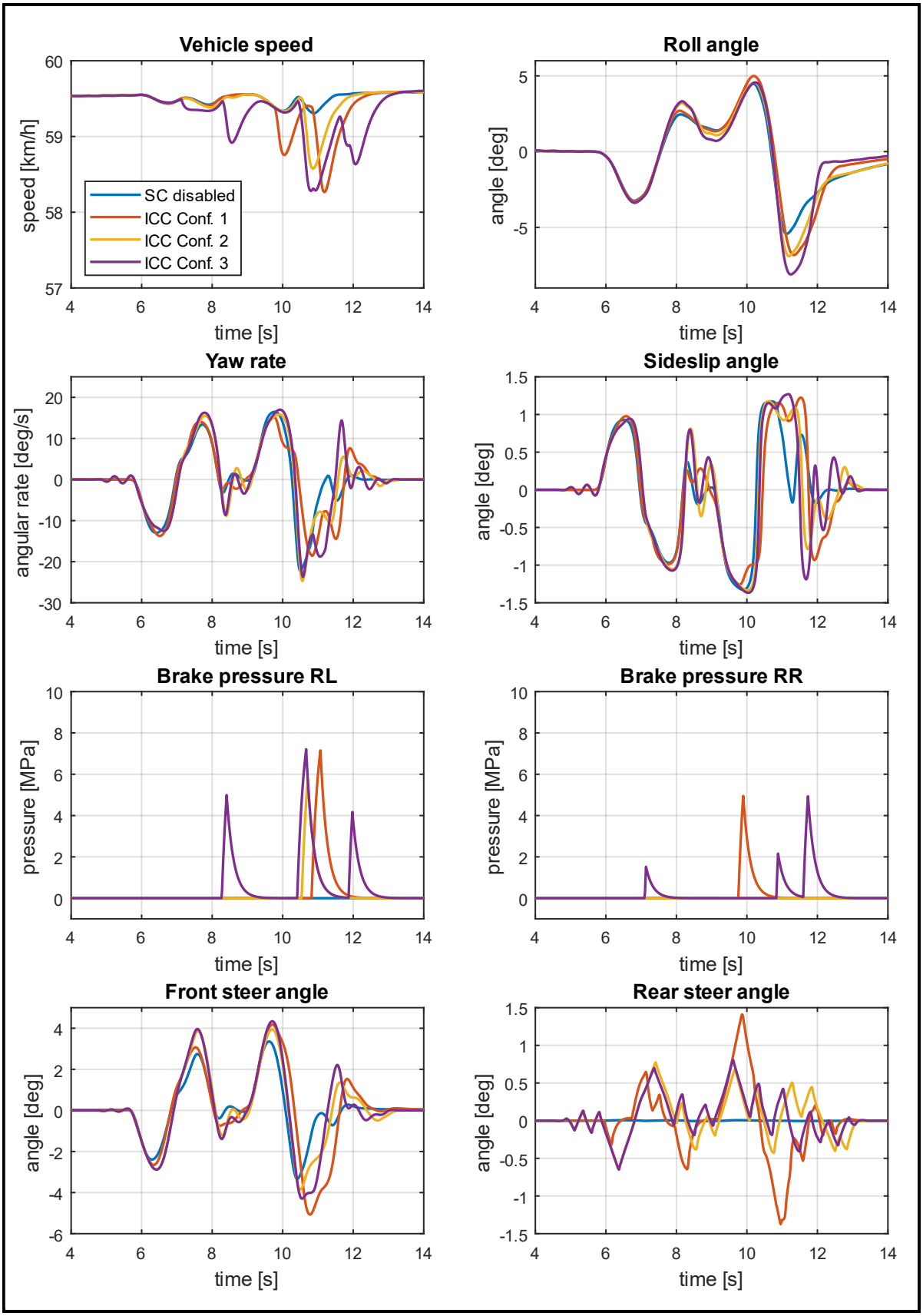

Figure 6-22: Vehicle states for the DLC on a smooth road with integrated SC systems

As the difference in entry and exit speeds of the DLC manoeuvre is also an indicator of system performance, Table 6-1 presents entry and exit speeds of the vehicle which are taken at the start of Section 1 and end of Section 5 respectively for each run. A smaller difference indicates better performance. The data shows that ICC Configuration 1 and 3 have the largest loss of vehicle speed of all integrated systems, and stand-alone RDB has a larger loss of speed than stand-alone ARS. This data also points to the potential of ICC Configuration 2 since it has zero loss of vehicle speed.

Table 6-1: DLC entry and exit speeds for systems on a smooth road

System	Entry speed [km/h]	Exit speed [km/h]
SC disabled	59.5	59.5
ARS, PPLE	59.5	59.5
ARS, KMRE	59.5	59.5
RDB, PPLE	59.5	57.7
RDB, KMRE	59.5	59.0
ICC Conf. 1	59.5	58.5
ICC Conf. 2	59.5	59.5
ICC Conf. 3	59.5	58.7

ICC Configuration 2 is further explored in Figure 6-23 which shows a run performed with a different integration rule value so that RDB activates when $|\alpha_r| \geq 2°$ instead of once $|\alpha_r| \geq 3°$. The integrated control system shows improved path following and the vehicle remains inside the boundaries while having a small change in vehicle speed, with a $59.5\ km/h$ entry and $59.4\ km/h$ exit speed.

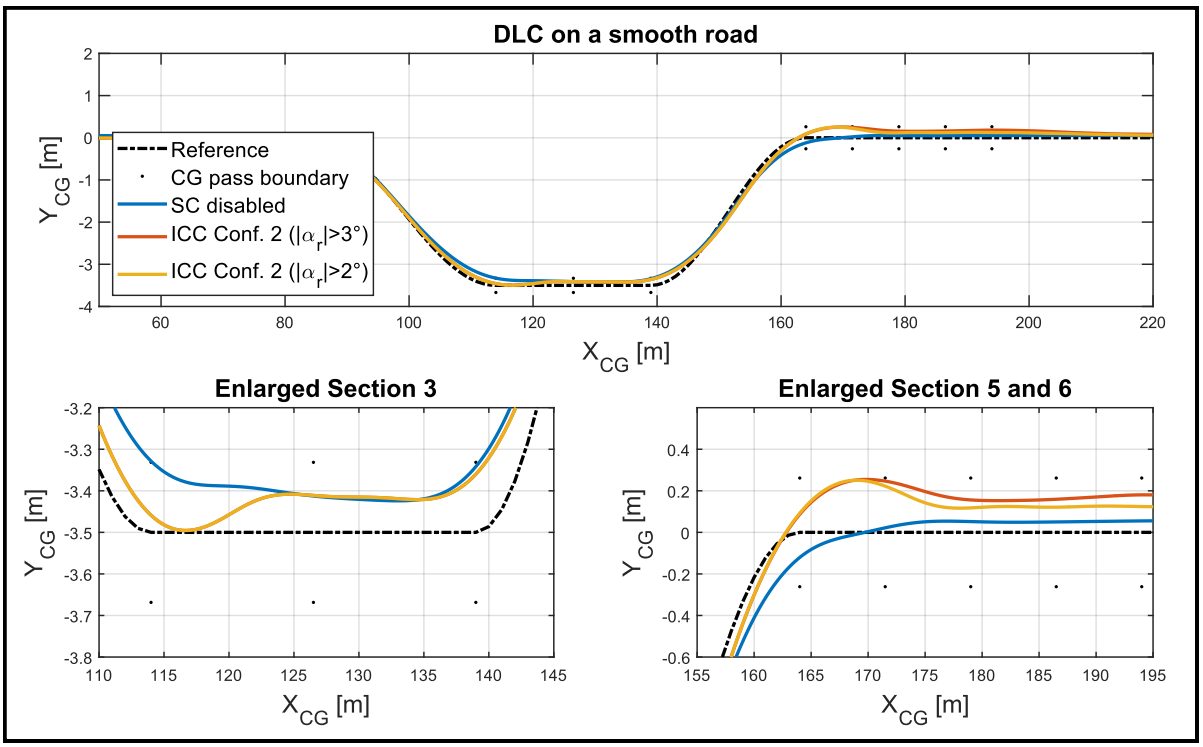

Figure 6-23: The DLC path on a smooth road showing the adapted ICC Configuration 2

Figure 6-24 shows vehicle states for systems including the adapted ICC Configuration 2 and indicates that both ICC Configuration 2 variations have similar peak absolute roll angles. The yaw rate and sideslip response of the integrated system seem to resemble that of the RDB system more with a lower integration rule value. It can be concluded that the KMRE reference model systems have the best closed-loop performance of the systems tested and the rear axle slip angle is an efficient tuning parameter that shapes the integrated system response towards either ARS or RDB behaviour.

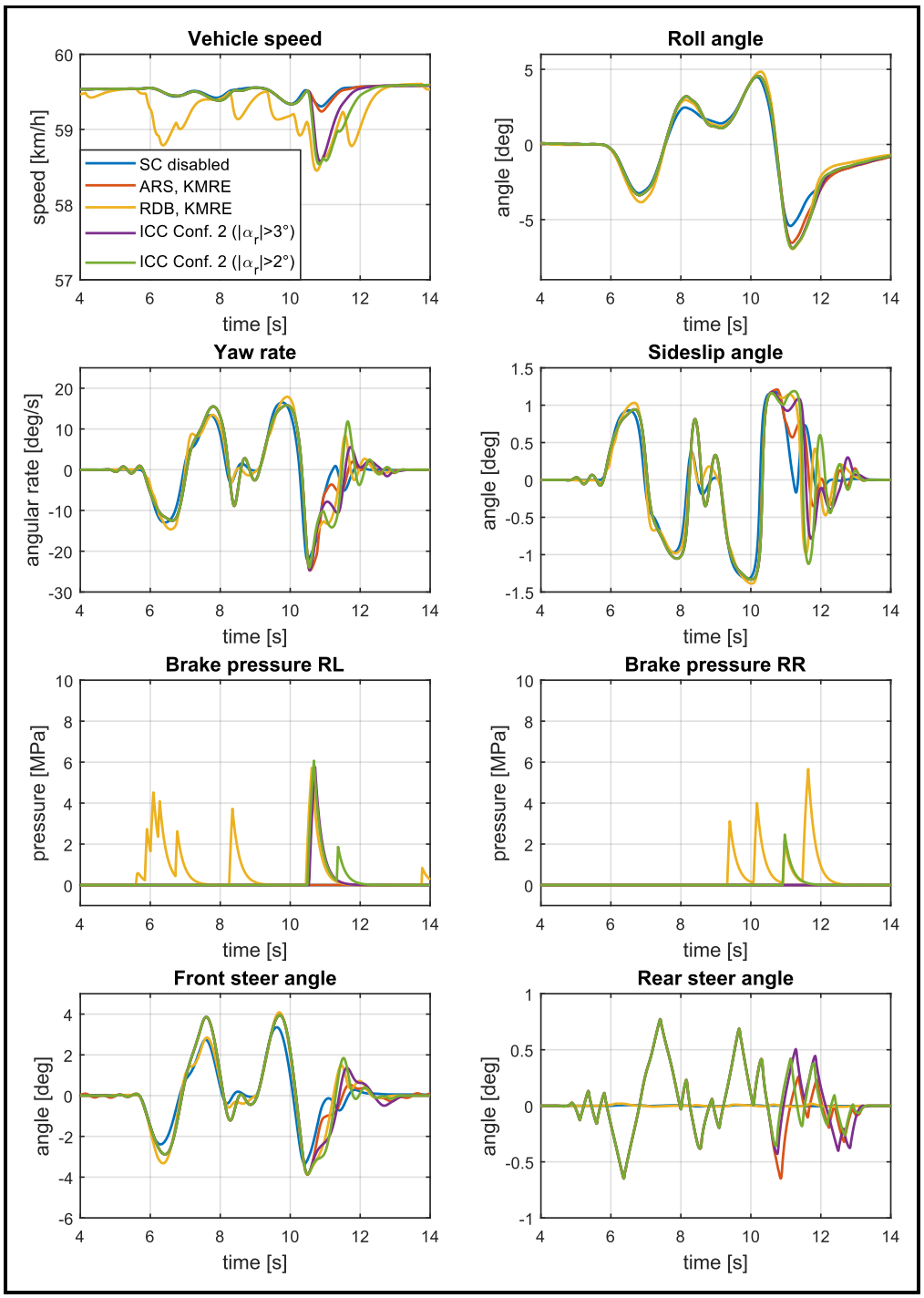

Figure 6-24: Vehicle states for the DLC on a smooth road with the adapted ICC Configuration 2

Figure 6-25 shows the same DLC manoeuvre done on a rough road with stand-alone SC systems. The displacement plot shows again that it is the ARS and RDB actuators with the KMRE SC reference model that are able to pass the test, while all other systems fail due to crossing the boundary. As for the smooth road, the RDB configuration better follows the desired path compared to ARS but takes longer to damp the yaw motion as the vehicle exits DLC Section 5. This test outcome also indicates, as for a smooth road, that sideslip-based control systems are likely not a good option for stability control on a high friction rough road if closed-loop responsiveness is the major concern. Figure 6-26 presents vehicle states during the manoeuvre which shows occurrence of LOC with a large peak absolute roll angle for the system using the RDB control strategy with the PPLE SC reference model. When reviewing the roll-angle results one should keep in mind that the relatively high roll angle peak of 10° does not cause roll-over of the vehicle, as established in Section 4.2.

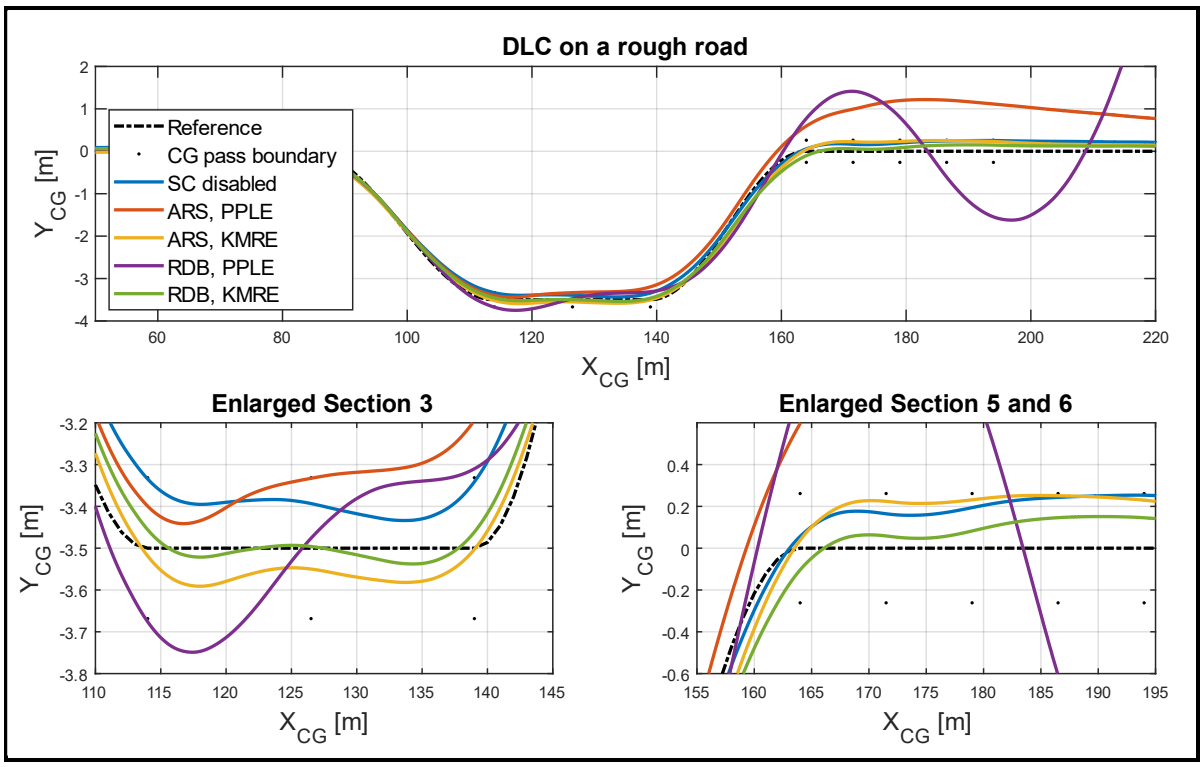

Figure 6-25: The DLC path on a rough road for the stand-alone SC systems

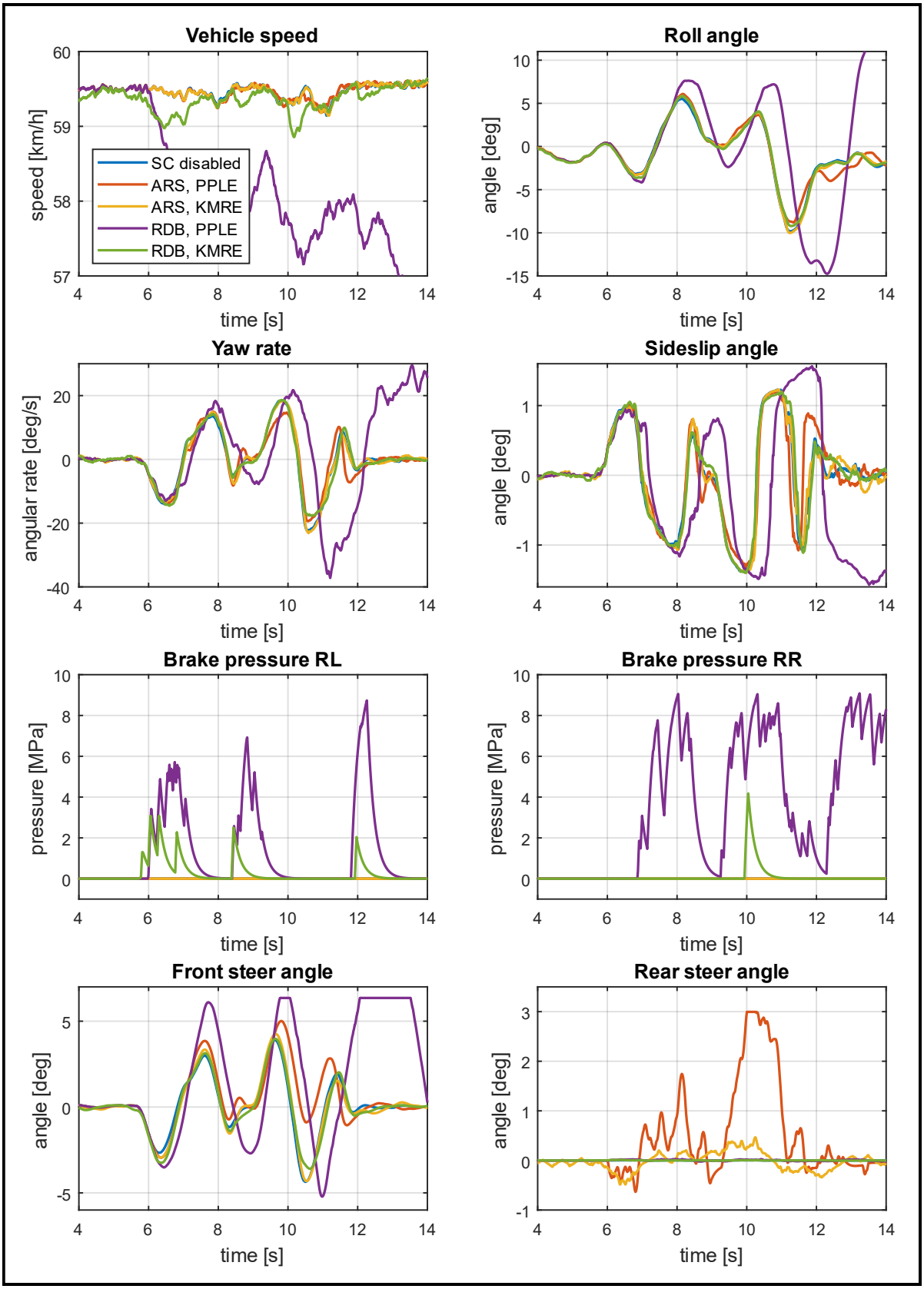

Figure 6-26: Vehicle states for a DLC on a rough road with stand-alone SC systems

Figure 6-27 shows displacement trajectories for a DLC manoeuvre performed with integrated stability systems on a rough road and Figure 6-28 shows vehicle states during the manoeuvre.

ICC Configuration 1 shows a notable improvement on stand-alone ARS and RDB using the PPLE SC reference model but nonetheless fails the test. ICC Configuration 2 passes the test, as well as ICC Configuration 3. Table 6-2 shows the course entry and exit speeds of which most brake-based systems show a large loss of speed, except for ICC Configuration 2 which has no loss of vehicle speed. ICC Configuration 3 has the largest loss of speed of the systems that passed the test.

Table 6-2: DLC entry and exit speeds for the rough road

System	Entry speed [km/h]	Exit speed [km/h]
SC disabled	59.5	59.6
ARS, PPLE	59.5	59.6
ARS, KMRE	59.5	59.6
RDB, PPLE	59.5	57.4
RDB, KMRE	59.4	59.3
ICC Conf. 1	59.5	58.7
ICC Conf. 2	59.5	59.5
ICC Conf. 3	59.5	58.9

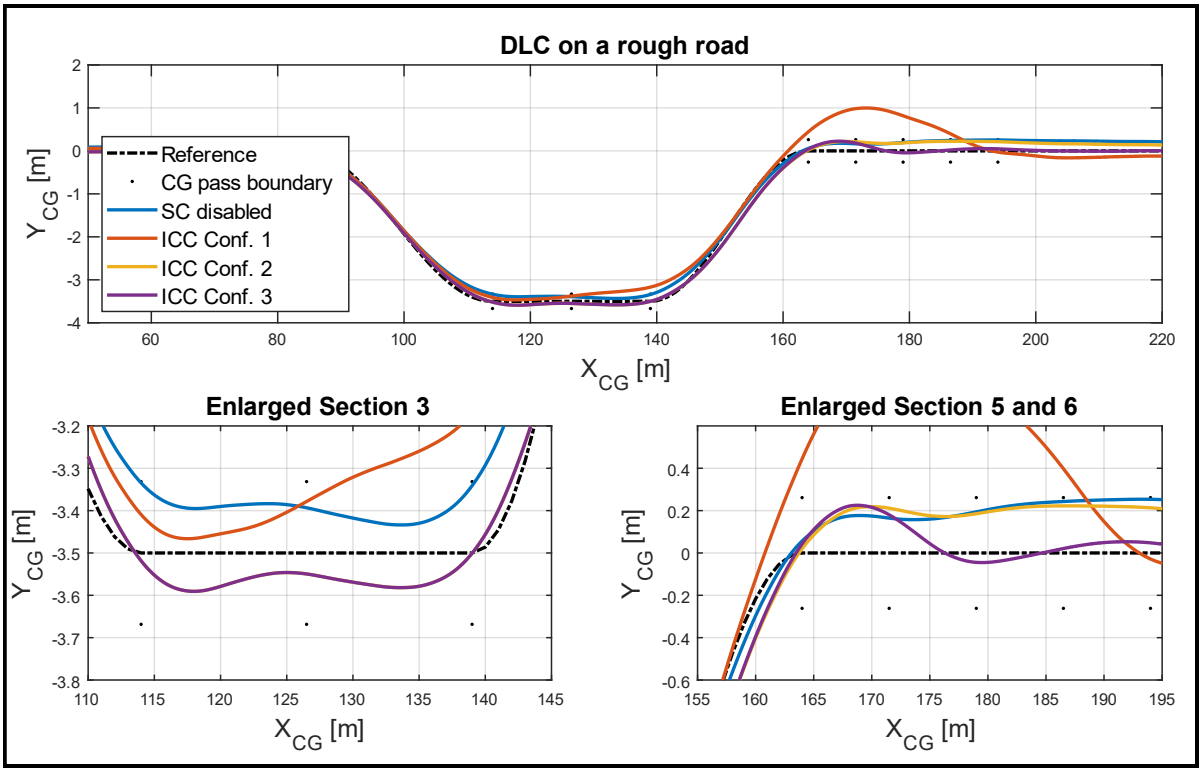

Figure 6-27: The DLC path on a rough road for the integrated SC systems

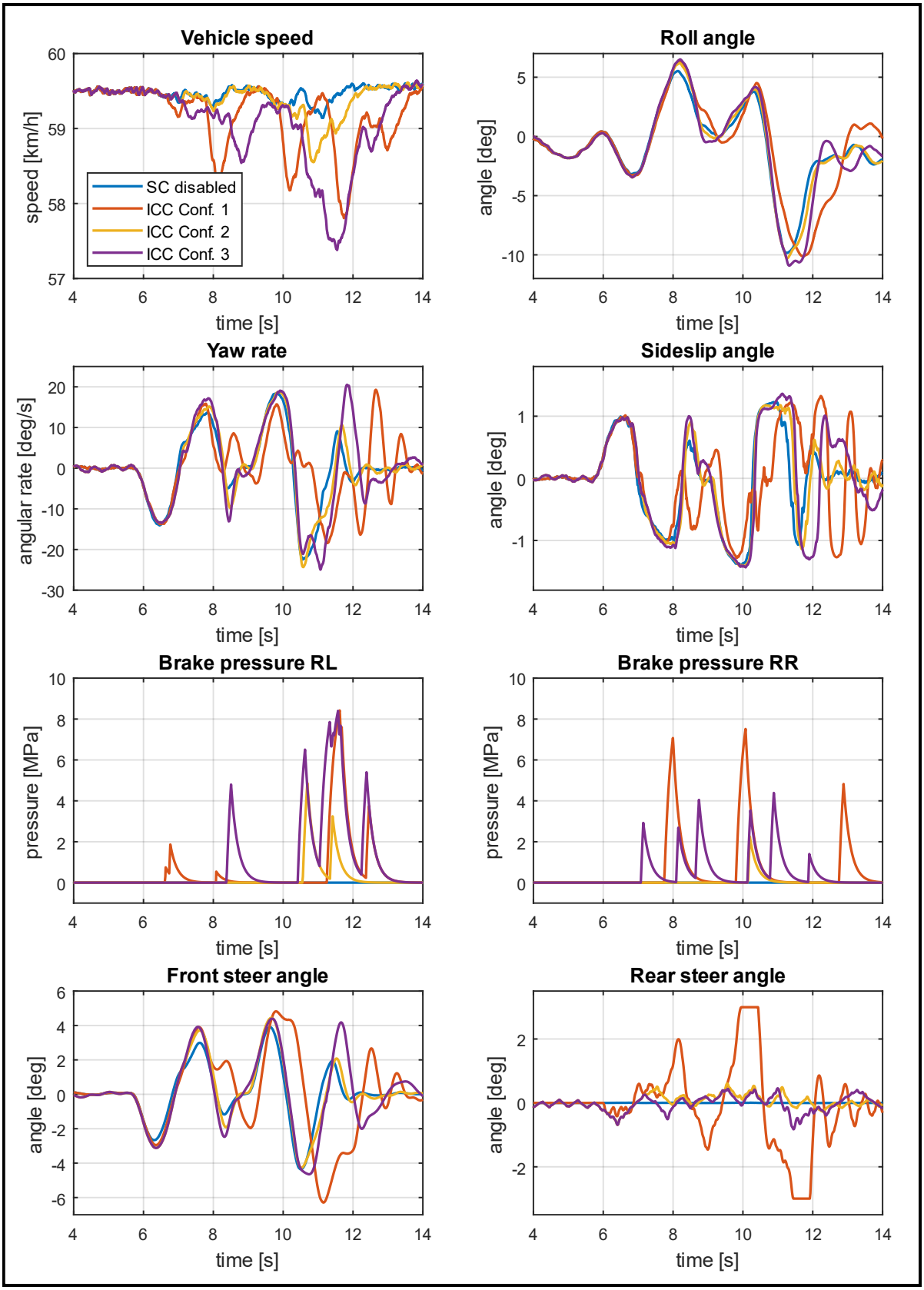

Figure 6-28: Vehicle states for a DLC on a rough road with integrated SC systems

In an attempt to see if tuning of the integration rule for ICC Configuration 2 may further improve system performance, Figure 6-29 shows the DLC displacement trajectory of the test

vehicle with an adapted ICC Configuration 2 where brake integration occurs when $|\alpha_r| \geq 2°$, as opposed to the original rule of $|\alpha_r| \geq 3°$. Figure 6-30 shows vehicle states during the manoeuvre. The trajectory plot indicates that the choice of $|\alpha_r| \geq 2°$ increases the overshoot in Section 5, which is undesirable. The adapted integration rule vehicle has an entry speed of $59.5\ km/h$ and an exit speed of $59.4\ km/h$, indicating the loss of vehicle speed is higher than for the original ($|\alpha_r| \geq 3°$) integration rule system. Nonetheless, the integration of systems improves on the undesirable responses of stand-alone stability systems and the integration rule can be tuned to shape system response.

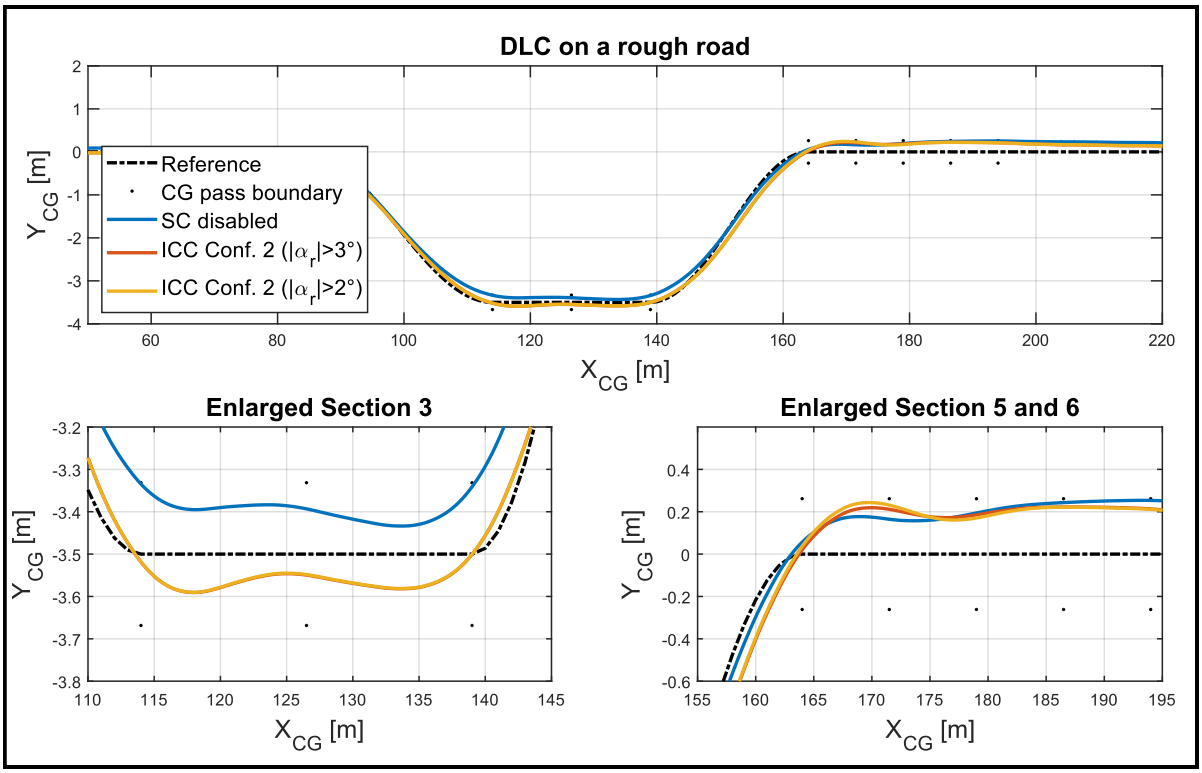

Figure 6-29: The DLC path on a rough road showing the adapted ICC Configuration 2

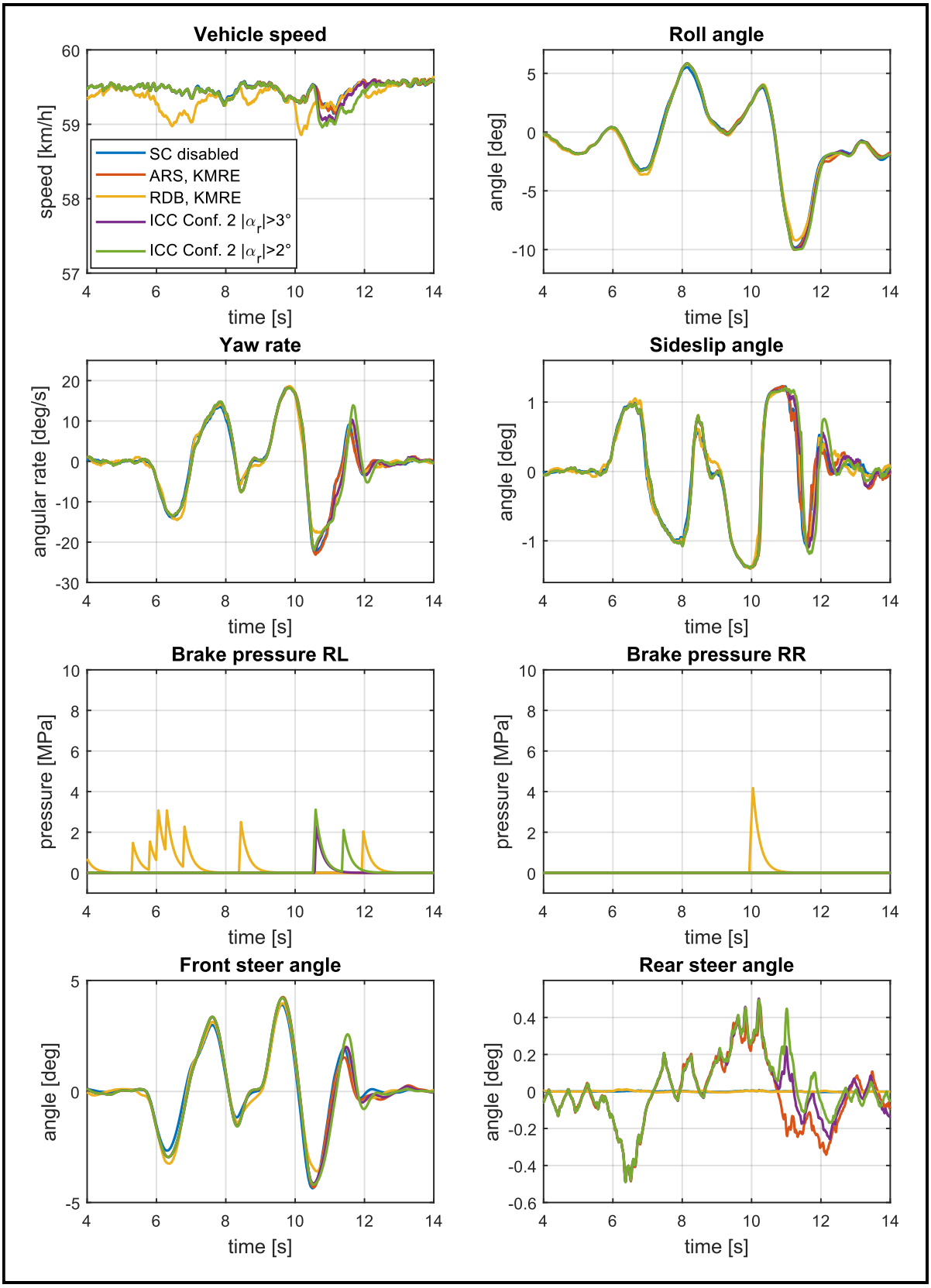

Figure 6-30: Vehicle states for the DLC on a rough road with the adapted ICC Configuration 2

Figure 6-31 shows the path following performance of smooth road tuned systems on a rough road, all with the KMRE SC reference model. The trajectories indicate that both the ARS and adapted ICC Configuration 2 systems have a large overshoot in Section 5. RDB is not shown here as it has the same gain for both smooth and rough roads. The poor ARS performance may be attributed to the different gains where the ARS on a smooth road is tuned for a gain of $k_{SMC} = 4000$ and for the rough road $k_{SMC} = 2000$. This large difference (50%) in gains is a cause for varying performance on different terrains since it is understood that if a gain moves past the optimal or lowest sum squared of the SMC sliding variable, the error value starts to increase again. This places the ARS system which is designed for smooth roads in a dangerous domain once on rough terrain. This highlights the danger of having a tuned system operate on a different terrain for which it is not tuned, stability in such an instance may be improved but is not guaranteed.

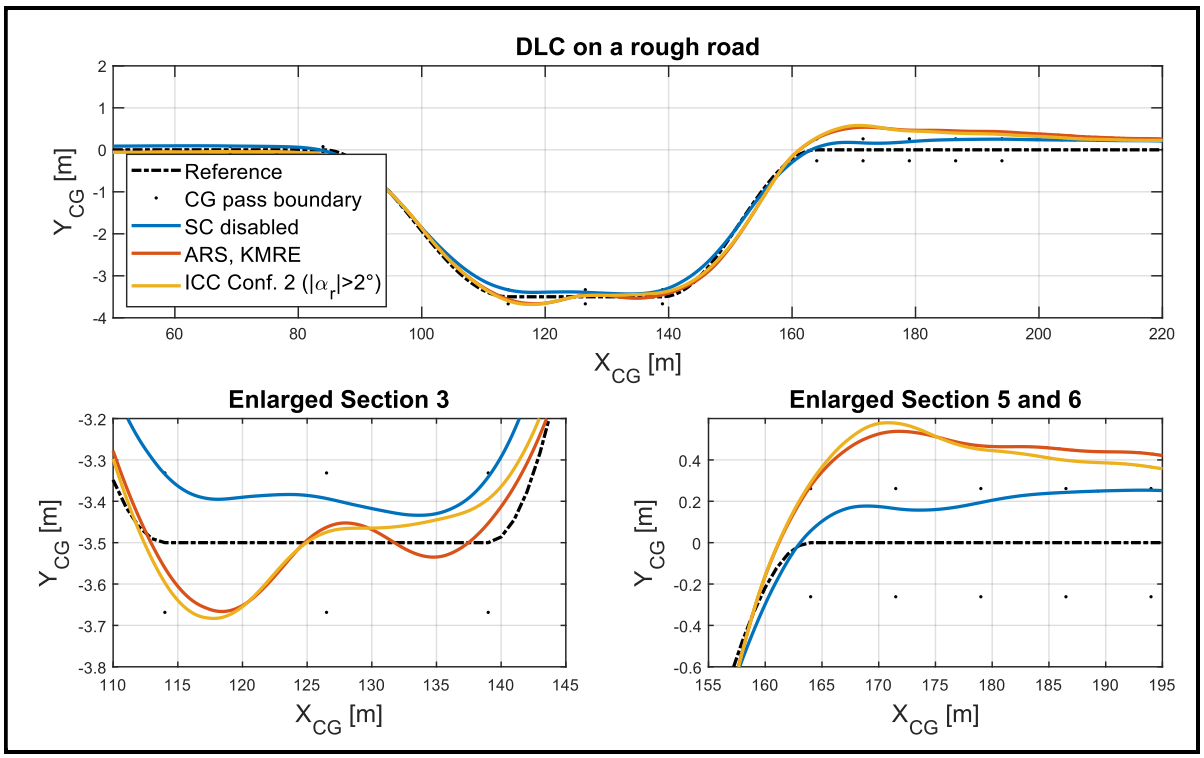

Figure 6-31: Path of smooth road tuned SC systems operating on a rough road

6.3 Chapter conclusion

This section concludes that SC systems with the PPLE SC reference model reduces the peak sideslip angle and peak yaw rate compared to the SC disabled (baseline) vehicle but offers little damping of those variables once a manoeuvre is complete. The inhibition of further development of sideslip angle and by the coupling mechanism, the yaw rate also has other effects such as a lower roll angle. These properties are desirable but negatively affect the path following ability of the vehicle and may leave the vehicle feeling unresponsive to the driver. This occurs on both a smooth and rough road and closed-loop testing proves the vehicle to be so unresponsive to further development of sideslip (and yaw rate) that the vehicle cannot effectively follow a DLC path. The PPLE SC reference model can ultimately not be recommended for stability control based on the behaviour observed for a closed-loop DLC.

The KMRE SC reference model is useful for allowing large yaw rate and sideslip angle peak development while being good at damping those responses once the manoeuvre is complete. This in turn improves the path following ability of the vehicle but leads to larger roll angles compared to the PPLE reference model. With this (KMRE) reference model, it was observed that RDB on both terrains could follow a DLC path better than ARS.

The best integrated system was found to be ICC Configuration 2 which employs the KMRE SC reference model and actives RDB once the rear axle slip angle reaches a set threshold. It was also the brake-based SC system with the lowest loss of vehicle speed on both a smooth and rough road. The results indicate that the rear steering angle at which integration occurs is an efficient and necessary tuning parameter to shape integrated SC response to be more similar to either ARS or RDB stand-alone SC responses. The advantage of such an integration rule is that a single tuneable parameter determines how the different SC systems are integrated.

It was determined that a SC system tuned for a specific terrain is not guaranteed to have the same performance on a different terrain, especially if the difference in their optimal SMC gains are large. As increasing SMC gain tends to show decreasing sum of error or sliding variable over a manoeuvre, at some point the gain reaches an apparent maximum and the error grows again with increasing gain. If a system SMC gain is then high on one terrain and the vehicle is placed on a different terrain without changing the gain to suit that terrain, the control system may be in a domain where it operates with a suboptimal error. Such a SC system may have worse performance than a SC disabled vehicle. A possible solution in this case is to use the lowest SMC gain of all terrains but then the control system would have suboptimal performance on all but one terrain. Further to this, it may also be reasonable to assume that an integration rule that was tuned for a set of operating conditions (road classification and vehicle properties) will not have the same performance under different conditions.

CHAPTER SEVEN
CONCLUSION AND RECOMMENDATION

The aim of this study was to investigate whether there is an improvement achievable in the lateral stability of an off-road vehicle by integrated control of chassis control systems and how the performance of such systems compares for smooth and rough roads. This was achieved by posing the following research questions:

a. What are objective indicators of lateral stability?
b. What are the causes of lateral instability for on-road and off-road conditions?
c. Which chassis control systems can be coordinated to improve lateral stability for on-road and off-road conditions?
d. How does coordinated chassis control system performance compare to stand-alone systems for lateral stability on on-road and off-road conditions?
e. How does the performance of chassis control systems for lateral stability differ for on-road versus off-road conditions, is there a universal configuration?

For (a), a literature review identified three indicators of lateral stability namely the understeer gradient, phase plane location and kinematic model reference error. The understeer gradient is a function of vehicle build as it is determined by vehicle physical properties (lateral load transfer, cornering stiffness, weight distribution, etc.) and is a steady-state indicator. The phase plane location approach specifies that a vehicle is stable if the sideslip angle and rate are within a set boundary on the plane. It is a real-time indicator of lateral stability. Use of the phase plane may be more effective on smooth terrain than on rough terrain since the rough road excitations cause rapid changes in sideslip angle and rate that may place the vehicle in and out of the bounded region at a high frequency. The kinematic model reference error is a real-time indicator of lateral stability that compares current vehicle state against a kinematic model that is based on steady-state vehicle behaviour.

(b) A literature review identified the cause of lateral instability to be factors that reduce the tyre's lateral force generating capability. Such factors are high vehicle sideslip angle and yaw rate, lateral load transfer (regardless of terrain), while tyre normal force fluctuations also have this effect but is specific to rough terrain.

(c) A plethora of chassis control systems may be employed to improve lateral stability, by either directly controlling for sideslip angle and yaw rate, or by mitigating other factors that lead to reduced tyre lateral force generating capability. Controllers such as differential braking may generate a restoring moment to control sideslip angle and yaw rate according to a reference model and the same can be achieved with active steering.

The actuators chosen for this study were rear differential braking (RDB) and active rear steering (ARS) based on availability of hardware and scope of study. Two stability control (SC) reference model options were investigated, namely the phase plane location error (PPLE) and the kinematic model reference error (KMRE). The PPLE reference model activates once the vehicle is outside a bounded region on the $\beta - \dot{\beta}$ phase plane and attempts to limit development of vehicle states beyond the boundary. The KMRE reference model relates the front steering angle with an expected yaw rate and sideslip angle. Open-loop tests, by way of a sine with dwell manoeuvre at $60\ km/h$, indicated promising results for SC with the PPLE reference model as it had good lateral displacement and low peak roll angles but with poor yaw rate damping, while those with the KMRE reference model had good yaw rate damping but with higher peak roll angles and generally lower lateral displacement. Closed-loop testing, by way of a double lane change (DLC) manoeuvre at $60\ km/h$, showed that SC with the PPLE reference model could easily swerve to the opposite lane but then vehicle responsiveness would be limited by the controller so that the driver model cannot steer the vehicle on the path. For this reason, the PPLE reference model is not recommended as a reference model on high friction smooth or rough roads as it limits development of sideslip angle and rate and by the coupling mechanism the yaw rate. Stability control with the KMRE reference model works both ways in that it will not only limit but also increase yaw rate or sideslip angle based on the reference. This allows for the development of large yaw rate peaks when the front steering angle is large, while the response is damped once the angle is reduced. This makes for a control system that can both follow a path very well but also damp yaw rate and sideslip once a manoeuvre is complete. The KMRE SC reference model is recommended for both smooth and rough roads with a high friction coefficient.

(d) Considering the performance of stand-alone SCs with the KMRE reference model, it was found that RDB systems have the best path following ability for a DLC. ARS SCs were found to have worse path following ability than RDB systems, but with better yaw rate damping. This may be because ARS has a larger moment arm than RDB. Other trends were also observed such as that all brake-based systems lead to a large loss of vehicle speed. This was observed for both terrains. Of the three decision layer configurations listed in Section 5.3.1, Configuration 2 which uses the KMRE reference model and activates RDB based on rear tyre slip angle was shown to be the best configuration. The rear axle slip angle as integration rule is an effective tuning parameter, that can shape integrated system response to exhibit more or less RDB or ARS behaviour. When suitably chosen, the stability-controlled vehicle would have the good path following of RDB with the good yaw rate damping and low loss of vehicle speed seen for ARS systems. The integrated system consequently creates a best-of-both mix of RDB and ARS with proper tuning of the integration rule.

(e) Due to limited actuator bandwidth, there is an optimal sliding mode control (SMC) gain for each control strategy. As the gain is increased, the sum of squared sliding variable or error (taken over the duration of a manoeuvre) would decrease and then at some point increase again. This optimal gain is dependent on the control strategy, road classification and SMC sliding variable zeta weighting. RDB with the KMRE SC reference model showed no difference in SMC gain or sliding variable zeta weighting for different terrains which meant that the RDB controller tuned for smooth roads also performed well on rough roads, and vice versa. This was not the case for ARS with the KMRE SC reference model, which had a large difference in SMC gain and zeta weighting depending on terrain and was unstable on a terrain for which it was not tuned. It can be concluded that a universal SMC gain and sliding variable weighting for a control strategy does not exist, however by settling for the lowest SMC gain of all terrains, the control system may not perform optimally on all terrains, but at least be robust. Zeta weighting does not appear to be

such a big performance influencer as SMC gain and so it would be possible to select either 0, 0.5 or 1 as a universal weighting. This may be due to the high surface friction of the roads used.

Future work should focus on:

1. Experimental validation of results which was not possible for this study due to the COVID-19 pandemic and financial constraints.
2. Creating a SMC gain schedule for a larger range of operating conditions so that the controllers may always use their optimal settings for different speeds and terrains.
3. Developing or including existing means of accurately estimating the ISO8608:2016 road classification while driving.
4. Including active or semi-active suspension control in the systems integration.

CHAPTER EIGHT
REFERENCES

Ackermann, J., Bünte, T. & Odenthal, D., 1999. *Advantages of active steering for vehicle dynamics control.* Vienna, 32nd International Symposium on Automotive Technology and Automation.

Bakker, E., Pacejka, H. B. & Lidner, L., 1989. A new tire model with an application in vehicle dynamics studies. *SAE Technical Paper,* Issue 890087, pp. 101 - 113.

Bardawil, C., Talj, R., Francis, C., Charara, A. & Doumiati, M., 2014. Integrated vehicle lateral stability control with different coordination strategies between active steering and differential braking. *17th International IEEE Conference on Intelligent Transportation Systems (ITSC),* pp. 314-319.

Becker, C. M., 2008. *Profiling of rough terrain* [Online]. Available at: https://repository.up.ac.za/handle/2263/36661 [Accessed 5 May 2021].

Blundell, M. & Harty, D., 2015. *The Multibody systems approach to vehicle dynamics.* Oxford: Elsevier Ltd..

Botes, W., Botha, T. & Els, S. P., 2020. Sideslip Angle Estimation Using a Kinematics Based Unscented Kalman Filter and Digital Image Correlation. *Advances in Dynamics of Vehicles on Roads and Tracks,* pp. 1635 - 1642.

Botha, T. R., 2011. *High speed autonomous off-road vehicle steering* [Online]. Available at: https://repository.up.ac.za/handle/2263/29665 [Accessed 12 June 2020].

Botha, T. R. & Els, P. S., 2015. Digital image correlation techniques for measuring tyre-road interface parameters: Part 1 – Side-slip angle measurement on rough terrain. *Journal of Terramechanics,* Volume 61, pp. 87-100.

Burden, R. L., Faires, D. J. & Burden, A. M., 2014. *Numerical Analysis.* 10th ed. Boston: Cengage.

Burton, D., Delaney, A., Newstead, S., Logan, D. & Fildes, B., 2004. *Effectiveness of ABS and vehicle stability control systems,* Melbourne: Royal Automobile club of Victoria (RACV).

Canale, M. & Fagiano, L., 2010. Comparing rear wheel steering and rear active differential approaches to vehicle yaw control. *Vehicle System Dynamics,* 48(5), pp. 529-546.

Chen, K., Pei, X. & Guo, X., 2016 (1). Longitudinal/Lateral Stability Analysis of Vehicle Motion in the Nonlinear Region. *Mathematical Problems in Engineering,* Volume 16, pp. 5-15.

Chen, W., Xiao, H., Wang, Q., Zhao, L. & Zhu, M., 2016 (2). *Integrated vehicle dynamics and control.* 1 ed. Capitol Singapore: John Wiley & Sons.

Chindamo, D., Lenzo, B. & Gadola, M., 2018. On the Vehicle Sideslip Angle Estimation: A Literature Review of Methods, Models, and Innovations. *Applied sciences,* 8(355), pp. 2-3.

Cronjé, P. H., 2008. *Improving off-road vehicle handling using an active anti-roll bar* [Online]. Available at: https://repository.up.ac.za/handle/2263/29832 [Accessed 1 April 2021].

Els, P. S., 2006. *The ride comfort vs. handling compromise for off-road vehicles* [Online]. Available at: https://repository.up.ac.za/handle/2263/43431 [Accessed 13 March 2020].

Euro NCAP, 2011. *The dynamic test of car electronic stablity control (ESC) systems protocol* [Online]. Available at: https://cdn.euroncap.com/media/1444/euro-ncap-esc-testing-protocol-v12.pdf [Accessed 22 April 2021].

European Commission, 2018. *Advanced driver assistance systems* [Online]. Available at: https://road-safety.transport.ec.europa.eu/system/files/2021-07/ersosynthesis2018-adas-summary.pdf [Accessed 5 February 2020].

European Patent Office, 2016. *Anton van Zanten* [Online]. Available at: https://www.epo.org/news-events/events/european-inventor/finalists/2016/vanzanten.html [Accessed 13 June 2020].

Forkenbrock, G. J. & Boyd, P. L., 2008. *Light vehicle ESC performance test development,* Washington: NHTSA.

Fu, C., Hoseinnezhad, R., Bab-Hadiashar, A. & Jazar, R., 2015. *International Journal of Vehicle Autonomous Systems,* Volume 13.

German Insurance Association, 2014. *Accident statistics and the potential of driver assistance systems* [Online]. Available at: https://m.udv.de/download/file/fid/8533 [Accessed 10 March 2020].

Gillespie, T. D., 1992. *Fundamentals of Vehicle Dynamics.* Pennsylvania: Society of Automotive Engineers.

Global NCAP, 2014. *Electronic Stability Control (ESC) Must Become Standard Fit Worldwide.* [Online]. Available at: https://www.globalncap.org/news/electronic-stability-control-esc-must-become-standard-fit-worldwide [Accessed 22 January 2023].

Gordon, T., Howell, M. & Felipe , B., 2003. Integrated Control Methodologies for Road Vehicles. *Vehicle System Dynamics,* 40(1-3), pp. 157-190.

Gough, V. E., 1963. Tyres and air suspension. *Advances in Automobile Engineering,* p. 59.

Hamersma, H. A., 2017. *ABS braking on rough terrain* [Online]. Available at: https://repository.up.ac.za/handle/2263/61607 [Accessed 2 February 2020].

Hamersma, H. A., Botha, T. R. & Els, S. P., 2014. The dynamic rolling radius of a pneumatic tyre on hard terrains. *International Journal of Vehicle Systems Modelling and Testing,* 11(3), pp. 234-251.

Hamersma, H. & Els, P. S., 2021. Vehicle suspension force and road profile prediction on undulating roads. *Vehicle System Dynamics,* 59(10), pp. 10-16.

Hu, J., Flannagan, C., Bao, S., McCoy, R., Siasoco, K. & Barbat, S., 2015. Integration of Active and Passive Safety Technologies - A Method to Study and Estimate Field Capability. *Stapp Car Crash Journal,* Volume 59.

International Organization for Standardization, 2016. *ISO 8608:1995 Mechanical vibration — Road surface profiles — Reporting of measured data* [Online]. Available at: https://www.iso.org/standard/71202.html [Accessed 2 June 2020].

International Organization for Standardization, 2018. *ISO 3888-1:2018 Passenger cars - Test track for a severe lane-change manoeuvre - Part 1: Double lane-change* [Online]. Available at: https://www.iso.org/standard/67973.html [Accessed 11 June 2020].

Joa, E. & Sohn, K., 2018. Integrated chassis control for vehicle stabilty under various road friction conditions. *SAE international,* Issue 0552, pp. 1 - 10.

Khachane, D. & Shrivastav, A., 2016. Antilock Braking System and Its Advancement. *International Research Journal of Engineering and Technology (IRJET),* 3(5), pp. 2221 - 2225.

Kyriakidis, M., van de Weijer, C., van Arem, B. & Happee, R., 2015. *The deployment of Advanced Driver Assistance Systems in Europe.* Boreaux, 22nd ITS World Congress.

Lenzo, B. & De Castro, R., 2019. Vehicle Sideslip Estimation for Four-Wheel-Steering Vehicles Using a Particle Filter. *The IAVSD International Symposium on Dynamics of Vehicles on Roads and Tracks,* pp. 1624-1634.

Levant, A., 1993. Sliding order and sliding accuracy in sliding mode control. *International Journal of Control,* 58(6), pp. 1247-1263.

Levant, A., 1998. Robust exact differentiation via sliding mode technique. *Automatica,* 34(3), pp. 379-384.

Li, B. & Fu, Z.-J., 2016. Coordinated control of active steering and active roll control systems for enhanced vehicle lateral dynamics. *International Journal of Vehicle Performance,* 2(4), pp. 418 - 434.

Lippmann, S. A. & Nanny, J. D., 1967. A quantitative analysis of the enveloping forces of passenger car tires. *SAE,* Issue 670174, pp. 1-10.

Mokhiamar, O. & Abe, M., 2006. How the four wheels should share forces in an optimum cooperative chassis control. *Control Engineering Practice,* Volume 14, pp. 295-304.

MSC Software, 2021. *Adams* [Online]. Available at: https://www.mscsoftware.com/product/adams [Accessed 16 June 2021].

MSC Software, 2021. *Adams/Tire Documentation* [Online]. Available at: https://help.mscsoftware.com/bundle/Adams_2021.3_Adams_Tire_User_Guide/resource/Adams_2021.3_Adams_Tire_User_Guide.pdf [Accessed 25 March 2020].

National Highway Traffic Safety Administration, 2011. *Estimating Lives Saved Annually by Electronic Stability Control* [Online]. Available at: https://crashstats.nhtsa.dot.gov/Api/Public/ViewPublication/811545 [Accessed 5 December 2019].

National Highway Traffic Safety Administration, 2017. *Crashes by First Harmful Event, Manner of Collision, and Crash Severity* [Online]. Available at: https://cdan.nhtsa.gov/tsftables/tsfar.htm [Accessed 2 March 2020].

Pacejka, H. B., 2006. *Tyre and vehicle dynamics.* 2 ed. Rotterdam: Butterworth-Heinemann.

Papelis, Y. E., Watson, G. S. & Brown, T. L., 2010. An empirical study of the effectiveness of electronic stability control system in reducing loss of vehicle control. *Accident Analysis and Prevention,* Volume 42, pp. 929-934.

Peenze, A. J., 2020. *Model predictive suspension control on off-road vehicles* [Online]. Available at: https://repository.up.ac.za/handle/2263/79302 [Accessed 17 August 2021].

Penny, W. C. W., 2015. *Anti-lock braking system performance on rough terrain* [Online]. Available at: https://repository.up.ac.za/handle/2263/56099 [Accessed 5 February 2020].

Penny, W. & Els, S., 2016. The test and simulation of ABS on rough, non-deformable terrains. *Journal of Terramechanics,* Volume 67, pp. 1-10.

Poovendran, K., 2018. *Integrated brake based torque vectoring control of vehicle yaw rate and side-slip angle* [Online]. Available at: https://repository.up.ac.za/handle/2263/72669 [Accessed 18 May 2020].

Rajamani, R., 2006. *Vehicle dynamics and control.* Minnesota: Springer.

Reif, I. K., 2014. *Brakes, Brake Control and Driver Assistance Systems.* 1 ed. Friedrichshafen: Springer.

Reinelt, W., Klier, W., Lundquist, C., Reimann, G., Schuster, W. & Großheim, R., 2004. Active front steering for passenger cars: System modeling and functions. *IFAC Advances in Automotive Control,* pp. 679 - 684.

Robert Bosch GmbH, n.d. *Start of developing Bosch's anti-lock braking system ABS* [Online]. Available at: https://www.bosch.com/stories/beginnings-of-abs/ [Accessed 15 June 2020].

Savitski, D., Ivanov, V., Augsburg, K., Dhaens, M., Els, S. & Sandu, C., 2015. *State-of-the-art and future developments in integrated chassis control for ground vehicles.* Rome, International Society for Terrain-Vehicle Systems.

Seeber, R. & Horn, M., 2017. Stability proof for a well-established super-twisting parameter setting. *Automatica,* Volume 84, pp. 241-243.

SKF, 2018. *Electric cylinders CASM-32/40/63* [Online]. Available at: https://www.skf.com/skf/campaign/IDemarketing/casm/it/media/CASM-brochure_complete.pdf [Accessed 11 November 2020].

Slotine, J.-J. E. & Li, W., 1991. *Applied nonlinear control.* 1st ed. New Jersey: Prentice Hall.

Smakman, H., 2000. *Functional integration of slip control with active suspension for improved lateral vehicle dynamics,* Delft: TUDelft.

Strauss, R., 2016. *Brake based integrated rollover prevention and yaw control for an off-road vehicle* [Online]. Available at: https://repository.up.ac.za/handle/2263/61339 [Accessed 17 September 2020].

Transport Canada, 2017. *Techanical Standards Document: No. 126,* Ottawa: Transport Canada.

Thoresson, M. J., 2007. *Efficient Gradient-Based Optimisation of Suspension Characteristics for an Off-Road Vehicle* [Online]. Available at: https://repository.up.ac.za/handle/2263/26984 [Accessed 17 December 2021].

Utkin, V. I., 1992. *Sliding modes in control and optimization.* Heidelberg: Springer-Verlag.

Uys, B. P., 2007. *Rollover of off-road vehicle* [Online]. Available at: https://repository.up.ac.za/handle/2263/25210 [Accessed 16 August 2020].

Wang, S., Zhao, X. & Yu, Q., 2019. Vehicle Stability Control Strategy Based on Recognition of Driver Turning Intention for Dual-Motor Drive Electric Vehicle. *Mathematical Problems in Engineering,* Volume 2020.

World Health Organization, 2018. *Global status report on road safety 2018: summary* [Online]. Available at: https://www.who.int/publications-detail-redirect/9789241565684 [Accessed 19 January 2020].

Xie, X., Jin, L., Jiang, Y. & Guo, B., 2018. Integrated dynamics control system with ESC and RAS for a distributed electric vehicle. *IEEE Access,* 6(2018), pp. 18694 - 18704.

Yim, S., 2020. Comparison among Active Front, Front Independent, 4-Wheel and 4-Wheel Independent Steering Systems for Vehicle Stability Control. *Electronics,* 9(798), pp. 1-13.

Zheng, S., Tang, H., Han, Z. & Zhang, Y., 2006. Controller design for vehicle stability enhancement. *Control Engineering Practice,* Volume 14, pp. 1413 - 1421.

Zhu, B., Chen, Y. & Zhao, J., 2014. Integrated Chassis Control of Active Front Steering and Yaw Stability Control Based on Improved Inverse Nyquist Array Method. *The Scientific World Journal,* Volume 2014, pp. 1-14.

APPENDIX A
COMMERCIAL ABS ALGORITHM

Invention of ABS is accredited to Bosch who implemented the first production-ready ABS in 1978 (Robert Bosch GmbH, n.d.) whose solution has since become known as the Bosch ABS algorithm. Commercial ABS works by taking wheel speed measurements that are passed to an electronic control unit (ECU). The ECU then determines whether the brake line pressure of each wheel should be increased, decreased or sustained. This is commonly referred to as the pump, dump and hold cycles of ABS respectively, that is realized by the ECU interfacing with a hydraulic modulator.

The requirements placed on ABS focusses on the dynamic braking response of the vehicle as listed by Reif (2014):

1. ABS should ensure that the vehicle retains its handling stability and steerability on all types of road surfaces; from dry roads to black ice.
2. The system should utilize the available traction between the tires and the road to the maximum degree, giving handling stability and steerability precedence over minimizing braking distance.

ABS assumes a theoretical curve of friction coefficient versus brake slip, as illustrated by the curve in Figure A-1 where region a is referred to as the stable region having a linear response and region b the unstable zone. Figure A-2 shows the relationship between the brake torque and the tyre-road interface torque during initial braking with a stable linear response and unstable region also corresponding to the regions a and b of Figure A-1. In the stable region, wheel deceleration is limited to a small rate whereas in the unstable zone it increases at a rapid rate. It is this mechanism of rapid deceleration that ABS exploits to detect and maintain peak friction.

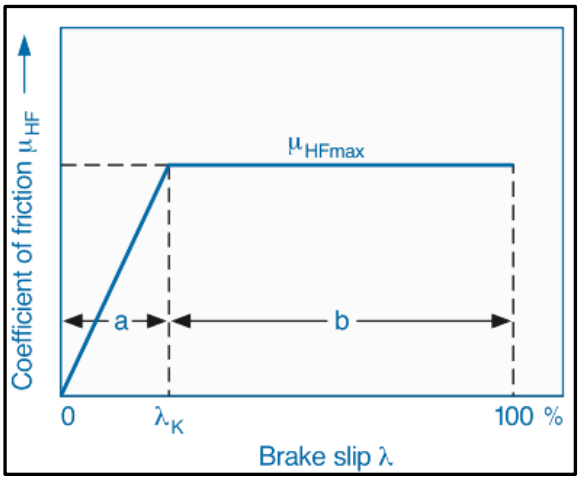

Figure A-1: A plot of the friction coefficient vs. brake slip used by the ABS algorithm (Reif, 2014)

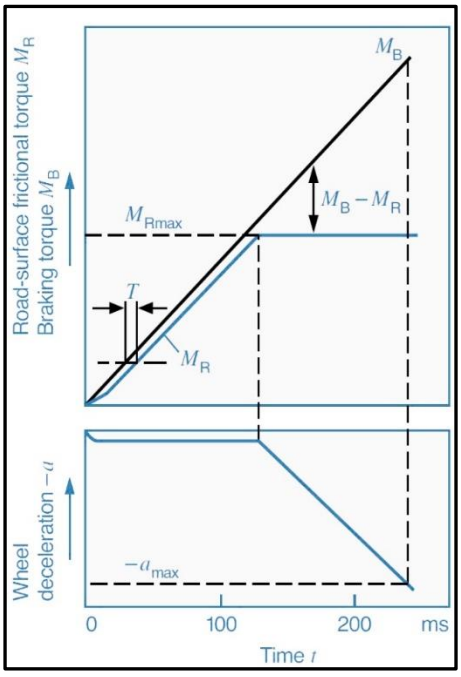

Figure A-2: Wheel deceleration torque vs. road-surface friction torque (Reif, 2014)

As tyre longitudinal slip is not directly measurable, the ECU approximates its value from the vehicle reference speed and the wheel speed measurement with Equation A-1.

$$\kappa = -\frac{v_x - \omega r_e}{v_x} \tag{A-1}$$

Figure A-3 shows the ABS sequence that results in the brake pressure modulation as shown in Figure A-4. Six parameters govern the algorithm which were determined to be as in Table A-1 for the experimental vehicle. Phase 1 is the initial braking phase that shows an increase in brake pressure, causing the rate of wheel deceleration to rise until it exceeds the threshold a_{min}. When the threshold is reached, the hydraulic modulator is set to the "maintain pressure" setting and phase 2 is entered. For phase 2, pressure is maintained and not reduced since the wheel might still be in the stable zone of friction coefficient vs. slip shown in Figure A-1 with potential for reducing braking distance. Phase 3 begins if the braking wheel slip is greater than the slip switching threshold ($-\lambda_{max}$) and the hydraulic modulator is set to the "reduce pressure" setting so long as the wheel deceleration exceeds the a_{min} threshold. Phase 3 transitions to phase 4 once the wheel deceleration drops below this threshold and a pressure maintenance phase follows. During phase 4, the wheel acceleration increases and triggers phase 5 if the angular acceleration is less than A or phase 4 has been maintained for longer than t_{hold}. Brake pressure increases as long as the wheel acceleration remains above A. In phase 6, the brake pressure remains constant while the wheel acceleration is above a_{max} . Phase 7 begins when the wheel acceleration drops below a_{max} which is the stable zone for the friction coefficient vs. slip and is slightly under braked. Brake pressure is increased in stages until the wheel deceleration passes the a_{min} threshold. At the start of phase 8, brake pressure is reduced until wheel deceleration is less than the a_{min} threshold or the slip above the switching threshold ($-\lambda_{max}$).

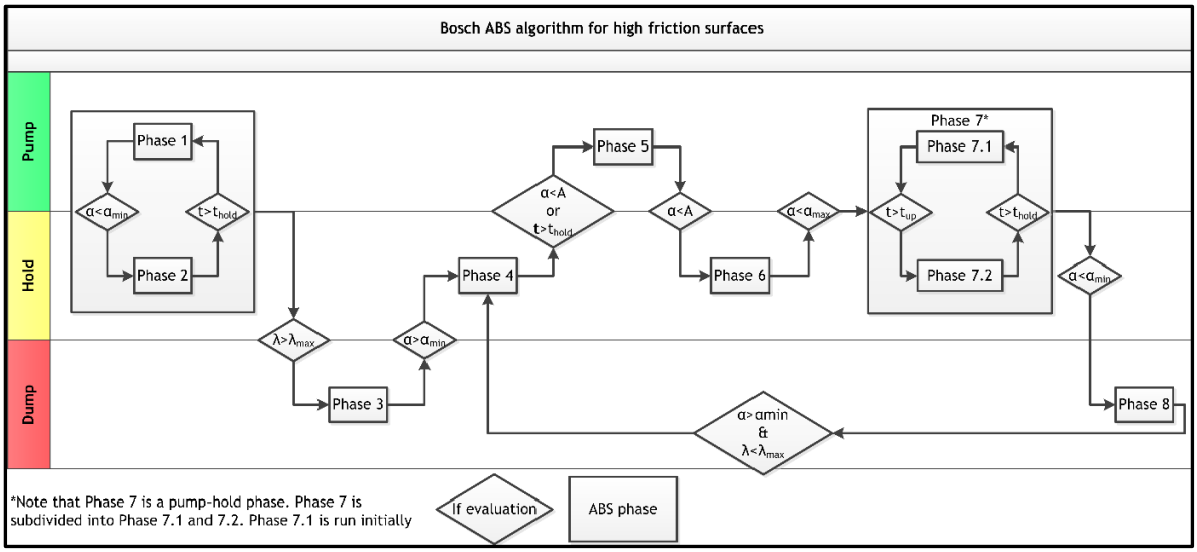

Figure A-3: A commercial ABS algorithm for high friction surfaces (Hamersma, 2017)

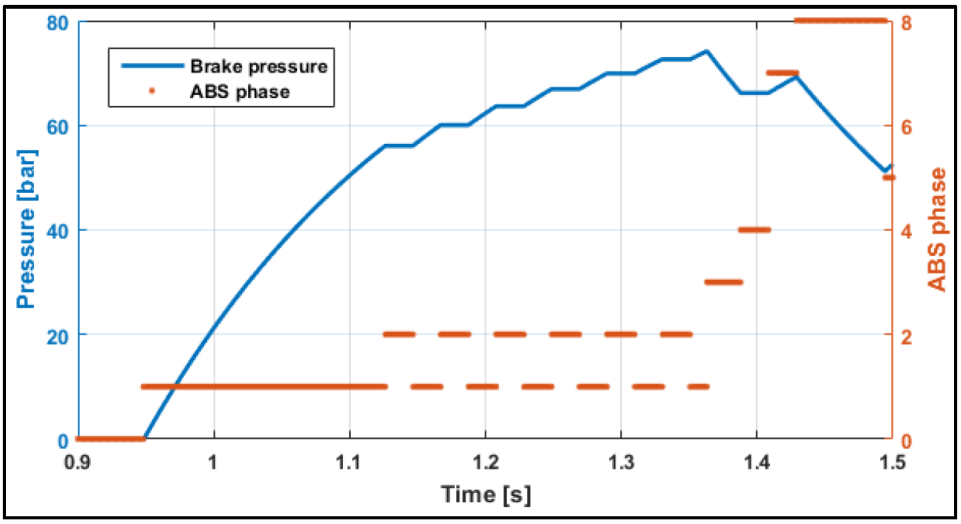

Figure A-4: Brake pressure modulation for one commercial ABS cycle (Hamersma, 2017)

Table A-1: Measured commercial ABS thresholds (Penny & Els, 2016)

Parameter	Value	Unit
A	25	rad/s^2
α_{max}	5	rad/s^2
α_{min}	-100	rad/s^2
λ_{max}	0.2	–
t_{up}	20	ms
t_{hold}	20	ms

APPENDIX B
STATE ESTIMATORS AND EVALUATORS

B.1 Sideslip angle estimator

Sideslip angle measurement is a well-known challenge among researchers and the general consensus is that it cannot be directly measured on typical production vehicles. Solutions such as digital image correlation (DIC) (Botha & Els, 2015) have been employed to accurately measure sideslip by optical means, however that requires having a camera pointed at the road surface which may be subject to environmental conditions that limit the possible applications. The difficulty of measuring sideslip has led to the development of countless published techniques of estimation, yet no single one is widely accepted as the 'gold-standard'. Chindamo, et al. (2018) summarizes the research efforts into two broad categories: observer based and neural-network based approaches. This study employs an observer-based method to estimate the lateral velocity as described by Equation B-1 from which the sideslip angle is calculated with Equation B-2.

$$\dot{\hat{v}}_y = a_y - \dot{\psi} v_x - K_{v_y}(a_y - \hat{a}_y(t, \hat{v}_y)) \tag{B-1}$$

$$\beta = \tan^{-1}\left(\frac{\hat{v}_y}{v_x}\right) \tag{B-2}$$

Where,

$$\hat{a}_y(t, \hat{v}_y) = \frac{\sum_{i=1}^{4} Y_i}{m} \tag{B-3}$$

Equation B-3 is the sum of tyre lateral forces, based on the last estimated normal force and tyre slip angles, divided by the vehicle mass. The 89 MF tyre model of Section 5.1 is used to calculate tyre lateral force. A gain K_{v_y} is chosen by cycling through a linear number range and choosing a value that minimizes the objective function shown in Equation B-4, where n is the number of sampling points.

$$q = \sum_{i=1}^{n}((\beta_{measured} - \beta_{estimated})^2) \tag{B-4}$$

The optimal gain value differs for different road conditions and vehicle speeds, however since this study mainly concerns a DLC done at $60\ km/h$, that is the speed for which the estimator is tuned. The data of the $60\ km/h$ DLC runs of Section 4.2 are used for tuning and comparing estimator results as shown in Figure B-1. In the figure, the right column shows the cost function output as function of gain and the left column a comparison between measured and

estimated sideslip values for the minimizing gain. The gain values of $K_{v_y} = 0.41$ and $K_{v_y} = 0.55$ are chosen for smooth and rough roads respectively. Selection of these gains result in an RMSE of $0.21°$ and $0.29°$ respectively, with 83.6% and 83.4% of absolute error values being below that RMSE, respectively. The results show that acceptable correlation is obtained with the sideslip estimator.

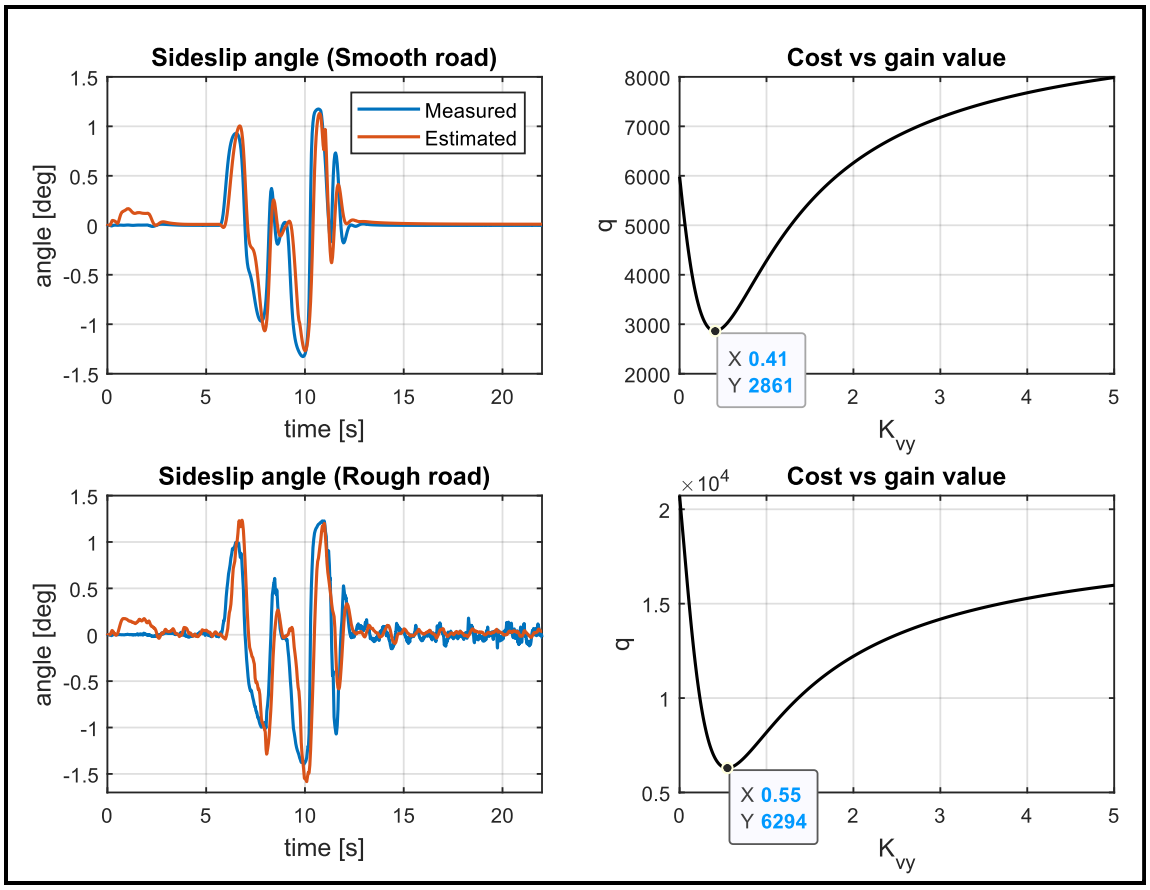

Figure B-1: The gain values which lower the cost function on different road conditions (right) and a comparison of the resulting sideslip estimator values against measured values (left) for a DLC at 60 km/h

B.2 Rear axle slip angle evaluator

The rear axle slip angle is obtained with Equation B-5 (Lenzo & De Castro, 2019) which simplifies the two tires per axle to one tyre placed in the middle of the axle, similar to the single track (bicycle) model.

$$\alpha_r = \tan^{-1}\left(\frac{\hat{v}_y - l_r \times \dot{\psi}}{v_x}\right) - \delta_r \qquad \text{(B-5)}$$

Figure B-2 shows a comparison of rear axle slip angle calculated with Equation B-5 against the measured value. The data of the $60\ km/h$ DLC runs of Section 4.2 are used as the measured value. In the figure, the measured value is directly measured in MSC Adams and is the numeric average of the two rear tires' slip angle. The smooth road run has an RMSE of 0.16° with 85.4% of absolute error values below that value and the rough road has an RMSE of 0.34°

with 80.1% of absolute error values below that value. The plot together with the RMSE values indicate that acceptable results are obtained with the evaluator.

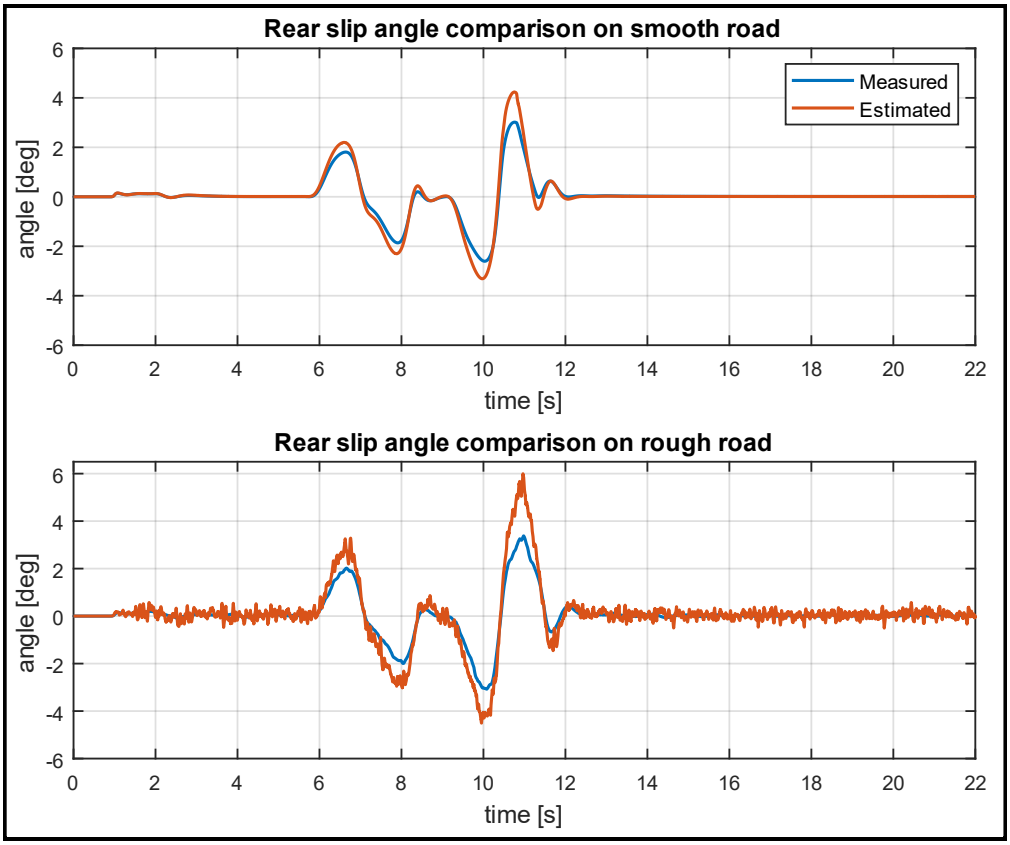

Figure B-2: A comparison of measured and estimated rear axle slip angle on a smooth (top) and rough (bottom) road for a DLC at 60 km/h

B.3 Tyre normal force estimator

A suspension force estimating Kalman filter is adapted to yield the tyre normal force (Hamersma & Els, 2021). The estimation process consists of two steps, the first estimates the states as in Equation B-6 where $z_i, i = 1 \ldots 4$ are the vertical displacements of the unsprung masses and z_5 the sprung mass displacement. The estimator takes the vertical acceleration data as input (Equation B-7) and updates the measurement based on the observation vector (Equation B-8).

$$\hat{x}_k = \begin{bmatrix} z_1 & \dot{z}_1 & z_2 & \dot{z}_2 & z_3 & \dot{z}_3 & z_4 & \dot{z}_4 & z_5 & \dot{z}_5 & \theta_x & \dot{\theta}_x & \theta_y & \dot{\theta}_y \end{bmatrix}^T \tag{B-6}$$

$$u_k = [\ddot{z}_1 \quad \ddot{z}_2 \quad \ddot{z}_3 \quad \ddot{z}_4 \quad \ddot{z}_5]^T \tag{B-7}$$

$$z_k = \begin{bmatrix} x_{FL} & x_{FR} & x_{RL} & x_{RR} & \dot{\theta}_x & \dot{\theta}_y & z_5 \end{bmatrix}^T \tag{B-8}$$

Step two estimates the states as in Equation B-9 where $z_{0i}, \mathrm{i} = 1 \ldots 4$ represents the road displacement experienced by that tyre based on the point-follower model. The estimator takes the estimated suspension forces as input (Equation B-10) and updates the observation based on the estimated unsprung mass displacements and velocities as in Equation B-11. Once the road displacements are estimated, the tyre normal force is calculated with

Equation B-12 where $k_t = 450 \times 10^3\ N/m$. The reader may refer to the published paper for the full system and gain matrices.

$$\hat{x}_k = [z_1 \quad \dot{z}_1 \quad z_{01} \quad z_2 \quad \dot{z}_2 \quad z_{02} \quad z_3 \quad \dot{z}_3 \quad z_{03} \quad z_4 \quad \dot{z}_4 \quad z_{04}]^T \tag{B-9}$$

$$u_k = [F_{FL} \quad F_{FR} \quad F_{RL} \quad F_{RR}]^T \tag{B-10}$$

$$z_k = [\hat{z}_1 \quad \dot{\hat{z}}_1 \quad \hat{z}_2 \quad \dot{\hat{z}}_2 \quad \hat{z}_3 \quad \dot{\hat{z}}_3 \quad \hat{z}_4 \quad \dot{\hat{z}}_4]^T \tag{B-11}$$

$$F_N = k_t \times (z_{0i} - z_i) \tag{B-12}$$

The estimator performance is verified by comparing its output to MSC Adams's directly measured tyre normal force. The comparison re-uses the DLC data of Section 4.2 for the case of $60\ km/h$ vehicle speed. Figure B-3 presents comparative tyre normal force curves for a smooth road and Figure B-4 a comparison of the signal FFTs. The same is presented for a rough road in Figure B-5 and Figure B-6. The figures show that the estimator is capable of predicting tyre normal force and better estimates signals with a higher normal force excitation frequency.

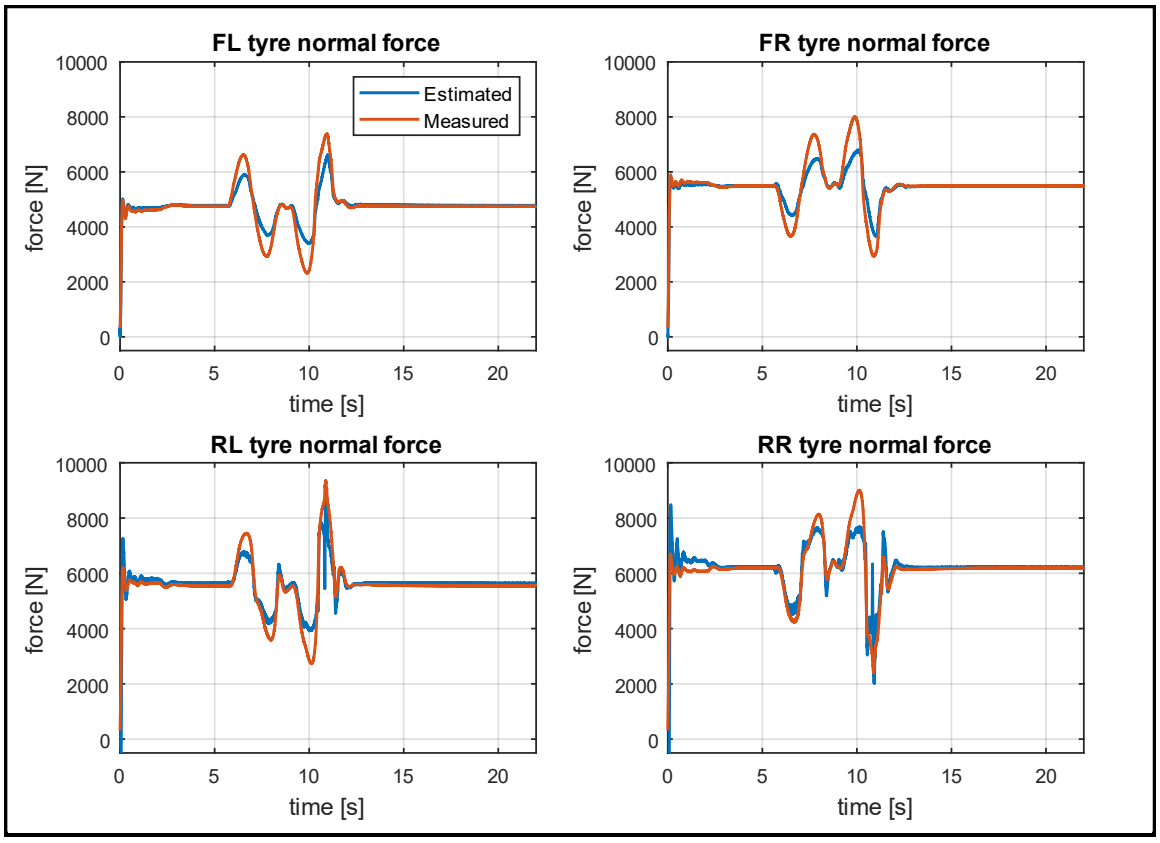

Figure B-3: Comparison of estimated and measured tyre normal force on a smooth road (DLC at 60 km/h)

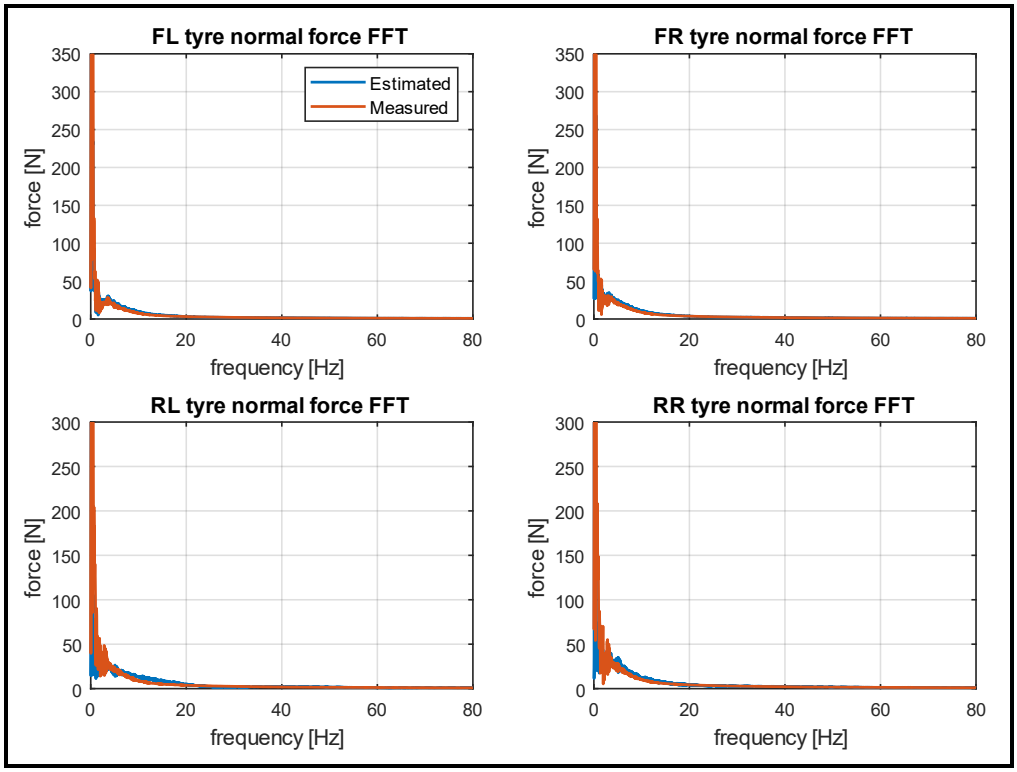

Figure B-4: Comparison of estimated and measured tyre normal force FFT on a smooth road (DLC at 60 km/h)

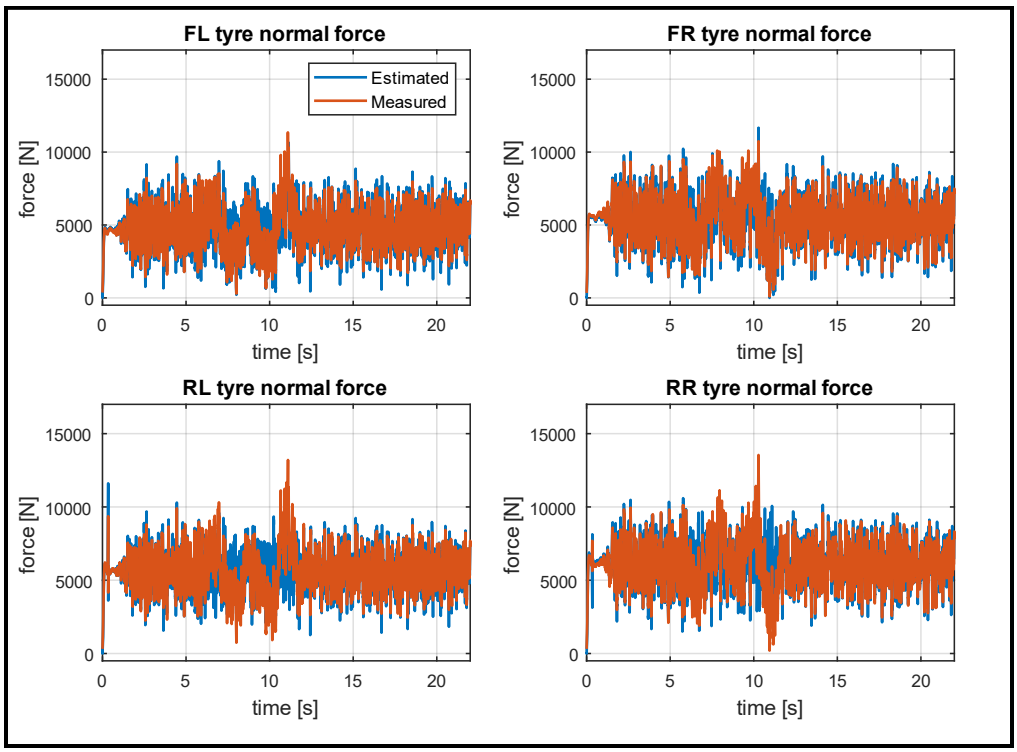

Figure B-5: Comparison of estimated and measured tyre normal force on a rough road (DLC at 60 km/h)

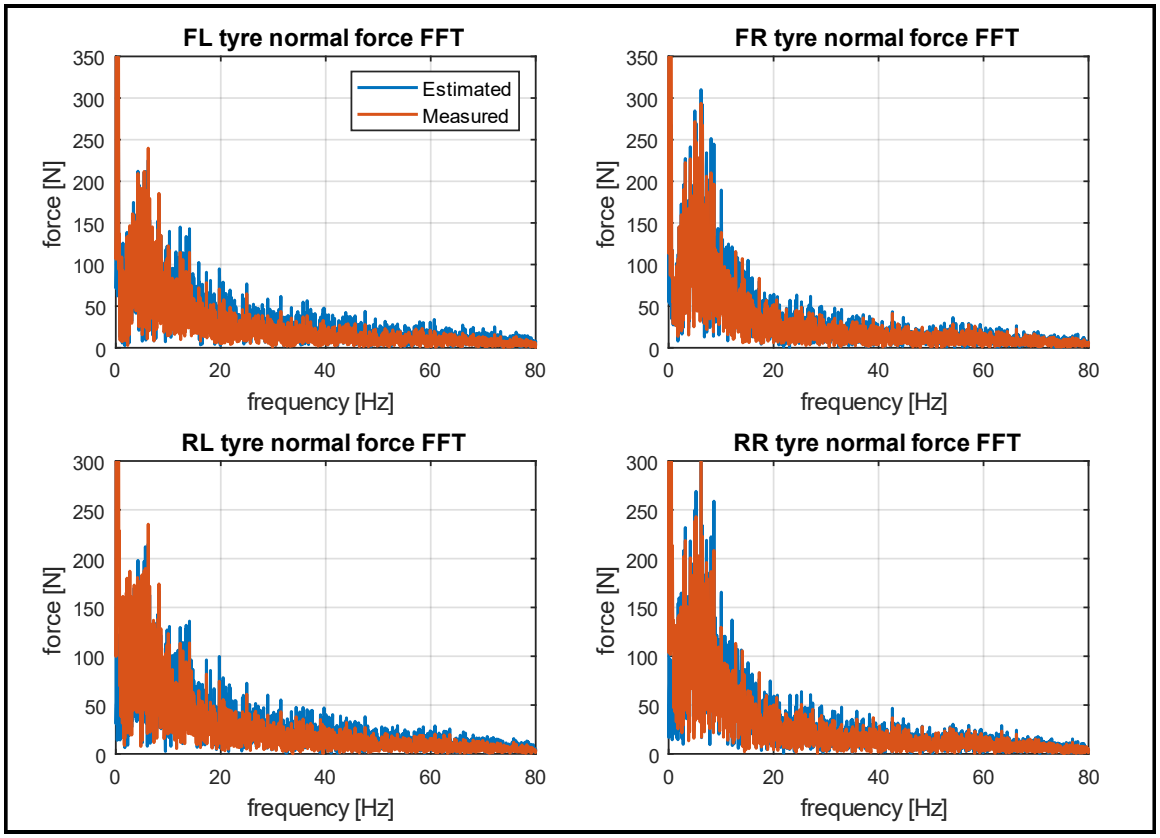

Figure B-6: Comparison of estimated and measured tyre normal force FFT on a rough road (DLC at 60 km/h)

APPENDIX C
ARS hardware model blocks

The active rear steering utilizes an SKF CASM-40-BS linear actuator paired with a BirCraft BALVDC-600-12-1 12 V motor for which the dynamic model including the steering links and wheels' inertia are shown in Figure C-1. The actuator model was developed by the VDG.

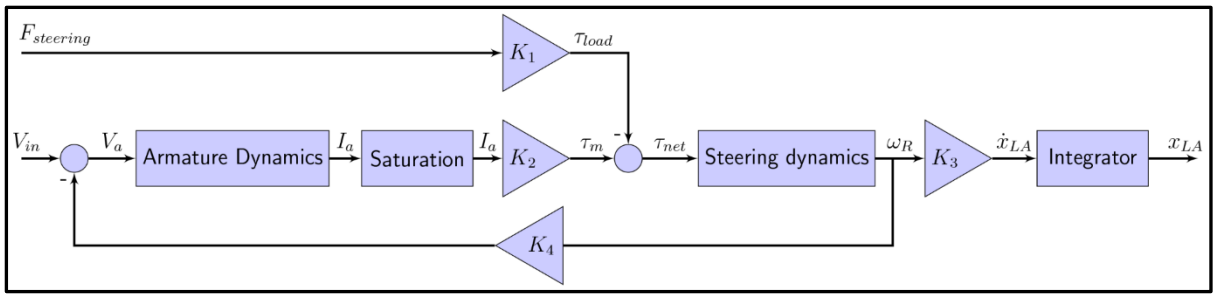

Figure C-1: The linear actuator emulating block diagram

In the diagram, the input V_{in} is a value from -12 V to 12 V and $F_{steering}$ the actuator imposed steering force. The motor current saturation limits are [-94.4 A, 94.4 A] and the gains K_1 … K_4 as formulated in Equation C-1 to Equation C-4. The armature dynamics are formulated in Equation C-5 and the steering dynamics in Equation C-6. The number of teeth on the linear actuator ($teeth_{LA}$) is 60 and on the motor ($teeth_m$) is 34. According to the specification sheet (SKF, 2018), the lead of the ball-screw linear actuator is 5 mm and its efficiency 85%.

$$K_1 = \frac{lead}{2\pi \times efficiency} \times \frac{teeth_{LA}}{teeth_m} \tag{C-1}$$

$$K_2 = 0.0351 \tag{C-2}$$

$$K_3 = \frac{0.005 \times lead(\frac{teeth_m}{teeth_{LA}})}{2\pi} \tag{C-3}$$

$$K_4 = 0.0351 \tag{C-4}$$

$$Armature\ dynamics = \frac{1}{0.00012s + 0.127} \tag{C-5}$$

$$Steering\ dynamics = \frac{1}{0.0030s} \tag{C-6}$$

APPENDIX D

Normalized radar plot polygon area

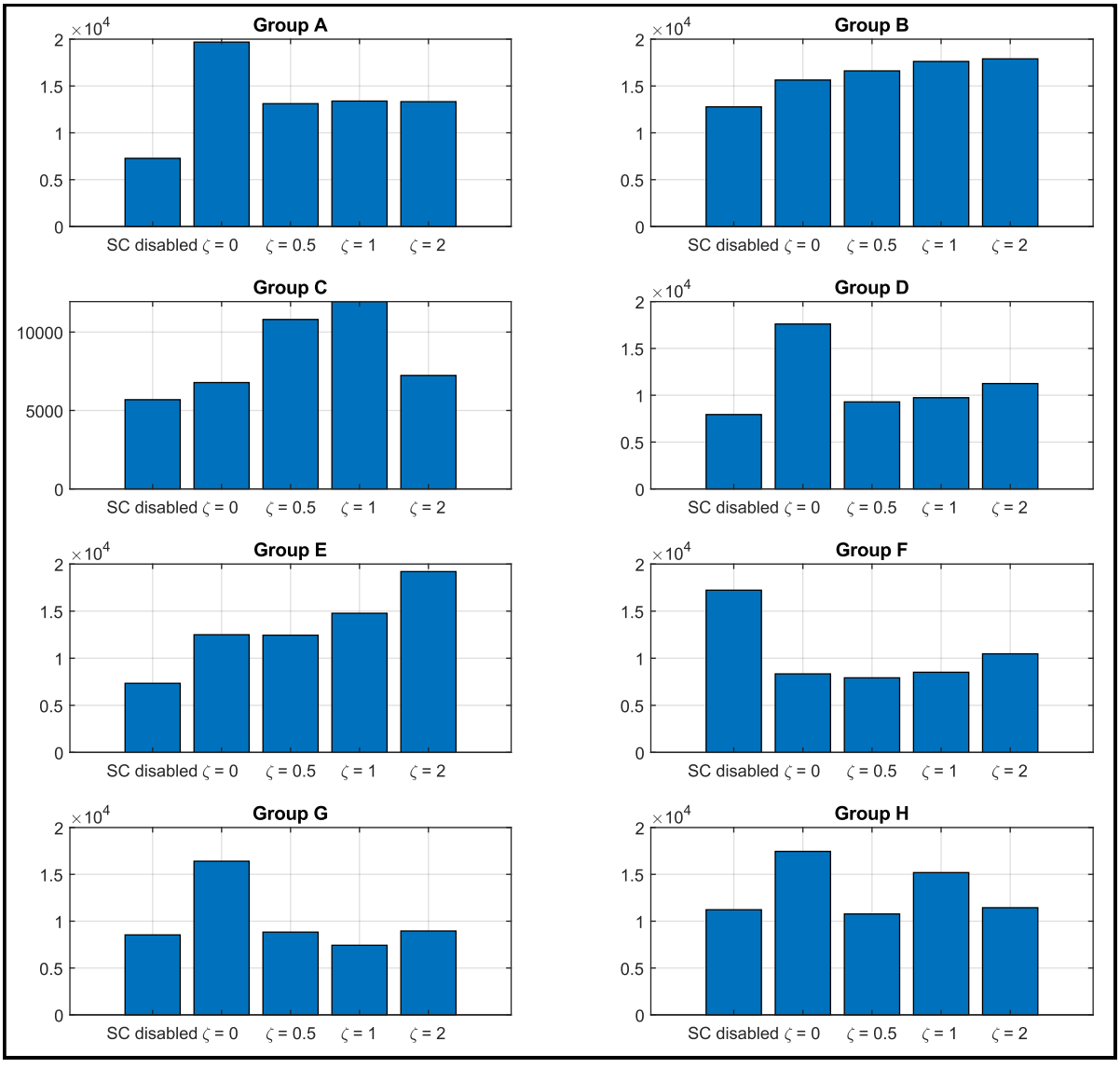

Figure D-1: Normalized radar plot polygon area for Group A-H of Figure 5-24